

Topological Sensitivity analysis in 3D time–harmonic dynamics in a viscoelastic layer

Alejandro E. Martínez-Castro* ¹, Inas H. Faris* ², and Rafael Gallego* ³

* Dept. Structural Mechanics, University of Granada

Ed. Politécnico de Fuentenueva, 18071 Granada, Spain

¹amcastro@ugr.es, ²inas@ugr.es, ³gallego@ugr.es (corresponding author)

Keywords: Topological Derivative, Inverse Problem, Lamb modes, Waveguides

Abstract. The use of the Topological Derivative as an image–method to elucidate an initial guess point to initiate inverse algorithms based on gradient computations is explored in this communication. The three-dimensional single layer domain in time–harmonics dynamics is considered.

The derivative of an specific cost function respect to the volume of a small cavity is obtained in terms of the properties of the non-damaged state (response when no cavity exists). The topological sensitivity is evaluated as a closed–form expression, in which an specific frequency–dependent term is added to the expression given for the static 3D problem.

Topological sensitivity is used as a basis for inverse identification in two approaches: i) the direct use of the topological sensitivity computation to plot a map of hidden shapes (not only cavities), combining multi-frequency experiments, and ii) the use of the volume series expansion of the cost function to predict the size of hidden cavities.

Numerical tests have been done in order to validate topological sensitivity evaluation, and both kind of approaches are explored for some multi-frequency experiments.

Introduction

The identification of defects (ellipsoidal cavities) in a 3D viscoelastic solid is mathematically treated as an optimization problem. The different algorithms require an initial guess point, because the solution is strongly dependent on this first step. The topological sensitivity is an image method that predicts an initial shape and location of the cavities. In this work, the technique is explored in the context of a particular 3D elastodynamic problem.

The solid in this case is a single layer, a three-dimensional solid limited by two parallel planes. The identification of a parameterized cavity requires a cost function. Such function is built, for a trial position of the cavity, through the misfit between the experimental data measurements at selected points, and the one obtained solving the forward problem for the trial position of the cavity.

The Topological Sensitivity (or Topological Derivative) of some variable dependent on the size of a small cavity is the slope at the origin of the expansion curve in terms of the cavity volume. The use of this derivative in the context of Boundary Integral Equations was first introduced by Gallego and Rus [1] in the context of elastostatic 2D problems. Since that, the number of papers focused on the Topological Derivative as an image method to solve inverse identification problems has increased. For 2D problems, see works by Gallego and Rus [1–4]. In the context of 3D problems, Guzina and Bonnet have presented important contributions [6–8]. Also Faris and Gallego [5] have presented the topological sensitivity in 3D elastic solids based on the standard Boundary Integral Equation. The present work extends topological sensitivity approach to 3D elastodynamic problems.

Direct Problem

In reference to Figure 1, the host domain is a three–dimensional layer Ω , thickness h . The identification cavity is an sphere, centered at \mathbf{z} and radius r . Let Γ_z be the cavity boundary. In reference to the cartesian basis

$\{O; x_1, x_2, x_3\}$, it is defined the region $\Omega = \{(x_1, x_2, x_3) | 0 \leq x_3 \leq h\}$. At certain points \mathbf{x}^f corresponding to the upper layer, a set of time-harmonics sources are considered.

$$\mathbf{f}(\mathbf{x}) = \sum_{m=1}^{NS} P_m e^{i\omega t} \delta(\mathbf{x} - \mathbf{x}^f) \quad (1)$$

Also, a set of observation (or measurement points) are considered, \mathbf{x}^m in which displacements \mathbf{u}^m are measured for each cavity location, and compared with experimental measurements \mathbf{u}^e .

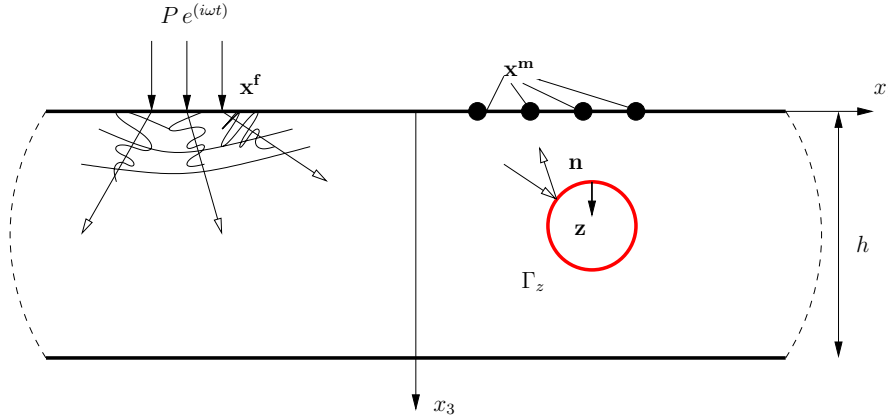


Figure 1: Spherical cavity in a single layer domain. Sources and measurement points

The material is elastic, isotropic (λ, μ) and density ρ . Damping is included through rates ξ_α y ξ_β and the complex-valued material modules $\lambda = \lambda^*$ y $\mu = \mu^*$, corresponding principle [9].

$$\begin{aligned} \lambda^* + 2\mu^* &= (\lambda + 2\mu) [1 + 2i\xi_\alpha(\omega)], & \xi_\alpha &\geq 0 \\ \mu^* &= \mu [1 + 2i\xi_\beta(\omega)], & \xi_\beta &\geq 0 \end{aligned}$$

The boundary conditions for the upper and lower surfaces of Ω are $\mathbf{t} = 0$ (traction-free). The layer is infinite in directions x_1, x_2 ; thus, the radiation boundary condition is applied at these directions. At the cavity surface Γ_z traction-free condition is imposed ($\mathbf{t} = 0$). See at figure (1) the outward normal \mathbf{n} in Γ_z .

The forward problem is the computation of displacements \mathbf{u} at Γ . This problem is numerically solved by the Boundary Element Method, including an specific Green function for the layer [10].

Topological sensitivity boundary integral equation

At this domain Ω , bounded by the parallel planes Γ , the displacement \mathbf{u} at an internal point $\mathbf{y} \in \Omega$ is computed by evaluating the Green function. This problem will be called the *Non-Damaged State*. The presence of a traction-free small cavity bounded by Γ_z located at \mathbf{z} produces the modified displacement field $\tilde{\mathbf{u}}$ at \mathbf{y} . This second state will be called the *Damaged State*. The Boundary Integral Equation (BIE) for the internal displacement field $\tilde{\mathbf{u}}$ is

$$c_k^i(\mathbf{y}) \tilde{u}_k(\mathbf{y}) = - \int_{\Gamma_z} t_k^i(\mathbf{x}; \mathbf{y}) \tilde{u}_k(\mathbf{x}) d\Gamma(\mathbf{x}) \quad (2)$$

with $c_k^i = \delta_k^i$ the Kronecker Delta and t_k^i is the traction Green's function.

The displacement field at the cavity boundary can be split as $\tilde{u}_k = u_k^0 + \delta \tilde{u}_k$, where u_k^0 is a rigid solid displacement, and $\delta \tilde{u}_k$ is the displacement field relative to the center \mathbf{z} due to the local state of stresses.

The second-term in Eq. (2) can be transformed, by applying the Divergence Theorem at Γ_z , and taking into account the sing of the normal \mathbf{n} , as:

$$\int_{\Gamma_z} t_k^i(\mathbf{x}; \mathbf{y}) \tilde{u}_k(\mathbf{x}) d\Gamma(\mathbf{x}) = \frac{4}{3} \pi r^3 \rho \omega^2 u_j^i(\mathbf{z}; \mathbf{y}) u_j^0(\mathbf{z}) + \sigma_{jk}^i(\mathbf{z}; \mathbf{y}) \int_{\Gamma_z} n_j(\mathbf{x}) \delta u_k^\infty(\mathbf{x}) d\Gamma(\mathbf{x}) \quad (3)$$

with u_j^i the Displacement Green's Function; u_j^0 the displacement field at the Non Damaged State at the cavity center, evaluated with the Green's function; σ_{jk}^i is the traction Green's function.

The integral term in Eq. (3) includes displacement field δu_k^∞ . This field is the solution of the static displacement field at the cavity embedded at the 3D infinite space, applying uniform remote tensions $\sigma_{ij}(\mathbf{z})$.

The integral can be evaluated as a closed-form formula, considering:

$$\sigma_{jk}^i(\mathbf{z}; \mathbf{y}) \int_{\Gamma_z} n_j(\mathbf{x}) \delta u_k^\infty(\mathbf{x}) d\Gamma(\mathbf{x}) = \frac{4}{3} \pi r^3 \sigma_{jk}^i I_{jk} \quad (4)$$

with tensor I_{jk} evaluated as:

$$\begin{aligned} I_{jk} &= - \left[A \sigma_{jk}^\infty - B \delta_{jk} \sigma_{ii}^\infty \right] \frac{1}{\mu} \\ A &= \frac{15(1-\nu)}{2(7-5\nu)} \\ B &= \frac{3(1-\nu)(1+5\nu)}{4(7-5\nu)(1+\nu)} \end{aligned} \quad (5)$$

The Topological Derivative is defined as the first-derivative of $\tilde{u}_k(\mathbf{y})$ respect to the cavity volume $V = \frac{4}{3} \pi r^3$ of ; thus

$$\frac{\partial \tilde{u}_k(\mathbf{y})}{\partial V} = -\rho \omega^2 u_j^k(\mathbf{z}; \mathbf{y}) u_j^0(\mathbf{z}) - \sigma_{ji}^k(\mathbf{z}; \mathbf{y}) I_{ji} \quad (6)$$

Topological Sensitivity of the Cost Function

Equation (6) permits the computation of the first volume derivative for all the displacements and related variables. In the context of Inverse Problems, the interest is focused on the Cost Function and its sensitivity equation. For this problem, the cost function is split into two terms: discrepancy between measurement and experimental points, and some a-priori volume information. Thus,

$$\mathcal{J}(\Gamma) = \frac{Q}{2} \sum_{n=1}^{NEP} (\overline{\mathbf{u}^m} - \mathbf{u}^e) \cdot (\mathbf{u}^m - \mathbf{u}^e) + \frac{G}{2} (V - V^{ref})^2 \quad (7)$$

with NEP the number of experimental points in \mathbf{x}^m where response is measured. Parameters Q and G are coefficients used to weight the a-priori data, and the global cost function.

Taking into account the volume derivative of displacement given in Eq. (6) the Topological Sensitivity of the Cost Function can be written as:

$$\mathcal{T}(\mathbf{z}) = \frac{\partial \mathcal{J}}{\partial V} = Q \sum_{n=1}^{NEP} (\overline{\mathbf{u}^m} - \mathbf{u}^e) \cdot \delta \mathbf{u}^m - G V^{ref} \quad (8)$$

This value depends on the center position \mathbf{z} . It can be computed at each point in a domain. An heuristic approach common in the literature consider that possible cavity location is given by the set of points in which $\mathcal{T} < 0$, because it means that, at such locations, the presence of a cavity contributes to reduce the cost function. Combined with multi-frequency tests it is possible to elucidate the shapes of the internal hidden objects.

$\{O; x_1, x_2, x_3\}$, it is defined the region $\Omega = \{(x_1, x_2, x_3) | 0 \leq x_3 \leq h\}$. At certain points \mathbf{x}^f corresponding to the upper layer, a set of time-harmonics sources are considered.

$$\mathbf{f}(\mathbf{x}) = \sum_{m=1}^{NS} P_m e^{i\omega t} \delta(\mathbf{x} - \mathbf{x}^f) \quad (1)$$

Also, a set of observation (or measurement points) are considered, \mathbf{x}^m in which displacements \mathbf{u}^m are measured for each cavity location, and compared with experimental measurements \mathbf{u}^e .

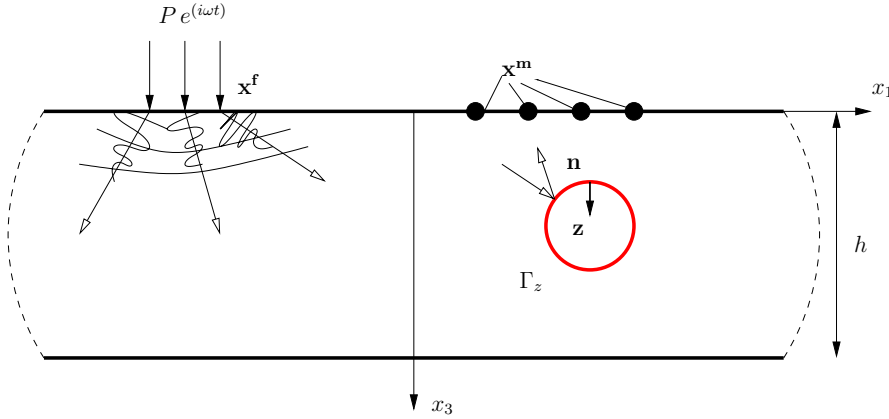


Figure 1: Spherical cavity in a single layer domain. Sources and measurement points

The material is elastic, isotropic (λ, μ) and density ρ . Damping is included through rates ξ_α y ξ_β and the complex-valued material modules $\lambda = \lambda^*$ y $\mu = \mu^*$, corresponding principle [9].

$$\begin{aligned} \lambda^* + 2\mu^* &= (\lambda + 2\mu) [1 + 2i\xi_\alpha(\omega)], & \xi_\alpha &\geq 0 \\ \mu^* &= \mu [1 + 2i\xi_\beta(\omega)], & \xi_\beta &\geq 0 \end{aligned}$$

The boundary conditions for the upper and lower surfaces of Ω are $\mathbf{t} = 0$ (traction-free). The layer is infinite in directions x_1, x_2 ; thus, the radiation boundary condition is applied at these directions. At the cavity surface Γ_z traction-free condition is imposed ($\mathbf{t} = 0$). See at figure (1) the outward normal \mathbf{n} in Γ_z .

The forward problem is the computation of displacements \mathbf{u} at Γ . This problem is numerically solved by the Boundary Element Method, including an specific Green function for the layer [10].

Topological sensitivity boundary integral equation

At this domain Ω , bounded by the parallel planes Γ , the displacement \mathbf{u} at an internal point $\mathbf{y} \in \Omega$ is computed by evaluating the Green function. This problem will be called the *Non-Damaged State*. The presence of a traction-free small cavity bounded by Γ_z located at \mathbf{z} produces the modified displacement field $\tilde{\mathbf{u}}$ at \mathbf{y} . This second state will be called the *Damaged State*. The Boundary Integral Equation (BIE) for the internal displacement field $\tilde{\mathbf{u}}$ is

$$c_k^i(\mathbf{y}) \tilde{u}_k(\mathbf{y}) = - \int_{\Gamma_z} t_k^i(\mathbf{x}; \mathbf{y}) \tilde{u}_k(\mathbf{x}) d\Gamma(\mathbf{x}) \quad (2)$$

with $c_k^i = \delta_k^i$ the Kronecker Delta and t_k^i is the traction Green's function.

The displacement field at the cavity boundary can be split as $\tilde{u}_k = u_k^0 + \delta\tilde{u}_k$, where u_k^0 is a rigid solid displacement, and $\delta\tilde{u}_k$ is the displacement field relative to the center \mathbf{z} due to the local state of stresses.

Table (1) shows that Eq.(6) is correct. At higher frequencies, results shows better results, according to the properties of the Green's function.

Once the displacement are validated, a set of numerical tests have been done to validate the use of the Topological Derivative in the context of inverse identification problems. As occurs with other works published in the literature, the authors show that, for this domain, the Topological Derivative can be used to give good initial guesses solutions, or even, combining tests at several frequencies, produces solutions of the inverse problem.

References

- [1] R. Gallego and G. Rus. Identification of Cracks and Cavities Using the Topological Sensitivity Boundary Integral Equation. *Proc. IABEM 2002 Conference. Austin, Texas*, (2002)
- [2] G. Rus and R. Gallego. Boundary integral equation for inclusion and cavity shape sensitivity in harmonic elastodynamics. *Engineering Analysis with Boundary Elements* , **29**, 77–91 (2005)
- [3] R. Gallego and G. Rus. Identification of cracks and cavities using the topological sensitivity boundary integral equation. *Computational Mechanics* , **33**, 154–163 (2004)
- [4] L. Comino, R. Gallego and G. Rus. Combining topological sensitivity and genetic algorithms for identification inverse problems in anisotropic materials *Computational Mechanics* , **41**, 231–242 (2008)
- [5] I. H. Faris and R. Gallego. Determination of the elastic response of materials with defects in three dimensional domains using BEM and Topological Derivative. *Proceedings of the Boundary Element Techniques Conference* , 107–112 (Seville, Spain, 2008)
- [6] B. B. Guzina, M. Bonnet, Topological Derivative for the Inverse Scattering of Elastic Waves, *Q. Jl. Mech. Appl. Math.* **57**, 161–179, (2004)
- [7] M. Bonnet, B. B. Guzina, Sounding of finite solid bodies by way of topological derivative, *International Journal for Numerical Methods in Engineering* **61**, 2344–2373, (2004)
- [8] B. B. Guzina and M. Bonnet, Small-inclusion asymptotic of misfit functionals for inverse problems in acoustics, *Inverse Problems* **22**, 1761–1785, (2006)
- [9] R. M. Christensen, *Theory of viscoelasticity*, Academic Press, New York (1971).
- [10] A. Martínez-Castro y R. Gallego. Three-dimensional Green's function for time-harmonic dynamics in a viscoelastic layer. *International Journal of Solids and Structures*, **44**, 4541–4558 (2007)

Wear prediction in tribometers using a 3D Boundary Elements formulation

L. Rodríguez-Tembleque^{1*}, R. Abascal², M.H. Aliabadi³

¹ Departamento de Mecánica de los Medios Continuos, Escuela Técnica Superior de Ingenieros, Camino de los descubrimientos s/n, E41092 Sevilla, SPAIN

luisroteso@us.es

² Departamento de Mecánica de los Medios Continuos, Escuela Técnica Superior de Ingenieros, Camino de los descubrimientos s/n, E41092 Sevilla, SPAIN

abascal@us.es

³Department of Aeronautics, Faculty of Engineering, Imperial College, South Kensington Campus, London SW7 2AZ, UK

m.h.aliabadi@imperial.ac.uk

Keywords: Boundary Elements Method, Contact Mechanics, Rolling-Contact, Wear Simulation, Wear Modeling.

Abstract. The present work shows a new methodology for wear simulation in contact and rolling-contact 3D problems applied to wear prediction in tribometers. The formulation is based on the Boundary Element method (BEM) for computing the elastic influence coefficients, and on projection functions over the augmented Lagrangian for contact restrictions fulfilment. The material loss of the bodies is modeled using the Archard's linear wear law. The methodology is applied to simulate wear on pin-on-disc and twin-disc tribometers. Results will show the total wear depth evolution in every case, compared with other specific formulation on the literature related to wear and tribometers.

Introduction

Wear study in mechanical components is often tackled experimentally using tribometers (pin-on-disc and twin-disc). The present work applied the Boundary Elements methodology developed in [1] and based on [2, 3] and [4], to the study of wear in these systems. The resulting wear depths computed are compared using the Global Incremental Wear Model (GIWM) presented by Hegadekatte [5] and the Pödra and Andersson's Model (PAM) presented in [6].

The present formulation is based on the Boundary Element method (BEM) for computing the elastic influence coefficients, and on projection functions over the augmented Lagrangian for contact restrictions fulfilment. The material loss of the bodies is modelled using the Archard's linear wear law which is one of the most used models for engineering applications. The methodology is applied to wear prediction in tribometers, but is general and valid for different wear problems. The validation of the formulation is carried out simulating wear on different kind of tribometers which have been previously studied in models such as [6] and [7, 5].

Contact kinematic equations

Modeling wear on the contact surfaces of two bodies requires to include the wear depth variable on the contact kinematic equations. Consequently, the contact gap for the pair I of nodes in contact, can be expressed for the instant (k) as:

$$(\mathbf{k}^{(k)})_I = (\mathbf{u}^{2(k)})_I - (\mathbf{u}^{1(k)})_I + (\mathbf{k}_{go}^{(k)})_I + (\mathbf{C}_{gn} \mathbf{w}^{(k)})_I, \quad (1)$$

where \mathbf{k} is the contact pairs gap vector, \mathbf{u}^α is the solid Ω^α ($\alpha = 1, 2$) nodal displacements vector, \mathbf{k}_{go} is the sum of the contact pairs geometric gap vector and the relative rigid body motions, \mathbf{w} is the contact pairs wear depth, and \mathbf{C}_{gn} is a boolean matrix which establishes the relation between the normal component of contact pairs gap and the wear depth.

Rolling kinematic equations

For rolling contact problems, it has to be considered the tangential slip velocity distribution for every rotation (k). Vector \mathbf{s}_t stores the tangential slip velocity of every contact pair I , $(\mathbf{s}_t)_I$, which can be written as [4]

$$(\mathbf{s}_t^{(k)})_I = (\bar{\mathbf{c}})_I + \mathbf{D}_r(\mathbf{k}_t^{(k)})_I \quad (2)$$

being $(\mathbf{k}_t)_I$ the pair I tangential slip vector, $(\mathbf{s}_t)_I$ the pair I slip velocity vector, $(\bar{\mathbf{c}})_I$ the pair I creep vector, and \mathbf{D}_r is an algebraic matrix operator:

$$\mathbf{D}_r = \begin{bmatrix} v_{t,1} \frac{\partial}{\partial X_{t1}} + v_{t,2} \frac{\partial}{\partial X_{t2}} & 0 \\ 0 & v_{t,1} \frac{\partial}{\partial X_{t1}} + v_{t,2} \frac{\partial}{\partial X_{t2}} \end{bmatrix} \quad (3)$$

Modeling the bodies

The boundary integral equations for a body Ω , can be written in a matrix form as:

$$\mathbf{H}\mathbf{u} - \mathbf{G}\mathbf{p} = \mathbf{F} \quad (4)$$

where the vector \mathbf{u} represents the nodal displacements, and \mathbf{F} contains the applied boundary conditions. These equations are well known and can be found in many books like [8] or [9].

For the two bodies Ω^α ($\alpha = 1, 2$) in contact, the Equations (4) have to be regrouped as:

$$\mathbf{A}_x^\alpha \mathbf{x}^\alpha + \mathbf{A}_p^\alpha \mathbf{p}_c^\alpha = \mathbf{F}^\alpha \quad (5)$$

where \mathbf{x}^α is the nodal unknowns vector which contains the unknowns outside the potential contact zone (\mathbf{x}_p^α), and the nodal displacements vector on the potential contact zone (\mathbf{u}_c^α). \mathbf{p}_c^α is the nodal contact tractions vector, \mathbf{A}_x^α are the columns of \mathbf{H}^α and \mathbf{G}^α matrices, and \mathbf{A}_p^α are the columns of \mathbf{G}^α matrix corresponding to the contact nodes.

The equations (1) and (5), can be rewritten for two solids contact, in the following way:

$$\mathbf{R}^1 \mathbf{x}^1 + \mathbf{R}^2 \mathbf{x}^2 + \mathbf{R}_\lambda \boldsymbol{\Lambda} + \mathbf{R}_g \mathbf{k} - \mathbf{F} = \mathbf{0}, \quad (6)$$

being,

$$\mathbf{R}^1 = \begin{bmatrix} \mathbf{A}^1 \\ \mathbf{0} \\ (\mathbf{C}_1)^T \end{bmatrix} \quad \mathbf{R}^2 = \begin{bmatrix} \mathbf{0} \\ \mathbf{A}^2 \\ -(\mathbf{C}_2)^T \end{bmatrix} \quad \mathbf{R}_\lambda = \begin{bmatrix} \mathbf{A}_p^1 \tilde{\mathbf{C}}_1 \\ -\mathbf{A}_p^2 \tilde{\mathbf{C}}_2 \\ \mathbf{0} \end{bmatrix} \quad (7)$$

$$\mathbf{R}_g = \begin{bmatrix} \mathbf{0} \\ \mathbf{0} \\ \mathbf{C}_g \end{bmatrix} \quad \mathbf{F} = \begin{bmatrix} \mathbf{b}^1 \\ \mathbf{b}^2 \\ \mathbf{C}_g \mathbf{k}_{g0} \end{bmatrix} + \begin{bmatrix} \mathbf{0} \\ \mathbf{0} \\ \mathbf{C}_{g_n} \mathbf{w}^{(k)} \end{bmatrix}$$

\mathbf{C}_α ($\alpha = 1, 2$) is a boolean matrix which allows to extract the contact nodes displacements from \mathbf{x}^α , and \mathbf{C}_g is the identity matrix ($\mathbf{C}_g = \mathbf{I}$).

Contact model

The rolling contact restrictions for every contact pair I are summarized in: the *Non-penetration condition*, the *Coulomb friction law* and the *Principle of maximum energy dissipation*. The mathematical expressions for these contact restrictions, can be classified into two groups: normal and tangential.

- *Normal direction*: The unilateral contact conditions can be written, in the form of a complementarity relation, as:

$$(\mathbf{k}_n)_I \geq 0 \quad ; \quad (\mathbf{p}_n)_I \leq 0 \quad ; \quad (\mathbf{p}_n)_I (\mathbf{k}_n)_I = 0 \quad (8)$$

- *Tangential direction*: For tangential direction, the fulfilment of friction law and principle of maximum dissipation is guaranteed by:

$$\|(\mathbf{p}_t)_I\| \leq \mu |(\mathbf{p}_n)_I| \quad ; \quad (\mathbf{s}_t)_I = -\lambda(\mathbf{p}_t)_I \quad ; \quad \lambda \geq 0 \quad ; \quad (\mathbf{s}_t)_I (\|(\mathbf{p}_t)_I\| - \mu |(\mathbf{p}_n)_I|) = \mathbf{0} \quad (9)$$

Using the projection defined in [4, 10], over the augmented tractions, the rolling contact restrictions (8-9) can be written as

$$\begin{aligned} (\mathbf{p}_n)_I &= \mathbb{P}_n [(\mathbf{p}_n)_I + r_n(\mathbf{k}_n)_I] \\ (\mathbf{p}_t)_I &= \mathbb{P}_t [(\mathbf{p}_t)_I - r_t(\mathbf{s}_t)_I] \end{aligned} \quad (10)$$

Wear model

One of the most used model for engineering applications is the linear wear equation, the Archard's wear law (Archard, 1953). This law considers that the wear arises from the adhesive forces set up when atoms come into intimate contact. This kind of wear is known as a *Delamination Wear* and it occurs when the sliding speed remains at low levels, such as the surface heating can be neglected, and the applied load not exceed a limit where seizure takes place. The expression for the Archard's wear law could be written as:

$$W_w = k_w F_n D_s \quad (11)$$

and shows that the volumetric wear of one body is proportional to the product between the applied load and the sliding distance (D_s). The constant k_w is defined as: $k_w = K/H$, where the constants K and H are respectively, the non-dimensional wear coefficient and the hardness of the material in contact. For Archard [11], the constant K represents the probability that a fragment will be formed at an adhesive joint resulting in a wear particle.

In order to simulate numerically the wear on contact surfaces, we can write (11) in a differential equation form, for every contact pair I , as

$$(\dot{w})_I = k_w (\mathbf{p}_n)_I \|(\mathbf{s}_t)_I\| \quad (12)$$

using the nodal wear depth vector (w), the nodal normal pressure vector (\mathbf{p}_n), and the nodal tangential slip vector (\mathbf{s}_t).

The wear depth is computed from the tangential slip ratios, for contact problems, or from the slip velocity, for rolling-contact problems. The contact pair I wear depth for an instant (or rotation) (k) is expressed in an incremental form

$$(\mathbf{w}^{(k)})_I = (\mathbf{w}^{(k-1)})_I + (\Delta \mathbf{w}^{(k)})_I \quad (13)$$

where the pair I wear depth increment ($(\Delta \mathbf{w}^{(k)})_I$) is computed for a contact simulation, as:

$$(\Delta \mathbf{w}^{(k)})_I = k_w (\mathbf{p}_n^{(k)})_I \|(\mathbf{k}_t^k)_I - (\mathbf{k}_t^{(k-1)})_I\| \quad (14)$$

and for a rolling contact simulation, as: $(\Delta \mathbf{w}^{(k)})_I = (\Delta \mathbf{w}^{(k)})_{\Pi_r}$, being

$$(\Delta \mathbf{w}^{(k)})_{\Pi_r} = \sum_{I \in \{\Gamma_c \cap \Pi_r\}}^{N_I} \Delta \tau k_w (\mathbf{p}_n^{(k)})_I \|(\mathbf{s}_t^{(k)})_I\| \quad (15)$$

Expression (15) calculates the wear depth increment for every contact pair I belonging to the rotation plane Π_r , being (k) the number of rotations. N_I is the number of contact pairs that are located in the rotation direction (parallel to V), $\Delta t = T/N_I$, and T is the solid particle time of residence of a solid particle in the contact zone, traveling with velocity V . The same scheme is used by Jendel in [12], but considering, in this work, the elastic slip velocity.

Results

Next some numerical examples are going to be presented. All of them are solved using the iterative algorithm presented in [1].

Example1. Pin-on-disc

To validate the formulation the pin-on-disc experiment, Figure 1a, is initially considered. Pödra and Andersson [6] and Hegadekatte et al. [7, 5] proposed two models to estimate the wear depth evolution in this kind on systems. The Pödra and Andersson's Model (PAM) and the Hegadekatte's one (Global Incremental Wear Model: GIWM) are compared, in terms of wear depth, with the proposed formulation BEM Wear Model (BEMWM).

Figure 1b shows the wear depth evolution for a pin on a rotating disc as a function of the sliding distance. The parameters of the problem are:

material	silicon nitride (Si_3N_4)
wear coefficient (k_w [mm^2/N])	$13.5 \cdot 10^{-9}$
Young's modulus (E_p, E_d [N/mm^2])	$304 \cdot 10^3$
Poisson's ration (ν)	0.24
Normal load (F_n [N])	$200 \cdot 10^{-3}$

The BEM simulation approximates the solids domains by a elastic half-space, discretizing the boundary with a quadrilateral mesh elements.

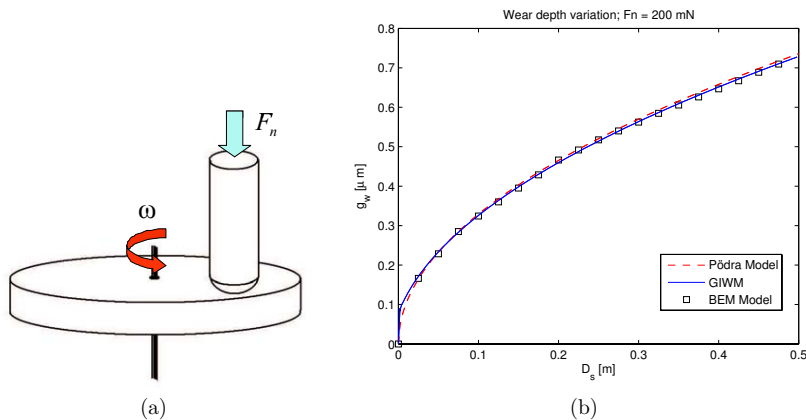


Figure 1: (a) Schematic of the Pin-on-Disc tribometer. (b) Wear depth evolution for a pin as a function of the sliding distance, comparing the results from the PAM, the GIWM and the BEM wear model, for a normal load of 200 mN.

Example2. Twin-disc

The next example is a twin-disc tribometer (see Figure 2a) example. The applied normal force is $F = 300N$, the discs geometric parameters are: $R_{11} = 32.5mm$, $R_1 = 125mm$ and $R_2 = 32.3mm$, $Creep = 0.5\%$ and 0.5% , the materials properties: $E_1 = E_2 = 208 \cdot 10^3 N/mm^2$ and $\nu = 0.3$, and the wear coefficient: $k_w = 2 \cdot 10^{-6} mm^2/N$. The BEM simulation approximates the solids domains by a elastic half-space, discretizing the boundary with a quadrilateral mesh elements.

Figure 2b shows the total wear depth evolutions during 30000 rotations, obtained for the BEMWM and the GIWM.

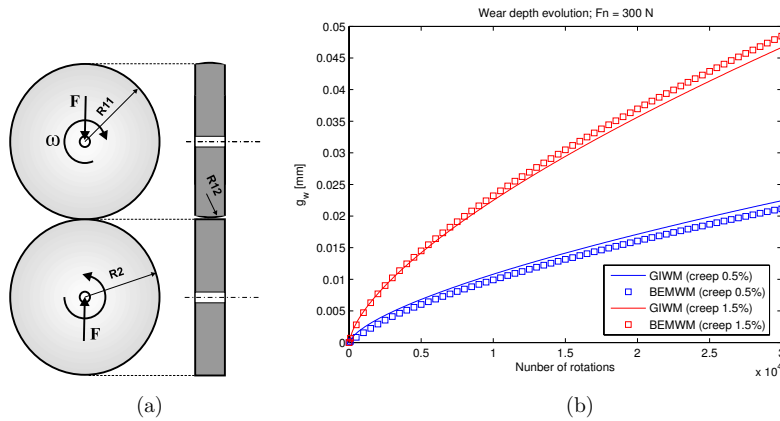


Figure 2: (a) Schematic of the twin-disc tribometer. (b) Wear depth evolution for a disc as a function of the number of rotations in comparison to the results from the GIWM and the BEMWM, for a normal load of 300 N.

Summary and conclusions

This work presents new methodology for wear simulation in contact and rolling-contact 3D problems using the BEM for computing the elastic influence coefficients, and the projection functions for rolling-contact restrictions fulfilment. The material loss of the bodies is modeled using the Archard's linear wear law. The methodology is applied to wear prediction in tribometers, but is general and valid for different wear problems. The comparison with the previous models such as [6] and [7, 5] has a very good agreement, so the proposed methodology seems to be a useful numerical tool for wear computing in 3D problems.

Acknowledgments

This work was funded by the *Consejería de Innovación Ciencia y Empresa de la Junta de Andalucía*, Spain, research project P05-TEP-00882, and by the *Ministerio de Educación y Ciencia*, Spain, research project DPI2006-04598.

References

- [1] L. Rodríguez-Tembleque, R. Abascal, and Aliabadi M.H. A boundary element formulation for 3d wear simulation in rolling-contact problems. In Abascal R. and Aliabadi M.H., editors, *Advances in Boundary Elements Techniques IX*. EC, Ltd., UK, 2008.
- [2] G.K. Sfantos and M.H. Aliabadi. Wear simulation using an incremental sliding boundary element method. *Wear*, 260(9-10):1119–1128, 2006.
- [3] G.K. Sfantos and M.H. Aliabadi. A boundary element formulation for three-dimensional sliding wear simulation. *Wear*, 5-6(262):672–683, 2007.
- [4] R. Abascal and L. Rodríguez-Tembleque. Steady-state 3d rolling-contact using boundary elements. *Comm. Num. Meth. Eng.*, 23(10):905–920, 2007.

- [5] V. Hegadekatte, N. Kurzenhäuser, N. Huber, and O. Kraft. A predictive modeling scheme for wear in tribometers. *Tribology International*, 41:1020–1031, 2008.
- [6] P. Pödra and S. Andersson. Simulating sliding wear with finite element method. *Tribology International*, 32(2):71–81, 1999.
- [7] V. Hegadekatte, N. Kurzenhäuser, N. Huber, and O. Kraft. Modeling and simulation of wear in a pin on disc tribometer. *Tribology letters*, 24:51–60, 2006.
- [8] C.A. Brebbia and J. Domínguez. *Boundary Elements: An Introductory Course (second edition)*. Computational Mechanics Publications, 1992.
- [9] M.H. Aliabadi. *The Boundary Element Method Vol 2: Application in Solids and Structures*. Wiley, London, 2002.
- [10] R. Abascal and L. Rodríguez-Tembleque. Fast 3d contact mechanics bem algorithm. In Selvadurai A.P.S., Tan C.L., and Aliabadi M.H., editors, *Advances in Boundary Elements Techniques VI*. EC, Ltd., UK, 2005.
- [11] J.F. Archard. Contact and rubbing of flat surfaces. *J. Appl. Phys.*, 24:981–988, 2006.
- [12] T. Jendel. Prediction of wheel profile wear - comparisons with field measurements. *Wear*, 253(1-2):89–99, 2002.

The Meshless Analog Equation Method for the Buckling of Plates with Variable Thickness

Aristophanes J. Yiotis¹, John T. Katsikadelis²

¹School of Civil Engineering, National Technical University of Athens

Athens, GR-15773, Greece, e-mail: fgiotis@otenet.gr

²Office of Theoretical and Applied Mechanics, Academy of Athens

& School of Civil Engineering, National Technical University of Athens

Athens, GR-15773, Greece, e-mail: jkats@central.ntua.gr

Keywords: Meshless Analog Equation Method (MAEM), Buckling, Plates, Variable Thickness.

Abstract. A new purely meshless method to solve buckling plate problems is presented. The method is based on the concept of the analog equation of Katsikadelis. It converts the fourth order partial differential equation with variable coefficients describing the response of the plate under the combined action of membrane forces to an equivalent static linear equation for plates with constant stiffness subjected to a fictitious source (load), the analog equation, under the same boundary conditions. The fictitious source is represented by MQ-RBFs. Integration of the analog equation allows the approximation of the sought solution by new RBFs. Then inserting the solution and its derivatives into the original governing equation of the problem and the associated boundary conditions and collocating at the mesh-free nodal points, yields a typical eigenvalue problem for the series coefficients, which yields the buckling load and permits the evaluation of the buckling modes. To overcome the problem of multiple boundary conditions the δ -technique is used. The introduced arbitrary integration constants enable to control the conditioning of the coefficient matrix and increase the accuracy by minimizing the Rayleigh quotient. This procedure gives optimal values of the shape parameter of the new RBFs. The studied examples demonstrate the efficiency and the accuracy of the developed method.

Introduction

The buckling problem of plates with arbitrary variable thickness is very important especially in weight sensitive industries, where optimized plate buckling analysis is required. Previous studies on this problem have been mainly restricted to rectangular and circular plates with unidirectional variation of thickness and specific boundary conditions [1-3]. The solution techniques employed are based on approximate analytical methods by expanding the deflection in Fourier series and using the Ritz method to derive the buckling equation. Except for the limitations on the geometry of plate, boundary conditions and thickness variation law, another important limitation of approximate methods is the assumption of uniform inplane compression, which can be realized only under specific inplane boundary conditions and which is not the case in realistic engineering problems. It is known that the inplane boundary conditions affect considerably the buckling load as shown in [4]. In an attempt to overcome these limitations Haric et al. [5] presented a semi-numerical-semi-analytical technique based on the finite strip method for rectangular plates with various but still unidirectional thickness variation laws.

In the field of BEM there have been some publications regarding the solution of linear buckling [6] and recently post-buckling plate problems [7] with constant stiffness. Nerantzaki and Katsikadelis [8] presented a solution for the buckling of plates with variable thickness, free from any limitations, using the concept of the AEM [9]. Later the present authors transformed this method to a purely boundary-one [10].

The mesh-free MQ-RBFs (multiquadric radial basis functions) method presented recently [11] has attracted the interest of the investigators, because it enjoys exponential convergence and is very simple to implement. The major drawback of this method is the ill-conditioning of the coefficient matrix. In some recent papers [12-14] a new RBFs method has been presented for the solution of problems governed by PDEs of second and fourth order. The method is based on the concept of the analog equation of Katsikadelis, according to which the original equation is converted into a substitute equation, the analog equation, under a fictitious source. The fictitious source is represented by radial basis functions series of multiquadric type. Integration of the analog

equation yields the sought solution as series of new radial basis functions. Then inserting the solution and its derivatives into the original governing equation of the problem and the existing boundary conditions and collocating at the mesh-free nodal points, yields a typical eigenvalue problem for the series coefficients, which yields the buckling loads and permits the evaluation of the corresponding buckling modes. To overcome the problem of multiple boundary conditions the δ -technique is used. The introduced arbitrary integration constants enable to control the conditioning of the coefficient matrix and increase the accuracy by minimizing the Rayleigh quotient. This procedure yields also optimal values for the shape parameter of the new RBFs. Several examples illustrate the method and useful conclusions are drawn for its accuracy and efficiency.

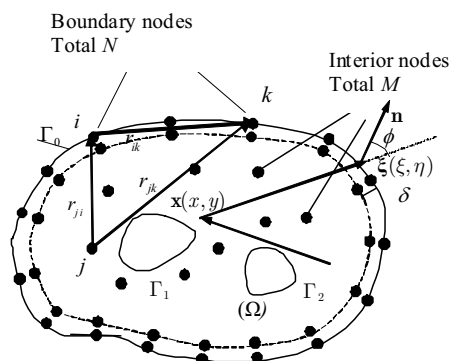


Fig. 1: Thin plate: Boundary and domain collocation points.

Statement of the Problem

Consider a thin elastic plate of variable thickness $h = h(\mathbf{x})$, $\mathbf{x} : \{x, y\} \in \Omega$ occupying the two-dimensional multiply connected region Ω of the x, y plane, bounded by the $K + 1$ curves $\Gamma_0, \Gamma_1, \Gamma_2, \dots, \Gamma_K$. The curves Γ_i ($i = 0, 1, 2, \dots, K$) may be piece-wise smooth. Assuming that there is no abrupt variation in thickness, the expressions for bending and twisting moments derived for plates of constant thickness apply with sufficient accuracy to this case also and the equilibrium of a plate element subjected to a distributed transverse load $g(\mathbf{x})$ and inplane forces $N_x = N_x(\mathbf{x})$, $N_y = N_y(\mathbf{x})$ and $N_{xy} = N_{xy}(\mathbf{x})$ yield the following differential equation in terms of the deflection $w(\mathbf{x})$ [8]

$$D\nabla^4 w + 2D_{,x}(\nabla^2 w)_{,x} + 2D_{,y}(\nabla^2 w)_{,y} + \nabla^2 D \nabla^2 w - (1 - \nu)(D_{,xx} w_{,yy} - 2D_{,xy} w_{,xy} + D_{,yy} w_{,xx}) - (N_x w_{,xx} + 2N_{xy} w_{,xy} + N_y w_{,yy}) = g(\mathbf{x}) \quad (1)$$

where $D(\mathbf{x}) = Eh(\mathbf{x})^3 / 12(1 - \nu^2)$ is the variable flexural rigidity of the plate. Moreover the deflection w of the plate must satisfy the following boundary conditions [15] on the boundary $\Gamma = \bigcup_{i=0}^K \Gamma_i$

$$Vw + k_T w = 0 \text{ or } w = 0 \text{ on } \Gamma \quad (2a)$$

$$Mw + k_R w_{,n} = 0 \text{ or } w_{,n} = 0 \text{ on } \Gamma \quad (2b)$$

$$k_T^{(k)} w^{(k)} - \llbracket Tw \rrbracket_k = 0 \text{ or } w^{(k)} = 0 \text{ at corner point } k \quad (2c)$$

The coefficients k_T and k_R express the transverse and rotational elastic support stiffness respectively. The term $\llbracket Tw \rrbracket_k$ represents the discontinuity jump of the twisting moment at the corner.

Taking into account that the flexural rigidity D is a function of the variables x and y and using curvilinear coordinates n, s , the bending moment M , the effective shear force V and the twisting moment acting along the boundary of the plate appearing in eqs (2) may be written as

$$M = -D \left[\nabla^2 + (\nu - 1) \left(\frac{\partial^2}{\partial s^2} + \kappa \frac{\partial}{\partial n} \right) \right] \quad (3a)$$

$$V = -D \left[\frac{\partial}{\partial n} \nabla^2 - (\nu - 1) \left(\frac{\partial^2}{\partial s \partial n} - \kappa \frac{\partial}{\partial s} \right) \right] + 2 \frac{\partial D}{\partial s} (\nu - 1) \left(\frac{\partial^2}{\partial n \partial s} - \kappa \frac{\partial}{\partial s} \right) - \frac{\partial D}{\partial n} \left[\nabla^2 + (\nu - 1) \left(\frac{\partial^2}{\partial s^2} + \kappa \frac{\partial}{\partial n} \right) \right] \quad (3b)$$

$$T = D(1 - \nu) \left(\frac{\partial^2}{\partial s \partial n} - \kappa \frac{\partial}{\partial s} \right) \quad (3c)$$

in which $\kappa = \kappa(s)$ is the curvature of the boundary; $\partial/\partial s$ and $\partial/\partial n$ denote differentiation with respect to the arc length of the boundary s and the outward normal n to it, respectively.

Since the linear buckling problem is considered, the inplane forces N_x, N_y, N_{xy} are *a priori* known because they are established by solving independently the plane stress problem for plates with variable thickness, which is described by the 2-D Navier-type differential equations for non-homogeneous bodies [12].

The differential equation for buckling is derived from eq. (1) by taking $g = 0$ and expressing the inplane external boundary forces in terms of a parameter λ . Thus, the buckling problem is reduced to the following eigenvalue problem

$$D \nabla^4 w + 2D_{,x} (\nabla^2 w)_{,x} + 2D_{,y} (\nabla^2 w)_{,y} + \nabla^2 D \nabla^2 w - (1 - \nu) (D_{,xx} w_{,yy} - 2D_{,xy} w_{,xy} + D_{,yy} w_{,xx}) - \lambda (N_x w_{,xx} + 2N_{xy} w_{,xy} + N_y w_{,yy}) = 0 \quad \text{in } \Omega \quad (4)$$

together with the boundary conditions (2).

The MAEM Solution

The eigenvalue problem described by eq. (4) with the boundary conditions (2) is solved using the MAEM as follows.

Since the governing equation of the problem is of fourth order, following Katsikadelis [12], we obtain the analog equation of the problem

$$\nabla^4 w = b \quad \text{in } \Omega \quad (5)$$

where $b = b(x)$ is an unknown fictitious source. Eq. (5) under the boundary conditions (2) can give the solution of the problem, if the fictitious source $b(x)$ is first established. Approximating the fictitious source by MQ-RBFs series, we can write

$$\nabla^4 w = \sum_{j=1}^{M+N} \alpha_j f_j \quad \text{in } \Omega \quad (6)$$

where $f_j = \sqrt{r^2 + c^2}$, $r = \|\mathbf{x} - \mathbf{x}_j\|$, c the shape parameter; M, N represent the number of collocation

points inside Ω and on Γ respectively. Eq. (6) is integrated to yield the solution

$$w = \sum_{j=1}^{M+N} \alpha_j \hat{w}_j \quad (7)$$

where $\hat{w}_j = \hat{w}_j(r)$ is the general solution of

$$\nabla^4 \hat{w}_j = f_j, \text{ for } f_j = \sqrt{r^2 + c^2} \quad (8)$$

This is a fourth order ordinary differential equation with respect to r , which can be written in polar coordinates and directly integrated to yield

$$\begin{aligned} \hat{w}_j = & \frac{1}{225} f^5 + \frac{2}{45} c^2 f^3 - \frac{7}{60} c^4 f + \frac{7}{60} c^5 \ln(c+f) \\ & - \frac{1}{12} \ln(c+f) c^3 f^2 - \frac{1}{12} c^5 + \frac{1}{12} c^3 r^2 - \frac{1}{6} c^5 \ln(r) \quad r \neq 0 \\ & + \frac{1}{4} G r^2 [\ln(r) - 1] + \frac{1}{4} F r^2 + K \ln(r) + K_1 \end{aligned} \quad (9)$$

where G, F, K, K_1 are arbitrary integration constants. For $r = 0$ it is $K = 0, G = 0$ (the last one for the derivatives to be finite). The arbitrary integration constants G, F, K, K_1 play an important role in the method, because together with the shape parameter c control the conditioning of the coefficient matrix and the accuracy of the results. Note that the solution of eq. (8) can be always established [15].

The solution is approximated by

$$w \simeq \sum_{j=1}^{M+N} \alpha_j \hat{w}_j \quad (10)$$

Subsequently, differentiating eq. (10) and collocating at nodal points, we obtain all the derivatives of the sought solution involved in the original differential eq. (4)

$$\mathbf{w} = \mathbf{W}\mathbf{a}, \quad \mathbf{w}_{,k} = \mathbf{W}_{,k}\mathbf{a}, \quad \mathbf{w}_{,kl} = \mathbf{W}_{,kl}\mathbf{a}, \quad \mathbf{w}_{,klm} = \mathbf{W}_{,klm}\mathbf{a} \quad (11a,b,c,d)$$

in which each of the subscripts k, l, m designate x or y and $\mathbf{W}, \dots, \mathbf{W}_{,klm}$ are known $(M+N) \times (M+N)$ matrices.

Finally collocating eqs (4) and (2) at the $M+N$ nodal points inside the domain Ω and on the boundary Γ using eqs (11), we obtain the following eigenvalue problem

$$(\mathbf{A} - \lambda \mathbf{B})\mathbf{a} = 0 \quad (12)$$

where \mathbf{A} and \mathbf{B} are known real matrices. Eq. (12) yields the values of the buckling parameter λ . The corresponding buckling modes can be found using eq. (11a).

The second boundary condition (2b) according to the δ -technique [16] is imposed on a node having a distance $\pm\delta$ from the boundary node (Fig. 1), on which the first boundary condition has been imposed in the direction normal to the boundary arc where δ is a very small number. In this investigation the value $\delta = 1.d - 7$ has been used. Though this technique increases the number of the collocation points, it avoids the formulation of singular matrices.

Optimal Values of Shape Parameter c , Constants G, F, K, K_1 and Centers of RBFs

The optimal value of the buckling parameter λ is dependent on the shape parameter, the integration constants and the centers of the multiquadric functions. It can be obtained as follows:

Premultiplying eq. (12) by $-\lambda^{-1}\mathbf{A}^{-1}$ (this matrix is always invertible [17]) and using $\lambda^{-1} = \mu$ leads to the typical eigenvalue problem:

$$(\mathbf{A}^{-1}\mathbf{B} - \mu\mathbf{I})\mathbf{a} = 0 \tag{13}$$

The matrix $(\mathbf{A}^{-1}\mathbf{B})^T \mathbf{A}^{-1}\mathbf{B} = \mathbf{C}$ is real symmetric and using the Rayleigh quotient relation we obtain:

$$\mu_1^2 = \frac{1}{\lambda_{M+N}^2} \leq \frac{\mathbf{a}^T \mathbf{C} \mathbf{a}}{\mathbf{a}^T \mathbf{a}} \leq \mu_{M+N}^2 = \frac{1}{\lambda_1^2} \tag{14}$$

where $\mathbf{a}(c, G, F, K, K_1)$ the eigenvector of \mathbf{C} associated with the μ_{M+N} eigenvalue. Therefore the buckling parameter λ can be found as:

$$\lambda_1 = \mu_{M+N}^{-1} = \min\left(\frac{\mathbf{a}^T \mathbf{a}}{\mathbf{a}^T \mathbf{C} \mathbf{a}}\right)^{1/2} \tag{15}$$

(we should recall that for every real nonsingular matrix $\mathbf{P}(\nu, \nu)$ there is always a symmetric square root \mathbf{X} of the symmetric matrix $\mathbf{P}^T \mathbf{P}$ so that)

$$\mathbf{X} = \mathbf{T} \text{diag}(\sqrt{\rho_1}, \dots, \sqrt{\rho_\nu}) \mathbf{T}^T \tag{16}$$

where ρ_1, \dots, ρ_ν the eigenvalues (positive numbers) and \mathbf{T} the eigenvectors matrix of the $\mathbf{P}^T \mathbf{P}$ matrix.

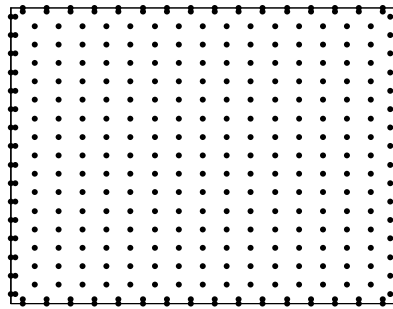


Figure 2: Boundary and domain nodal points of the plate of the examples for $N = 128, M = 225$.

Numerical Examples

Example 1. A rectangular simply supported plate with linearly varying thickness. A rectangular simply supported plate $(\alpha \times b)$ with linearly varying thickness $h = h_0(1 + \beta x / a)$, $\beta = h_\alpha / h_0 - 1$ has been analyzed; h_0 and h_α are the plate thickness at $x = 0$ and $x = \alpha$. The plate is uniformly compressed in the x direction, that is $N_x \neq 0, N_y = N_{xy} = 0$. The computed buckling parameters $\lambda_m = N_x b^2 / \pi^2 D_M$, where $D_M = Eh_M^3 / 12(1 - \nu^2)$, $h_M = (h_0 + h_\alpha) / 2$ are presented in Table 1 as compared with those given by other existing solutions. The optimal values of the shape parameter and the integration constants obtained for various numbers of the collocation points are given in Table 2.

		h_α / h_0				
a / b		1.125	1.250	1.500	1.750	2.000
1.00	Ref. [5]	3.970	3.878	3.720	3.560	3.317
	Ref. [3]	3.966	3.882	3.638	3.364	3.100
	Ref. [8]	3.994	3.902	3.631	3.322	3.019
	Ref. [10]	3.990	3.877	3.631	3.323	3.089
	Present	3.987	3.886	3.214	3.330	3.023
1.50	Ref. [5]	4.144	3.862	3.373	2.967	2.642
	Ref. [3]	4.146	3.861	3.339	2.908	2.557
	Ref. [8]	4.203	3.899	3.340	2.872	2.484
	Present	4.141	3.870	3.327	2.702	2.223

Table 1. Values for buckling parameter λ_m for a simply supported plate with linear variation in thickness subjected to constant uniform force in the x -direction ($\nu = 1/3$).

a / b	h_α / h_0	N	M	c	G	F	K	K_1
1.00	1.125	128	225	0.17709	3.4295d-2	-2.8717d-3	-9.70d-3	6.077d-4
	1.250	128					-9.50d-3	
	1.500	128					-10.70d-3	
	1.750	256					-8.80d-3	
	2.000	256					-7.55d-3	
1.50	1.125	128	345	0.17709	3.4295d-2	-2.8717d-3	-6.50d-3	6.077d-4
	1.250	128					-6.50d-3	
	1.500	128					-6.13d-3	
	1.750	128					-5.50d-3	
	2.000	128					-6.00d-3	

Table 2. Optimal values of the shape parameter and the integration constants obtained for various numbers of the collocation points in example 1.

Example 2. A rectangular simply supported plate with exponentially varying thickness. A rectangular simply supported plate ($\alpha \times b$) with exponentially varying thickness ($h = h_0 \exp\left\{(x/a) \ln(h_\alpha/h_0)\right\}$) has been analyzed. The plate is uniformly compressed in the x direction as in the previous example. The buckling parameters are presented in Table 3 as compared with those given by other solutions. The optimal values of the shape parameter and the integration constants obtained for various numbers of the collocation points are given in Table 4. In both examples the results are in very good agreement.

		h_α / h_0				
a / b		1.125	1.250	1.500	1.750	2.000
1.00	Ref. [5]	4.073	4.000	3.950	3.843	3.686
	Ref. [3]	3.972	3.901	3.700	3.476	3.262
	Ref. [8]	4.000	3.922	3.698	3.451	3.212
	Ref. [10]	3.991	3.932	3.702	3.449	3.218
	Present	3.992	3.877	3.727	3.456	2.942
1.50	Ref. [5]	4.184	3.949	3.541	3.206	2.933
	Ref. [3]	4.153	3.884	3.407	3.024	2.715
	Ref. [8]	4.210	3.924	3.417	3.008	2.678
	Present	4.201	3.922	3.418	3.236	2.705

Table 3. Values for buckling parameter λ_m for a simply supported plate with exponential thickness variation subjected to constant uniform force in the x -direction ($\nu = 1/3$).

Conclusions

A new truly meshless method, the MAEM (Meshless Analog Equation Method) has been developed for the buckling analysis of plates with variable thickness. The developed method is based on the concept of the

analog equation, which converts the original differential equation with variable coefficients in a plate equation with constant stiffness under a fictitious source. The method is demonstrated by applying it to the solution of the buckling problem. The use of MQ-RBFs to approximate the fictitious source and integration leads to the approximation of the sought solution by new RBFs, which have key advantages over the direct MQ-RBFs collocation method, summarized as:

- Since the method allows the control of the condition number, an invertible coefficient matrix for the evaluation of the RBFs expansion coefficients can be always established.
- The method gives accurate results, because the new RBFs approximate accurately not only the solution itself but also its derivatives.
- The method depends only on the order of the differential operator and not on the specific problem.

Moreover, as other RBFs methods:

- It is truly meshless, hence no domain (FEM) or boundary (BEM) discretization and integration is required. It also avoids establishment of fundamental solutions and evaluation of singular integrals.

Other conclusions regarding the merits of the method are:

- The shape of plate may be arbitrary. All type of support conditions for bending and inplane deformations may be prescribed.
- The thickness variation may be arbitrary and any inplane edge loading may be applied.
- The method is suitable for plate optimization in buckling analysis and can be employed for problems in other dimensions, of other type (parabolic and hyperbolic) as well as nonlinear ones.

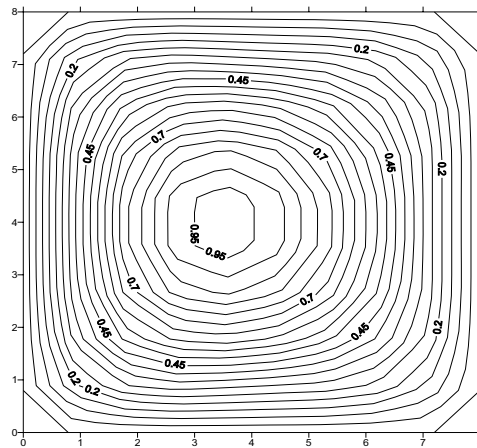


Fig. 3: 1st buckling mode for a square simply supported plate with linear variation in thickness subjected to constant uniform force in the x -direction ($h_\alpha / h_0 = 1.125$).

a / b	h_α / h_0	N	M	c	G	F	K	K_1
1.00	1.125	128	225	0.17709	3.4295d-2	-2.8717d-3	-9.65d-3	6.077d-4
	1.250	128					-9.40d-3	
	1.500	256					-9.80d-3	
	1.750	256					-7.83d-3	
	2.000	256					-7.10d-3	
1.50	1.125	128	345	0.17709	3.4295d-2	-	-6.38d-3	6.077d-4
	1.250	128				-6.34d-3		
	1.500	128				-5.70d-3		
	1.750	256				-6.30d-3		
	2.000	256				--5.40d-3		

Table 4. Optimal values of the shape parameter and the integration constants obtained for various numbers of the collocation points in example 2.

References

- [1] Bulson, P. S., *The Stability of Flat Plates*, Elsevier, New York, (1959).
- [2] Vol'mir, A. S., *Stability of Elastic Systems*, AD 628 508, Foreign Technology Division, Wright-Patterson Air Base, Ohio, (1965).
- [3] Wittrik, W. H. and Ellen, C. H., Buckling of tapered rectangular plates in compression, *Aeronaut. Quart.*, **13**, 308-326, (1962).
- [4] Katsikadelis, J. T. and Sapountzakis, E. J., A BEM Solution to Dynamic Analysis of Plates Subjected to Inplane Forces, *Proceedings of the 1992 ESDA Conference, ASME PD-Vol.47-5, Structural Dynamics and Vibrations*, eds. Ertas A., Ovunc B., Konuk I., Istanbul, 41-48, (1992).
- [5] Harik, L. E., Liu, X. and Ekambaram, R., Elastic stability of plates with varying rigidities, *Computers and Structures*, **38**, 161-168, (1991).
- [6] Manolis, G.D., Beskos, D. E. and Pineros, M. F., Beam and plate stability by boundary elements, *Computers and Structures*, **22(6)**, 917-923, (1989).
- [7] Katsikadelis, J. T. and Babouskos, N., The Post-Buckling Analysis of Plates. A BEM Based Meshless Variational Method, *Proceedings of 8th HSTAM International Congress on Mechanics*, **Vol I**, 177-184, Patras, Greece, (2007).
- [8] Nerantzaki, M. S. and Katsikadelis, J. T., Buckling of plates with variable thickness-an analog equation solution, *Engineering Analysis with Boundary Elements*, **18**, 149-154, (1996).
- [9] Katsikadelis, J. T., The analog equation method-a powerful BEM-based solution technique for solving linear and nonlinear engineering problems, in *Boundary Element Method XVI*, C. A. Brebbia (Ed.), *CLM Publications, Southampton*, 167-182, (1994).
- [10] Katsikadelis, J. T. and Yiotis, A. J., The BEM for buckling of plates with variable thickness. An analog equation solution, *Proceedings of the 4th National Conference on Steel Structures*, Patras, Greece, **vol. I**, 175-182, (2002).
- [11] Kansa, E. J. "Highly accurate methods for solving elliptic partial differential equations". In: Brebbia, C.A., Divo, E. and Poljak, D. (eds.), *Boundary Elements XXVII*, WIT Press, Southampton, 5-15, (2005).
- [12] Katsikadelis, J. T., "The 2D elastostatic problem in inhomogeneous anisotropic bodies by the meshless analog equation method", *Engineering Analysis with Boundary Elements*, **32**, 12, 997-1005, (2008).
- [13] Katsikadelis, J. T., "The meshless analog equation method. -I. Solution of elliptic partial differential equations", *Archive of Applied Mechanics*, DOI 10.1007/s00419-008-0294-6, (2009).
- [14] Yiotis, A. J. and Katsikadelis, J. T., The Meshless Analog Equation Method for the solution of plate problems, *Proceedings of 6th GRACM International Congress on Computational Mechanics*, Thessaloniki, Greece, (2008).
- [15] Katsikadelis, J. T. and Armenakas A. E., A New Boundary Equation Solution to the Plate Problem, *ASME, Journal of Applied Mechanics*, **56**, 364-374, (1989).
- [16] Ferreira, A. J. M., Roque, C. M. C. and Martins, P. A. L. S., Analysis of thin isotropic rectangular and circular plates with multiquadrics, *Strength of Materials*, **37**, 2, 163-173, (2005).
- [17] Goldberg, M. A, Chen C. S. and Bowman H., Some recent results and proposals for the use of radial basis functions in the BEM, *Engineering Analysis with Boundary Elements*, **23**, 285-296, (1999).

Large-scale multiple scattering analysis of SH waves using time-domain FMBEM

T. Saitoh¹, Ch. Zhang², S. Hirose³ and T. Fukui⁴

¹University of Fukui, 3-9-1, Bunkyo, Fukui-shi, Fukui, Japan, tsaitoh@u-fukui.ac.jp

²University of Siegen, D-57068 Siegen, Germany, c.zhang@uni-siegen.de

³Tokyo Institute of Technology, 2-12-1, O-okayama, Meguro-ku, Tokyo, Japan, shirose@cv.titech.ac.jp

⁴University of Fukui, 3-9-1, Bunkyo, Fukui-shi, Fukui, Japan, tak@taku.anc-d.fukui-u.ac.jp

Keywords: Convolution quadrature method (CQM), Fast multipole method (FMM), Time-domain, Multiple scattering

Abstract. This paper presents a new fast multipole boundary element method (FMBEM) for multiple scattering analyses in time-domain. The conventional time-domain BEM has two disadvantages: 1) The numerical instability in time stepping procedure, and 2) much computational time and memory. Our proposed method overcomes these two disadvantages using the convolution quadrature method (CQM) for 1) and the fast multipole method (FMM) for 2). As numerical examples, the large-scale multiple scattering of SH waves by many inclusions is conducted by the proposed method in this paper.

Introduction

Various composite materials are used as structural materials in many industries. Many multiple scattering problems have been solved so far by using approximate theories of composite materials and by reducing the size of the problems because the direct computations of the multiple scattering problems need much computational time and memory[1]. If, however, the multiple scattering problems can be solved more efficiently by a direct method, it might be meaningful in terms of simulating true wave fields.

Recently, the fast multipole boundary element method (FMBEM), which is the coupling of the boundary element method and the fast multipole method (FMM) developed by Greengard and Rokhlin[2], has been developed by some researchers for large-scale problems[3]. This method can reduce computational time and memory for the problems using the fast multipole algorithm drastically. In fact, the numerical examples of the multiple scattering using FMBEM in frequency domain can be seen in the past paper[4].

However, there are not so many numerical examples of the multiple scattering problems using FMBEM in time-domain compared with frequency-domain because time-domain BEM has the instability problem in time stepping procedure. Although Takahashi et al.[5] proposed an efficient time-domain BEM with the plane wave time domain (PWTD) algorithm to improve the computational efficiency of the conventional time-domain BEM, the numerical instability of time-domain BEM remains a hindrance. Therefore, it is an important key for multiple scattering problems in time-domain to develop an efficient and stable method.

In this paper, we propose a new time-domain BEM using both the convolution quadrature method (CQM) developed by Lubich[6] and the fast multipole method (FMM) for multiple scattering analyses. The use of CQM can improve the numerical instability in time stepping procedure very much for small time increments. On the other hand, FMM can overcome the computational efficiency problem of the conventional time-domain BEM for the large scale problems with several thousands of unknowns.

In this paper, first, we discuss the conventional time-domain BEM formulation for the multiple scattering of SH waves by many inclusions. Next, we show the brief description of our proposed method with both CQM and FMM. Finally, numerical results for multiple scattering of SH waves are demonstrated with the proposed method in time-domain.

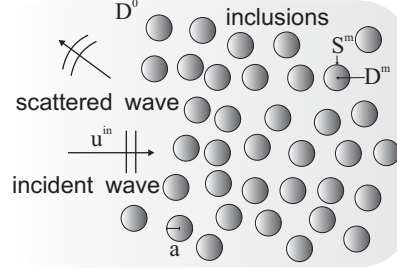


Figure 1 Multiple scattering model.

Conventional Time-domain BEM Formulation for Multiple Scattering of SH waves

We consider the multiple scattering of SH waves by inclusions as shown in Fig.1, where all the inclusions with radius a are composed of same material. The antiplane displacement u satisfies the governing equation as follows:

$$\nabla^2 u = \frac{1}{c^2} \frac{\partial^2 u}{\partial t^2} \quad (1)$$

where c is the velocity of SH waves, which is defined by $c = \sqrt{\mu/\rho'}$. In addition, ρ' and μ are the density and the shear modulus, respectively. When the incident SH wave u^{in} hits the boundary S^m ($m = 1, \dots, n_s$) of each inclusion D^m ($m = 1, \dots, n_s$), scattered waves are generated by the interaction with the inclusions. Assuming the zero initial conditions, we obtain the time-domain boundary integral equations for D^0 and for each inclusion D^m at time t as follows:

$$\frac{1}{2}u(\mathbf{x}, t) = u^{\text{in}}(\mathbf{x}, t) + \int_{S^0} U(\mathbf{x}, \mathbf{y}, t) * p(\mathbf{y}, t) dS_y - \int_{S^0} T(\mathbf{x}, \mathbf{y}, t) * u(\mathbf{y}, t) dS_y \quad \text{for } D^0 \quad (2)$$

$$\frac{1}{2}u(\mathbf{x}, t) = \int_{S^m} U(\mathbf{x}, \mathbf{y}, t) * p(\mathbf{y}, t) dS_y - \int_{S^m} T(\mathbf{x}, \mathbf{y}, t) * u(\mathbf{y}, t) dS_y \quad \text{for } D^m \quad (3)$$

where $U(\mathbf{x}, \mathbf{y}, t)$ and $T(\mathbf{x}, \mathbf{y}, t)$ denote the time-domain fundamental solution and its double layer kernel for SH wave propagation, respectively. In addition, p is the traction component corresponding to the antiplane displacement u . The solutions of the multiple scattering problem are obtained by solving the boundary integral equations defined in eq (2) and eq (3) with the continuity boundary conditions as follows:

$$u_{m+} = u_{m-}, \quad p_{m+} = -p_{m-} \quad \text{on } S^m \quad (4)$$

where the subscript $+$ and $-$ show the antiplane displacement u (traction p) outside and inside the inclusion with boundary S^m .

In general, the boundary integral equations defined in eq (2) and eq (3) can be solved by the conventional time-domain BEM[7]. If, however, a large number of elements are required in the multiple scattering problems, eqs (2) and (3) might not be solved by the conventional time-domain BEM efficiently and directly because huge computational time and memory are required. Moreover, the numerical scheme sometimes causes numerical instability for small time increments. To overcome these difficulties, both CQM and FMM are applied to the conventional time-domain BEM for the multiple scattering problems.

CQ-BEM Formulation for Multiple Scattering of SH Waves

Since CQ-BEM, which is the time-domain BEM based on CQM, has been done by some researchers[8, 9], we will summarize only the concept and essential formulas of CQ-BEM here.

In solving the system of the boundary integral equations defined in eqs (2) and (3) numerically, the boundary surface S^0 and S^m are discretized into M^0 and M^m elements, respectively, due to a piecewise constant approximation of the unknown displacement u and traction p . Applying CQM to the convolution integrals in eqs (2) and (3) yields the following discretized boundary integral equations with a time increment Δt as follows:

$$\frac{1}{2}u(\mathbf{x}, n\Delta t) = u^{\text{in}}(\mathbf{x}, n\Delta t) + \sum_{\alpha=1}^{M^0} \sum_{k=1}^n \left[A_0^{n-k}(\mathbf{x}, \mathbf{y}^\alpha) p^\alpha(k\Delta t) - B_0^{n-k}(\mathbf{x}, \mathbf{y}^\alpha) u^\alpha(k\Delta t) \right] \quad \text{for } D^0 \quad (5)$$

$$\frac{1}{2}u(\mathbf{x}, n\Delta t) = \sum_{\alpha=1}^{M^m} \sum_{k=1}^n \left[A_m^{n-k}(\mathbf{x}, \mathbf{y}^\alpha) p^\alpha(k\Delta t) - B_m^{n-k}(\mathbf{x}, \mathbf{y}^\alpha) u^\alpha(k\Delta t) \right] \quad \text{for } D^m \quad (6)$$

where A_Γ^{n-k} and B_Γ^{n-k} are the influence functions which are defined by

$$A_\Gamma^{n-k}(\mathbf{x}, \mathbf{y}) = \frac{\mathcal{R}^{-(n-k)}}{L} \sum_{l=0}^{L-1} \int_{S^\Gamma} \hat{U}(\mathbf{x}, \mathbf{y}, s_l) e^{-\frac{2\pi i(n-k)l}{L}} dS_{\mathbf{y}}, \quad \Gamma = 0 \quad \text{or} \quad m \quad (7)$$

$$B_\Gamma^{n-k}(\mathbf{x}, \mathbf{y}) = \frac{\mathcal{R}^{-(n-k)}}{L} \sum_{l=0}^{L-1} \int_{S^\Gamma} \hat{T}(\mathbf{x}, \mathbf{y}, s_l) e^{-\frac{2\pi i(n-k)l}{L}} dS_{\mathbf{y}}, \quad \Gamma = 0 \quad \text{or} \quad m. \quad (8)$$

In eqs (7) and (8), the parameter \mathcal{R} has to be $\mathcal{R} < 1$ and is taken as $\mathcal{R}^L = \sqrt{\epsilon}$ where ϵ shows the assumed error in the computation of eqs (7) and (8). Moreover, $\hat{U}(\mathbf{x}, \mathbf{y}, s)$ and $\hat{T}(\mathbf{x}, \mathbf{y}, s)$ are the Laplace domain fundamental solution and its double layer kernel in time-domain SH wave propagation problems as follows:

$$\hat{U}(\mathbf{x}, \mathbf{y}, s) = \frac{1}{2\pi\mu} K_0(sr), \quad \hat{T}(\mathbf{x}, \mathbf{y}, s) = \mu \frac{\partial}{\partial n_y} \hat{U}(\mathbf{x}, \mathbf{y}, s) \quad (9)$$

where r is given by $r = |\mathbf{x} - \mathbf{y}|$, K_n is the modified Bessel function of the second kind, and $\partial/\partial n_y$ shows the partial derivative with respect to the outward normal direction on \mathbf{y} . In addition, s is defined by $s = s_l/c = \delta(z_l)/(c\Delta t)$ where $z_l = \mathcal{R}e^{2\pi i l/L}$. To determine $\delta(z_l)$, we use the backward differential formula (BDF) of order two as follows:

$$\delta(z_l) = (1 - z_l) + \frac{(1 - z_l^2)}{2}. \quad (10)$$

Note that eqs (7) and (8) are identical to the discrete Fourier transform. Therefore, the calculations of eqs (7) and (8) can be evaluated by means of the FFT algorithm. Arranging eqs (5) and (6), we can obtain the discretized boundary integral equations at the n -th step as follows:

$$\begin{aligned} & \frac{1}{2}u(\mathbf{x}, n\Delta t) + \sum_{\alpha=1}^{M^0} [B_0^0(\mathbf{x}, \mathbf{y}^\alpha) u^\alpha(n\Delta t) - A_0^0(\mathbf{x}, \mathbf{y}^\alpha) p^\alpha(n\Delta t)] \\ &= u^{\text{in}}(\mathbf{x}, n\Delta t) + \sum_{\alpha=1}^{M^0} \sum_{k=1}^{n-1} \left[A_0^{n-k}(\mathbf{x}, \mathbf{y}^\alpha) p^\alpha(k\Delta t) - B_0^{n-k}(\mathbf{x}, \mathbf{y}^\alpha) u^\alpha(k\Delta t) \right] \quad \text{for } D^0 \quad (11) \end{aligned}$$

$$\begin{aligned} & \frac{1}{2}u(\mathbf{x}, n\Delta t) + \sum_{\alpha=1}^{M^m} [B_m^0(\mathbf{x}, \mathbf{y}^\alpha) u^\alpha(n\Delta t) - A_m^0(\mathbf{x}, \mathbf{y}^\alpha) p^\alpha(n\Delta t)] \\ &= \sum_{\alpha=1}^{M^m} \sum_{k=1}^{n-1} \left[A_m^{n-k}(\mathbf{x}, \mathbf{y}^\alpha) p^\alpha(k\Delta t) - B_m^{n-k}(\mathbf{x}, \mathbf{y}^\alpha) u^\alpha(k\Delta t) \right] \quad \text{for } D^m. \quad (12) \end{aligned}$$

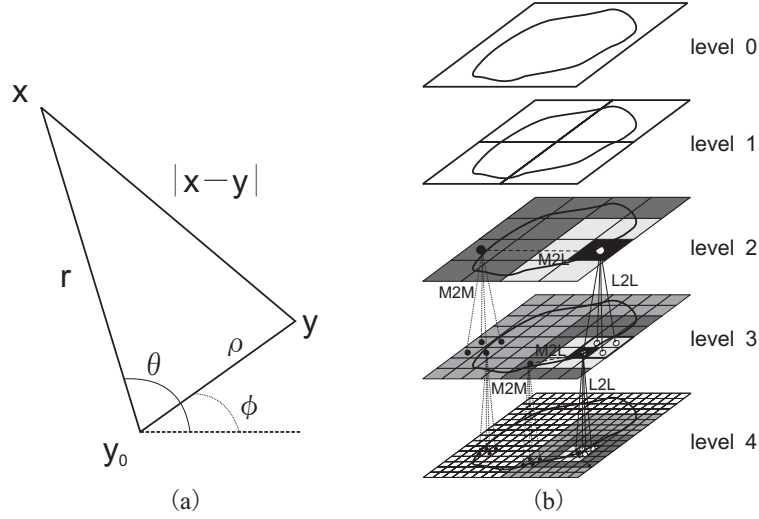


Figure 2 Fast multipole method. (a) Graf's addition theorem (b) The hierarchy structures of FMBEM.

Rewriting eqs (11) and (12) in the matrix form due to the boundary conditions (4), we have

$$\begin{bmatrix} T_0^0 & -U_0^0 \\ \vdots & \vdots \\ T_1^0 \cdots 0 & U_1^0 \cdots 0 \\ \vdots & \vdots \\ 0 \cdots T_m^0 & 0 \cdots U_m^0 \end{bmatrix} \begin{bmatrix} \mathbf{u}_1^n \\ \vdots \\ \mathbf{u}_m^n \\ \mathbf{p}_1^n \\ \vdots \\ \mathbf{p}_m^n \end{bmatrix} = \begin{bmatrix} \mathbf{u}_1^{n,\text{in}} \\ \vdots \\ \mathbf{u}_m^{n,\text{in}} \\ \mathbf{0} \\ \vdots \\ \mathbf{0} \end{bmatrix} - \sum_{k=1}^{n-1} \begin{bmatrix} T_0^{n-k} & -U_0^{n-k} \\ \vdots & \vdots \\ T_1^{n-k} \cdots 0 & U_1^{n-k} \cdots 0 \\ \vdots & \vdots \\ 0 \cdots T_m^{n-k} & 0 \cdots U_m^{n-k} \end{bmatrix} \begin{bmatrix} \mathbf{u}_1^k \\ \vdots \\ \mathbf{u}_m^k \\ \mathbf{p}_1^k \\ \vdots \\ \mathbf{p}_m^k \end{bmatrix} \quad (13)$$

where U_Γ^{n-k} and T_Γ^{n-k} are the coefficient matrices assembled from the element contributions in eqs (7) and (8) respectively, and \mathbf{u}_1^k and \mathbf{p}_1^k are the antiplane displacement and traction vectors at the k -th step, respectively. Moreover, $\mathbf{0}$ shows the zero matrix or vector. In eq (13), all the quantities on the right-hand side are known for the n -th time step. Therefore, the unknown values \mathbf{u}_m^n and \mathbf{p}_m^n ($m = 1, \dots, n_s$) can be obtained by solving the above equation. Unfortunately, we cannot solve a large-scale problem with the large number of elements efficiently and directly using the conventional time-domain BEM because the required computational complexity and memory are proportional to the number of elements obviously from eq (13). Therefore, CQ-BEM was accelerated by the fast multipole method (FMM) in this research.

FMBEM Formulation Based on CQM for Multiple Scattering of SH waves

FMM proposed by Greengard and Rokhlin[2] is a technique to reduce the computational time and memory for large-scale problems. Since the application of FMM to CQ-BEM can be seen in other published papers (for example, see the paper of Saitoh[10]), we will summarize only the essential formulas here.

The main formulas of FMM can be derived from Graf's addition theorem. Now, we consider a point \mathbf{y}_0 near the source point \mathbf{y} as shown in Fig.2(a). Using Graf's addition theorem for the field point \mathbf{x} and the source point \mathbf{y} in polar coordinate system originated at the point \mathbf{y}_0 as shown in Fig.2(a), we obtain the multipole expansions of the fundamental solution and its double layer kernel defined in eq (9) as follows:

$$\hat{U}(\mathbf{x}, \mathbf{y}, s) = \frac{1}{2\pi} \sum_{n=-\infty}^{\infty} M_n^U(\mathbf{y}_0) K_n(sr) e^{in\theta}, \quad \hat{T}(\mathbf{x}, \mathbf{y}, s) = \frac{1}{2\pi} \sum_{n=-\infty}^{\infty} M_n^T(\mathbf{y}_0) K_n(sr) e^{in\theta} \quad (14)$$

where $M_n^U(\mathbf{y}_0)$ and $M_n^T(\mathbf{y}_0)$ are called the multipole moments, which are given by

$$M_n^U(\mathbf{y}_0) = I_n(s\rho)e^{-in\phi}, \quad M_n^T(\mathbf{y}_0) = \mu \frac{\partial}{\partial n_y} M_n^U(\mathbf{y}_0). \quad (15)$$

In eq (15), I_n is the modified Bessel function of the first kind. Once the multipole moments are obtained, we can quickly evaluate the matrix-vector products of eq (13) using the fast multipole algorithm with the hierarchy structures as shown in Fig.2(b). The translation formulas for the fast multipole algorithm, M2M, M2L, and L2L, are also derived from Graf's addition theorem as follows:

$$\begin{aligned} M_n' &= \sum_{m=-\infty}^{\infty} M_m I_{n-m}(s\rho) e^{-i(n-m)\phi} : \text{M2M} \\ L_n &= \frac{1}{2\pi} \sum_{m=-\infty}^{\infty} (-1)^m M_m K_{n+m}(s\rho) e^{i(n+m)\phi} : \text{M2L} \\ L_n' &= \sum_{m=-\infty}^{\infty} (-1)^{n-m} L_m I_{n-m}(s\rho) e^{i(n-m)\phi} : \text{L2L} \end{aligned} \quad (16)$$

where the superscript prime indicates new multipole and local expansion coefficients. Moreover, ρ and ϕ are the polar coordinate components of an original multipole and local point based on a new multipole and local expansion point.

However, there is still one problem to resolve before we implement FMBEM. The modified Bessel functions I_n and K_n used in eq (16) tend exponentially to infinity for large and small argument z , respectively. This fact sometimes causes the numerical instability of the formulas defined in eq (16). To overcome the problem, we used the scaled modified Bessel functions $\check{I}_n(z) = e^{-z} I_n(z)$ and $\check{K}_n(z) = e^z K_n(z)$ in this research.

Numerical Examples

Our proposed method is applied to analyze the multiple scattering of SH waves by the rectangular arrangements of 8×8 inclusions with radius a of individual inclusion and the inclusion spacing $3a$ between two adjacent inclusions along the x_1 and x_2 axis as shown in Fig.3(a). In the numerical calculations, each boundary S^m is divided into 64 elements. The total number of unknowns per time step is 8192. The incident wave is assumed to be a plane SH wave, which is given by

$$u^{\text{in}}(\mathbf{x}, t) = u_0(1 - \cos 2\pi\beta), \quad \begin{cases} \beta = \frac{a}{\lambda_0} \left(\frac{c_0 t}{a} - \frac{x_1 + 11.5a}{a} \right) & \text{for } 0 \leq \beta \leq 1 \\ \beta = 0 & \text{for otherwise.} \end{cases} \quad (17)$$

Figure 3(b)-(d) show the total displacement u/u_0 around inclusions at times $c_0 t/a = 0.8, 8.64$ and 20.48 , respectively. The velocity and the mass density in the surrounding matrix D^0 are given by $c_0 \simeq 0.43c_m$, $\rho_0 \simeq 1.375\rho_m$ where c_m and ρ_m are the velocity of SH waves and the mass density, respectively, in each inclusion. In this analysis, the time interval is $c_0 \Delta t/a = 0.08$ and the incident wave length is $\lambda_0/a = 0.8$. In addition, \mathcal{R} is assumed to be $\mathcal{R} = 0.95609320$ ($\epsilon = 10^{-10}$) and the total time step is $N = L = 256$. FMM was only applied to accelerate the computation of the dense matrix-vector products of the upper half of the second term in the right hand side of eq (13) because the lower half of the matrix in the right hand side of eq (13) consists of the diagonal blocks U_i^{n-k} and T_i^{n-k} ($i = 1, \dots, m$). We can see the scattered waves and the transmitted waves generated by the interaction between the incident wave and the inclusions. In addition, we can see the large displacements ahead of the incident wave front because the wave velocity in the inclusions is faster than that in the surrounding matrix. Note that this problem could not be solved by the conventional time-domain BEM because of the restriction of the memory.

Conclusions

In this paper, the time-domain FMBEM based on CQM was developed for the multiple scattering of SH waves. As numerical examples, multiple scattering of SH waves by many inclusions were demonstrated. Further examples will be presented at the conference.

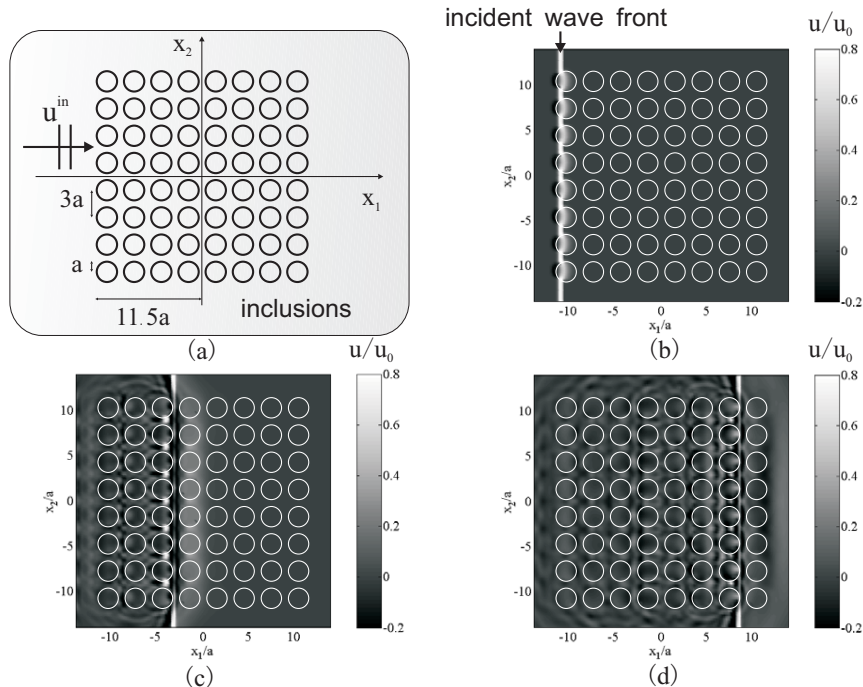


Figure 3 Numerical results by the proposed method. (a) Analysis model (b)-(d) Time variations of u/u_0 around the inclusions at $c_0t/a = 0.8, 8.64$ and 20.48 , respectively.

References

- [1] L-W. Cai and J. H. Williams, Jr.: *Large-scale multiple scattering problems*, *Ultrasonics*, **37**, 453-462 (1999a).
- [2] L. Greengard and V. Rokhlin: *A fast algorithm for particle simulations*, *Journal of Computational Physics*, **73**, 325-348 (1987).
- [3] N. Nishimura: *Fast multipole accelerated boundary integral equation methods*, *Appl. Mech. Rev.*, **55**, 299-324 (2002).
- [4] T. Satoh, S. Hirose and T. Fukui: *Application of fast multipole boundary element method to multiple scattering analysis of acoustic and elastic waves*, *Review of Progress in Quantitative Nondestructive Evaluation*, **26**, 79-86 (2006).
- [5] T. Takahashi, N. Nishimura and S. Kobayashi: *A fast BIEM for three-dimensional elastodynamics in time domain*, *Engineering analysis with BE.*, **27**, 491-506 (2003).
- [6] C. Lubich: *Convolution quadrature and discretized operational calculus I*, *Numer. Math.*, **52**, 129-145 (1988).
- [7] W. J. Mansur and C. A. Brebbia: *Transient elastodynamics using a time-stepping technique*, In: *Boundary Elements*, C. A. Brebbia, T. Futagami and M. Tanaka (Eds), 677-698 (1983).
- [8] M. Schanz and V. Struckmeier: *Wave propagation in a simplified modelled poroelastic continuum: Fundamental solutions and a time domain boundary element formulation*, *Numer. Math.*, **64**, 1816-1839 (2005).
- [9] Ch. Zhang: *Transient elastodynamic antiplane crack analysis of anisotropic solids*, *Int. J. Solids and Structures*, **37**, 6107-6130 (2006).
- [10] T. Saitoh, S. Hirose and T. Fukui: *Convolution quadrature boundary element method and acceleration by fast multipole method in 2-D viscoelastic wave propagation*, *Theoretical and applied mechanics Japan*, **57**, 385-393 (2009).

BEM for shallow water

Gregory Baker, Jeong-Sook Im
Department of Mathematics, The Ohio State University
231 W. 18th Ave, Columbus, OH43210,
baker@math.ohio-state.edu

Abstract: Boundary integral methods have been successfully applied to the motion of water waves in deep water. In two-dimensional periodic geometry, the boundary integrals have a pole singularity that may be easily removed, and spectral methods can be applied to generate highly accurate water waves even during breaking. By including a boundary integral along bottom topography, boundary integral methods can be easily adapted to the motion of water waves in shallow water. Unfortunately, the standard numerical approach suffers two difficulties. First, the integrands have strong variations when the water surface is close to the bottom (very shallow water) and even spectral accuracy requires excessive resolution. Second, the standard iteration based on the Neumann series converges very slowly since some of the eigenvalues are close to one for shallow water. We mitigate both these difficulties by adapting the removal of the pole singularity through analytic continuation and by designing a preconditioner based on a flat water surface over a flat bottom. We are able to track waves of permanent form and compare them to the cnoidal waves predicted by shallow water theory. The agreement is good only if the amplitudes are quite small.

Key-Words: Hydrodynamics, water waves, shallow water approximation.

1 Introduction

Water surface waves in oceans and lakes are generally generated by wind. They are then capable of propagating to all other regions with important consequences to shipping and the shoreline as well as of general importance to the environment as a result of the coupling between water waves and the atmosphere. It is not surprising, then, that much attention is given to the statistical properties of water waves since the statistics govern most of the potential impacts [1].

Since viscous effects are very small at water surfaces, the usual approximation is to assume the fluid is incompressible and inviscid, at least in the vicinity of the surface. Further, the flow is taken as irrotational, an assumption that seems reasonable except when wave breaking occurs. The equations of motion for the water are the Euler equations together with kinematic and dynamic conditions at the surface.

Boundary integral methods [2, 3, 4, 5] provide an attractive way to track the motion of a water surface since the calculation of the surface velocity can be performed with high accuracy, an important requirement for reliable results. There is no need to determine information other than on the surface, effectively reducing the dimensions of the problem by one.

Boundary integral methods have played an important role in assessing the dynamics of ocean waves [6] where the depth of the ocean is large. They have also been used to check the reliability of weakly nonlinear ocean wave models frequently used to study ocean waves. In general, the wave amplitudes must be quite small in order for these weakly nonlinear models to be reliable. Alternatively, the amplitude expansion must be conducted to fourth order for agreement between boundary integral methods and pseudo-spectral methods to be good [7].

Boundary integral methods for water of finite depth [2] have proved less successful for two main reasons. The close approach of two boundaries in boundary integral methods induce rapid variations in the integrands that require excessive resolution to restore high accuracy [8]. The other difficulty is that the eigenvalues of the boundary integral operators approach one, substantially increasing the number of iterations needed to generate the Neumann series. We have found new methods to mitigate both these difficulties.

Given our new ability to track the water surface even in very shallow water, we are now able to test the shallow water approximations, in particular, the Korteweg-DeVries equation which describes the propagation of waves of permanent form.

2 Mathematical formulation

We consider the two-dimensional incompressible, inviscid and irrotational fluid flow of water bounded above by a free surface and below by a fixed boundary. Let $z = x + iy$ represent a complex-valued field point where x lies along the horizontal axis and y along the vertical axis. Let the free surface and rigid boundary be given in parametric form $z_F(p)$ and $z_B(p)$, respectively. We restrict our attention to flows that are 2π -periodic in both the bottom boundary and the surface. The fluid velocity can be determined from a complex potential $\Phi = \phi + i\psi$, where ϕ is the regular velocity potential and ψ is the streamfunction. The complex velocity $w = u + iv$, where u and v are the x and y velocity components respectively, is given by

$$w^*(z) = \frac{d\Phi}{dz} \quad (1)$$

where the * superscript implies complex conjugation.

Following [2], we represent the complex potential in terms of a real dipole distribution $\mu_F(p)$ along the free surface and an imaginary dipole distribution $\mu_B(p)$ along the boundary.

$$\Phi(z) = \frac{1}{4\pi i} \int_0^{2\pi} \mu_F(q) z_{F,q}(q) \cot \frac{1}{2}[z - z_F(q)] dq + \frac{1}{4\pi} \int_0^{2\pi} \mu_B(q) z_{B,q}(q) \cot \frac{1}{2}[z - z_B(q)] dq. \quad (2)$$

The subscript q on z_F and z_B refers to differentiation. Define

$$I_{ab}(p) = \frac{1}{4\pi i} \int_0^{2\pi} \mu_b(q) z_{b,q}(q) \cot \frac{1}{2}[z_a(p) - z_b(q)] dq, \quad (3)$$

where a, b may be either F or B and the integral is to be taken in the principal-valued sense when necessary. Take the limit as z approaches the free surface from below, $\Phi(z) \rightarrow \Phi(z_F(p)) = \Phi_F(p)$. Then,

$$\Phi_F(p) = I_{FF}(p) + I_{FB}(p) + \frac{1}{2}\mu_F(p). \quad (4)$$

The velocity of the free surface can now be determined from (1) and (4) applied at the surface,

$$w_F^*(p) = \frac{\Phi_{F,p}(p)}{z_{F,p}(p)}. \quad (5)$$

If a surface particle is tagged with the label p , then its motion may be determined as

$$\frac{\partial z_F}{\partial t}(p) = w_F(p), \quad (6)$$

where the partial derivative is chosen to emphasize that p is kept fixed. This is the definition of Lagrangian motion. To compute the surface velocity (5), we need to compute Φ_F from (4), which in turn requires knowledge of the dipole strengths. The dipole strengths are determined by the application of Bernoulli's equation at the free surface, and the requirement that there is no normal fluid velocity component at the bottom boundary.

Bernoulli's equation determines how the velocity potential changes in time. The rate of change of the potential on the free surface, keeping p fixed, is

$$\frac{\partial \phi_F}{\partial t}(p) = \frac{1}{2}|w_F(p)|^2 + gy_F(p), \quad (7)$$

where g is the acceleration due to gravity. For the moment, imagine that ϕ_F has been determined. Then, (4) leads to an integral equation for the dipole strengths,

$$\mu_F(p) = 2\phi_F(p) - 2\Re \{I_{FF}(p) + I_{FB}(p)\}. \quad (8)$$

Finally, we must ensure that there is no normal velocity component at the bottom boundary. Take the limit of Φ as z approaches the bottom from above. Then, $\Phi \rightarrow \Phi(z_B(p)) = \Phi_B(p)$, where

$$\Phi_B(p) = I_{BF}(p) + I_{BB}(p) - \frac{1}{2}\mu_B(p). \quad (9)$$

The fluid velocity at the bottom boundary will be

$$w_B^*(p) = \frac{\Phi_{B,p}(p)}{z_{B,p}(p)}. \quad (10)$$

The normal component of the velocity will be $\Im\{z_{B,p} w_B^*\}$. We ensure that this normal component is zero if we impose the requirement that $\Im\{\Phi_B\}$ is zero. In other words the streamfunction is zero along the bottom boundary. Thus, from (9),

$$\mu_B(p) = 2\Im\{I_{BF}(p) + I_{BB}(p)\}. \quad (11)$$

This completes the derivation of the boundary integral technique. If z_F , z_B and ϕ_F are known at some time t , then we proceed as follows. Solve the coupled Fredholm integral equations (8) and (11) to determine μ_F and μ_B . Then Φ_F can be evaluated by (4); since ϕ_F is already known, only ψ_F needs to be determined by (4). The surface velocity may now be calculated by (5), and the surface location may be updated in time by (6). Finally, (7) may be used to update the surface potential. Fortunately, the integral equations (8) and (11) may be solved by iteration.

$$\mu_F^{(n+1)}(p) = 2\phi_F(p) - 2\Re\{I_{FF}^{(n)}(p) + I_{FB}^{(n)}(p)\}, \quad (12)$$

$$\mu_B^{(n+1)}(p) = 2\Im\{I_{BF}^{(n+1)}(p) + I_{BB}^{(n)}(p)\}. \quad (13)$$

3 Numerical Method

Since the geometry is assumed periodic, we may use the Fourier series as the basis for approximation. In particular, the surface and boundary locations may be written in the form

$$z(p) = p + \sum_{k=-M}^M A_k e^{ikp}. \quad (14)$$

The series is truncated with $2M = N$, the number of points on a surface, and the Fast Fourier Transform may be used to determine A_k . The derivatives of the surface and boundary locations are then

$$z_p(p) = 1 + \sum_{k=-M}^M ik A_k e^{ikp}. \quad (15)$$

The inverse Fast Fourier transform then gives the derivatives at the surface points. The same procedure can be used to evaluate the derivatives of any surface quantity such as μ , ϕ , ψ , etc.

By far the most important part of the numerical method is the treatment of the integrals. Consider first the principal-valued integrals I_{FF} and I_{BB} . The standard procedure is to remove the pole by using the result,

$$\frac{1}{4\pi i} \int_0^{2\pi} z_{b,q}(q) \cot \frac{1}{2}[z_a(p) - z_b(q)] dq = \frac{1}{2} \begin{cases} -1 & \text{if } z_a(p) \text{ lies above the surface } z_b(q), \\ 0 & \text{if } z_a(p) = z_b(p), \\ 1 & \text{if } z_a(p) \text{ lies below the surface } z_b(q). \end{cases} \quad (16)$$

The middle choice allows us to write

$$I_{FF} = \frac{1}{4\pi i} \int_0^{2\pi} (\mu_F(q) - \mu_F(p)) z_{F,q}(q) \cot \frac{1}{2}[z_F(p) - z_F(q)] dq, \quad (17)$$

$$I_{BB} = \frac{1}{4\pi} \int_0^{2\pi} (\mu_B(q) - \mu_B(p)) z_{B,q}(q) \cot \frac{1}{2}[z_B(p) - z_B(q)] dq. \quad (18)$$

The integrands (17) and (18) have limiting values, $-\mu_{F,p}(p)/(2\pi i)$ and $-\mu_{B,p}(p)/(2\pi)$ respectively, as $q \rightarrow p$. The integral may be evaluated numerically by the composite trapezoidal rule with spectral accuracy.

The other integrals, I_{FB} and I_{BF} have smooth integrands and the composite trapezoidal method may be applied directly. However, it is well known that the numerical results may contain large errors if the local spacing

between the surfaces is less than ten times the local spacing of the points on the surfaces [8]. A new method has been developed and tested in which the poles in the complex q -plane are also removed in I_{FB} and I_{BF} [9].

The starting point is the determination of the locations Q_F and Q_B such that

$$z_F(Q_F) - z_B(p) = 0, \quad (19)$$

$$z_B(Q_B) - z_F(p) = 0. \quad (20)$$

Clearly, Q_F is the location of a pole in the integrand of I_{BF} and Q_B is the location of a pole in the integrand of I_{FB} . They are functions of p . For a fixed choice of p , Newton's method may be applied to (19) and (20) to find Q_F and Q_B . The analytic continuation of $z_F(q)$ and $z_B(q)$ is achieved by their Fourier series representation (14) where p may be complex. Analytic continuation is an ill-posed operation. However, we anticipate that the pole locations will be close to the real axis of q if the surfaces are close together. Our examples below will confirm this expectation. Nevertheless, this modification should only be applied when the surfaces are closer than ten times the local point spacing on the surfaces.

The nearby poles in the integrands of I_{FB} and I_{BF} may now be removed by using (16).

$$I_{FB}(p) = \frac{1}{4\pi} \int_0^{2\pi} [\mu_B(q) - \mu_B(Q_B)] z_{kq}(q) \cot \frac{1}{2} [z_F(p) - z_B(q)] dq - \frac{i}{2} \mu_B(Q) \quad (21)$$

$$I_{BF}(p) = \frac{1}{4\pi i} \int_0^{2\pi} [\mu_F(q) - \mu_F(Q_F)] z_{kq}(q) \cot \frac{1}{2} [z_B(p) - z_F(q)] dq + \frac{1}{2} \mu_F(Q) \quad (22)$$

The dipole strengths μ_F and μ_B must also be analytically continued through their Fourier series representation.

To demonstrate the effectiveness of the pole removal, we illustrate the procedure and results for the simple case of a flat surface $z_F = p$ and flat bottom $z_B = p - iH$. We make the choice $\mu_F = 2\alpha \sin(p)$ and $\mu_B = 2\beta \cos(p)$. Then,

$$\Phi_F = (\alpha + \beta e^{-H}) \sin(p) + i(\alpha - \beta e^{-H}) \cos(p), \quad (23)$$

$$\Phi_B = (\beta + \alpha e^{-H}) \sin(p) - i(\beta - \alpha e^{-H}) \cos(p). \quad (24)$$

In addition, we add the requirement $\beta = \alpha \exp(-H)$, which makes $\psi_B = 0$ along the bottom boundary. This requirement is not necessary for the tests reported here but it is consistent with our interest in tracking water waves above a flat bottom.

The straightforward application of the trapezoidal rule to the integrals in (4) without pole removal in I_{FB} gives numerical results with errors displayed in Fig. 1: we set $\alpha = 0.15$. For large enough H the error is just due to round-off, a reflection of spectral accuracy. The error grows exponentially in magnitude as H decreases below about $5h$, where h is the spacing between surface markers. The point is clearly made that many surface markers are needed for high accuracy when the depth is small.

For the simple case of a flat surface and boundary, the location of the poles $Q_F = p - iH$ and $Q_B = p + iH$ are easily found. The result of removing the poles also in I_{FB} and I_{BF} is illustrated in Fig. 2 for the same conditions

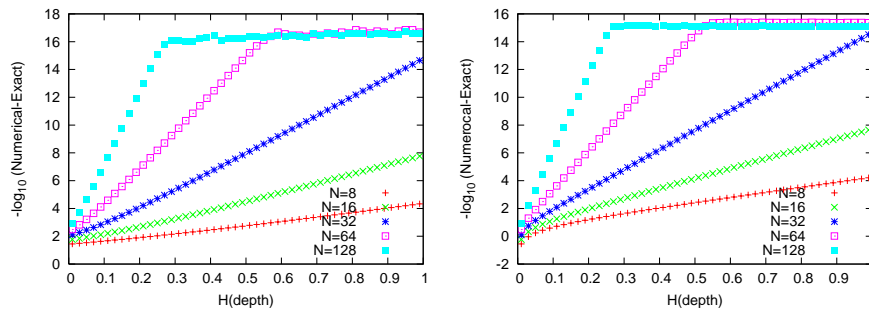


Figure 1: The maximum absolute error in ϕ_F (Left) and ψ_F (Right) as the depth H is varied.

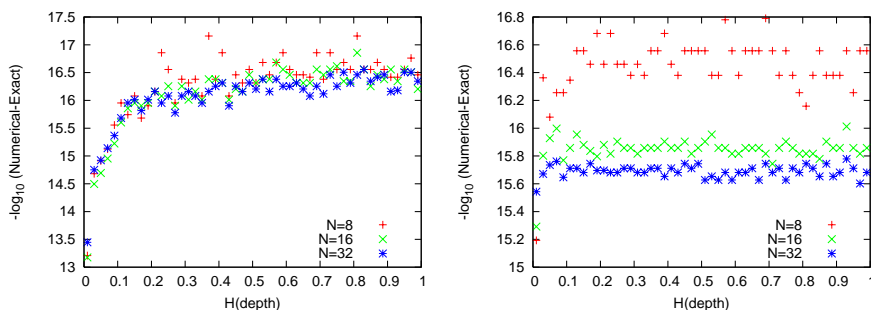


Figure 2: The maximum absolute error in ϕ_F (Left) and ψ_F (Right) as the depth H is varied.

as in Fig. 1. The error has been effectively removed. The slight increase in the error in ϕ_F is caused by round-off errors and can be further reduced by careful coding. We allow it here simply to illustrate the need to beware of round-off effects. The impressive reduction in errors means that accuracy is determined essentially by the nature of the Fourier series for μ_F and μ_B . If the amplitudes of the high modes are significant, then there must be enough surface markers to resolve the variations in the dipole strengths, typically four points are needed to resolve a Fourier mode.

The remaining difficulty occurs in the behavior of the iterative procedure (12) and (13). Take the simple case of a flat surface and bottom, and let the dipole strengths have the Fourier series

$$\mu_F(p) = a_0 + \sum_{k=1}^{\infty} (a_k \cos(kp) + b_k \sin(kp)), \quad (25)$$

$$\mu_B(p) = c_0 + \sum_{k=1}^{\infty} (c_k \cos(kp) + d_k \sin(kp)). \quad (26)$$

and suppose the surface potential has the Fourier series

$$\phi_F(p) = m_0 + \sum_{k=1}^{\infty} (m_k \cos(kp) + n_k \sin(kp)). \quad (27)$$

Then the iterative procedure leads to a balance of Fourier terms.

$$a_k^{(n+1)} = 2m_k + d_k^{(n)} e^{-kH}, \quad c_k^{(n+1)} = b_k^{(n+1)} e^{-kH}, \quad (28)$$

$$b_k^{(n+1)} = 2n_k - c_k^{(n)} e^{-kH}, \quad d_k^{(n+1)} = -a_k^{(n+1)} e^{-kH}. \quad (29)$$

The eigenvalues of the iteration are $\exp(-2kH)$ with multiplicity 2 for $k > 0$ but there is a complete set of eigenvectors. Typical of iterative solutions to elliptic problems, the largest eigenvalue $\exp(-H)$ is associated with the eigenvector with the slowest variation. The smaller H is, the closer the eigenvalue is to 1 and the slower the convergence rate for the iteration.

The obvious choice for an improved iteration is to use the results for the flat surface and bottom as a preconditioner. The first step is to compute the residuals,

$$R_F(p) = 2\phi_F(p) - \mu_F^{(n)}(p) - 2\Re\{I_{FF}^{(n)}(p) + I_{FB}^{(n)}(p)\}, \quad (30)$$

$$R_B(p) = -\mu_B^{(n)}(p) + 2\Im\{I_{BF}^{(n)}(p) + I_{BB}^{(n)}(p)\}, \quad (31)$$

where the integrals are evaluated with the current guesses $\mu_F^{(n)}$ and $\mu_B^{(n)}$. The second step is to find their Fourier

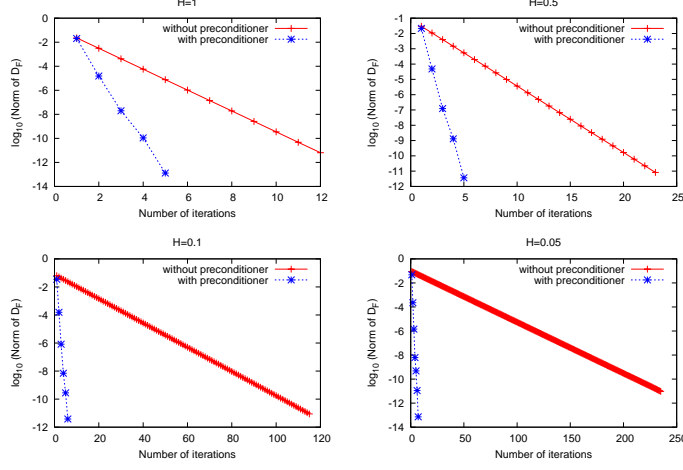


Figure 3: $\log_{10}(\max(|D_F|))$ after each iteration step with and without the preconditioner as the depth H is varied.

representation.

$$R_F(p) = A_0 + \sum_{k=1}^{\infty} (A_k \cos(kp) + B_k \sin(kp)), \quad (32)$$

$$R_B(p) = C_0 + \sum_{k=1}^{\infty} (C_k \cos(kp) + D_k \sin(kp)). \quad (33)$$

The residuals become the inhomogeneous terms for the integral equations with a flat surface and bottom. These equations can be solved exactly for the new Fourier coefficients of μ_F and μ_B . First, find α_k , β_k , γ_k and δ .

$$\alpha_k^{(n+1)} - e^{-kH} \delta_k^{(n+1)} = A_k, \quad \gamma_k^{(n+1)} - e^{-kH} \beta_k^{(n+1)} = C_k, \quad (34)$$

$$\beta_k^{(n+1)} + e^{-kH} \gamma_k^{(n+1)} = B_k, \quad \delta_k^{(n+1)} + e^{-kH} \alpha_k^{(n+1)} = D_k. \quad (35)$$

Then, set

$$a_k^{(n+1)} = a_k^{(n)} + \alpha_k, \quad b_k^{(n+1)} = b_k^{(n)} + \beta_k, \quad c_k^{(n+1)} = c_k^{(n)} + \gamma_k, \quad d_k^{(n+1)} = d_k^{(n)} + \delta_k.$$

Of course, the precondition works exactly if the surface is flat. Since we wish to apply the boundary integral method when there are waves on the surface, we test the effectiveness of the preconditioner on a perturbed surface $z_F = p + i\epsilon \cos(p)$. The norm of the displacement, $D_F = \mu_F^{(n+1)} - \mu_F^{(n)}$, is shown after each iteration in Fig. 3 for the cases with and without the preconditioner for the choice $\epsilon = 0.01$. The number of surface and boundary markers is 128, much more than necessary but it does check the numerical stability of the preconditioner. Without the preconditioner, the residual converges very slowly when the depth is small. With the preconditioner, the displacement converges at essentially the same rate no matter how shallow the water.

4 Application to the KdV equation

The Korteweg-deVries equation describes long wave propagation in shallow water and is a simplest equation which incorporates both nonlinearity and dispersion. The equation is derived from the full Euler equations with

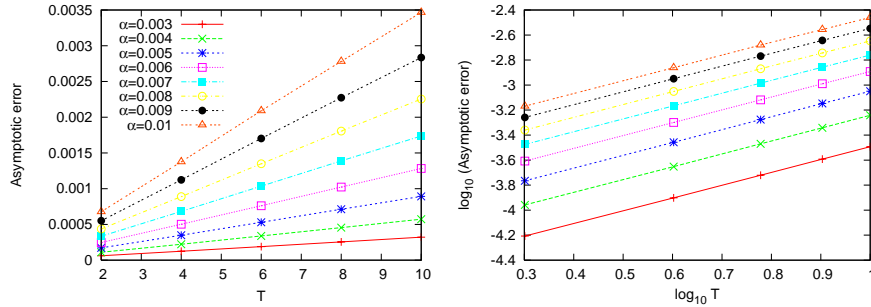


Figure 4: Error in time for different α on linear scales (left) and log-log scales (right).

two parameters

$$\alpha = \frac{A}{H}, \quad \beta = \frac{H^2}{L^2}, \tag{36}$$

where A is a typical wave amplitude, H is the undisturbed depth of the water and L is a typical wavelength. The unidirectional propagation of waves is given asymptotically by

$$\eta_t + \eta_x + \frac{3}{2}\alpha\eta\eta_x + \frac{\beta}{6}\eta_{xxx} + O(\alpha^2, \alpha\beta, \beta^2) = 0, \tag{37}$$

where η gives the surface elevation [10].

The solution of the KdV equation has a travelling wave of permanent form, that is, a wave which does not change its shape and which propagates at constant speed. The solution may be written in the form

$$\eta(x, t) = \alpha H \left\{ \frac{1}{m^2} \left(1 - m^2 - \frac{E(m)}{K(m)} \right) + \alpha \operatorname{cn}^2 \left(\frac{K(m)}{\pi} (x - Ut) \right) \right\}, \tag{38}$$

where $\sqrt{3\beta}\pi = 2HK(m)$, $m^2 = \alpha/\beta$, and $K(m)$ and $E(m)$ are the complete elliptic integrals of the first and second kind, respectively. The function $\operatorname{cn}(x)$ is the cnoidal Jacobian elliptic function. By the definition of m , $\alpha < \beta$. The velocity of propagation is

$$U = \sqrt{H} \left[1 + \beta \left(1 - \frac{m^2}{2} - \frac{3}{2} \frac{E(m)}{K(m)} \right) \right]. \tag{39}$$

The time scale is determined by setting $g = 1$. There is also an expression for the velocity potential on the surface which can be used to specify an initial condition for the boundary integral method, along with (38).

Asymptotic analysis [11] indicates that the error between the solution $\eta(x, t)$ to the KdV equation and the full Euler equations $y(x, t)$ has the form

$$E = \max |\eta(x, t) - y(x, t)| \approx (C_0\alpha^2 + C_1\alpha\beta + C_2\beta^2)T(t). \tag{40}$$

Here $T(t) = \sqrt{\beta/H} t$. By using the boundary integral method described here, we can determine the error precisely. For the results reported here, we need no more than 128 surface markers. We use the standard Runge-Kutta 4th-order method to advance the solution in time with a time step 1/16. We solve the integral equations iteratively until the residual is less than 10^{-14} . To prevent the growth of round-off errors in time we applied a spectral filter which cuts off the Fourier coefficients if they are less than 10^{-14} in magnitude.

We made sure through resolution studies that the accuracy of the numerical results is good enough to study the behavior of the error. Typically the errors are about 10^{-12} .

First, we show the behavior of the error in time in Fig. 4 with the choice $\beta = 3\alpha$. Next, we fix T and set $\beta = k\alpha$. The quadratic behavior of the asymptotic error in α is evident in Fig. 5. Also evident is that the errors

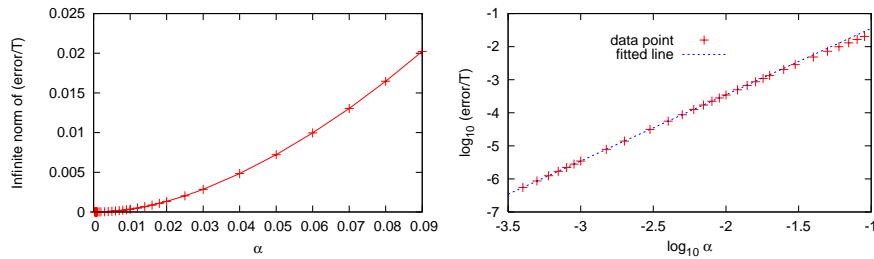
Figure 5: Asymptotic error as α varies; linear on the left and log-log on the right

Table 1: Coefficients in the error for different times

T	C_0	C_1	C_2
2	0.10 ± 0.01	-0.073 ± 0.001	0.39 ± 0.01
4	0.065 ± 0.001	-0.050 ± 0.001	0.39 ± 0.01
6	0.059 ± 0.001	-0.043 ± 0.001	0.39 ± 0.01
8	0.059 ± 0.001	-0.039 ± 0.001	0.39 ± 0.01
10	0.055 ± 0.001	-0.033 ± 0.001	0.39 ± 0.01

become significant when $\alpha \approx 0.1$. For the range of α where the quadratic behavior is accurate, we determine an average value for $E/(T\alpha^2)$ for fixed T and k . Then for fixed T , we determine the coefficients C_0 , C_1 and C_2 by a form-fit for various k . We repeat the process for different T . The results are given in Table 1. The coefficient C_2 dominates the error. Indeed, it is difficult even with the high accuracy of the calculations to determine C_0 and C_1 with confidence except that they are very small.

5 Conclusion

Two modifications to the boundary integral method, pole removal and the use of a preconditioner has allowed direct confirmation of asymptotic models for shallow water.

Acknowledgements: The research was supported by NSF (grant OCE-0620885).

References:

- [1] G. J. Komen, L. Cavaleri, M. Donelan, K. Hasselmann, S. Hasselmann and P. A. E. M. Jansen, *Dynamics and Modelling of Ocean Waves*, Cambridge University Press, 1994.
- [2] G. R. Baker, D. I. Meiron and S. A. Orszag, *J. Fluid Mech.*, 123, 1982, pp. 477–501.
- [3] G. R. Baker, D. I. Meiron and S. A. Orszag, *Physica* 12D, 1984.
- [4] J. T. Beale, *Math. Comput.*, 70, 2001, p. 977.
- [5] P. Milewski and J. Keller, *Stud. Appl. Math.*, 37, 1998, p. 149.
- [6] A. Hayslip, J. Johnson and G. Baker, *IEEE Trans. Geosc. Rem. Sens.*, 41, 2003, pp. 2287–2293.
- [7] K. Berger, G. Baker and J. Johnson, *Intern. J. Comput. Fluid Dyn.* 17, 2003, pp. 219–224.
- [8] G. Baker and M. Shelley, *J. Comput. Phys.* 64, 1986, pp. 112–132.
- [9] G. Baker and N. Golubeva, in *Advances in Boundary Element Techniques, VIII*, Naples, Italy (2007).
- [10] G. Whitham, *Linear and nonlinear waves*, John Wiley & Sons Inc., (1974).
- [11] J. Bona, T. Colin and D. Lannes, *Arch. Ration. Mech. Anal.*, 178, 2005, pp. 373–410.

Influence of Infill Walls in the Dynamic Response of Buildings via a Boundary Element Modeling

N.P. Bakas¹, N.G. Babouskos², F.T. Kokkinos³ and J.T. Katsikadelis⁴

^{1,2} School of Civil Engineering, National Technical University of Athens,
Zografou Campus, GR-15773 Athens, Greece

³ Department of Civil & Infrastructure Engineering,
Technological Educational Institute of Athens, GR-12210 Athens, Greece
fkokkinos@teiath.gr

⁴ School of Civil Engineering, National Technical University of Athens,
Zografou Campus, GR-15773 Athens, Greece
jkats@central.ntua.gr

Keywords: shear walls, masonry walls, infilled frames, multi-storey buildings, open ground storey buildings, soft storey, weak storey, reinforced concrete structures, dynamic analysis, Boundary Element Method, substructures

Abstract. The infill masonry walls are seldom included in numerical analysis of reinforced concrete structural systems, since masonry panels are generally considered as non-structural components. However, these panels affect the structural response, although the complexity they introduce to the analysis, generally keep them unaccounted for. The typical construction type in many countries is reinforced concrete structures with masonry infill walls. Therefore, it is crucial to understand the contribution of infill walls to earthquake response of these structures. In this study, the frames of the structure, infilled or not, along with the shear walls are considered to be two-dimensional substructures and they are modeled using the boundary element method and subregioning techniques. Special contact conditions between the masonry infill and the surrounding reinforced concrete frame may be accounted for by introducing appropriate interface conditions for the cases of separation, tensionless bond, friction and slip. The total stiffness of the building is obtained considering two translational and one rotational degree of freedom at each storey level and by assembling the corresponding flexibilities of the substructures, i.e. frames and walls. This is then incorporated into the dynamic analysis of the building in order to determine its response, study the effect of the masonry infill, of the open ground floor (pilotis) and soft-storeys.

Introduction

Masonry infill walls are found in most existing concrete frame building systems because they are often cost-effective and suitable for temperature and sound insulation purposes. In these structures, exterior masonry walls and interior partitions, usually regarded as nonstructural architectural elements, are built as an infill between the frame members. The usual practice in the structural design of infill-frames is to ignore the structural interaction between the frame and infill implying that the infill has no influence on the structural behavior of the building except for its mass. Although, there are a few national codes which have addressed the effects of infill in the analysis and design of masonry infilled reinforced concrete frames, they differ greatly in the manner these effects are to be considered in the design process from aseismic performance point of view [1]. However, the actual behavior of such structures observed during past earthquakes shows that their response is often wrongly predicted during the design stage. Masonry infill walls may have significant positive or negative effects on the global behavior of buildings as real interaction between the

infill panel and frame results in premature failure of the frame in some cases, and in improved performance in others [2, 3]. These effects are generally positive: masonry infill walls can increase global stiffness and strength of the structure. On the other hand, potentially negative effects may occur such as torsional effects induced by in plan-irregularities, soft-storey effects induced by irregularities and short column effects. Hence, further investigation of the actual behavior of these frames is warranted, with a goal towards developing a displacement-based approach to their design considering infill walls as structural components.

In conventional analysis of infilled frame systems, the masonry infill wall is modeled using either the equivalent diagonal strut model [4, 5] or a refined continuum model [6, 7]. The former is simple and computationally attractive but is theoretically weak. First, identifying the equivalent nonlinear stiffness of the infill masonry structures using diagonal struts is not straightforward, especially in the presence of openings, such as doors or windows, in the wall. Furthermore, it is also not possible to predict the damaged area of masonry either. The latter method based on continuum model can provide an accurate computational representation of both material and geometry aspects [8, 9].

The structural system for a reinforced concrete building consists of open frames (bare frame model), reinforced concrete walls (shear wall model) and frames with masonry infill (infilled frame model). In the present work, all these different models are considered as two-dimensional plane stress problems of the mathematical theory of elasticity. The governing equations are the Navier equations of equilibrium along with appropriate boundary conditions. A numerical solution to this problem may be obtained either through a boundary-only model and application of the boundary element method (BEM), or a domain model based on the finite element method. However, it is preferable to adopt the boundary element model since it requires a reduced number of degrees of freedom for an accurate solution, the nodal points are all located on the boundary, where the different components of the building are interacting, and finally, the BEM computes the stress field in the interior of the structure with the same degree of accuracy as it does for the unknown boundary quantities [10, 11]. The lateral stiffness of the typical single-bay, single-story infilled frame obtained by the BEM, is used to construct the total lateral stiffness of multistory frames with several bays that are found in buildings. The assembly procedure is performed through the lateral flexibility of the individual frames rather than the stiffness. The proposed methodology may also account for the modified stiffness of the infilled frame due to special contact conditions at the interface between the surrounding frame and the infill wall [12]. The lateral stiffnesses of all the frames of a building are combined into the total (global) stiffness of the building and along with the total mass are used in the dynamic analysis to determine the natural frequencies, the mode shapes and the response of the structure under earthquake.

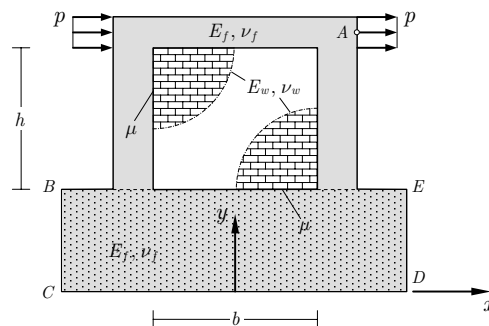


Fig. 1: Geometry and loading of the typical single-bay, single-story infilled frame

Boundary Integral Equations

The typical frame with an infill wall is shown in fig. (1). The bottom side is considered to be clamped to the rectangular foundation *BCDE* for better implementation of the fixed support conditions at the bottom side of the columns and the infill wall. The structure is subjected to lateral load at the top, which may be applied either at the two ends of the beam (fig. 1) or it may be distributed along the top of the beam in the horizontal direction. The material constants and the thickness of the concrete frame and the masonry infill are different.

The boundary integral equations pertaining to the plane elastostatic problem incorporate the fundamental solution of Navier’s equations in terms of the displacement components, which is the well-known Kelvin’s solution [10]. Its components represent a two-point second order tensor known as Green’s tensor and it may be written using indicial notation as

$$U_{ij} = -\frac{1}{8\pi G} \left[(3 - \nu) \delta_{ij} \ell nr - (1 + \nu) r_i r_j + \frac{7 - \nu}{2} \delta_{ij} \right] \quad (i, j = 1, 2) \tag{1}$$

where *G* is the shear modulus, ν the Poisson’s ratio and *r* the distance between field and source point

$$r = \sqrt{(x_1 - \xi_1)^2 + (x_2 - \xi_2)^2} \quad \text{and} \quad r_{,i} = \frac{\partial r}{\partial x_i} = \frac{x_i - \xi_i}{r} \tag{2}$$

From the physical point of view, the component $U_{ij}(P, Q)$ of the two-dimensional elasticity fundamental solution expresses the displacement in the x_i direction at a field point $P(x_1, x_2)$ of an infinite plane medium due to a concentrated unit body force applied at a source point $Q(\xi_1, \xi_2)$ in the x_j direction. The constant term in eq. (1) can be omitted, because it produces only rigid body displacements which do not influence the stresses and the strains.

The tractions produced on the boundary due to the concentrated force are expressed as

$$T_{ij} = -\frac{1 - \nu}{4\pi r} \left[\left(\delta_{ij} + 2 \frac{(1 + \nu)}{(1 - \nu)} r_i r_j \right) r_{,n} + (r_i n_j - r_j n_i) \right] \quad (i, j = 1, 2) \tag{3}$$

where partial derivatives of *r* are assumed to be with respect to the coordinates x_1 and x_2 of the boundary point *p* (eq. 2) and $\hat{n}(n_1, n_2)$ is the outward unit vector normal to the boundary at point $p(x_1, x_2) \in \Gamma$. The derivative of *r* in the direction of \hat{n} is given as

$$r_{,n} = r_{,i} n_i = r_{,1} n_1 + r_{,2} n_2 \tag{4}$$

The integral representation of the solution to the plane elasticity problem yields the displacement component in the x_j direction at point $Q(\xi_1, \xi_2)$ inside the domain Ω or $q(\xi_1, \xi_2)$ on the boundary Γ in the form

$$c_{ji} u_j(Q) = \int_{\Omega} U_{ij}(P, Q) b_i(P) d\Omega_P + \int_{\Gamma} [U_{ij}(p, Q) t_i(p) - T_{ij}(p, Q) u_i(p)] ds_p \tag{5}$$

where $b_i(P)$ are the body forces at point $P(x_1, x_2) \in \Omega$ and $u_i(p)$, $t_i(p)$ are the boundary displacements and tractions, respectively, at point $p(x_1, x_2) \in \Gamma$. The coefficient c_{ji} is equal to $\frac{1}{2} \delta_{ji}$ at points $q(\xi_1, \xi_2) \in \Gamma$ where the boundary is smooth, δ_{ji} at points $Q(\xi_1, \xi_2) \in \Omega$ and 0 at points outside the domain Ω .

The frame is divided into several subregions, which may be the beam, the two columns and the masonry infill wall. Each of them is discretized along the boundary into elements for which it is assumed that the

unknown quantities, displacement or traction components, are constant. The discrete form of eq. (5) for region i relates the components of all the boundary nodal displacements $\{u\}_i$ to the corresponding tractions $\{t\}_i$ in the following way

$$\left(\frac{1}{2}[T] + [H]_i\right)\{u\}_i - [G]_i\{t\}_i = \{F\}_i \quad (6)$$

The matrix equations for all the subregions are combined into a single equation which is solved for the unknown displacements along the free sides and both displacements and tractions along the interfaces. The interface conditions between the different materials (concrete and masonry), may be set to accommodate either perfect bonding or more complex conditions, such as tensionless bond, frictional contact, separation and slip, as it is suggested in [12]. More specifically, this may be done through an iterative boundary element technique based on the total deformation formulation concept. Deformed configurations for perfect bond and frictional slip with tensionless bonding are depicted in fig. (2), while the influence of the various types of interface conditions are presented in fig. (3).

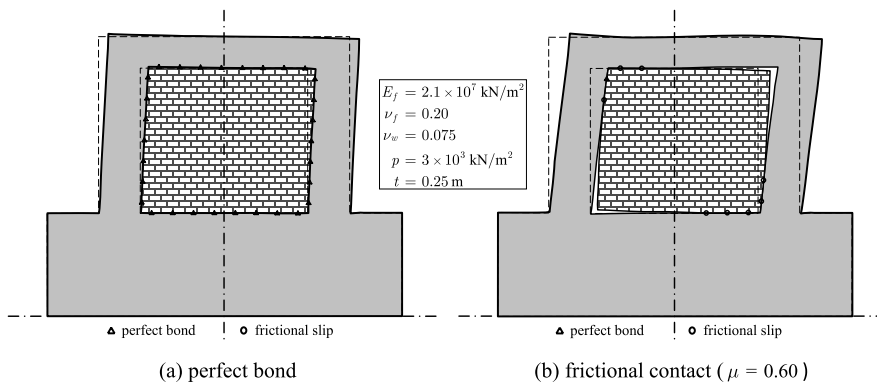


Fig. 2: Deformation of single-bay, single-story infilled frame ($E_w = 0.20E_f$, $\nu_f = 0.20$, $\nu_w = 0.075$)

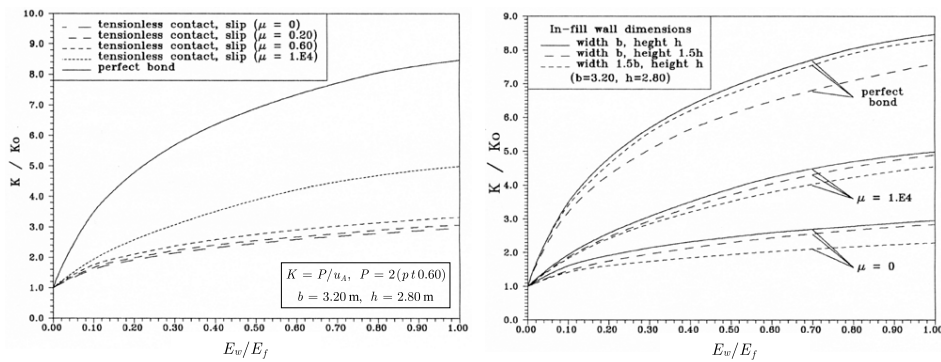


Fig. 3: Influence of infill wall in the lateral stiffness of single-bay, single-story infilled frame for different interface conditions and wall dimensions (K_0 stiffness of bare frame)

Substructures and Total Lateral Frame Stiffness

The boundary element method may be easily applied in the aforementioned way for the analysis of multi-story multi-bay frames of any dimensions and complexity. However, even for medium sized buildings, this numerical method requires many degrees of freedom and produces large stiffness matrices. Of course the dimensions are much smaller than those involved in domain methods and BEM remains clearly more economical than FEM. Considering, that in a typical building there are many frames along both main directions and also that their stiffness matrices should be incorporated into the building's total stiffness, it becomes necessary to find an alternative approach for the dynamic analysis of multistory buildings.

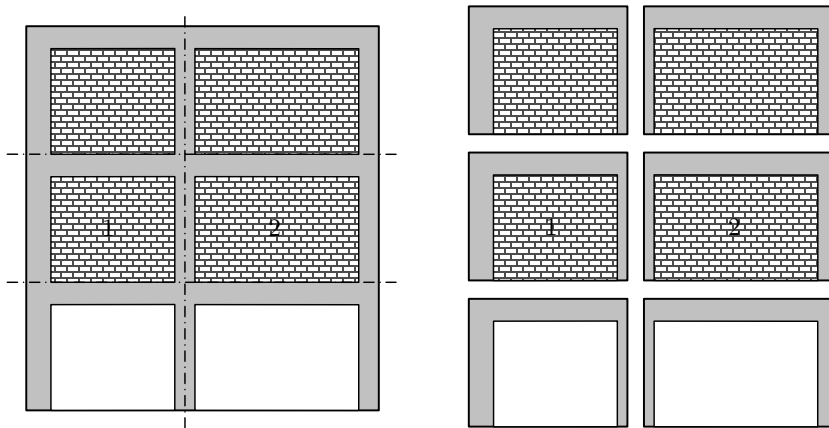


Fig. 4: Three-storey two-bay infilled frame divided into single-bay frame substructures

Application of the BEM to multi-storey multi-bay frames with masonry infill walls reveals that rotations at the ends of beams and also axial deformations of the reinforced concrete members are negligible compared to the lateral displacements. Adjacent frames on a storey undergo the same horizontal displacements and therefore the combined stiffness at each level may be obtained by summing up lateral stiffnesses of all the individual frames. Based on these observations, a methodology is developed for determining in a simple way the total stiffness of a multistorey frame. It requires the decomposition of the multi-storey frame into one-bay frames (fig. 4) whose stiffness is obtained using BEM modeling, both for the reinforced concrete frame and the masonry wall (if it is present). The combined stiffness at each storey is determined by adding the lateral stiffnesses of the frames of that storey and finally, the total stiffness of the structure is calculated through the flexibilities of all the storeys.

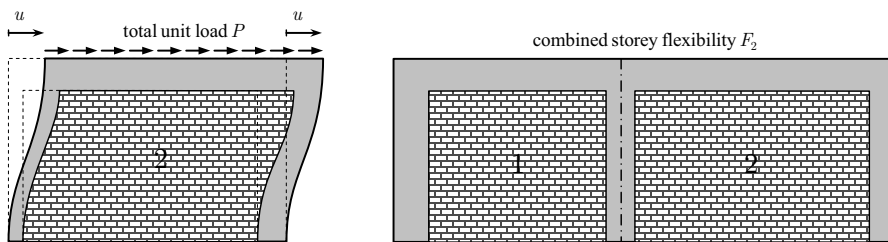


Fig. 5: Lateral stiffness of a single infilled frame and total storey flexibility

The frame of fig. (4) is divided into six single-bay frame substructures. Each of these frames is analyzed for distributed shear loading along its beam (fig. 5) using the boundary element method and appropriate conditions at the concrete-masonry interface. For example, the lateral stiffness K_2 and flexibility F_2 of the second storey is determined from the stiffnesses k_1^2 and k_2^2 of frames #1 and #2, respectively,

$$K_2 = k_1^2 + k_2^2 \quad \text{and} \quad F_2 = \frac{1}{K_2} = \frac{1}{k_1^2 + k_2^2} \quad (7)$$

where $k_2^2 = P/u$ as it is shown in fig. (5). The flexibilities F_1 and F_3 of the first and third storeys are obtained in exactly the same way.

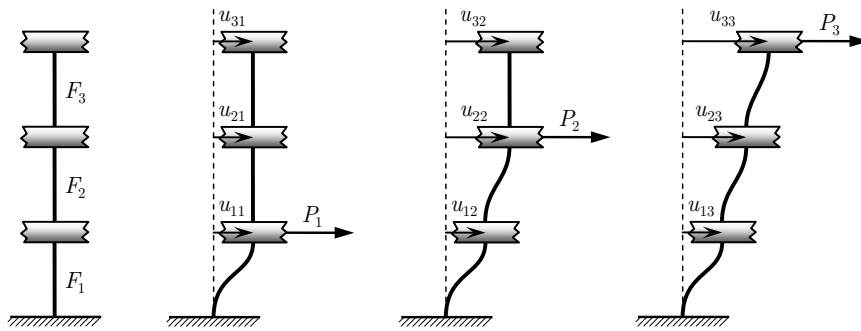


Fig. 6: Lateral loads and displacements of a three-storey frame for the evaluation of its total flexibility

The frame of fig. (4) has three degrees of freedom, which are the lateral displacements of the storeys. Denoting by F_1 , F_2 and F_3 the total flexibilities at each storey and by u_{ij} the horizontal displacement of the i -th storey due to lateral load P_j at the j -th storey ($i, j = 1, 2, 3$), the following relations hold (fig. 6)

$$\text{force } P_1 \text{ at storey 1: } u_{11} = u_{21} = u_{31} = F_1 P_1 \quad (8a)$$

$$\text{force } P_2 \text{ at storey 2: } u_{12} = F_1 P_2, \quad u_{22} = u_{32} = u_{12} + F_2 P_2 = (F_1 + F_2) P_2 \quad (8b)$$

$$\begin{aligned} \text{force } P_3 \text{ at storey 3: } u_{13} &= F_1 P_3, \quad u_{23} = u_{13} + F_2 P_3 = (F_1 + F_2) P_3, \\ u_{33} &= u_{23} + F_3 P_3 = (F_1 + F_2 + F_3) P_3 \end{aligned} \quad (8c)$$

In matrix notation, the response vector is expressed in terms of the force vector through the flexibility matrix

$$\{U\} = [F]\{P\} \Rightarrow \begin{Bmatrix} u_1 \\ u_2 \\ u_3 \end{Bmatrix} = \begin{Bmatrix} u_{11} & u_{12} & u_{13} \\ u_{21} & u_{22} & u_{23} \\ u_{31} & u_{32} & u_{33} \end{Bmatrix} = \begin{Bmatrix} F_1 & F_1 & F_1 \\ F_1 & (F_1 + F_2) & (F_1 + F_2) \\ F_1 & (F_1 + F_2) & (F_1 + F_2 + F_3) \end{Bmatrix} \begin{Bmatrix} P_1 \\ P_2 \\ P_3 \end{Bmatrix} \quad (9)$$

For an N -storey multi-bay frame the number of degrees of freedom becomes N . The flexibility matrix $[F]$ is constructed in exactly the same way as in the above example and its inverse yields the total stiffness matrix $[K]$. The latter may then be used in the dynamic analysis, either of the N -storey frame, or it may be included in a building's global stiffness matrix for a study of its dynamic response. The expression for $[K]$ is

$$[F] = \begin{bmatrix} F_1 & F_1 & F_1 & \dots & F_1 \\ F_1 & (F_1 + F_2) & (F_1 + F_2) & \dots & (F_1 + F_2) \\ F_1 & (F_1 + F_2) & (F_1 + F_2 + F_3) & \dots & (F_1 + F_2 + F_3) \\ \vdots & \vdots & \vdots & \ddots & \vdots \\ F_1 & (F_1 + F_2) & (F_1 + F_2 + F_3) & \dots & (F_1 + F_2 + F_3 + \dots + F_N) \end{bmatrix} \quad \text{and} \quad [K] = [F]^{-1} \quad (10)$$

Dynamic Analysis and Numerical Application

There is a general agreement among researchers that infilled frames have greater strength as compared to frames without infill walls. The presence of the infill walls increases the lateral stiffness considerably. Due to the change in stiffness and mass of the structural system, the dynamic characteristics change as well. Recent earthquakes have revealed that infill walls have an important effect on the resistance and stiffness of buildings. However, the effect of infill walls on the building response under seismic loading is very complex and math intensive issue. The proposed methodology is practical, easily adaptable and models accurately the real behavior of structural systems. In the sequel, the adopted approach for the dynamic analysis is demonstrated through the study of a four-storey reinforced concrete frame structure with different amount of masonry infill walls and open first storey (fig. 7). The effect of infill walls is investigated by comparing the results to those obtained for the case of open frames.

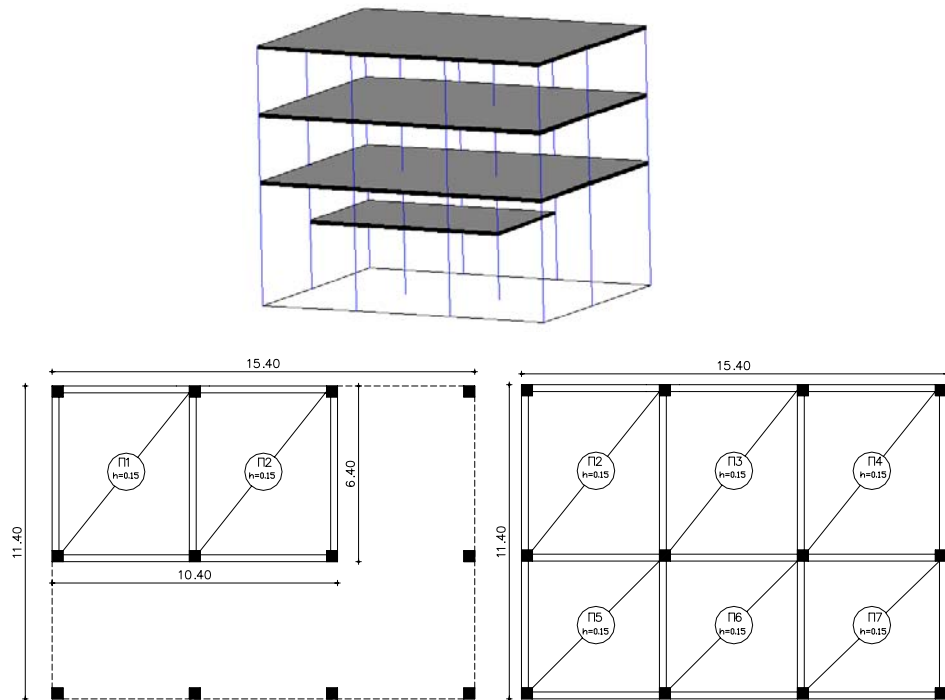


Fig. 7: Four-storey building elevation and floor plans

The eigenfrequencies and the corresponding eigenmodes of the structure are determined from the equation

$$([K] - \omega_i^2 [m]) [b^i] = 0 \quad (i = 1, 2, \dots, 12) \quad (11)$$

in which $[K]$ is the total stiffness matrix of the structure and $[m]$ its mass matrix. The system is considered to have three degrees of freedom per storey, two translational and one rotational. The stiffness of all frames of the building is incorporated into the total stiffness of the building for the cases of bare and infilled frames. The corresponding mode vectors for each of the eigenfrequencies ω_i is obtained from the expression

$$([K] - [m]\omega_i)[b^i] = [0] \quad (12)$$

by setting one of the entries of $[b^i]$ equal to 1, since the system is indefinite being homogeneous with zero determinant. The normalized mode shapes may then be defined as

$$[\Phi^i] = \frac{1}{\max(b_j^i)} \begin{bmatrix} 1 \\ b_2^i \\ \vdots \\ b_N^i \end{bmatrix} \quad (i = 1, 2, \dots, 12) \quad (13)$$

For each eigenmode the generalized mass and the participation factor are

$$[M^i] = [\Phi^i]^T [m] [\Phi^i] \quad \text{and} \quad L_i = [\Phi^i]^T [m] [r] \quad (14)$$

where $[r]$ is the static influence vector, which defines the direction of the seismic force (x or y direction), becoming $[r_x]$ or $[r_y]$, respectively,

$$\begin{aligned} [r_x] &= [1 \ 0 \ 0 \ \vdots \ 1 \ 0 \ 0 \ \vdots \ \vdots \ \vdots \ 1 \ 0 \ 0]_{12 \times 12}^T \\ [r_y] &= [0 \ 1 \ 0 \ \vdots \ 0 \ 1 \ 0 \ \vdots \ \vdots \ \vdots \ 0 \ 1 \ 0]_{12 \times 12}^T \end{aligned} \quad (15)$$

The resulting eigenfrequencies for the four-storey building of fig. (7) are given in Table 1 for the case of open frames and the case of infill masonry walls.

Eigenfrequencies		
	Open frames	Masonry infilled frames
1	10.29	8.83
2	10.73	10.43
3	14.34	13.47
4	35.58	44.31
5	36.26	45.60
6	49.96	60.48

Table 1: Eigenfrequencies of the building with and without masonry infills

The displacements and rotations of the structure are calculated using the following expression

$$u_i^{rk} = \frac{(L_k^r)^2}{M_i^k} \Phi_i^k \frac{SA(T_k)}{\omega_k^2} \quad (16)$$

where $SA(T_k)$ is the spectral acceleration of the structure using the Greek 2000 Aseismic Code response spectrum with 5% damping. The maximum value of each degree of freedom is the superposition of all the eigenmode displacements using the Complete Quadratic Combination (CQC) method

$$\max u_k = \sqrt{\sum_{i=1}^N \sum_{j=1}^N \varepsilon_{ij} u_i^k u_j^k} \quad \text{and} \quad \varepsilon_{ij} = \frac{8z^2 \left(1 + \frac{\omega_j}{\omega_i}\right) \left(\frac{\omega_j}{\omega_i}\right)^{\frac{2}{3}}}{\left[1 - \left(\frac{\omega_j}{\omega_i}\right)^2\right]^2 + 4z^2 \frac{\omega_j}{\omega_i} \left(1 + \frac{\omega_j}{\omega_i}\right)^2} \quad (17)$$

where $i, j = 1, 2, \dots, N$, N is the number of degrees of freedom ($N = 12$), z is the damping of the structure (5%) and u_i^k are the displacement components of the k -th eigenmode. The ratio $(L_k^i)^2 / M_i^k$ is the acting mass of each eigenmode, having dimensions of mass and physical meaning the participation of each eigenmode to the oscillation of the whole system.

The maximum values for the earthquake response of the building for the cases of infilled and bare frames are given graphically in figs. (8) and (9) and the deformed shape of the building for earthquake excitation in the y direction are shown in fig. (10). It is evident that the presence of shear walls reduces drastically the storey rotations, while it produces larger displacements for the open ground storey.

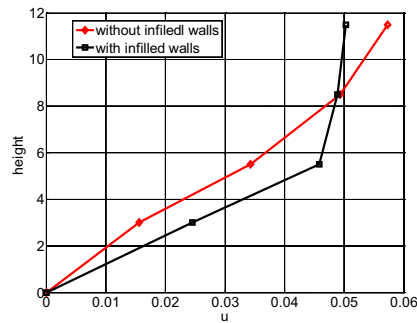


Fig. 8: Maximum displacements u at each storey for earthquake forces in the x direction

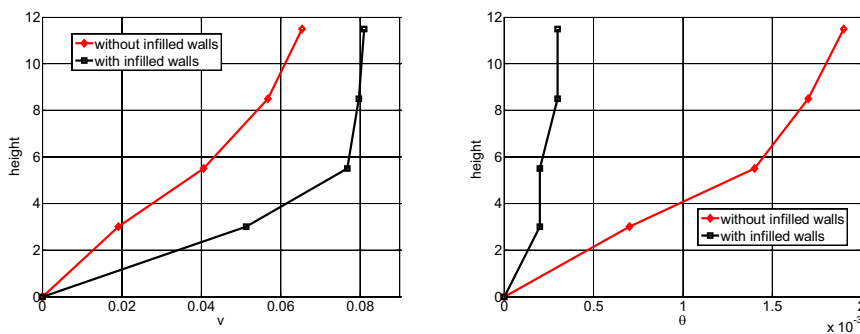


Fig. 9: Maximum displacements v and rotations θ at each storey for earthquake forces in the y direction

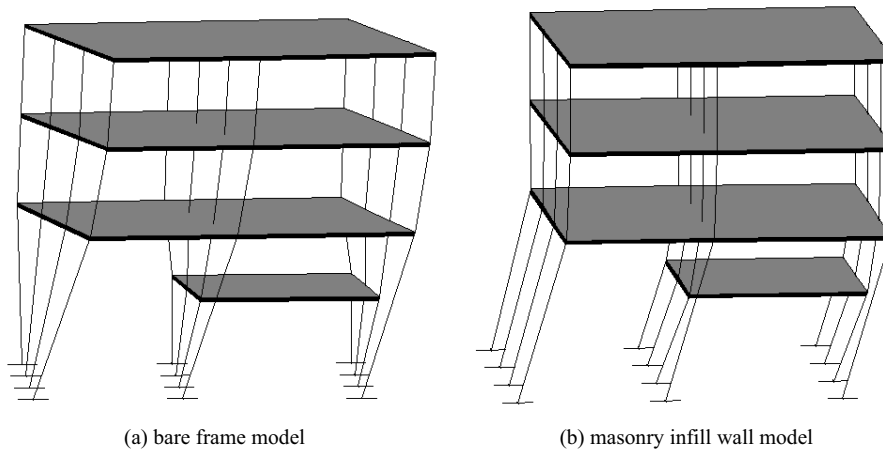


Fig. 10: Deformation of the four-storey structure for earthquake in the y direction

References

- [1] B.K. Hemant, C.R. Durgesh and K.J. Sudhir, "Code Approaches to Seismic Design of Masonry-Infilled Reinforced Concrete Frames: A State-of-the-Art Review", *Earthquake Spectra*, **22**(4), 961-983, (2006).
- [2] S. Harpal, D.K. Paul and V.V. Sastry, "Inelastic Dynamic Response of Reinforced Concrete Infilled Frames", *Computers and Structures*, **69**, 685-693, (1998).
- [3] M.J. Nollet and B.S. Smith, "Stiffened-Story Wall-Frame Tall Building Structure", *Computers and Structures*, **66**(2-3), 225-240, (1998).
- [4] B. Stafford-Smith, "Behavior of square infilled frames", *ASCE Journal of the structural engineering division*, **91**, 381-403, (1966).
- [5] F.J. Crisafulli, A.J. Carr and R. Park, "Analytical Modelling of Infilled Frame Structures - A General Review", *Bulletin of the New Zealand Society for Earthquake Engineering*, **33**(1), 30-47, (2000).
- [6] G.M. Calvi and D. Bolognini, "Seismic Response of Reinforced Concrete Frames Infilled with Masonry Panels Weakly Reinforced", *Journal of Earthquake Engineering*, **5**(2), 153-185, (2001).
- [7] K.A. Korkmaz, F. Demir and M. Sivri, "Earthquake Assessment of R/C Structures with Masonry Infill Walls", *International Journal of Science & Technology*, **2**(2), 155-164, (2007).
- [8] L.T. Phan, D.R. Todd and H.S. Lew, "Strengthening methodology for lightly reinforced concrete frames-II. Recommended calculation techniques for the design of infill walls", *Building and Fire Research Laboratory, National Institute of Standards and Technology, U.S. Dept. of Commerce*, (1994).
- [9] M. Griffith, "Seismic Retrofit of RC Frame Buildings with Masonry Infill Walls: Literature Review and Preliminary Case Study", *Institute for the Protection and Security of the Citizen, Joint Research Centre, European Commission*, (2008).
- [10] J.T. Katsikadelis, "Boundary Elements, Theory & Application", Elsevier (2003).
- [11] J.T. Katsikadelis and F.T. Kokkinos, "Static and dynamic analysis of composite shear walls by the boundary element method", *Acta Mechanica*, **68**, 231-250, (1987).
- [12] J.T. Katsikadelis and F.T. Kokkinos, "Analysis of composite shear walls with interface separation, friction and slip using BEM", *Int. J. Solids Structures*, **30**(13), 1825-1848, (1993).

Radial Integration BEM for Nonlinear Heat Conduction and Stress Analysis of Thermal Protection Systems

Xiao-Wei Gao¹, Jing Wang² and Ch. Zhang³

¹ School of Aeronautics and Astronautics, Dalian University of Technology, Dalian, 116024, China,
Email: xwgao@dlut.edu.cn

² Department of Engineering Mechanics, Southeast University, Nanjing, 210096, China,
Email: wangjing060730@qq.com

³ Department of Civil Engineering, University of Siegen, D-57068 Siegen, Germany,
Email: c.zhang@uni-siegen.de

Keywords: Heat conduction, Thermoelasticity, Radial integration method, Boundary element method, Thermal protection systems.

Abstract. In this paper, a robust boundary element method for solving 2D and 3D nonlinear heat conduction and thermal stress problems is presented based on the use of the radial integration method (RIM) which results in an algorithm without the need of internal cells. In the method, material properties are allowed to be any type functions of the temperature and the Newton-Raphson iteration scheme is employed to solve the resulting nonlinear equation set. Numerical results are given to demonstrate the efficiency of the proposed method.

Introduction

Hypersonic spacecrafts usually aviate under a severe aerodynamic heating environment. To prevent the aerodynamic heating from burning the spacecraft structure, the surface of the structure is covered with a thermal protection system (TPS) [1]. TPS consists of multi-layered materials and/or sub-structures such as coating materials, ceramic tiles, strain isolation pad, adhesive materials, and honeycomb cores. When the outside surface of TPS is subjected to a high temperature, the thermal stress between the layers of TPS may become very high, even to an extent of failure. Previous investigation shows that the thermal stress induced in laminated structures is the main cause of structural failure [2]. Therefore the analysis of the heat conduction and thermal stresses is significantly important for a reliable design of TPS.

The boundary element method (BEM) has distinctive advantages in solving problems of fracture mechanics [3] and elastic problems [4], since it only needs to discretize the boundary of the problem into elements. However, the conventional BEM is not so attractive in solving nonhomogeneous, nonlinear and thermoelasticity problems, since domain integrals are inevitably introduced in the resulting integral equations [5]. A direct evaluation of domain integrals requires the discretization of the domain into internal cells. This severely eliminates the distinct advantage of BEM. To overcome this disadvantage, Nardini and Brebbia [6] developed the dual reciprocity method (DRM) to transform the domain integrals into equivalent boundary integrals. To avoid using particular solutions required in the DRM, Gao proposed the radial integration method (RIM) [7] which can transform any domain integrals to the boundary based on a pure mathematical manipulation. RIM has been successfully applied to solve thermoelasticity [8], elastic inclusion [9], and creep damage

mechanics problems [10]. In view of the robustness and simplicity of RIM in evaluating domain integrals without using internal cells, Hematiyan [11] gave a very good assessment to RIM, and Albuquerque et al. [12] compared RIM to DRM numerically through applications to dynamic problems with a more positive conclusion.

Although thermoelasticity problems with constant material properties have been solved using the boundary-only element method based on RIM [8], this methodology has yet not been applied to heat conduction and thermoelasticity problems with material properties (conductivity and Young's modulus) being functions of the temperature, which is the feature of the TPS structure subjected to a high temperature loading. The main objective of this paper is devoted to this subject. First, boundary-domain integral equations for temperature and displacements are derived from the weighted residual forms of governing equations of steady-state heat conduction and elasticity problems. Then, the domain integrals arising in the integral equations are transformed into equivalent boundary integrals using RIM, resulting in a pure boundary element solution algorithm. The material properties are allowed to be any type functions of the temperature and the Newton-Raphson iteration scheme is employed to solve the resulting nonlinear equation set. Numerical examples are presented to demonstrate the efficiency of the proposed method.

Boundary-Domain Integral Equations for Nonlinear Heat Conduction Problems

We consider a steady-state heat conduction problem with the conductivity k depending on the temperature T . The governing equation for such a problem can be expressed as

$$\frac{\partial}{\partial x_i} \left(k(T) \frac{\partial T}{\partial x_i} \right) = 0. \quad (1)$$

The weighted residual form of the above equation can be written using the weight function G as

$$\int_{\Omega} G \frac{\partial}{\partial x_i} \left(k \frac{\partial T}{\partial x_i} \right) d\Omega = 0, \quad (2)$$

where Ω is the domain of the problem. Integrating eq (2) by parts twice and using Gauss' divergence theorem, it follows that

$$\int_{\Omega} G \frac{\partial}{\partial x_i} \left(k \frac{\partial T}{\partial x_i} \right) d\Omega = \int_{\Gamma} G k \frac{\partial T}{\partial x_i} n_i d\Gamma - \int_{\Gamma} k T \frac{\partial G}{\partial x_i} n_i d\Gamma + \int_{\Omega} T \frac{\partial G}{\partial x_i} \frac{\partial k}{\partial x_i} d\Omega + \int_{\Omega} k T \frac{\partial}{\partial x_i} \left(\frac{\partial G}{\partial x_i} \right) d\Omega, \quad (3)$$

where Γ is the boundary of Ω and n_i is the i -th component of the outward normal vector to Γ . By taking the weight function G as the Green's function, i.e.,

$$G(\mathbf{x}, \mathbf{y}) = \begin{cases} \frac{1}{2\pi} \log \left(\frac{1}{r} \right), & \text{for 2D,} \\ \frac{1}{4\pi r}, & \text{for 3D,} \end{cases} \quad (4)$$

the following boundary-domain integral equation can be derived

$$\tilde{T}(\mathbf{y}) = - \int_{\Gamma} G(\mathbf{x}, \mathbf{y}) q(\mathbf{x}) d\Gamma(\mathbf{x}) - \int_{\Gamma} \frac{\partial G(\mathbf{x}, \mathbf{y})}{\partial \mathbf{n}} \tilde{T}(\mathbf{x}) d\Gamma(\mathbf{x}) + \int_{\Omega} V(\mathbf{x}, \mathbf{y}) \tilde{T}(\mathbf{x}) d\Omega(\mathbf{x}), \quad (5)$$

where $r = \|\mathbf{x} - \mathbf{y}\|$, $\tilde{T}(\mathbf{x}) = k(T)T(\mathbf{x})$ is the normalized temperature, and

$$V(\mathbf{x}, \mathbf{y}) = \frac{1}{k(T)} \frac{\partial G(\mathbf{x}, \mathbf{y})}{\partial x_i} \frac{\partial k(T)}{\partial x_i}. \quad (6)$$

Equation (5) is valid only for internal points. As described in many books on BEM [3-5], a boundary integral equation for the boundary points can be easily obtained by letting $\mathbf{y} \rightarrow \Gamma$.

Transformation of Domain Integrals into Boundary Integrals Using RIM

To avoid the discretization of the domain Ω into internal cells for evaluating the domain integral appearing in eq (5), the radial integration method (RIM) [7, 8] is used to transform the domain integral to the boundary integral. Since RIM can only be directly applied to domain integrals with known integrands, the normalized temperature included in eq (5) needs to be approximated by a series of prescribed basis functions as done in DRM [6]. For this purpose, the normalized temperature is expressed as

$$\tilde{T}(\mathbf{x}) = \sum_A \alpha^A \phi^A(R) + a^k x_k + a_0, \quad (7a)$$

$$\sum_A \alpha^A = \sum_A \alpha^A x_k^A, \quad (7b)$$

where $R = \|\mathbf{x} - \mathbf{x}^A\|$ is the distance from the application point A to the field point \mathbf{x} , α^A and a^k are unknown coefficients to be determined by applying the point A to each node [7, 8]. The radial basis function $\phi^A(R)$ used here is the 4-th order spline-type radial basis function (RBF) of the form

$$\phi^A(R) = \begin{cases} 1 - 6\left(\frac{R}{d_A}\right)^2 + 8\left(\frac{R}{d_A}\right)^3 - 3\left(\frac{R}{d_A}\right)^4, & 0 \leq R \leq d_A, \\ 0, & d_A \leq R, \end{cases} \quad (8)$$

where d_A is the support size for the application point A . By substituting eq (8) into the domain integral in eq (5) and using RIM to transform it into a boundary integral, we obtain the following integral relation

$$\int_{\Omega} \frac{\partial G(\mathbf{x}, \mathbf{y})}{\partial x_i} \frac{\partial \ln[k(T)]}{\partial x_i} \tilde{T}(\mathbf{x}) d\Omega(\mathbf{x}) = \sum_A \alpha^A \int_{\Gamma} \frac{1}{r^\alpha(\mathbf{z}, \mathbf{y})} \frac{\partial r}{\partial n} F^A(\mathbf{z}, \mathbf{y}) d\Gamma(\mathbf{z}) + a^k \int_{\Gamma} \frac{r_k}{r^\alpha(\mathbf{z}, \mathbf{y})} \frac{\partial r}{\partial n} F^1(\mathbf{z}, \mathbf{y}) d\Gamma(\mathbf{z}) + (a^k y_k + a^0) \int_{\Gamma} \frac{1}{r^\alpha(\mathbf{z}, \mathbf{y})} \frac{\partial r}{\partial n} F^0(\mathbf{z}, \mathbf{y}) d\Gamma(\mathbf{z}), \quad (9)$$

where

$$F^A(\mathbf{z}, \mathbf{y}) = \int_0^{r(\mathbf{z}, \mathbf{y})} V(\mathbf{x}, \mathbf{y}) \phi^A r^\alpha dr, \quad (10a)$$

$$F^1(\mathbf{z}, \mathbf{y}) = \int_0^{r(\mathbf{z}, \mathbf{y})} V(\mathbf{x}, \mathbf{y}) r^{\alpha+1} dr, \quad (10b)$$

$$F^0(\mathbf{z}, \mathbf{y}) = \int_0^{r(\mathbf{z}, \mathbf{y})} V(\mathbf{x}, \mathbf{y}) r^\alpha dr. \quad (10c)$$

In the radial integrals eqs (10), the field coordinates x_i can be expressed in terms of the integration variable r using $x_i = y_i + r_i r$, in which both y_i and r_i are constant in eqs (10) [7]. It is noted that the radial integrals in eqs (10) are regular and can be computed numerically by using standard Gaussian quadrature for every field point. More details on the subject can be found for instance in references [7, 8].

Computation of the Derivatives of the Heat Conductivity

From eq (6) it can be seen that the derivatives of the heat conductivity k with respect to spatial coordinates are included in the kernel function $V(\mathbf{x}, \mathbf{y})$. Using the definition $\tilde{T}(\mathbf{x}) = k(T)T(\mathbf{x})$ we have

$$\frac{\partial k(T)}{\partial x_i} = \frac{\partial k(T)}{\partial T} \frac{\partial T}{\partial x_i} = \frac{\partial \ln[k(T)]}{\partial T} \left\{ \frac{\partial \tilde{T}}{\partial x_i} - \tilde{T} \frac{\partial \ln[k(T)]}{\partial x_i} \right\}. \quad (11)$$

There are two ways to compute $\partial \tilde{T} / \partial x_i$ involved in eq (11). One is to differentiate eq (5) with respect to the source point to obtain an integral equation for $\partial \tilde{T} / \partial x_i$. The other is to use the RBF expression eq (7). The latter one is simple and hence adopted in this analysis. Thus,

$$\frac{\partial \tilde{T}}{\partial x_i} = \sum_A \alpha^A \frac{\partial \phi^A}{\partial x_i} + a^i. \quad (12)$$

From eq (8) it follows that

$$\frac{\partial \phi^A}{\partial x_i} = -12 \frac{x_i - x_i^A}{d_A^2} \left[1 - 2 \left(\frac{R}{d_A} \right) + \left(\frac{R}{d_A} \right)^2 \right], \quad \text{for } 0 \leq R \leq d_A, \quad (13a)$$

and

$$\frac{\partial \phi^A}{\partial x_i} = 0, \quad \text{for } R > d_A. \quad (13b)$$

Formulation for Thermoelasticity with Variable Coefficients

In a similar manner to the derivation of eq (5) and using the governing equations of the thermoelasticity problems [8], the following boundary-domain integral equations for the displacements and the stresses can be obtained

$$\begin{aligned} \tilde{u}_i(\mathbf{y}) = & \int_{\Gamma} U_{ij}(\mathbf{x}, \mathbf{y}) t_j(\mathbf{x}) d\Gamma(\mathbf{x}) - \int_{\Gamma} T_{ij}(\mathbf{x}, \mathbf{y}) \tilde{u}_j(\mathbf{x}) d\Gamma(\mathbf{x}) \\ & + \int_{\Omega} V_{ij}(\mathbf{x}, \mathbf{y}) \tilde{u}_j(\mathbf{x}) d\Omega(\mathbf{x}) + \int_{\Omega} U_{ij,j}(\mathbf{x}, \mathbf{y}) \hat{T}(\mathbf{x}) d\Omega(\mathbf{x}), \end{aligned} \quad (14)$$

$$\begin{aligned} \sigma_{ij}(\mathbf{y}) = & \int_{\Gamma} U_{ijk}(\mathbf{x}, \mathbf{y}) t_k(\mathbf{x}) d\Gamma(\mathbf{x}) - \int_{\Gamma} T_{ijk}(\mathbf{x}, \mathbf{y}) \tilde{u}_k(\mathbf{x}) d\Gamma(\mathbf{x}) \\ & + \int_{\Omega} V_{ijk}(\mathbf{x}, \mathbf{y}) \tilde{u}_k(\mathbf{x}) d\Omega(\mathbf{x}) + \int_{\Omega} \Psi_{ij}(\mathbf{x}, \mathbf{y}) [\hat{T}(\mathbf{x}) - \hat{T}(\mathbf{y})] d\Omega(\mathbf{x}) \\ & + \hat{T}(\mathbf{y}) \int_{\Gamma} r \ln r \frac{\partial r}{\partial n} \Psi_{ij}(\mathbf{x}, \mathbf{y}) d\Gamma(\mathbf{x}) - \delta_{ij} h \hat{T}(\mathbf{y}) + F_{ijk}(\mathbf{y}) \tilde{u}_k(\mathbf{y}), \end{aligned} \tag{15}$$

where U_{ij} , T_{ij} , V_{ij} , U_{ijk} , T_{ijk} , V_{ijk} and F_{ijk} can be found in [13], and Ψ_{ij} and h are given as follows

$$\Psi_{ij} = \frac{(1-2\nu)}{2\alpha\pi(1-\nu)r^\beta} (\delta_{ij} - \beta r_i r_j), \quad h = \frac{(1+\beta)(1-2\nu)}{6(1-\nu)}, \tag{16}$$

in which $\beta=2$ (for 2D) or $\beta=3$ (for 3D) and $\alpha=\beta-1$. The remaining quantities in eqs (14) and (15) are defined as

$$\tilde{u}_j = \mu u_j, \quad \hat{T} = \frac{2(1+\nu)\alpha}{1-2\nu} \tilde{T}. \tag{17}$$

In eq (17), μ and α represent the shear modulus and the thermal expansion coefficient, respectively, both being the functions of the temperature T . The domain integrals included in eqs (14) and (15) are also transformed to the boundary integrals by using RIM. The procedure is the same as described in the previous section and in references [8, 13].

System Equations and Multi-Domain BEM Solution Technique

In the boundary-domain integral equation (5) for heat conduction problem, the unknown variable T (the temperature) is included in the kernel V and this makes the resulting system equations nonlinear. An iteration procedure is required to solve the nonlinear equation set. The Newton-Raphson iterative method is adopted in the study. More details of the method can be found in many references, e.g. in reference [5].

TPS is usually composed of different materials or sub-structures. Therefore, in order to solve such complex problems using BEM, the multi-domain technique can be applied. In this analysis, the three-step multi-domain BEM (MDBEM) presented in [14] is adopted for both heat conduction and thermoelasticity problems. The three-step MDBEM was particularly developed for solving nonhomogenous and nonlinear problems. One of its features is that large-scale problems can be solved efficiently by this method.

Numerical Examples

Example 1: Heat conduction over a square plate

To verify the presented method, we consider in the first example a 2D heat conduction problem over a square plate with a dimension of 1m×1m, for which the analytical solution is available. Figure 1 shows the boundary conditions and the dependence of the conductivity on the temperature T . Figure 2 gives the computed temperature using different internal points, which show a very good agreement between the present numerical results and the analytical result. Also, it can be seen from Fig. 2 that the present method is very insensitive to the used numbers of internal nodes.

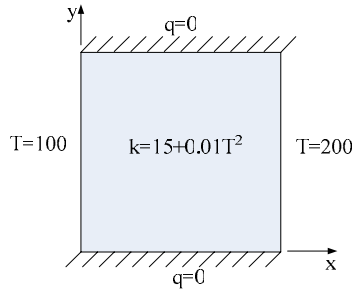


Fig. 1: 2D heat conduction model

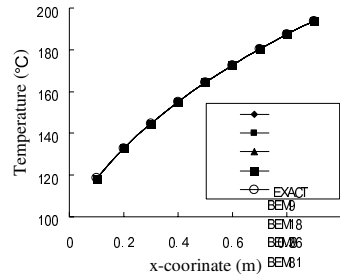


Fig. 2: Computed temperature

Example 2: Thermal stress analysis over a honeycomb structure

The second example is a honeycomb structure which is commonly used in TPS. The structure consists of upper and lower cover plates with a thickness of 0.125mm and the honeycomb core with a wall thickness being 0.035mm, a wall height being 7.11mm, and a width of each honeycomb being 4.76mm. The structure has a total of 100 honeycombs with the global dimension of 49.98mm×42.56mm×7.36mm. Figure 3 shows the BEM model consisting of 8946 four-noded boundary and interface elements with 8484 nodes. In the BEM model, the upper and lower plates, the honeycomb wall, and the hollow volume filling with air are treated as different sub-domains. The heat conductivities are $7.8 \times 10^{-5} \text{ W}/(\text{mm} \cdot \text{K})$ for the upper and lower plates, $1.7 \times 10^{-4} \text{ W}/(\text{mm} \cdot \text{K})$ for the honeycomb wall, and $2.3 \times 10^{-5} \text{ W}/(\text{mm} \cdot \text{K})$ for the filled air. The thermal boundary conditions are given as follows: the top and bottom surfaces are specified with the temperature $T(x, y, z) = -\frac{225xz}{49.98 \times 7.36} - \frac{75x}{49.98} + \frac{600z}{7.36} + 200 \text{ (K)}$ and the side surfaces are adiabatic.

Firstly, the heat conduction computation is performed to obtain the temperature distribution in the structure, and then the thermoelasticity computation is carried out using the obtained temperature. In the thermoelasticity computation, the material parameters are taken as $E = 280 \text{ GPa}$ and $\nu = 0.25$, and the thermal expansion coefficient is $\alpha = 2.47 \times 10^{-6} \text{ mm}/\text{K}$. The top surface is uniformly imposed by traction conditions of $\tau_x = 0.05 \text{ MPa}$ and $\tau_z = -0.5 \text{ MPa}$, the bottom surface is fixed, and the side surface is traction free. Figure 5 shows the computed temperatures at points shown in Fig. 4, which are located below the inner surface of the upper plate with a distance of 0.01mm to the inner surface. The computed heat flux q_z , displacement u_x and stress σ_{xx} at these selected points are presented in Figs. 6, 7 and 8 respectively.

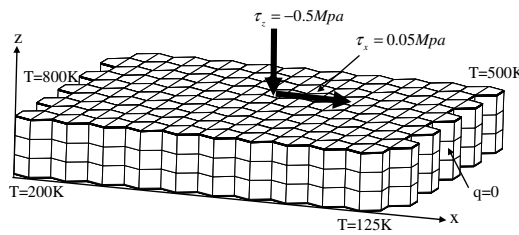


Fig. 3: BEM model and boundary conditions

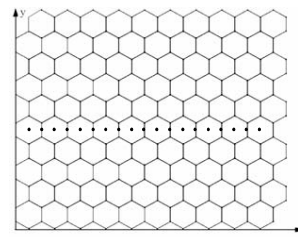


Fig. 4: Points for results plotting

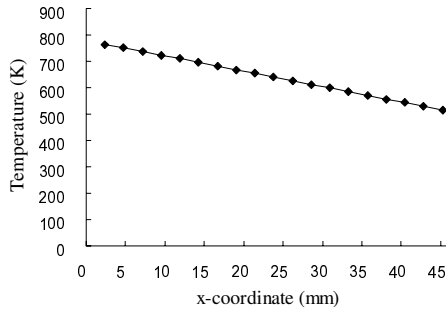


Fig. 5: Distribution of temperature

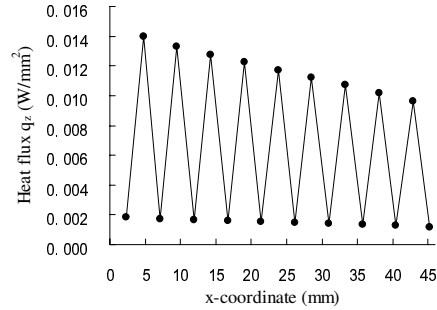


Fig. 6: Distribution of heat flux q_z

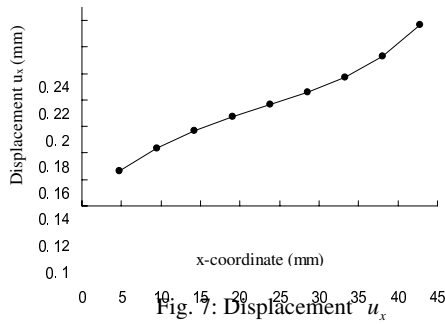


Fig. 7: Displacement u_x

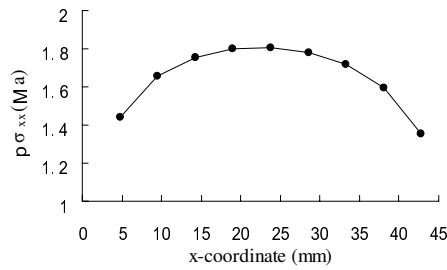


Fig. 8: Stress σ_{xx}

From Fig. 6, we can see that the heat flux q_z has a much larger value on the honeycomb side wall than in the filled hollow air. This important phenomenon captured in the example is attributed to the discretization of the two surfaces of the honeycomb side wall into boundary elements. Since the thickness of the wall is very small, nearly singular problems exist in computing the boundary integrals. An unequally-spaced element subdivision technique is used in the paper to evaluate the nearly singular integrals, based on the modification of the corresponding subroutines published in reference [5]. On the other hand, Fig. 8 shows that the computed stress σ_{xx} is much larger than the imposed tractions. This indicates that the thermal stress is an important factor in the fracture and failure analysis of TPS.

Summary

In this paper, an advanced boundary element method to solve nonlinear heat conduction and thermoelasticity problems based on the radial integration method is presented. The implemented method is efficient to perform thermal stress analysis for TPS. Multi-domain BEM is adopted to solve the multi-material problems and an unequally-spaced element subdivision technique is used to deal with the nearly singular problems occurring in the thin walled structures. Numerical examples are presented and discussed to demonstrate the efficiency of the proposed method.

Acknowledgements

Support by the National Natural Science Foundation of China (10872050) and the German Research Foundation (DFG) is gratefully acknowledged.

References

- [1] D.D. Liu, P.C. Chen, L. Tang, K.T. Chang and X.W. Gao *Proc. of AIAA/AAAF 11th International Space Planes and Hypersonic Systems and Technologies Conference*, Orleans, France, 29 Sept. - 4 Oct. 2002.
- [2] J. Hohe, S. Goswami and W. Becker *Computational Materials Science*, **26**, 71-79 (2003).
- [3] M.H. Aliabadi *Applied Mechanics Reviews*, **50**, 83-96 (1997).
- [4] C.A. Brebbia and J. Dominguez *Boundary Elements: An Introductory Course*, McGraw-Hill Book Co., London (1992).
- [5] X.W. Gao and T.G. Davies *Boundary Element Programming in Mechanics*. Cambridge, London, New York: Cambridge University Press (2002).
- [6] D. Nardini and C.A. Brebbia *Boundary Element Methods in Engineering* (C.A. Brebbia, Editor), Berlin: Springer (1982), pp. 312-26.
- [7] X.W. Gao *Engineering Analysis with Boundary Elements*, **26**, 905-16 (2002).
- [8] X.W. Gao *International Journal for Numerical Methods in Engineering*, **57**, 975-90 (2003).
- [9] C.Y. Dong, S.H. Lo and Y.K. Cheung *Engineering Analysis with Boundary Elements*, **28**, 623-632 (2004).
- [10] H. Gun *Engineering Analysis with Boundary Elements*, **29**, 749-755 (2005).
- [11] M.R. Hematiyan *Computational Mechanics*, **39**, 509-520 (2007).
- [12] E.L. Albuquerque, P. Sollero and W.P. Paiva *Commun. Numer. Meth. Eng.*, **23**, 805-818 (2007).
- [13] X.W. Gao, Ch. Zhang and L. Guo *Engineering Analysis with Boundary Elements*, **31**, 974-982 (2007).
- [14] X.W. Gao, L. Guo and Ch. Zhang *Engineering Analysis with Boundary Elements*, **31**, 965-973 (2007).

BEM formulation to analyze non-saturated porous media

Wilson W. WUTZOW¹, Ahmed BENALLAL¹, Wilson S. VENTURINI²

¹ 61, avenue du Président Wilson. F-94230 Cachan, France, wutzow@lmt.ens-cachan.fr

² Av Trabalhador São-carlense, 400, São Carlos, 13566-590, Brazil, venturin@sc.usp.br

Keywords: Porous media, non-saturated domains, boundary elements

Abstract.

In this article a BEM formulation developed to analyse the behaviour of saturated porous media is extended to the non-saturated case. The poroelastic theory for non-saturated media used to derive the integral representation is due to Coussy and derived from a free energy potential, for which the capillary pressure and the interface energy are taken into account. The saturation level is described by the Van Genuchten model. The BEM formulation is derived by using the standard Kelvin fundamental solutions for static solids. Thus, domain integrals appear in the all needed integral representations. The formulation is illustrated on a simple example.

Introduction

The analysis of porous solids with fluids moving inside under quasi-static conditions is very important to several applications in engineering. Biot [1] was the first to propose a coupled theory for three-dimensional consolidation for isotropic materials and incompressible fluids. In the following works Biot [2,3] and Biot & Willis [4] have extended the theory to general anisotropic materials with viscoelastic behaviour and compressible fluids.

The boundary element method is widely used in this context and particularly for poro-elastic quasi-static systems. Indeed there is a considerable amount of works dealing with porous media in the boundary element framework, see e.g. Cheng & Liggett [5], Dargush & Banerjee [6], Cheng & Detournay [7], Cavalcanti & Telles [8], Soares [9], Benallal et al [10].

While the modelling and analysis of the saturated case is well established now, the situation is far from that in the non-saturated case and several models are still debated. Regarding this subject we want to point out the work due to Alonso & Delage [11]. We also mention the systematic use of thermodynamics and the description in the framework of fully and partially saturated porous materials by Coussy [12], Coussy & Fleureau [13], Coussy [14, 15], Coussy et al [16] and Dormieux et al [17]. In some of these recent works, the porous media model is further enriched by taking into account the capillary pressure and interface energy effects.

In this work the boundary element formulation as first developed for saturated porous media problems proposed by Benallal et al [12] is extended to incorporate the non-saturated case and applied to problems where the skeleton is assumed to be elastic. The Biot's formulation is used for the description of the saturated porous environments and an energetic consistent formulation based on the works of Coussy is adopted for its extension to the framework of unsaturated porous media. For this case the interface energy and the capillary pressure are taken into account to formulate the problem. The saturation level is given by the Van Genuchten's model.

The integral equations to derive the algebraic representation for the solid mechanics and the potential problems are obtained by using the simple static fundamental solutions. The resulting domain integrals to take into account the variations of rigidity, capillary pressure and saturation. A simple example is then solved to demonstrate the potentiality of the proposed formulation.

Governing equations and constitutive relations

Consider a non-saturated porous body of domain Ω and boundary Γ over which capillary pressure p^c , porosity ϕ and the saturation are given by:

$$p^c = p^g - p^\ell \quad \phi = \phi^\ell + \phi^g \quad S^\ell = \phi^\ell / \phi \quad S^g = \phi^g / \phi \quad S^\ell + S^g = 1 \quad (1a,b,c,d,e)$$

where p^g and p^ℓ are the liquid and gas pressures, S^ℓ and S^g represent the saturation parts and ϕ^ℓ and ϕ^g are the saturations parts; the superscripts n and g defines liquid and gas parts respectively.

For the isothermal case and neglecting the domain loads one can write the Clausius-Duhem inequality as follows:

$$\sigma_{ij} : \frac{d\varepsilon_{ij}}{dt} + (p^\ell S^\ell + p^g S^g) \frac{d\phi}{dt} - \phi p^c \frac{dS^\ell}{dt} - \frac{d\Psi_{sq}(\varepsilon_{ij}, S^\ell, \phi)}{dt} \geq 0 \quad (2)$$

where σ_{ij} and ε_{ij} are the stress and strain states and Ψ_{sq} is the total free energy of the solid part.

Equation (2) gives the total free energy of the structural system, including also the interface energy. Incompressibility is not assumed, i.e., $d\varepsilon_{ij} : I > d\phi$, being I the identity tensor. Thus, the state equations for the poroelastic problem are:

$$\sigma_{ij} = \partial \Psi_{sq} / \partial \varepsilon_{ij} \quad \phi p^c = \partial \Psi_{sq} / \partial S^\ell \quad p^\ell S^\ell + p^g S^g = \partial \Psi_{sq} / \partial \phi \quad (3a,b,c)$$

Taking into account that the solid part is deformable, the capillary effects depend on the liquid part saturation and that Ψ_{sq} is the total energy, including the interface energy ψ_γ and the solid part energy ψ_s , assumed independent on the liquid part saturation one can write

$$\Psi_{sq}(\varepsilon_{ij}, S^\ell, \phi) = \Psi_\gamma(S^\ell, \phi) + \Psi_s(\varepsilon_{ij}, \phi) = \phi U(\phi, S^\ell) + \Psi_s(\varepsilon_{ij}, \phi) \quad (4)$$

where U is the interfacial energy per unit of porous volume and therefore ϕU is the interfacial energy.

The averaged fluid pressure π is given by

$$\pi = p^\ell S^\ell + p^g S^g - \frac{2}{3} \int_{S^\ell}^I p^c dS^\ell = p^\ell S^\ell + p^g S^g - \frac{2}{3} U(\phi, S^\ell) \quad (5)$$

To obtain this expression we have assumed the micro-macro approximation to consider the porous geometry due to Coussy & Fleureau [13]. Moreover, the interface energy is taken into account by the following relation

$$U(\phi, S^n) = \int_{S^n}^I p^c dS^n \quad (6)$$

The free energy potential can be only dependent on the strain tensor ε_{ij} , on the liquid part saturation and on the total Lagrangian porosity. By assuming the separation of the interface and the solid strain energy parts one can obtain the specific free energy from eq (4), in which the part referred to the domain strain is given by [13]

$$\psi_s(\phi, \varepsilon_{ij}) = \frac{1}{2} \varepsilon_{ij} E_{ijkl}^d \varepsilon_{kl} + \frac{1}{2} \left(-btr(\varepsilon_{ij}) + (\phi - \phi_0) + \frac{\pi_0}{M} \right) M \left(-btr(\varepsilon_{ij}) + (\phi - \phi_0) + \frac{\pi_0}{M} \right) \quad (7)$$

where π_0 is the equivalent pressure of the previous increment.

Integral equations

The equilibrium equations for a non-saturated poroelastic solid is given by

$$\sigma_{ij,j}^e - b\pi_i + b_i = 0 \quad (8)$$

where σ_{ij}^e represents a like elastic stress tensor given by $\sigma_{ij}^e = E_{ijkl} \varepsilon_{kl}$, b_i is the body forces and b is the Biot's coefficient of effective stress.

The Somigliana identity can now be derived taking into account eq (8) as follows

$$C_{ij}u_j = - \int_{\Gamma} T_{ij}^* U_j d\Gamma + \int_{\Gamma} u_{ij}^* T_j d\Gamma + b \int_{\Omega} \delta_{ijk} \varepsilon_{ijk}^* \pi d\Omega \quad (9)$$

From eq (9) one can derive the stress integral representation by differentiating it and applying Hooke's law, to obtain the stress integral representation as follows

$$\sigma_{ij} = - \int_{\Gamma} S_{ijk} U_k d\Gamma + \int_{\Gamma} D_{ijk} T_k d\Gamma + b \int_{\Omega} \delta_{kij} E_{ijk} \pi d\Omega + b g_{ij}(\pi) \quad (10)$$

where the free term resulting from the differentiation of the strong singular integral in eq (9) is given by

$$g_{ij}(\pi) = - \frac{1}{8(1-\nu)} [2\pi + (1-4\nu)\delta_{ij}\pi] \quad (11)$$

The integral representations for the fluids part are derived from Darcy's law. For the liquid and gas phases this is given by

$$M_i^l + k^{ls^l} \frac{k^\phi}{\mu^l} (p_i^l - f_i^l) = 0 \quad M_i^g + k^{gs^l} \frac{k^\phi}{\mu^g} (p_i^g - f_i^g) = 0 \quad (12a,b)$$

where k^{ls^l} and k^{gs^l} are the permeability of the liquid and the gas, μ^i represent phase viscosity and k^ϕ is the intrinsic permeability.

To simplify the representation we replace M_i^l and M_i^g by $\bar{M}_i^l k^{ls^l} k^\phi / \mu^l$ and $\bar{M}_i^g k^{gs^l} k^\phi / \mu^g$. Then, the following integral equations are derived for the liquid and gas

$$cp^l = \int_{\Gamma} p^* \bar{M}^l d\Gamma - \int_{\Gamma} M^* p^l d\Gamma - \int_{\Omega} p^* \bar{M}_{ii}^l d\Omega \quad (13a)$$

$$cp^g = \int_{\Gamma} p^* \bar{M}^g d\Gamma - \int_{\Gamma} M^* p^g d\Gamma - \int_{\Omega} p^* \bar{M}_{ii}^g d\Omega \quad (13b)$$

By differentiating eqs (13) the pressure gradient integral representations are obtained

$$cp_{,j}^l = - \int_{\Gamma} S_j^l p^l d\Gamma + \int_{\Gamma} D_j^l \bar{M}^l d\Gamma - \int_{\Omega} D_j^l \bar{M}_{ii}^l d\Omega \quad (14a)$$

$$cp_{,j}^g = - \int_{\Gamma} S_j^g p^g d\Gamma + \int_{\Gamma} D_j^g \bar{M}^g d\Gamma - \int_{\Omega} D_j^g \bar{M}_{ii}^g d\Omega \quad (14b)$$

Algebraic equations and system solution

As usual for non-linear boundary elements, to obtain the algebraic representations from the integral equations derived in the previous section, one has to approximate the boundary values along the boundary discretized into elements and the internal values over cells. We have used continuous and discontinuous linear boundary elements and internal cells. All domain values are approximated by using only internal nodes, therefore all cells adjacent to boundary are discontinuous. After this approximation one can derive the algebraic representation for the solid phase from eqs (9) and (10). Before assuming the space discretization the relevant integral equations must be expressed in rates and then transformed into their incremental forms. Then, after performing the time integrals over a typical time increment $\Delta t = t_{n+1} - t_n$ to have all values expressed in increments one can carried out all the boundary element and internal cell integrals to obtain the following algebraic equation written in terms of increments

$$[H]\{\Delta U\} = [G]\{\Delta T\} + [Q]\{\Delta \pi\} \quad (15a)$$

$$\{\Delta \sigma\} = -[H']\{\Delta U\} + [G']\{\Delta U\} + [Q']\{\Delta \pi\} \quad (15b)$$

where the matrices $[H]$, $[G]$, $[Q]$, $[H']$, $[G']$ and $[Q']$ are obtained from the evaluation of the integrals in Eqs. (9) and (10) over the discretized boundary and domain, while the vectors $\{\Delta U\}$, $\{\Delta T\}$, $\{\Delta \pi\}$ and $\{\Delta \sigma\}$ represent, respectively, incremental variables with displacements and tractions along the boundary and total pore pressures and total stresses in the domain.

Equations (15) can be solved in terms of $\{\Delta \sigma\}$ to give

$$\{\Delta \sigma\} = \{\Delta N^e\} + b[Q^e][D]\{\Delta \pi\} \quad (16)$$

where $\{\Delta N^e\}$ gives the elastic solution of the solid without the fluid effects and $b[Q^e][D][S^x]$ contains the averaged fluid pressure at the porous effects [10].

In order to introduce eq (16) into the final system of algebraic relations it has to be further modified to be written in terms of strain increments. For this purpose we have to take into account that the total stress increment is replaced by an elastic part $\Delta \sigma_{ij}^e = E_{ijkl} \Delta \epsilon_{kl}$ and the averaged fluid pressure at the porous effects $-b\{\Delta \pi\}$ is given by

$$-b\{\Delta \pi\} = [M^e]\{p_{(n+1)}^e\} + [M^{eg}]\{p_{(n+1)}^g\} + \{V^e\} \quad (17)$$

being $M^e = -bS_{(n+1)}^e$, $M^{eg} = -bS_{(n+1)}^{eg}$ and $V^e = -b\left(-\frac{2}{3}U_{(n+1)}^e - \pi_n\right)$

Similarly, one can obtain the algebraic forms of the integral eqs (13) for the boundary points

$$[H^f]\{p^e\} = [G^f]\{\bar{M}^e\} - [S^f]\{\bar{M}_{i,i}^e\} \quad (18a)$$

$$[H^f]\{p^g\} = [G^f]\{\bar{M}^g\} - [S^f]\{\bar{M}_{i,i}^g\} \quad (18b)$$

and for pressure algebraic representation at the internal points

$$\{p_{(i)}^e\} = -[H_i^e]\{p^e\} + [G_i^e]\{\bar{M}^e\} - [S_i^e]\{\bar{M}_{i,i}^e\} \quad (19a)$$

$$\{p_{(i)}^g\} = -[H_i^g]\{p^g\} + [G_i^g]\{\bar{M}^g\} - [S_i^g]\{\bar{M}_{i,i}^g\} \quad (19b)$$

where $\{p_{(i)}^e\}$ and $\{p_{(i)}^g\}$ are the liquid and gas porous pressure at internal points. The matrices are obtained by integrating boundary elements and internal cells.

Equations (19) are modified by replacing the boundary values obtained by solving eqs (18).

$$\{p_{(i)}^e\} = \{N^e\} - [\bar{S}^e]\{\bar{M}_{i,i}^e\} \quad \{p_{(i)}^g\} = \{N^g\} - [\bar{S}^g]\{\bar{M}_{i,i}^g\} \quad (20a,b)$$

$$\{p_{(i,j)}^e\} = \{N^{e,j}\} - [\bar{S}^{e,j}]\{\bar{M}_{i,i}^e\} \quad \{p_{(i,j)}^g\} = \{N^{g,j}\} - [\bar{S}^{g,j}]\{\bar{M}_{i,i}^g\} \quad (20c,d)$$

where the vector $\{N^x\}$ and the new matrices $[\bar{S}^x]$ are resulting from the algebraic described operations.

To build the global system of equations, eqs (20) have to be modified by replacing the flux divergents $\bar{M}_{i,i}^e$ and $\bar{M}_{i,i}^g$ in terms of the main problem increment values, strain, liquid and gas pressures, and liquid and gas pressure gradients. Moreover, the Biot's modulus is given in terms of the saturation.

$$\{\bar{M}_{i,i,(n+1)}^e\} = [M^{te}]\{\Delta \epsilon_{ij}\} + [M^{te}]\{p_{(n+1)}^e\} + [M^{te}]\{p_{(n+1)}^g\} + [M^{te,i}]\{p_{i,(n+1)}^e\} + \{V^e\} \quad (21a)$$

$$\{\bar{M}_{i,i,(n+1)}^g\} = [M^{tg}]\{\Delta \epsilon_{ij}\} + [M^{tg}]\{p_{(n+1)}^e\} + [M^{tg}]\{p_{(n+1)}^g\} + [M^{tg,i}]\{p_{i,(n+1)}^g\} + \{V^g\} \quad (21b)$$

Thus, from values \bar{M}_{ij}^l and \bar{M}_{ij}^g computed at $n+1$ one can obtain liquid and gas pressure pressures, strain and liquid and gas pressure gradients at $n+1$ by using eqs (21).

The global system can be build from the modified algebraic eqs (16) and (20) as follows

$$\begin{bmatrix} [E] & [[Q^e]+[i]][D][M^{e'}] & 0 & [[Q^e]+[i]][D][M^{e''}] & 0 \\ [\bar{S}^l][M^{e'}] & [i]+[\bar{S}^l][M^{e''}] & [\bar{S}^l][M^{e''}] & [\bar{S}^l][M^{e''}] & 0 \\ [\bar{S}^l][M^{e''}] & [\bar{S}^l][M^{e''}] & [i]+[\bar{S}^l][M^{e''}] & [\bar{S}^l][M^{e''}] & 0 \\ [\bar{S}^l][M^{e''}] & [\bar{S}^l][M^{e''}] & 0 & [i]+[\bar{S}^l][M^{e''}] & [\bar{S}^l][M^{e''}] \\ [\bar{S}^l][M^{e''}] & [\bar{S}^l][M^{e''}] & 0 & [\bar{S}^l][M^{e''}] & [i]+[\bar{S}^l][M^{e''}] \end{bmatrix} \begin{Bmatrix} \{\Delta e\} \\ \{P_{(n+1)}^l\} \\ \{P_{(n+1)}^g\} \\ \{P_{(n+1)}^s\} \\ \{P_{(n+1)}^e\} \end{Bmatrix} = \begin{Bmatrix} \{\Delta N^e\} - [[Q^e]+[i]][D]\{V^e\} \\ \{\bar{N}_{(n+1)}^l\} - [\bar{S}^l]\{V^l\} \\ \{\bar{N}_{(n+1)}^g\} - [\bar{S}^g]\{V^g\} \\ \{\bar{N}_{(n+1)}^s\} - [\bar{S}^s]\{V^s\} \\ \{\bar{N}_{(n+1)}^e\} - [\bar{S}^e]\{V^e\} \end{Bmatrix} \quad (22)$$

In eqn (22), the matrices $[M^{e'}$] and the vectors $\{V^s\}$ depend on the saturation level. The matrices $[Q^e]$ and the vectors $\{\bar{N}^s\}$ are dependent only on the domain geometry and initial material properties.

Numerical results

To illustrate the applicability of the proposed formulation, we analyse the example of a rectangular domain (see Figure 1) in which we have the fluid moving inside a solid skeleton, therefore modifying the saturation condition with time.

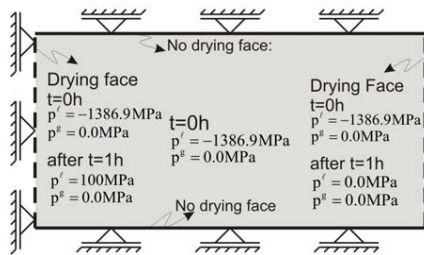


Figure 1. Analysed domain. Boundary and initial conditions.

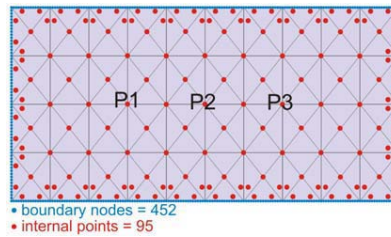


Figure 2. discretizations.

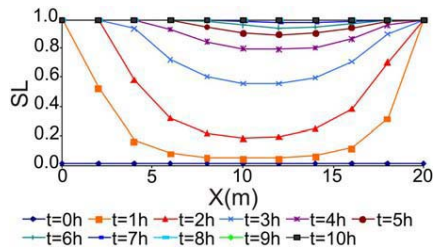


Figure 3. Saturation level (SL) evolution along the central horizontal axis x.

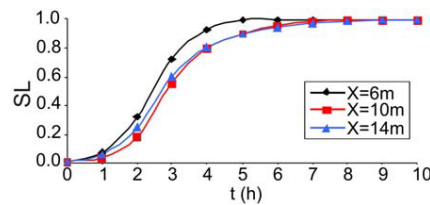


Figure 4. Saturation level (SL) evolution at $P_1(6m, 5m)$, $P_2(10m, 5m)$ e $P_3(14m, 5m)$.

The adopted data to run this example are given by: Young's modulus $E = 2000MPa$, Poisson's ration $\nu = 0$ and Biot's coefficient $b = 0.8$. The compressibility parameter of the skeleton is $K_0 = E_0/3(1 - 2\nu_0)$ which gives the compressibility of the porous material $K^s = K_0/(1 - b)$ and the Biot's modulus $M = K^s/(b - \phi_0)$, with ϕ_0 being the initial porosity. The viscosities for the liquid and air are $\mu^l = 1.003e^{-6} MPa.s$ and $\mu^g = 1.00e^{-1} MPa.s$, respectively. The compressibility for the

liquid and air are $K^l = 5.00e^{-4} MPa^{-1}$ and $K^g = 1.00e^{-1} MPa^{-1}$. The initial porosity is $\phi_0 = 0.15 \phi_0$, while the intrinsic permeability is constant and equal to $K^\phi = 1.00e^{-12} m/s$. At time $t = 0s$ the saturation level was 0.01 (1%) and the gas pressure was $p^g = 0MPa$. The boundary conditions are defined in Figure 1 and the adopted discretization in Figure 2. for the Van Genuchten model we have chosen residual liquid saturation $S^{lr} = 0$; $\alpha = 0.01327$; $m = 0.612553$ e $\chi = 1$.

Figures 3 and 4 show how the saturation evolves along the middle horizontal axis and at discrete points defined in the domain.

Conclusions

A domain boundary element formulation for saturated and non-saturated porous media is presented. The integral representations are all derived by using simple static fundamental solutions. Thus, non-linear effects are obtained by domain correcting terms. Domain integrals are also required to take into account the crossed terms. The formulation has been implemented and the numerical results obtained demonstrated that the formulations is appropriate to deal with this complex problem.

Acknowledgments

To FAPESP – São Paulo State Research Foundation for the support given to this work.

References

- [1] M.A. Biot *Journal of Applied Physics*, **12**, 155-164 (1941).
- [2] M.A. Biot *Journal of Applied Physics*, **26**, 182-185 (1955).
- [3] M.A. Biot *Journal of Applied Physics*, **27**, 459-467 (1956).
- [4] M.A. Biot and D.G. Willis *Journal of Applied Mechanics*, **24**, 594-601 (1957).
- [5] A.H.D. Cheng and J.A. Liggett *Int. J. Num. Meth. Eng.*, **20**, 255 - 278 (1984).
- [6] G.F. Dargush and P.K. Banerjee *Int J Num Meth Eng*, **28**, 2423-2449 (1989).
- [7] A.H.D. Cheng and E. Detournay *Int J Solid Struct*, **35**, 4521-4555 (1998).
- [8] M.C. Cavalcanti and J.C.F. Telles *Eng. An. Bound. El.*, **27**, 145-157 (2003).
- [9] D. Soares Jr., J.C.F. Telles and W.J. Mansur *Eng. An. Boud. El.*, 30(5) 363-370 (2006).
- [10] A. Benallal, A.S. Botta and W.S. Venturini *Comp. Meth. Appl. Mch. Eng.*, **197**, 4626-4644 (2008)
- [11] E.E. Alonso, and P. Delage *Proceeding of the International Congress on Unsaturated Soils (Unsat'95)*, Paris, Vol. 3, Balkema, Rotterdam (1995).
- [12] O. Coussy *Mécanique des Milieux Poreux*, Technip, Paris (1991).
- [13] O. Coussy and J.M. Fleureau *Mécanique des sols non saturés*, Hermes Science (2002).
- [14] O. Coussy *Mechanics of Porous Continua*, John Wiley & Sons (1995).
- [15] O. Coussy *Poromechanics*, John Wiley & Sons (2004).
- [16] O. Coussy, R. Eymard and T. Lassabatère *J. Engineering Mechanics*, **124**, 658-667 (1998).
- [17] L. Dormieux, J. Sanahuja and S. Maghous *C. R. Mecanique*, **334**, 19-24 (2006).

Implementation of a symmetric boundary integral formulation for cohesive cracks in homogeneous media and at interfaces

L. Távara¹, V. Mantič¹, A. Salvadori², L. J. Gray³, F. París¹

¹Escuela Técnica Superior de Ingenieros, Universidad de Sevilla
Camino de los Descubrimientos s/n, 41092 Sevilla, Spain
ltavara@esi.us.es, mantic@esi.us.es, paris@esi.us.es

²Department of Civil Engineering, University of Brescia
Via Branze 38, 25123 Brescia, Italy
alberto@ing.unibs.it

³Computer Science and Mathematics Division, Oak Ridge National Laboratory
Oak Ridge, TN 37831-6367, USA
graylj1@ornl.gov

Abstract. A symmetric boundary integral formulation for cohesive cracks growing in the interior of homogeneous linear elastic isotropic media and/or at interfaces between these media is developed and implemented in a numerical code. The solution of a problem that includes cohesive cracks depends on the cohesive law adopted. In the present work, models based on the concept of free energy density per unit undeformed area are considered. The corresponding constitutive cohesive equations present a softening branch which induces to the problem a potential instability. Thus, the development and implementation of a suitable solution algorithm capable of following the growth of the cohesive zone becomes an important issue. An arc-length control combined with a Newton-Raphson algorithm for iterative solution of nonlinear equations is used. The Boundary Element Method is very attractive for modeling cohesive crack problems as all nonlinearities are located on the boundaries (including the crack boundaries) of linear elastic domains. A Galerkin approximation scheme, applied to a suitable symmetric integral formulation, ensures an easy treatment of cracks in homogeneous media and excellent convergence behavior of the numerical solution. Numerical results for the wedge split test are presented and compared with experimental results available in the literature.

Keywords: Cohesive crack model, crack growth, Symmetric Galerkin Boundary Element Method, Arc-length method.

Introduction

Computational Fracture Mechanics has traditionally been based on Linear Elastic Fracture Mechanics (LEFM) concepts assuming the presence of a crack. This fact made difficult to study crack initiation. Recently, other models have been intensively developed, e.g. the Cohesive Zone Models (CZMs) [1, 2, 3], that assume hypotheses different from those adopted in LEFM, and avoid the presence of a stress singularity at the crack tip. These models are suitable to study both crack initiation and propagation, and also to estimate the maximum allowable load of a structure. In the present work, the Ortiz - Pandolfi [3] CZM is implemented in a 2D Symmetric Galerkin BEM (SGBEM) [4, 5, 6] code. The original version of this code [7] solved plane elastic problems including multi-material (homogenous isotropic linear-elastic) solids having traction-free cracks inside the homogenous components. The materials were considered to be perfectly bonded along their interfaces. The SGBEM and the implementation details of the algorithm employed herein are discussed in [4, 5, 6, 7]. Constitutive equations of a CZM include a representation of a softening branch, which induces to the problem with cohesive cracks a potential instability. Thus, the development and implementation of a suitable solution algorithm capable of following the evolution of the cohesive zone (modeling the crack growth) becomes an important issue. An arc-length control combined with a Newton-Raphson algorithm for iterative solution of nonlinear equations is used in the present work [8, 9].

Cohesive Zone Models

Cohesive zone models combine the Strength of Materials formulation for crack initiation, where the crack path is known a priori, with the Fracture Mechanics for crack propagation. In a cohesive zone formulation displacement discontinuities across the crack, δ_i , are related to the traction vector, t_i , in a zone located ahead of the actual crack tip [1, 2, 3]. A constitutive law is required for modeling the behavior of the material in the process zone. The constitutive law may be formally written as $\mathbf{t} = \mathbf{t}(\boldsymbol{\delta})$. This relation is in its essence a non linear and non-invertible relation. This law can also be called holonomic, as it may work only when loads are monotonically increasing and no secondary effects (friction, others) may cause local unloadings. In a such a case only incremental form must be written. A fundamental aspect in the formulation of the constitutive model is the requirement that the energy dissipated at a crack propagation must be equal to the fracture energy, i.e., the following relation must be satisfied:

$$\int_0^{\delta_i^f} t_i d\delta_i = G_c \quad (1)$$

where δ_i^f is the (final) value of the relative displacement leading to the vanishing of cohesive forces.

Ortiz-Pandolfi Model. The relation between tractions and relative displacements in the cohesive zone proposed in [2, 3], requires the concept of *effective opening displacement* δ : $\delta = \sqrt{\delta_1^2 + \beta\delta_2^2}$, i.e., different weights are assigned to the normal opening displacement (δ_1) and sliding (tangential) displacement (δ_2) through the parameter β .

Following [2, 3] the existence of a free energy density per unit undeformed area, ϕ , is postulated. In isothermal conditions, under the assumption of isotropic material, it is possible to show that the cohesive law takes the form: $\mathbf{t} = \text{grad}_\delta[\phi]$ if it is assumed that the free energy ϕ depends on δ only through the effective opening displacement. This implies that:

$$\mathbf{t} = \text{grad}_\delta[\phi] = \frac{\partial\phi}{\partial\delta} \frac{\delta_1 \mathbf{n}_1 + \beta^2 \delta_2 \mathbf{n}_2}{\delta} \quad (2)$$

where \mathbf{n}_i is the unit vector in the i -direction. If no unloading is considered, a simple expression for the potential ϕ is furnished by the Smith and Ferrante universal binding law [3]:

$$\phi(\delta) = e\sigma_c\delta_c \left[1 - \left(1 + \frac{\delta}{\delta_c} \right) e^{-\frac{\delta}{\delta_c}} \right], \quad \frac{\partial\phi}{\partial\delta}(\delta) = t = e\sigma_c \frac{\delta}{\delta_c} e^{-\frac{\delta}{\delta_c}} \quad (3)$$

where $e \approx 2.718$ is the base of the natural logarithm, σ_c is the maximum cohesive normal traction and δ_c is a characteristic opening displacement.

Cohesive Zone Models and SGBEM

Cohesive crack in homogeneous media. Consider a body of an arbitrary shape Ω which contains a crack. The boundary Γ of the body Ω is composed of the non-crack boundary Γ_b and the crack surface Γ_c . The crack surface Γ_c consists of two coincident surfaces Γ_c^+ and Γ_c^- which represent the upper and lower crack surfaces respectively. As explained in [7, 10, 11, 12] it suffices to discretize one crack surface (e.g. the upper one) as the crack surfaces are usually symmetrically loaded, i.e. $\mathbf{t} = \mathbf{t}_c^+ = -\mathbf{t}_c^-$. Thus the Somigliana displacement (u -BIE) and traction (t -BIE) identities written for a point P in a smooth part of the boundary take the following form:

$$\frac{1}{2}u_k(P) = \int_{\Gamma_b} [U_{kj}(P, Q)t_j(Q) - T_{kj}(P, Q)u_j(Q)] dQ - \int_{\Gamma_c^+} [T_{kj}(P, Q)w_j(Q)] dQ \quad \text{on } \Gamma_u \quad (4)$$

$$\frac{1}{2}t_k(P) = \int_{\Gamma_b} [T_{kj}^*(P, Q)t_j(Q) - S_{kj}(P, Q)u_j(Q)] dQ - \int_{\Gamma_c^+} [S_{kj}(P, Q)w_j(Q)] dQ \quad \text{on } \Gamma_t \quad (5)$$

$$t_k(P) = \int_{\Gamma_b} [T_{kj}^*(P, Q)t_j(Q) - S_{kj}(P, Q)u_j(Q)] dQ - \int_{\Gamma_c^+} [S_{kj}(P, Q)w_j(Q)] dQ \quad \text{on } \Gamma_c \quad (6)$$

where $\mathbf{w} = \mathbf{u}_c^+ - \mathbf{u}_c^-$. The non-crack boundary Γ_b is formed by Γ_u and Γ_t , where Γ_u is the portion of the boundary with prescribed displacements \mathbf{u}_u and Γ_t is the portion of the boundary with prescribed tractions \mathbf{t}_t . As tractions are prescribed on the crack surface, only t -BIE is written for source points on Γ_c^+ . Discretizing a weak form of Equations (4-6) by using a Galerkin scheme, the following system is obtained in block matrix form:

$$\begin{bmatrix} \frac{1}{2}\mathbf{M}_{uu} + \mathbf{T}_{uu} & \mathbf{T}_{ut} & \mathbf{T}_{uc} \\ \mathbf{S}_{tu} & \mathbf{S}_{tt} & \mathbf{S}_{tc} \\ \mathbf{S}_{cu} & \mathbf{S}_{ct} & \mathbf{S}_{cc} \end{bmatrix} \begin{Bmatrix} \mathbf{u}_u \\ \mathbf{u}_t \\ \mathbf{w}_c \end{Bmatrix} = \begin{bmatrix} \mathbf{U}_{uu} & \mathbf{U}_{ut} & 0 \\ \mathbf{T}_{tu}^* & -\frac{1}{2}\mathbf{M}_{tt} + \mathbf{T}_{tt}^* & 0 \\ \mathbf{T}_{cu}^* & \mathbf{T}_{ct}^* & -\mathbf{M}_{cc} \end{bmatrix} \begin{Bmatrix} \mathbf{t}_u \\ \mathbf{t}_t \\ \mathbf{t}_c^+ \end{Bmatrix} \quad (7)$$

where, the subscripts u , t , and c represent the terms corresponding to the non-crack boundary with prescribed displacements Γ_u , non-crack boundary with prescribed tractions Γ_t , and the crack surface Γ_c , respectively. Thus \mathbf{t}_u represents unknown tractions and \mathbf{u}_t represents unknown displacements on the boundary Γ_u and Γ_t respectively; \mathbf{M} is a 'mass matrix' obtained from the free term of the integral equations. Equation (7) is rearranged into a suitable rate form $[A]\{\dot{x}\} = \{\dot{b}\}$ by: *i*) differentiating with respect to time, *ii*) multiplying the t -BIEs by -1 (for symmetry), and *iii*) making use of the relation $\dot{t}_i = k_{ij}\dot{\delta}_j$ in the crack cohesive zone, which relates the traction ($\dot{\mathbf{t}}(\mathbf{x}) = \dot{\mathbf{t}}_c^+(\mathbf{x})$) rate along the crack cohesive surface with the crack opening displacement ($\dot{\mathbf{w}}(\mathbf{x}) = -\dot{\delta}(\mathbf{x})$) rate, at a point $\mathbf{x} \in \Gamma_c$, in a specific period of time. In this way we finally arrive at the system written in terms of rates of elastic variables:

$$\begin{bmatrix} -\mathbf{U}_{uu} & \mathbf{T}_{ut} & \mathbf{T}_{uc} \\ \mathbf{T}_{tu}^* & -\mathbf{S}_{tt} & -\mathbf{S}_{tc} \\ \mathbf{T}_{cu}^* & -\mathbf{S}_{ct} & -\mathbf{S}_{cc} + \mathbf{KM}_{cc} \end{bmatrix} \begin{Bmatrix} \dot{\mathbf{t}}_u \\ \dot{\mathbf{u}}_t \\ \dot{\mathbf{w}}_c \end{Bmatrix} = \begin{Bmatrix} -(\frac{1}{2}\mathbf{M}_{uu} + \mathbf{T}_{uu})\dot{\mathbf{u}}_u + \mathbf{U}_{ut}\dot{\mathbf{t}}_t \\ \mathbf{S}_{tu}\dot{\mathbf{u}}_u + (\frac{1}{2}\mathbf{M}_{tt} - \mathbf{T}_{tt}^*)\dot{\mathbf{t}}_t \\ \mathbf{S}_{cu}\dot{\mathbf{u}}_u - \mathbf{T}_{ct}^*\dot{\mathbf{t}}_t \end{Bmatrix} \quad (8)$$

The final coefficient matrix of this system is symmetric due to the reciprocity relations of the integral kernel tensors as shown in [4, 5, 12]. In [12] a similar matrix is obtained for the case of traction free cracks. The only difference is the lower right-hand diagonal block of the linear system matrix $-\mathbf{S}_{cc} + \mathbf{KM}_{cc}$, where \mathbf{K} is the tangent elastic stiffness matrix obtained from the cohesive law. It can be shown that the product \mathbf{KM}_{cc} keeps the desired symmetry, if \mathbf{K} is symmetric.

Interface cohesive crack. The formulation for the problem of several domains connected by cohesive interfaces was presented in [13, 14]. A short review of this formulation is presented in this section. For the sake of simplicity, let us consider two domains Ω^A and Ω^B with a single common interface Γ_w . The geometrical description of the interface is similar to the geometrical description of the crack. Then we can define $\dot{\mathbf{w}}(\mathbf{x}) = \dot{\mathbf{u}}_w^A(\mathbf{x}) - \dot{\mathbf{u}}_w^B(\mathbf{x})$ and $\dot{\mathbf{t}}(\mathbf{x}) = \dot{\mathbf{t}}_w^A(\mathbf{x})$ at a point $\mathbf{x} \in \Gamma_w$. Cohesive tractions \mathbf{t} and relative opening displacements \mathbf{w} are related by a non-linear vector function $\mathbf{t}(\mathbf{w}(\mathbf{x}))$, $\forall \mathbf{x} \in \Gamma_w$. Let us define vectors \mathbf{v} and \mathbf{z} as follows:

$$\dot{\mathbf{v}} = \frac{1}{2}(\dot{\mathbf{u}}_w^A + \dot{\mathbf{u}}_w^B) \quad , \quad \dot{\mathbf{z}} = \frac{1}{2}(\dot{\mathbf{u}}_w^A - \dot{\mathbf{u}}_w^B) = \frac{1}{2}\dot{\mathbf{w}} \quad (9)$$

Then using (4) and (5) for each domain, including three combinations of them for the interface (u -BIE^A - u -BIE^B, t -BIE^A - t -BIE^B, t -BIE^A + t -BIE^B), a suitable arrangement of the system of equations and after setting $\dot{\mathbf{t}} = -\mathbf{K}\dot{\mathbf{z}}$, the system can be written in block matrix form $[A]\{\dot{x}\} = \{\dot{b}\}$ where:

$$[A] = \begin{bmatrix} -\mathbf{U}_{uu}^A & \mathbf{T}_{ut}^A & 0 & 0 & \mathbf{U}_{uw}^A\mathbf{K} + \mathbf{T}_{uw}^A & \mathbf{T}_{uw}^A \\ \mathbf{T}_{tu}^{A*} & -\mathbf{S}_{tt}^A & 0 & 0 & -(\mathbf{T}_{tw}^{A*}\mathbf{K} + \mathbf{S}_{tw}^A) & -\mathbf{S}_{tw}^A \\ 0 & 0 & -\mathbf{U}_{uu}^B & \mathbf{T}_{ut}^B & -(\mathbf{U}_{uw}^B\mathbf{K} + \mathbf{T}_{uw}^B) & \mathbf{T}_{uw}^B \\ 0 & 0 & \mathbf{T}_{tu}^{B*} & -\mathbf{S}_{tt}^B & \mathbf{T}_{tw}^{B*}\mathbf{K} + \mathbf{S}_{tw}^B & -\mathbf{S}_{tw}^B \\ \mathbf{K}^T\mathbf{U}_{wu}^A & -\mathbf{K}^T\mathbf{T}_{wt}^A & -\mathbf{K}^T\mathbf{U}_{wu}^B & \mathbf{K}^T\mathbf{T}_{wt}^B & -\mathbf{K}^T(\mathbf{U}_{ww}^A + \mathbf{U}_{ww}^B)\mathbf{K} & -\mathbf{K}^T(\mathbf{T}_{ww}^A - \mathbf{T}_{ww}^B) \\ +\mathbf{T}_{wu}^{A*} & -\mathbf{S}_{wt}^A & -\mathbf{T}_{wu}^{B*} & +\mathbf{S}_{wt}^B & -\mathbf{K}^T(\mathbf{T}_{ww}^A + \mathbf{T}_{ww}^B) & -(\mathbf{S}_{ww}^A - \mathbf{S}_{ww}^B) \\ & & & & -(\mathbf{T}_{ww}^{A*} + \mathbf{T}_{ww}^{B*})\mathbf{K} & \\ & & & & -(\mathbf{S}_{ww}^A + \mathbf{S}_{ww}^B) & \\ \mathbf{T}_{wu}^{A*} & -\mathbf{S}_{wt}^A & \mathbf{T}_{wu}^{B*} & -\mathbf{S}_{wt}^B & -(\mathbf{T}_{ww}^{A*} - \mathbf{T}_{ww}^{B*})\mathbf{K} & -(\mathbf{S}_{ww}^A + \mathbf{S}_{ww}^B) \\ & & & & -(\mathbf{S}_{ww}^A - \mathbf{S}_{ww}^B) & \end{bmatrix} \quad (10)$$

$$\{\dot{x}\} = \{\dot{t}_u^A, \dot{t}_t^A, \dot{t}_u^B, \dot{t}_t^B, \dot{v}, \dot{z}\}^T \quad (11)$$

$$\{\dot{b}\} = \left\{ \begin{array}{l} (\frac{1}{2}M_{uu} + T_{uu})\dot{u}_u^A - U_{ut}\dot{t}_t^A \\ -S_{tu}\dot{u}_u^A + (\frac{1}{2}M_{tt} - T_{tt}^*)\dot{t}_t^A \\ (\frac{1}{2}M_{uu} + T_{uu})\dot{u}_u^B - U_{ut}\dot{t}_t^B \\ -S_{tu}\dot{u}_u^B + (\frac{1}{2}M_{tt} - T_{tt}^*)\dot{t}_t^B \\ \mathbf{K}^T(-T_{wu}\dot{u}_u^A + U_{wt}\dot{t}_t^A + T_{wu}\dot{u}_u^B - U_{wt}\dot{t}_t^B) - S_{wu}\dot{u}_u^A - T_{wt}^*\dot{t}_t^A + S_{wu}\dot{u}_u^B + T_{wt}^*\dot{t}_t^B \\ -(S_{wu}\dot{u}_u^A + T_{wt}^*\dot{t}_t^A + S_{wu}\dot{u}_u^B + T_{wt}^*\dot{t}_t^B) \end{array} \right\} \quad (12)$$

Non linear solution algorithm

The arc-length method is a powerful solution algorithm, allowing the evolution of the equilibrium states of a problem to be solved at various load levels [8]. All these equilibrium states trace the load-displacement response of the structure in which the applied load varies proportionally as a function of a unique load parameter called herein λ . In such a case, for a system with n degrees-of-freedom (DOF), the $n + 1$ unknowns $u = (x, \lambda)$ completely define the problem.

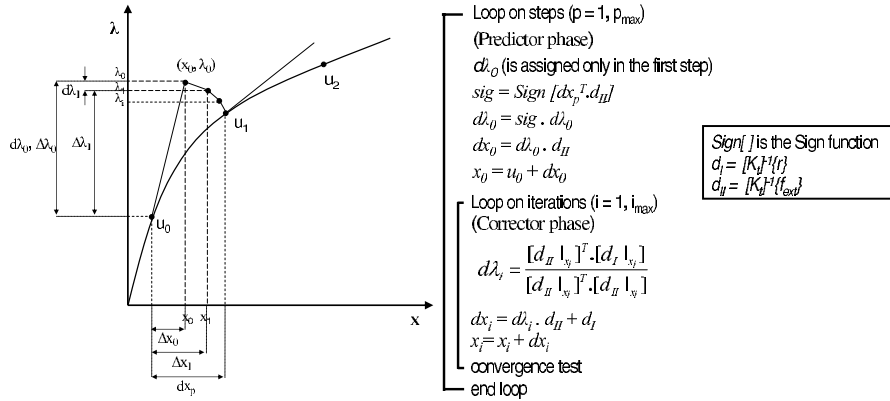


Figure 1: Graphic of the arc-length method and flow chart of the normal flow procedure, where K_t is the tangential stiffness matrix of the considered structure, $\{r\}$ is the residual vector and $\{f_{ext}\}$ is the external load and constraints vector.

In Figure 1 the variables used in the arc-length method are shown, where the vector u_p ($p =$ step number), in the case of SGBEM, is formed by the unknown displacements and tractions in a converged equilibrium point, while x_i ($i =$ iteration number) is the vector of unknowns in the Newton-Raphson iterations between two converged equilibrium points, before equilibrium is reached. (x_0, λ_0) corresponds to a predictor estimation. Several variants of the arc-length method have been proposed in literature in its discrete formulation, the one used in the present work is the normal-flow algorithm [9], where successive Newton-Raphson iterations converge to the equilibrium solution along a path which is normal (in an asymptotic sense) to the so-called Davidenko flow [9]. A very important issue of the procedure is to define a suitable scaling of the known and unknown variables involved in the solution of a nonlinear system of equations. The variables in the final system should have similar orders of magnitude, so as to aid the performance of the non-linear numerical solver.

Numerical Results

In order to verify the capability of the numerical model to reproduce experimental results, the wedge split test for a concrete mix, studied in [15], was modeled by the SGBEM code with the homogeneous cohesive crack approach. The material characteristics are Young's modulus $E = 25.2\text{GPa}$, Poisson's ratio $\nu = 0.22$, specific fracture energy $G_{Ic} = 101\text{J/m}^2$, and the parameter values for the Ortiz model

are maximum cohesive stress $\sigma_c = 2.3\text{MPa}$ and critical opening displacement $\delta_c = 1.61547 \times 10^{-5}\text{m}$. It is important to mention that in this case the parameter β is not used, due to the Mode I character of the problem.

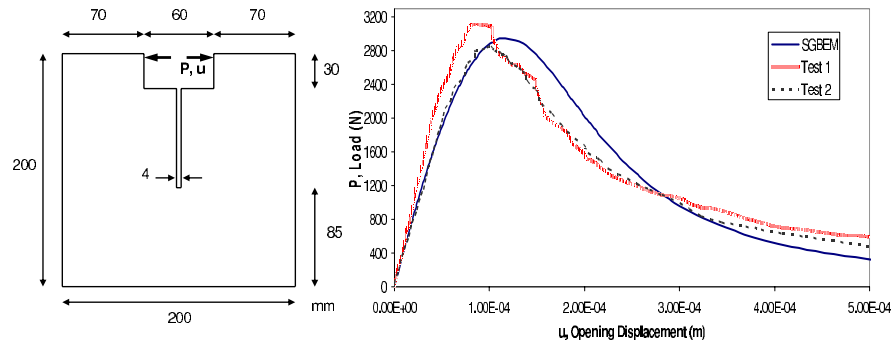


Figure 2: Specimen configuration of the wedge split test, and load-displacement curve prediction and experimental results [15].

The specimen dimensions and the numerical results obtained with the SGBEM code are represented by the load - displacement global response curve shown in Figure (2). The solution algorithm was implemented using the full Newton-Raphson method. The prediction phase includes the determination of the arc-length step size at each increment. The first step includes the selection of an appropriate value for the arc length $d\lambda_0$. The arc-length is adjusted from one step to the next using the following simple formula: $d\lambda_{p+1} = d\lambda_p(n/m)$, where m is the number of iterations that were required at the previous step and n is the (user specified) desired number of iterations at each step. This procedure allows larger steps to be taken when the solution is converging easily, and forces the solver to take smaller steps when convergence is more difficult. For the present work, n was selected between 3 and 4 so as to achieve the most favorable results in terms of computational time.

Conclusions

In the present work a symmetric boundary integral formulation for problems with cohesive cracks placed inside of homogeneous domains and between subdomains has been proposed and implemented. This new 2D SGBEM code is based upon previous results from [7, 13, 14]. This approach is likely to be suitable for engineering applications involving isotropic materials, e.g. for an analysis of crack initiation and growth in composites modeled as piecewise homogeneous materials at the micro-scale. The introduction of the cohesive zone requires an iterative solution procedure to solve the nonlinear equations resulting from the boundary integral formulation; the arc-length method with the normal flow procedure has been implemented. As shown by the numerical results, the cohesive zone formulation correctly modeled the experimentally observed crack growth behavior for the wedge split test. To adjust the parameters of the discrete model (σ_c and δ_c in the case of the Ortiz-Pandolfi model for Mode I), is the first step to predict the real behavior of structures. The present work is a starting point to study the possibilities of different cohesive models presented in literature, as well as different arc-length solver schemes applied in a SGBEM setting for the above mentioned application in composite materials.

Acknowledgments

The work was supported by the Junta de Andalucía (Projects of Excellence TEP-1207, TEP 02045 and P08-TEP 04051), the Spanish Ministry of Education and Science through Projects TRA2005-06764 and TRA2006-08077, and the Applied Mathematical Sciences Research Program of the Office of Mathematical, Information, and Computational Sciences, U.S. Department of Energy under contract

DE-AC05-00OR22725 with UT-Battelle, LLC. Part of the present work was performed at the Oak Ridge National Laboratory during the research stay of L.T., V.M. and A.S. which are grateful to Dr. L.J. Gray for the opportunity of visiting and working with him. The authors thank Dr. A.-V. Phan (University of South Alabama) for the original SGBEM code employed in this work.

References

- [1] Chandra N. and Shet C., A Micromechanistic Perspective of Cohesive Zone Approach in Modeling Fracture. *Computer Modeling in Engineering & Sciences*, **5:1**, 21–34 (2004).
- [2] Camacho G.T. and Ortiz M., Computational modelling of impact damage in brittle materials. *International Journal Solid & Structures*, **33**, 2899–2938, (1996).
- [3] Ortiz M. and Pandolfi A., Finite-Deformation irreversible cohesive elements for three dimensional crack propagation analysis. *International Journal for Numerical Methods in Engineering*, **44**, 1267–1283, (1999).
- [4] Bonnet M., G. Maier, and C. Polizzotto, Symmetric Galerkin boundary element method. *ASME Appl. Mech. Rev.*, **51:11**, 669–704 (1998).
- [5] Sutradhar A., Paulino G., Gray L., Symmetric Galerkin Boundary Element Method, *Springer*, (2008).
- [6] Gray L. J., Evaluation of singular and hypersingular Galerkin boundary integrals: direct limits and symbolic computation. In V. Sladek and J. Sladek, editors, *Singular Integrals in the Boundary Element Method, Advances in Boundary Elements, Computational Mechanics Publishers*, Chapter 2, pages 33-84. (1998).
- [7] Phan A. V., Napier J. A. L., Gray L. J., and Kaplan T. Symmetric-Galerkin BEM simulation of fracture with frictional contact. *International Journal for Numerical Methods in Engineering*, **57:6**, 835–851 (2003).
- [8] Fafard M. and Massicotte B., Geometrical Interpretation of the arc-length method. *Computers & Structures*, **46**, 603–615 (1993).
- [9] Ragon S.A., Grdal Z. and Watson L.T., A comparison of three algorithms for tracing nonlinear equilibrium paths of structural systems. *International Journal Solid & Structures*, **39**, 689–698 (2002).
- [10] Maier G., Novati G. and Cen Z., Symmetric boundary element method for quasi-brittle fracture and frictional problems. *Computational Mechanics*, **13**, 74–89 (1993).
- [11] Aliabadi M. H., The Boundary Element Method, *Wiley*, Vol 2 - Applications in Solids and Structures, (2002).
- [12] Gray L. J. and Paulino G. H., Symmetric Galerkin boundary integral fracture analysis for plane orthotropic elasticity. *Computational Mechanics*, **20**, 26–33 (1997).
- [13] Salvadori, A., A symmetric boundary integral formulation for cohesive interface problems. *Computational Mechanics*, **22**, 381–391 (2003).
- [14] Salvadori, A., Numerical simulations of cohesive interface problems via boundary integral equations. *Proceedings of IABEM 2006, Graz - Austria* (2006).
- [15] Denarié E. Saouma V.E. Iocco A. Varelas D., Concrete fracture process zone characterization with fiber optics. *Journal of Engineering Mechanics*, **127:5**, 494–502 (2001).

A fast multipole boundary element method for two-dimensional acoustic wave problems

V. Mallardo¹ and M. H. Aliabadi

Department of Aeronautics, Imperial College London, UK, mlv@unife.it, m.h.aliabadi@imperial.ac.uk

Keywords: Fast multipole method, Boundary Element Method, Helmholtz equation.

Abstract. The present paper intends to couple the Fast Multipole Method (FMM) with the Boundary Element Method (BEM) in 2D acoustic problems. The procedure is aimed at simplifying the integrals involved in the governing Boundary Integral Equations (BIEs) on the basis of the distance between source point and integration element. The multipole expansion and some suitable moment translations make the procedure much faster if compared to the conventional approach. An iterative solver is adopted to improve the overall computational efficiency. A simple numerical example is shown to demonstrate the reliability of the method.

Introduction

The BEM has been used to solve interior/exterior acoustic problems for many years because of its boundary only discretisation and automatic satisfaction of the radiation condition at infinity. The main drawback is related to the final system of equations which results to have dense, non-symmetrical and sometimes ill-conditioned coefficient matrices. Solving the system of equations becomes prohibitively expensive when applied at large-scale engineering problems. In fact, the computation of the coefficients of the matrices governing the discrete problem require $O(N^2)$ operations and another $O(N^3)$ operations are necessary to solve the system using any direct solver (let N be the number of equations).

In 1983 Rokhlin [1] proposed an algorithm for rapid solution of classical boundary value problems for the Laplace equation based on iteratively solving integral equations of potential theory. The CPU time requirement obtained was proportional to N . The starting point was the harmonic expansion of the kernel. The algorithm appeared to be the most efficient of the at that time available tools for the solution of large scale boundary value problems whenever the solution needed to be evaluated at a limited number of points. The procedure was then extended, a few years later, to two dimensional acoustic scattering in [2] where the author described a similar procedure capable to reduce the CPU time requirements of the algorithm to $N^{4/3}$. In both papers no connection with the BEM was introduced.

It took almost ten years for scientific community to realise the potential capability of coupling the FMM with the BEM. A comprehensive review of the fundamentals of FMM and FMM accelerated Boundary Integral Equation Method (BIEM) with reference to the Laplace and Helmholtz equations is surveyed in [3]. With conventional BIEM it is not possible to solve beyond several thousands of unknowns with a desktop computer. Actually, methods of solution of problems of the size of more than 10^8 unknowns (which roughly correspond to 10^6 unknowns in the BEM context) are investigated in FEM with massively parallel computers. With fast multipole accelerated BIEM, problems of the size of 10^6 unknowns can be handled even in desktop computers. However, the use of the FMM has increased the complexity in implementations of the BEM: the structure of the code changes completely and the pre-processor stage becomes more important than in the conventional approach. An interesting introduction to the Fast Multipole Boundary Element Method (FMBEM) for potential problems is presented in [4]: the structure of a FMBEM program along with the details of the method with reference to the Laplace equation are presented.

An adaptive FMBEM for 3D acoustic wave problems is investigated in [5] where the Burton-Miller formulation is applied to overcome the non-uniqueness difficulties. The adaptive approach is

¹on leave from the Department of Architecture, University of Ferrara, via Quartieri 8, 44100 Ferrara, Italy

demonstrated to be several times faster than the non-adaptive FMBEM while maintaining the accuracy of the BEM.

To the authors' knowledge [6] represents the unique application of the FMBEM to 2D acoustic problems. The FMM is used to accelerate the construction of the influence matrix in the BEM. The approach is of non-adaptive type and the number of floating-point operations is reduced from $O(N^2)$ to $O(N \log^a N)$ where a is a small constant independent on N .

This paper intends to present a FMBEM for two-dimensional acoustics aimed at noise control. The iterative solver generalised minimal residual (GMRES) is adopted to improve the overall computational efficiency. A numerical example is shown to demonstrate the accuracy and potentials for solving large-scale problems. After this Introduction, the integral equations which govern the 2D acoustic problem are presented along with the main relations of the FMM. Afterward, the algorithm and the integration schemes are detailed. Finally, a numerical example is investigated in order to measure the reliability of the procedure when compared to an analytical solution.

The FMBEM relations

The propagation of time-harmonic acoustic waves in a homogeneous isotropic acoustic medium (either finite or infinite) is described by the Helmholtz equation:

$$\nabla^2 p(\mathbf{x}) + k^2 p(\mathbf{x}) = 0 \quad (1)$$

under the boundary conditions:

$$p(\mathbf{x}) = \bar{p}(\mathbf{x}) \quad \mathbf{x} \in \Gamma_1 \quad (2a)$$

$$q(\mathbf{x}) = p(\mathbf{x})_{,n} = \bar{q}(\mathbf{x}) \quad \mathbf{x} \in \Gamma_2 \quad (2b)$$

where p is the acoustic pressure, $k = \omega/c$ with ω =angular frequency and c =sound velocity, comma indicates partial derivative, $\Gamma_1 \cup \Gamma_2 = \Gamma$, Γ is the boundary of the domain Ω under analysis, $n = n(\mathbf{x})$ is the outward normal to the boundary in \mathbf{x} , q is the flux and the barred quantities indicate given values.

The boundary value problem described by the above equations can be transformed into the following integral representation [7-8]:

$$c(\boldsymbol{\xi})p(\boldsymbol{\xi}) + \int_{\Gamma} q^*(\boldsymbol{\xi}, \mathbf{x})p(\mathbf{x})d\Gamma(\mathbf{x}) - \int_{\Gamma} p^*(\boldsymbol{\xi}, \mathbf{x})q(\mathbf{x})d\Gamma(\mathbf{x}) = 0 \quad (3)$$

where $c(\boldsymbol{\xi})$ occurs in the limiting process from the internal point to the boundary point, being equal to 0.5 if the tangent line to the boundary at $\boldsymbol{\xi}$ is continuous. The fundamental solutions p^* and q^* are given by:

$$p^*(\boldsymbol{\xi}, \mathbf{x}) = \frac{i}{4} H_0^{(1)}(kr) \quad (4a)$$

$$q^*(\boldsymbol{\xi}, \mathbf{x}) = -\frac{ik}{4} H_1^{(1)}(kr)r_{,n} \quad (4b)$$

where $H_0^{(1)}$ and $H_1^{(1)}$ are the Hankel function of the first kind, 0th and 1st order respectively, $r = \|\mathbf{x} - \boldsymbol{\xi}\|$ is the distance between the collocation point $\boldsymbol{\xi}$ and the field point \mathbf{x} .

The conventional BEM numerical procedure is based on two steps: first, the discretisation of the boundary Γ , second, the collocation of the eq (3) in each node in order to build a final (square) system of equations in the unknowns either p or q on the boundary. In the present contribution constant elements are adopted: with such a choice all the integrals involved are performed analytically. The discretised equation collocated at node $\boldsymbol{\xi}_i$ can be written as:

$$c(\boldsymbol{\xi}_i)p(\boldsymbol{\xi}_i) + \sum_{j=1}^n p_j \int_{\Gamma_j} q^*(\boldsymbol{\xi}_i, \mathbf{x})d\Gamma(\mathbf{x}) = \sum_{j=1}^n q_j \int_{\Gamma_j} p^*(\boldsymbol{\xi}_i, \mathbf{x})d\Gamma(\mathbf{x}) \quad (5)$$

The procedure requires the evaluation of either the integral of p^* or the integral of q^* on each boundary element.

For convenience, the complex notation is introduced, i.e. the collocation and field points are replaced by their complex representation:

$$\boldsymbol{\xi} = z_0 = \xi_1 + i \xi_2 \quad (6a)$$

$$\mathbf{x} = z = x_1 + i x_2 \quad (6b)$$

with $i = \sqrt{-1}$. With such an assumption it is simple to show that the fundamental solutions in $\boldsymbol{\xi}, \mathbf{x}$ coincide with their expression in complex notation:

$$p^*(\boldsymbol{\xi}, \mathbf{x}) = p^*(z_0, z) \quad (7a)$$

$$q^*(\boldsymbol{\xi}, \mathbf{x}) = q^*(z_0, z) \quad (7b)$$

The FMM relations intervene in the evaluation of integrals involved in the eq (5). The multipole expansion is the key point in reducing the CPU time which is necessary to evaluate each integral. If $F(z_0, z)f$ indicates either $p^*(z_0, z)q$ or $q^*(z_0, z)p$, the following *local expansion* can be obtained:

$$\int_{\Gamma_j} F(z_0, z) f d\Gamma(z) = \frac{i}{4} \sum_{p=-\infty}^{\infty} (-1)^p L_{-p}(z_L) I_p(z_0 - z_L) \quad (8)$$

where:

$$I_p(z) = (-i)^p J_p(kr) e^{ip\theta} \quad (9)$$

r, θ are the polar coordinates of z and J_p stands for the Bessel function of the p^{th} order.

The coefficients L_{-p} are given by the following *M2L translation*:

$$L_l(z_L) = \sum_{k=-\infty}^{\infty} O_{k+l}(z_L - z_C) P_{-k}(z_C) \quad (10)$$

where $\|z_0 - z_L\| \ll \|z_C - z_L\|$ must be satisfied and:

$$O_m(z) = i^m H_m^{(1)}(kr) e^{im\theta} \quad (11)$$

The term $P_k(z_C)$ is called *moment about z_C* , it is independent from the collocation point z_0 and it only needs to be computed once. The expression of M_k and N_k is given as follows:

$$M_k(z_C) = q \int_{\Gamma_j} I_k(z - z_C) d\Gamma(z) \quad (12a)$$

$$N_k(z_C) = n p \int_{\Gamma_j} \frac{\partial I_k(z - z_C)}{\partial z} d\Gamma(z) \quad (12b)$$

The point z_C is assumed to be located close to Γ_j so that $\max_{z \in \Gamma_j} \|z - z_C\| \ll \|z_0 - z_C\|$ holds. The series expansion eq (10) involving P_k can be truncated to $nexp$ terms with a good approximation if $nexp$ is set larger than kr_{max} (see [2] for details).

If the point z_C is moved to a new location $z_{C'}$, the following *M2M translation* is obtained:

$$P_p(z_{C'}) = \sum_{m=-\infty}^{\infty} I_{p-m}(z_C - z_{C'}) P_m(z_C) \quad (13)$$

Analogously, if the point for local expansion is moved from z_L to $z_{L'}$, the following *L2L expansion* is obtained:

$$L_l(z_L) = \sum_{k=-\infty}^{\infty} I_{l-k}(z_{L'} - z_L) L_k(z_{L'}) \quad (14)$$

The algorithm

The adaptive procedure starts from a square containing the entire boundary and then repeatedly divides it and the successive sub-cells into four sub-squares until a fixed maximum number of boundary elements is contained in each cell. In Fig. 1 the subdivision process up to the last level is depicted with the allowed maximum number of elements set to one. The last cells of the division process (in the figure the cells containing one element) are also called *leaves*.

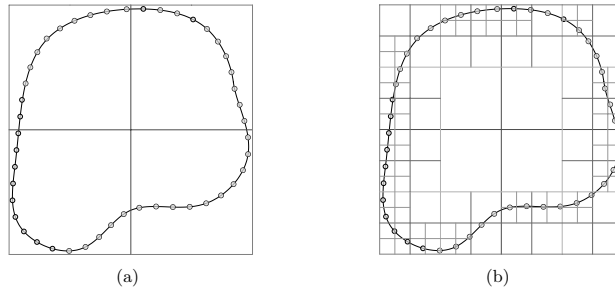


Figure 1: Square division up to level 1 (a) and up to level 4 (b)

For a given collocation node z_0 , the integral over the entire boundary is determined in different way on the basis of the distance $\|z - z_0\|$. If the integration element is *close* (where *close* means in one of the cells surrounding it, see Fig. 2a) to the collocation node, the integral contribution is determined directly as in the conventional BEM. In the present contribution such integrals are evaluated analytically and presented in the successive section. On the other hand, if the position of the integration element with respect to the collocation node is as depicted in Fig. 2b, i.e. the integration element belongs to the collocation node's parents, the eq (8) is applied via the *M2L translation*. Finally, the contribution from far cells (depicted in Fig. 2c) is obtained by the local expansion via the *L2L translation*.

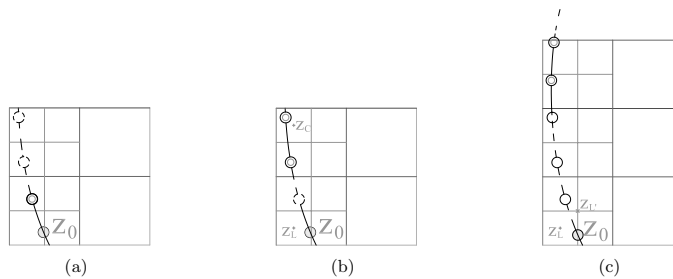


Figure 2: Direct (a), M2L (b) and L2L (c) integrations

The elements of the matrix A of the final system of equations $A\mathbf{x} = \mathbf{b}$ are not stored. The product $A\mathbf{x}_i$ is evaluated iteratively until the solution converges within a given tolerance. The Generalized Minimum Residual (GMRES) method is adopted. It was first proposed by [9] in order to solve large, sparse and nonsymmetric linear systems. The routine implemented in the paper allows the use of different preconditioning to accelerate the solution process.

The analytical integration

The FMBEM procedure requires the evaluation of some integrals. Some of them are involved in the direct integration whereas two integrals are necessary to evaluate the moments eq (12). The term H_{ii} involving the fundamental solution q^* when the source node belongs to the integration element is zero as constant elements are adopted (i.e. $r_n = 0$).

The diagonal term G_{ii} can be determined analytically by using the procedure presented in [10]:

$$\int_{\Gamma_{AB}} p^*(\boldsymbol{\xi}, \mathbf{x}) d\Gamma(\mathbf{x}) = \frac{i}{4} l_{AB} \left[H_0^{(1)}\left(k \frac{l_{AB}}{2}\right) + \frac{\pi}{2} \left(\hat{H}_0\left(k \frac{l_{AB}}{2}\right) H_1^{(1)}\left(k \frac{l_{AB}}{2}\right) - \hat{H}_1\left(k \frac{l_{AB}}{2}\right) H_0^{(1)}\left(k \frac{l_{AB}}{2}\right) \right) \right] \quad (15)$$

where $H_\nu(z)$ denotes the Struve function of order ν . A similar expression can be obtained when the source point does not belong to the integration element but it lies on the line AB .

The off-diagonal terms can be analytically evaluated only in the case $kr \leq 2$. The case $kr > 2$ can only be solved numerically. As a matter of fact, in the FMBEM context, a boundary discretisation which satisfies 6 – 8 elements for wavelength would never require such a numerical integration. The expression of G_{ij} and H_{ij} for $kr \leq 2$ are given by:

$$\int_{\Gamma_j} p^*(\boldsymbol{\xi}, \mathbf{x}) d\Gamma(\mathbf{x}) = -\frac{1}{2\pi} \sum_{i=1}^7 \left[\frac{A_i}{2} \bar{P}_{1,i} - B_i P_{2,i} \right] \begin{matrix} \boldsymbol{\xi}_B \\ \boldsymbol{\xi}_A \end{matrix} \quad (16a)$$

$$\int_{\Gamma_j} q^*(\boldsymbol{\xi}, \mathbf{x}) d\Gamma(\mathbf{x}) = \frac{ik}{2\pi} \left[\eta \sum_{i=1}^7 \left(\frac{D_i}{2} P_{1,i} + E_i P_{2,i-1} \right) \right] \begin{matrix} \boldsymbol{\xi}_B \\ \boldsymbol{\xi}_A \end{matrix} \quad (16b)$$

where the terms involved in the above expressions are reported in [11].

The integral expressing the *moment* is also evaluated analytically. No contributions are available in the scientific literature. The M_k term is analytically determined by a new procedure developed by the authors which starts from the Graf addition theorem (see for instance [12]):

$$H_\nu^{(1)}(\omega) = \sum_{m=-\infty}^{\infty} H_m^{(1)}(Z) J_m(z) e^{im\phi} \quad (17)$$

where ω , z and Z form a triangle in which ϕ is the angle between z and Z and ω is the angle between ω and Z . By the application of the above theorem it is possible to transform the integral involved in M_k into the sum of integrals involving the Bessel functions $J_m(t)$ only. Such integrals can be evaluated analytically by well-known expressions. N_k can be determined in a similar way as it is possible to show that:

$$\frac{\partial I_k(z - z_C)}{\partial z} = -ik I_{k-1}(z - z_C) \quad (18)$$

Numerical results

In order to demonstrate the accuracy of the proposed procedure, a numerical example, for which the analytical solution is available, is presented. The results refer to the wave propagation inside a cylinder of radius $R = 1$ for different values of the wave number. The analytical solution is available both for pressure and for flux given on the boundary. The number of boundary elements is always fixed in order to have 6 – 10 elements per wavelength. Table 1 presents the comparison between analytical and numerical values on the boundary.

Conclusions

In this paper an adaptive fast multipole boundary element method for solving 2D acoustic wave problems is presented. The procedure results to be useful to investigate the passive noise control of walls of any shape and for any value of the wave number. Numerical analyses are still in progress to compare the CPU time of the present method with both the BEM conventional approach and other numerical techniques.

		0.5	1.0	2.0	5.0
$\bar{\Gamma}$	Analytic	0.129	0.575	5.15	9.22
	FMBEM	0.133	0.558	5.36	8.76
$\bar{\Gamma}$	Analytic	7.75	1.74	0.194	0.108
	FMBEM	7.44	1.68	0.186	0.103

Table 1: Comparison between analytical and FMBEM solution on the boundary.

Acknowledgement

This work has been funded by the FP6 project SEAT AST5-CT-2006-030958. Financial support of the Italian MIUR-PRIN 2007 (Metodi agli elementi al contorno per problemi dipendenti dal tempo) is also gratefully acknowledged.

References

- [1] V. Rokhlin. Rapid solution of integral equations of classical potential theory, *J. Comput. Phys.*, 60:187–207, 1983
- [2] V. Rokhlin. Rapid solution of integral equations of scattering theory in two dimensions, *J. Comput. Phys.*, 86:414–439, 1990
- [3] N. Nishimura. Fast multipole accelerated boundary integral equation methods. *Appl. Mech. Rev.*, 55(4):299–324, 2000.
- [4] Y. J. Liu, N. Nishimura. The fast multipole boundary element method for potential problems: A tutorial. *Eng. An. Bound. Elem.*, 30:371–381, 2006.
- [5] L. Shen, Y. J. Liu. An adaptive fast multipole boundary element method for three-dimensional acoustic wave problems based on the Burton-Miller formulation. *Comput. Mech.*, 40:461–472, 2007.
- [6] J. T. Chen, K. H. Chen. Applications of the dual integral formulation in conjunction with fast multipole method in large-scale problems for 2D exterior acoustics. *Eng. An. Bound. Elem.*, 28:685–709, 2004.
- [7] L. C. Wrobel. *The Boundary Element Method Volume 1: Applications in Thermo-Fluids and Acoustics*. Wiley, Chichester, West Sussex, 2002.
- [8] M. H. Aliabadi. *The Boundary Element Method Volume 2: Applications in Solids and Structures*. Wiley, Chichester, West Sussex, 2002.
- [9] Y. Saad, M. Schultz. GMRES: A generalized minimal residual algorithm for solving non-symmetric linear systems. *SIAM J. Sci. Stat. Comput.*, 7:856–869, 1986.
- [10] K. M. Singh, M. Tanaka. Analytical integration of weakly singular integrals in boundary element analysis of Helmholtz and advection-diffusion equations. *Comput. Methods Appl. Mech. Engrg.*, 189:625–640, 2000.
- [11] P. S. Ramesh, M. H. Lean. Accurate integration of singular kernels in boundary integral formulations for Helmholtz equation. *Int. J. Numer. Methods Engrg.*, 31:1055–1068, 1991.
- [12] G. Watson. *A treatise on the theory of Bessel functions*. Cambridge University Press, 1966.

Nonlinear analysis of non-uniform beams on nonlinear elastic foundation

G.C. Tsiatas

Institute of Structural Analysis, School of Civil Engineering, National Technical University of Athens, Zografou Campus, GR-15773 Athens, Greece, gtsiatas@gmail.com

Keywords: Nonlinear analysis; Non-uniform beams; Nonlinear elastic foundation; Analog equation method

Abstract. In this paper a boundary integral equation solution to the nonlinear problem of non-uniform beams resting on nonlinear triparametric elastic foundation is presented, which permits also the treatment of nonlinear boundary conditions. The nonlinear subgrade model which describes the foundation includes the linear and nonlinear Winkler (normal) parameters and the linear Pasternak (shear) foundation parameter. The governing equations are derived in terms of the displacements for nonlinear analysis in the deformed configuration and for linear analysis in the undeformed one. Moreover, as the cross-sectional properties of the beam vary along its axis, the resulting coupled nonlinear differential equations have variable coefficients which complicate even more the mathematical problem. Their solution is achieved using the analog equation method (AEM) of Katsikadelis. Several beams are analyzed under various boundary conditions and load distributions, which illustrate the method and demonstrate its efficiency and accuracy. Finally, useful conclusions are drawn from the investigation of the nonlinear response of non-uniform beams resting on nonlinear elastic foundation.

Introduction

Beams resting on an elastic foundation are very often come across in engineering practice [1] and therefore an accurate and reliable method of analysis is required especially when the properties of their cross-section are variable. The complexity of the problem highly increases with the increase of the external applied load since the beam's transverse deflection influences the axial force and the resulting equations become coupled and nonlinear [2]. In this case, the linear elastic subgrade model is inadequate to describe the real behavior of the foundation and the use of a more sophisticated nonlinear one becomes inevitable.

The work has been done on the subject is limited only to the linear response of uniform beams on linear elastic foundation (for an analytic presentation see [3]), uniform beams on nonlinear elastic foundation [4-9] and non-uniform beams on nonlinear elastic foundation [10]. Distefano and Todeschini [4] presented the solution of a beam on nonlinear elastic foundation by means of the theory of quasilinearization. Sharma and DasGupta [5] studied the bending of axially constrained beams on nonlinear Winkler-type elastic foundation by an iteration method using Green's functions. Beaufait and Hoadley [6] used the midpoint difference method for the solution of elastic deformation of a beam supported on an elastic nonlinear foundation on rigid or elastic supports. A numerically integrated Finite Element Method developed in [7] for the analysis of three-dimensional, nonlinear Winkler foundation while Yankelevsky et al. presented an iterative procedure based on the exact stiffness matrix for beams on nonlinear Winkler foundation [8] and on nonlinear Winkler foundation with gaps [9]. Finally, Kuo and Lee [10] examined the static deflection of a general elastically end restrained non-uniform beam resting on a nonlinear elastic foundation by using the method of perturbation. To the author's knowledge publications on the solution to the general problem of the nonlinear analysis of non-uniform beams resting on nonlinear elastic foundation do not exist.

In this paper the nonlinear response of beams with variable properties resting on nonlinear elastic foundation is investigated. The governing equations are derived in terms of the displacements for nonlinear analysis in the deformed configuration and for linear analysis in the undeformed one. The linear analysis is performed in order to reveal the difference of the nonlinear response. The nonlinear model which describes the foundation includes the linear and nonlinear Winkler (normal) parameters and the linear Pasternak (shear) foundation parameter [11, 12]. Moreover, the variable cross-sectional properties of the beam result in governing differential equations with variable coefficients which complicate even more the mathematical problem. The solution of the problems was achieved using the analog equation method (AEM) of Katsikadelis. The method was developed for the nonlinear analysis of beams by Katsikadelis and Tsiatas [2] and has been used for the solution of complicated nonlinear beam problems (e.g. [13]). Using the principle of

the analog equation, the two coupled nonlinear differential equations with variable coefficients are replaced by two uncoupled linear ones pertaining to the axial and transverse deformation of a substitute beam with unit axial and bending stiffness, respectively, under fictitious load distributions. Several beams are analyzed under various boundary conditions and load distributions, which illustrate the method and demonstrate its efficiency and accuracy. Moreover, useful conclusions are drawn from the investigation of the nonlinear response of non-uniform beams resting on nonlinear foundation.

Governing equations

Consider an initially straight beam of length l having variable axial stiffness EA and bending stiffness EI , which may result from variable cross-section, $A = A(x)$, and/or from inhomogeneous linearly elastic material, $E = E(x)$; $I = I(x)$ is the moment of inertia of the cross-section. The x axis coincides with the neutral axis of the beam, which is bent in its plane of symmetry xz under the combined action of the distributed loads $p_x = p_x(x)$ and $p_z = p_z(x)$ in the x and z direction, respectively. It is assumed that there is no abrupt variation in cross-section of the beam so that the Euler-Bernoulli theory is valid [14, 15]. The beam is resting on a nonlinear elastic foundation. In the following the equilibrium equations in terms of the displacements are derived (a) for nonlinear response and (b) for linear response.

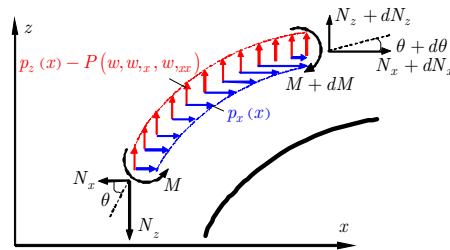


Figure 1: Forces and moments acting on the deformed element

Nonlinear theory. When the magnitude of the external applied loads is large, the nonlinear theory of finite strains must be employed [16]. However, in this work the external applied loads produce small strains as compared with the unity and the theory of moderate large deflections is considered. In this case the nonlinear kinematic relation retains the square of the slope of the deflection. The equilibrium equations are derived by considering the equilibrium of the deformed element [2] taking into account the subgrade reaction which is opposite to the distributed load $p_z = p_z(x)$ acting in the z direction (see Fig. 1). Thus, we obtain

$$N_{x,x} = -p_x(x), \quad N_{z,x} = -p_z(x) + P(w, w_x, w_{xx}), \quad M_{,x} = Q \quad (1, 2, 3)$$

where

$$N_x = N - Qw_{,x}, \quad N_z = Nw_{,x} + Q \quad (4, 5)$$

are the stress resultants in the x and z direction, respectively, and $P(w, w_x, w_{xx})$ is a nonlinear function of the deflection and its derivatives up to the second order representing the foundation reaction. It should be noted, however, that usual realistic foundation models depend mostly on the deflection and its second derivative [17], and without restricting the generality, the model that used in this investigation is [11, 12]

$$P(w, w_x, w_{xx}) = k_1 w + k_2 w^3 - k_3 w_{,xx} \quad (6)$$

where k_1 and k_2 are the linear and nonlinear Winkler (normal) foundation parameters, respectively, and k_3 is the linear Pasternak (shear) foundation parameter.

The axial force and the bending moment are evaluated by integrating appropriately the normal stress, that is

$$N = EA\left(u_{,x} + \frac{1}{2} w_{,x}^2\right), \quad M = -EIw_{,xx} \quad (7,8)$$

Substituting eqs (4), (5) and (6) into eqs (1) and (2) and using eq (3) to eliminate Q , yields

$$N_{,x} - (M_{,x} w_{,x})_{,x} = -p_x(x), \quad M_{,xx} + (Nw_{,x})_{,x} - (k_1 w + k_2 w^3 - k_3 w_{,xx}) = -p_z(x) \quad (9, 10)$$

which by virtue of eqs (7) and (8) become

$$\left[EA\left(u_{,x} + \frac{1}{2} w_{,x}^2\right)\right]_{,x} + (EIw_{,xx} w_{,x})_{,x} = -p_x(x) \quad (11)$$

$$-(EIw_{,xx})_{,xx} + \left[EA\left(u_{,x} + \frac{1}{2} w_{,x}^2\right)w_{,x}\right]_{,x} - (k_1 w + k_2 w^3 - k_3 w_{,xx}) = -p_z(x) \quad (12)$$

The pertinent boundary conditions are [2]

$$a_1 u(0) + a_2 N_x(0) = a_3 \quad \text{and} \quad \bar{a}_1 u(l) + \bar{a}_2 N_x(l) = \bar{a}_3 \quad (13, 14)$$

$$\beta_1 w(0) + \beta_2 N_z(0) = \beta_3 \quad \text{and} \quad \bar{\beta}_1 w(l) + \bar{\beta}_2 N_z(l) = \bar{\beta}_3 \quad (15, 16)$$

$$\gamma_1 w_{,x}(0) + \gamma_2 M(0) = \gamma_3 \quad \text{and} \quad \bar{\gamma}_1 w_{,x}(l) + \bar{\gamma}_2 M(l) = \bar{\gamma}_3 \quad (17, 18)$$

where $a_k, \bar{a}_k, \beta_k, \bar{\beta}_k, \gamma_k, \bar{\gamma}_k$ ($k = 1, 2, 3$) are given constants. Equations (13)-(18) describe the most general boundary conditions associated with the problem and can include elastic support or restraint.

Linear theory. Equation (9) after dropping the nonlinear term $M_{,x} w_{,x}$ it can be readily integrated independently [15]

$$N(x) = \int_x^l p(x) dx \quad (19)$$

Subsequently, eq (10) using eq (8) yields the linear counterpart of eq (12), that is, the linear bending equation of a non-uniform beam resting on nonlinear foundation

$$-(EIw_{,xx})_{,xx} + [N(x)w_{,x}]_{,x} - (k_1 w + k_2 w^3 - k_3 w_{,xx}) = -p_z(x) \quad (20)$$

together with the pertinent boundary conditions

$$\beta_1 w(0) + \beta_2 Q(0) = \beta_3 \quad \text{and} \quad \bar{\beta}_1 w(l) + \bar{\beta}_2 Q(l) = \bar{\beta}_3 \quad (21, 22)$$

$$\gamma_1 w_{,x}(0) + \gamma_2 M(0) = \gamma_3 \quad \text{and} \quad \bar{\gamma}_1 w_{,x}(l) + \bar{\gamma}_2 M(l) = \bar{\gamma}_3 \quad (23, 24)$$

The AEM solution for the nonlinear analysis of non-uniform beams

Equations (11) and (12) are solved using the AEM, as developed for the large deflection analysis of beams with variable stiffness by Katsikadelis and Tsiatas [2]. This method is applied to the problem at hand as follows. Let $u = u(x)$ and $w = w(x)$ be the sought solutions, which are two and four times differentiable, respectively, in $(0, l)$. Noting that eqs (11) and (12) are of the second order with respect to u and of fourth order with respect to w , one obtains by differentiating

$$u_{,xxx} = b_1(x), \quad w_{,xxxx} = b_2(x) \quad (25, 26)$$

Equations (25) and (26) describe the axial and bending linear response of a beam with constant unit axial and flexural stiffness subjected to the fictitious axial b_1 and transverse b_2 loads, respectively. They indicate that the solution of eqs (11) and (12) can be established by solving eqs (25) and (26) under the boundary conditions (13)-(18), provided that the fictitious load distributions b_1, b_2 are first determined. Note that eqs (25) and (26) are referred to as the analog equations to eqs (11) and (12). The fictitious loads are established by developing a procedure based on the integral equation method for one-dimensional problems. Thus, the integral representations of the solutions of eqs (25) and (26) are written as

$$u(x) = c_1x + c_2 + \int_0^l G_1(x, \xi) b_1(\xi) d\xi, \quad w(x) = c_3x^3 + c_4x^2 + c_5x + c_6 + \int_0^l G_2(x, \xi) b_2(\xi) d\xi \quad (27, 28)$$

where c_i ($i = 1, 2, \dots, 6$) are arbitrary integration constants to be determined from the boundary conditions and G_1, G_2 are the fundamental solutions (free space Green's functions) of eqs (25) and (26), respectively.

Substituting eqs (27), (28) and their respective derivatives into eqs (11) and (12) yields the equations, from which the fictitious sources b_1 and b_2 can be determined. This can be implemented only numerically as follows.

The interval $(0, l)$ is divided into N equal elements on which b_1 and b_2 are assumed to be constant. After discretization of eqs (27) and (28) we obtain using matrix notation

$$u(x) = \mathbf{H}_1(x)\mathbf{c}_1 + \mathbf{G}_1(x)\mathbf{b}_1, \quad w(x) = \mathbf{H}_2(x)\mathbf{c}_2 + \mathbf{G}_2(x)\mathbf{b}_2 \quad (29, 30)$$

where $\mathbf{G}_1(x)$ and $\mathbf{G}_2(x)$ are $1 \times N$ known matrices originating from the integration of the kernels $G_1(x, \xi)$ and $G_2(x, \xi)$ on the elements, respectively; $\mathbf{H}_1(x) = [x \ 1]$ and $\mathbf{H}_2(x) = [x^3 \ x^2 \ x \ 1]$; $\mathbf{c}_1 = \{c_1, c_2\}^T$; $\mathbf{c}_2 = \{c_3, c_4, c_5, c_6\}^T$; $\mathbf{b}_1, \mathbf{b}_2$ are the vectors containing the values of the fictitious loads at the nodal points, respectively.

Finally, collocating eqs (11) and (12) at the N nodal points and substituting the discretized eqs (29)-(30) and their respective derivatives yields the following equations

$$\mathbf{F}_1(\mathbf{b}_1, \mathbf{b}_2, \mathbf{c}) = -\mathbf{p}_x, \quad \mathbf{F}_2(\mathbf{b}_1, \mathbf{b}_2, \mathbf{c}) - \mathbf{P}(\mathbf{b}_2, \mathbf{c}) = -\mathbf{p}_z \quad (31, 32)$$

where $\mathbf{F}_i(\mathbf{b}_1, \mathbf{b}_2, \mathbf{c})$ are generalized stiffness vectors, $\mathbf{P}(\mathbf{b}_2, \mathbf{c})$ is the foundation's reaction vector and $\mathbf{c} = \{c_1, c_2, \dots, c_6\}^T$. Equations (31) and (32) constitute a system of $2N$ nonlinear algebraic equations with $2N + 6$ unknowns. The required six additional equations result from the boundary conditions. Thus, after substituting the relevant derivatives into eqs (13)-(18), we obtain

$$\mathbf{f}_i(\mathbf{b}_1, \mathbf{b}_2, \mathbf{c}) = \mathbf{0} \quad (i = 1, 2, \dots, 6) \quad (33)$$

The nonlinear equations (31)-(33) are solved numerically to yield $\mathbf{b}_1, \mathbf{b}_2$ and \mathbf{c} [2].

Numerical Examples

On the base of the procedure described in previous section a FORTRAN program has been written for establishing the nonlinear response of non-uniform beams resting on nonlinear foundation. In all examples the results have been obtained using $N = 21$ elements.

Cantilever beam with variable cross-section. A non-uniform cantilever beam with length $l = 1.0$ m has been studied solving both sets of equations (linear and nonlinear) in order to compare the results with those obtained by Kuo and Lee [10] using the small nonlinear foundation reaction $P = 500(1.6 - 2x + x^2)w + 250w^2$. The employed data are: $EI = 500(1 - 0.5x)^3$ kNm² and $p_z = p_{z0}(x^4 - x^5)$ kN/m. The linear analysis is first performed with $N(x) = -2500(1 - x)$ kN and $p_{z0} = 500$ kN/m. In Table 1 results for the deflection $w(x)$ and the bending moment $M(x)$ are presented at certain cross-sections for various values of N . The results are in very good agreement while the convergence and accuracy of the solution method is ensured for only $N = 21$ elements.

Subsequently the nonlinear response of the same beam was investigated with $EA = 266667(1 - 0.5x)$ kN and $p_x = -2500$ kN/m. In Fig. 2 the end deflection of the cantilever $w(l)$ versus the load p_{z0} for linear and nonlinear analysis is depicted. It is obvious that even for small nonlinear foundation reaction linear analysis is inadequate to predict the real response of the beam and the use of the nonlinear one is essential. In Table 2 results for the deflection $w(x)$, the axial force $N(x)$, the shear force $Q(x)$ and the bending moment $M(x)$ are presented as compared with those obtained from the linear response ($p_{z0} = 500$ kN/m).

	Present study			Kuo and Lee [10]
	$N = 11$	$N = 21$	$N = 31$	
$w(0.5)$	0.022	0.022	0.022	0.022
$w(1.0)$	0.082	0.082	0.081	0.082
$M(0.0)$	77.057	76.278	76.116	76.236
$M(0.5)$	36.505	36.319	36.279	36.373

Table 1: Deflection (m) and bending moment (kNm), for various values of N . Linear response

	$w(0.5)$	$w(1.0)$	$N(0.0)$	$N(0.5)$	$Q(0.0)$	$Q(0.5)$	$M(0.0)$	$M(0.5)$
Linear	0.022	0.082	-2500	-1250	6.213	11.950	76.278	36.319
Nonlinear	0.021	0.076	-2499	-1241	6.864	11.202	71.670	33.808

Table 2: Deflection (m), axial force (kN), shear force (kN) and bending moment (kNm) in Example 4.1. Linear and nonlinear response

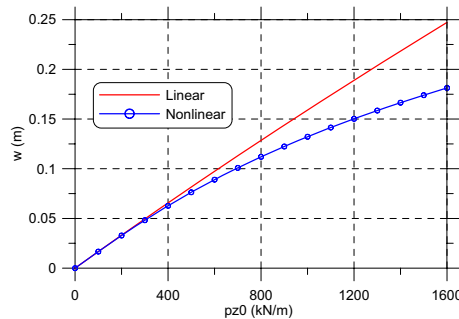


Figure 2: End deflection versus load

Rectangular beam with linearly varying height. The nonlinear response of a non-uniform rectangular beam with constant width b , variable height $h(x)$ and length $l = 3.0$ m resting on nonlinear foundation ($P = k_1 w + k_2 w^3 - k_3 w_{,xx}$) has been studied. The height of the beam varies according to the linear law $h(x) = h_0 + a(x - l/2)$ with $a = 2 \tan \phi$ being the taper ratio and h_0 the height at the half length. The employed data are: $E = 2.9 \times 10^6$ kN/m², $b = 0.1$ m, $h_0 = 0.20$ m, $p_x = 0$ kN/m and $p_z = 500$ kN/m. In order to examine the influence of the taper ratio on the nonlinear response, the volume of the beam, i.e. $V = bh_0 l$, was kept constant. The resulting beam should have no abrupt change of the cross-section so that the *Euler-Bernoulli* theory remains valid. Boley [14] has shown that, for a beam with unit constant width, a rate of change of the cross-section $|a| \simeq 0.35$ yields an error of 7.5%, while for $|a| \simeq 0.17$ the error is 1.8%. This was also verified by the author who treated the beam as a 2D elasticity problem and used the BEM to obtain the solution [18]. Three types of boundary conditions with immovable ends are considered (i) hinged-hinged, (ii) fixed-hinged and (iii) fixed-fixed.

In Tables 3, 4 and 5 results for the central deflections for various values of the three foundation parameters and the taper ratio are presented. It is observed that the deflections are most sensitive to the two linear parameter Pasternak foundation with cubic Winkler nonlinearity ($k_1 = k_2 = k_3 = 1000$) and the least sensitive to cubic Winkler foundation ($k_2 = 1000, k_1 = k_3 = 0$). It is also observed, that the deflections of the beam decrease with increasing the taper ratio, which means that the material must be shifted toward the end $x = l$ in order to obtain the minimum deflections. However, the differences of the deflections between the taper values $a = -0.05$ and $a = 0.05$ reduce as the foundation parameters k_1, k_2, k_3 increase. Moreover,

the percentage of the deflection reduction, as compared with the case $k_1 = k_2 = k_3 = 0$ is greater for taper ratio $a = -0.05$ and reduces for $a = 0.00$ and $a = 0.05$.

k_1	k_2	k_3	$a = -0.05$	$a = 0.00$	$a = 0.05$
0	0	0	0.36040	0.31272	0.28336
1000	0	0	0.28491	0.25546	0.23408
0	1000	0	0.35251	0.30825	0.28020
0	0	1000	0.28259	0.25176	0.23063
1000	1000	0	0.28015	0.25262	0.23206
1000	0	1000	0.21869	0.20154	0.18748
0	1000	1000	0.27822	0.24909	0.22871
1000	1000	1000	0.21653	0.20009	0.18640

Table 3: Central deflection of the hinged-hinged beam for various values of the three foundation parameters and the taper ratio

k_1	k_2	k_3	$a = -0.05$	$a = 0.00$	$a = 0.05$
0	0	0	0.31527	0.28207	0.26025
1000	0	0	0.24975	0.23038	0.21441
0	1000	0	0.30972	0.27871	0.25779
0	0	1000	0.24234	0.22242	0.20754
1000	1000	0	0.24653	0.22832	0.21289
1000	0	1000	0.18975	0.17910	0.16923
0	1000	1000	0.23956	0.22058	0.20616
1000	1000	1000	0.18839	0.17812	0.16848

Table 4: Central deflection of the fixed-hinged beam for various values of the three foundation parameters and the taper ratio

k_1	k_2	k_3	$a = -0.05$	$a = 0.00$	$a = 0.05$
0	0	0	0.31627	0.25324	0.19432
1000	0	0	0.24994	0.20675	0.16068
0	1000	0	0.31067	0.25086	0.19323
0	0	1000	0.23992	0.19390	0.15100
1000	1000	0	0.24680	0.20535	0.16006
1000	0	1000	0.18727	0.15757	0.12602
0	1000	1000	0.23720	0.19274	0.15049
1000	1000	1000	0.18598	0.15696	0.12574

Table 5: Central deflection of the fixed-fixed beam for various values of the three foundation parameters and the taper ratio

Elastically restrained rectangular beam with parabolically varied modulus of elasticity. To demonstrate the computational efficiency of the method the nonlinear response of an elastically restrained non-uniform rectangular beam with constant cross-section and parabolically varied modulus of elasticity $E = 2.9 \times 10^6 (1 + x^2)$ kN/m² resting on nonlinear foundation ($P = 10000w + 10000w^3 - 1000w_{,xx}$) has been studied. The employed data are: $b = 0.1$ m, $h = 0.20$ m, $l = 1.0$ m, $p_z = 5000(1 + x)$ kN/m, $p_x = -1500$ kN/m. Two types of classical boundary conditions, namely, hinged-hinged (H-H) and fixed-hinged (F-H) are considered as well as a hinged-hinged with a rotational elastic support (HRS-H) at $x = 0$ (all coefficients in boundary conditions are set to zero except from $a_1 = \beta_1 = \bar{a}_1 = \bar{\beta}_1 = \gamma_2 = \bar{\gamma}_2 = 1$ and $\gamma_1 = K_r$). In Figs. 3-6 the profiles of the deflection, the axial force, the shear force and the bending moment are presented, respectively, for various values of the rotational stiffness coefficient K_r . As it was expected with the increase of K_r the results tend to coincide with those obtained for fixed-hinged boundary conditions.

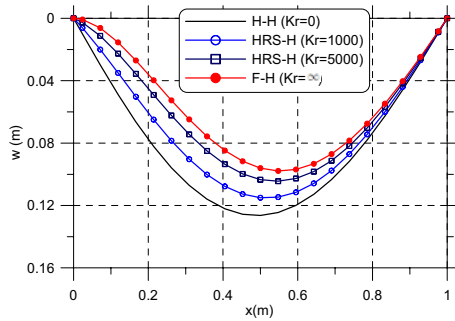


Figure 3: Profile of the deflection

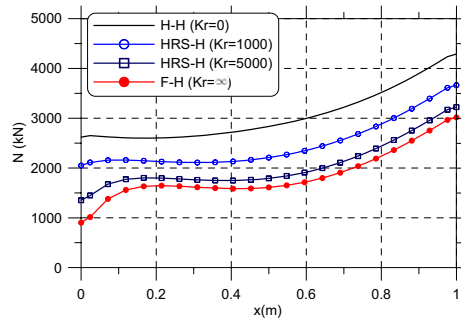


Figure 4: Profile of the axial force

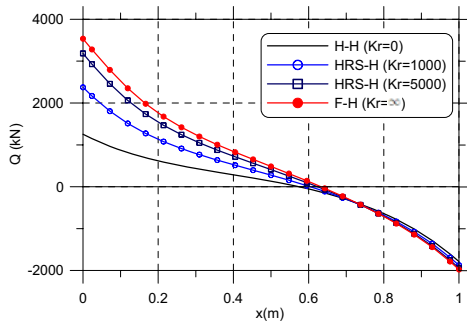


Figure 5: Profile of the shear force

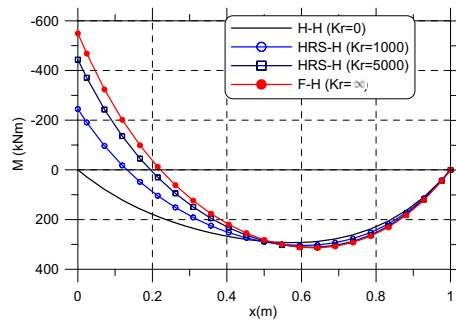


Figure 6: Profile of the bending moment

Conclusions

In this paper the nonlinear response of beams with variable properties resting on nonlinear elastic foundation is investigated. The solution of the derived coupled nonlinear governing equations with variable coefficients was achieved effectively using the analog equation method. This investigation has reached to certain interesting findings concerning the employed solution method, as well as the nonlinear response of non-uniform beams resting on nonlinear triparametric elastic foundation. These findings can be summarized as:

- The employed solution method exhibits stability and a small number of constant elements are adequate to obtain accurate results for the displacements and the stress resultants.
- Even for small nonlinear foundation reaction linear analysis is inadequate to predict the real response of the beam and the use of the nonlinear one is essential.
- The deflections are most sensitive to the two linear parameter Pasternak foundation with cubic Winkler nonlinearity and least sensitive to cubic Winkler foundation.
- For tapered beams with immovable ends (hinged-hinged, fixed-hinged and fixed-fixed) the deflections decrease with increasing the taper ratio. This suggests, shifting of the material towards the end $x = l$ in order to obtain the minimum deflections.
- However, the differences of the deflections between the taper values $a = -0.05$ and $a = 0.05$ reduce as the foundation parameters k_1, k_2, k_3 increase.
- Moreover, the percentage of the deflection reduction, as compared with the case $k_1 = k_2 = k_3 = 0$ is greater for taper ratio $a = -0.05$ and reduces for $a = 0.00$ and $a = 0.05$.

References

- [1] H.R.Öz and M.Pakdemirli Two-to-one internal resonances in a shallow curved beam resting on an elastic foundation. *Acta Mech.* **185**, 245-260 (2006).
- [2] J.T.Katsikadelis and G.C.Tsiatas Large deflection analysis of beams with variable stiffness. *Acta Mech.* **164**, 1-13 (2003).
- [3] Nii.Kim, S-S.Jeon and M-Y.Kim An improved numerical method evaluating exact static element stiffness matrices of thin-walled beam-columns on elastic foundations. *Comput. Struct.* **83**, 2003-2022 (2005).
- [4] N.Distefano and R.Todeschini A quasilinearization approach to the solution of elastic beams on nonlinear foundations. *Int. J. Solids Struct.* **11**, 89-97 (1975).
- [5] S.P.Sharma and S.DasGupta The bending problem of axially constrained beams on nonlinear elastic foundation. *Int. J. Solids Struct.* **11**, 853-859 (1975).
- [6] F.W.Beaufait and P.W.Hoadley Analysis of elastic beams on nonlinear foundations. *Comput. Struct.* **12**, 669-676 (1980).
- [7] A.F.Sayegh and F.K.Tso Finite element analysis of 3-d beam columns on a nonlinear foundation. *Comput. Struct.* **6**, 699-715 (1988).
- [8] D.Z.Yankelevsky, M.Eisenberger and M.A.Adin Analysis of beams on nonlinear winkler foundation. *Comput. Struct.* **31**, 287-292 (1989).
- [9] D.Z.Yankelevsky, M.A.Adin and M.Eisenberger Beams on nonlinear winkler foundation with gaps. *Comput. Geotech.* **6**, 1-11 (1988).
- [10] Y.H.Kuo and S.Y.Lee Deflection of nonuniform beams resting on a nonlinear elastic foundation. *Comput. Struct.* **51**, 513-519 (1994).
- [11] B.N.Singh, A.Lal and R.Kumar Nonlinear bending response of laminated composite plates on nonlinear elastic foundation with uncertain system properties. *Eng. Struct.* **30**, 1101-1112 (2008).
- [12] P.Malekzadeh and A.R.Vosoughi DQM large amplitude vibration of composite beams on nonlinear elastic foundation with restrained edges. *Commun. Nonlinear Sci. Numer. Simul.* **14**, 906-915 (2009).
- [13] E.J.Sapountzakis and V.G.Mokos Shear deformation effect in nonlinear analysis of spatial composite beams subjected to variable axial loading by beam. *Acta Mech.* **193**, 43-65 (2007).
- [14] B.A.Boley On the accuracy of the Bernoulli-Euler theory for beams of variable section. *ASME J. Appl. Mech.* **30**, 373-378 (1963).
- [15] J.T.Katsikadelis and G.C.Tsiatas Optimum design of structures subjected to follower forces. *Int. J. Mech. Sci.* **49**, 1204-1212 (2007).
- [16] H.Irschik and J.Gerstmayr A continuum mechanics based derivation of Reissner's large-displacement finite-strain beam theory: the case of plane deformations of originally straight Bernoulli-Euler beams. *Acta Mech.* DOI 10.1007/s00707-008-0085-8 (2008).
- [17] J.T.Katsikadelis and A.J.Yiotis The BEM for plates of variable thickness on nonlinear biparametric elastic foundation. An analog equation solution. *J. Eng. Math.* **46**, 313-330 (2003).
- [18] J.T.Katsikadelis *Boundary Elements: Theory and Applications*. Elsevier, Amsterdam-London (2002).

A BEM solution to the Saint-Venant torsion problem of micro-bars

G.C. Tsiatas¹ and J.T. Katsikadelis²

¹ Institute of Structural Analysis, School of Civil Engineering, National Technical University of Athens, Zografou Campus, GR-15773 Athens, Greece, gtsiatas@gmail.com

² Institute of Structural Analysis, School of Civil Engineering, National Technical University of Athens, Zografou Campus, GR-15773 Athens, Greece, jkats@central.ntua.gr

Keywords: Torsion; Microstructure; Couple stress theory; Strain gradient elasticity; Analog equation method; Method of fundamental solutions

Abstract. In this paper the Saint-Venant torsion problem of micro-bars of arbitrary cross section is solved. Two models of strain gradient elasticity are considered which originate from the classical couple stress theory. The first model contains two additional constants related to the microstructure of the isotropic material which, however, are difficult to determine. The second one is derived from the modified couple stress theory of Yang et al. and has only one material length scale parameter. Using a variational procedure the governing differential equation and the associated boundary conditions are derived in terms of the warping function. This is a fourth order partial differential equation representing the analog of a Kirchhoff plate having the shape of the cross section and subjected to a uniform tensile membrane force with mixed Neumann boundary conditions. Since the fundamental solution of the equation is known, the problem could be solved using the direct BEM. In this investigation, however, the Analog Equation Method (AEM) solution is applied and the results are cross checked using the Method of Fundamental Solutions (MFS). Numerical results are obtained and useful conclusions are drawn regarding the use of either couple stress model as well as the size effect on the torsional response of micro-bars, giving thus a better insight in the gradient elasticity approach of the deformable bodies.

Introduction

In recent years a need has been raised in engineering practice to predict accurately the response of micron-scale structures which are the components of microelectromechanical systems (MEMS). The behavior of such structures has been proven experimentally to be size dependent. Thus, the utilization of strain gradient (higher order) theories containing internal material length scale parameters is inevitable. The couple stress theory is a special case of these higher-order theories in which the effects of the dilatation gradient and the deviatoric stretch gradient are assumed to be negligible. An analytic presentation of the afore-mentioned theories can be found in [1-3]. Although, the strain gradient theories encounter the physical problem in its generality, they contain additional constants – besides the Lamé constants - which must be determined from the microstructure of the material.

The work that has been done on the Saint-Venant torsion problem of elastic micro-bars is limited only to the work of Tong et al. [4]. In their work the simplified couple stress model of Lam et al. [5] with three additional material length scale parameters is applied to the torsion problem. Since the dilatational strain gradients vanish identically, the particular model leads to the formulation of the torsional equation in terms of the warping function which contains only two material length scale parameters. Two formulations in terms of pseudo warping function and stress function are presented. However, the employed analytical solutions are restricted only to simple geometric shapes. That is, closed-form solutions for circular and thin-walled cross-section are presented while a series solution for rectangular microbars is also introduced. Moreover, the two additional constants, in this simplified couple stress model, are difficult to determine [5]. Therefore, gradient elastic models of only one additional material constant are desirable.

In this work the simplified couple stress theory of Yang et al. [6] is developed for the solution of the Saint-Venant torsion problem of micro-bars with arbitrary shape. Yang et al. modifying the classical couple stress theory (e.g. [7-8]) proposed a modified couple stress model in which only one material length parameter is needed to capture the size effect. This simplified couple stress theory is based on an additional equilibrium relation which forces the couple stress tensor to be symmetric. So far has been developed for the static bending [9] and free vibration [10] problems of a Bernoulli-Euler beam and for the static bending and free vibration problems of a Timoshenko beam [11]. Moreover, Park and Gao [12] solved analytically a

simple shear problem after the derivation of the boundary conditions and the displacement form of the theory.

The governing equilibrium equation and the pertinent boundary conditions in terms of the warping function are derived using the minimum potential energy principle. The resulting boundary value problem of the micro-bar is described by a fourth order partial differential equation, which represents the analogue of a Kirchhoff plate under uniform tensile membrane force with mixed Neumann type boundary conditions. Since the fundamental solution of the equation is known, the problem could be solved using the direct BEM for plates by establishing the integral representation via the Betti's reciprocal theorem. Nevertheless, the problem is solved more efficiently using the AEM with the simple fundamental solution of the biharmonic operator and the results are cross checked using the MFS. The employed numerical method is capable to handle micro-bars with complex geometries. Numerical results are obtained and useful conclusions are drawn regarding the use of either couple stress model as well as the size effect on the torsional response of micro-bars, giving thus a better insight in the gradient elasticity approach of the deformable bodies.

Problem formulation

Derivation of the governing equations. In the modified couple stress theory presented by Yang et al. [6], the strain energy density is a function of both strain tensor and the symmetric part of the curvature tensor which are conjugated with the stress tensor and the deviatoric part of the couple stress tensor. Thus, for a deformable body occupying the volume V the strain energy is given as

$$U = \frac{1}{2} \int_V (\boldsymbol{\sigma} : \boldsymbol{\varepsilon} + \mathbf{m} : \boldsymbol{\chi}) dV \quad (1)$$

where the strain tensor $\boldsymbol{\varepsilon}$, the symmetric part of the curvature tensor $\boldsymbol{\chi}$, the stress tensor $\boldsymbol{\sigma}$ and the deviatoric part of the couple stress tensor \mathbf{m} are defined as

$$\boldsymbol{\varepsilon} = \frac{1}{2}(\nabla \mathbf{u} + \mathbf{u} \nabla), \quad \boldsymbol{\chi} = \frac{1}{2}(\nabla \boldsymbol{\theta} + \boldsymbol{\theta} \nabla), \quad \boldsymbol{\sigma} = \lambda(\text{tr} \boldsymbol{\varepsilon}) \mathbf{I} + 2\mu \boldsymbol{\varepsilon}, \quad \mathbf{m} = 2\mu l^2 \boldsymbol{\chi} \quad (2a,b,c,d)$$

with \mathbf{u} being the displacement vector, $\boldsymbol{\theta}$ is the rotation vector defined as [6]

$$\boldsymbol{\theta} = \frac{1}{2} \text{curl} \mathbf{u} \quad (3)$$

λ , μ are the Lamé constants and l is a material length scale parameter. Note that the deviatoric part of the couple stress tensor \mathbf{m} defined in eq (2d) is symmetric due to the symmetry of $\boldsymbol{\chi}$ given in eq (2b).

Following Yang et al. [6] and Park and Gao [12], the work produced by the external forces is

$$W = \int_V (\mathbf{b} \cdot \mathbf{u} + \mathbf{c} \cdot \boldsymbol{\theta}) dV + \int_{\Omega} (\mathbf{t} \cdot \mathbf{u} + \mathbf{s} \cdot \boldsymbol{\theta}) d\Omega \quad (4)$$

where \mathbf{b} , \mathbf{c} , \mathbf{t} and \mathbf{s} are the body force, body couple, traction and surface couple, respectively, and Ω is the surface of V .

Consider now an elastic bar of length L with arbitrary cross-section occupying the two-dimensional domain Ω of arbitrary shape in the x, y plane bounded by the curve Γ which may be piecewise smooth, i.e. it may have a finite number of corners. The cross-section is constant along the length of the bar and is twisted by moments M_i applied at its ends. According to Saint-Venant's torsion theory [13], the deformation of the bar consists of (a) rotations of the cross-sections about an axis passing through the *twist center* of the bar and (b) warping of the cross-sections, which is the same for all sections. Choosing the origin of the coordinate system at the twist center of an end section, the rotation at a distance z is ϑz , where ϑ is a constant expressing the rotation of a cross-section per unit length. Assuming that this rotation is small, the displacement components of an arbitrary point are [13]

$$u = -\vartheta zy, \quad v = \vartheta zx, \quad w = \vartheta \phi(x, y) \quad (5)$$

where $\phi(x, y)$ is the *warping function*. Taking into account eqs (5) and eq (3) the displacement and rotation vectors of the micro-bar become, respectively,

$$\mathbf{u} = -\vartheta zy \mathbf{e}_1 + \vartheta zx \mathbf{e}_2 + \vartheta \phi(x, y) \mathbf{e}_3, \quad \boldsymbol{\theta} = \frac{1}{2} \vartheta (\phi_{,y} - x) \mathbf{e}_1 - \frac{1}{2} \vartheta (\phi_{,x} + y) \mathbf{e}_2 + \vartheta z \mathbf{e}_3 \quad (6a,b)$$

Substituting eqs (5) into eqs (2a,b) the nonzero components of the strain and curvature tensor are written as

$$\gamma_{xz} = \vartheta(\phi_{,x} - y), \quad \gamma_{zx} = \vartheta(\phi_{,y} + x) \quad (7a,b)$$

$$\chi_x = \frac{1}{2}\vartheta(\phi_{,xy} - 1), \quad \chi_y = -\frac{1}{2}\vartheta(\phi_{,xy} + 1), \quad \chi_z = \vartheta, \quad \chi_{xy} = \frac{1}{4}\vartheta(\phi_{,yy} - \phi_{,xx}) \quad (8a,b,c,d)$$

respectively. Moreover, the nonzero components of the stress (2c) and couple stress (2d) tensors, after the appropriate replacement of the Lamé constants by the modulus of elasticity E and the Poisson's ratio ν , take the following form

$$\tau_{xz} = G\vartheta(\phi_{,x} - y), \quad \tau_{yz} = G\vartheta(\phi_{,y} + x) \quad (9a,b)$$

$$m_x = l^2 G\vartheta(\phi_{,xy} - 1), \quad m_y = -l^2 G\vartheta(\phi_{,xy} + 1), \quad m_z = 2l^2 G\vartheta, \quad m_{xy} = \frac{1}{2}l^2 G\vartheta(\phi_{,yy} - \phi_{,xx}) \quad (10a,b,c,d)$$

where $G = E / 2(1 + \nu)$ is the shear modulus.

In the absence of body force and body couple and taking into account that the cylindrical surface of the micro-bar is traction and surface couple free ($W = 0$) the first variation of the total potential energy using eq (1) takes the form

$$\delta\Pi = \delta U - \delta W = \frac{1}{2} \int_V (\boldsymbol{\sigma} : \delta\boldsymbol{\varepsilon} + \mathbf{m} : \delta\boldsymbol{\chi}) dV \quad (11)$$

and using eqs (7)-(10) yields

$$\delta\Pi = \vartheta \int_{\Omega} \left[\tau_{xz} \delta\phi_{,x} + \tau_{yz} \delta\phi_{,y} - \frac{1}{2} m_{xy} \delta\phi_{,xx} + \frac{1}{2} m_{xy} \delta\phi_{,yy} + \frac{1}{2} (m_x - m_y) \delta\phi_{,xy} \right] d\Omega \quad (12)$$

which, after the transformation of the domain integral using twice the divergence theorem of Gauss, becomes

$$\begin{aligned} \delta\Pi = & -\vartheta \int_{\Omega} \left[\tau_{xz} \cdot_x + \tau_{yz} \cdot_y + \frac{1}{2} (m_{xy} \cdot_{xx} - m_{xy} \cdot_{yy} + m_y \cdot_{xy} - m_x \cdot_{xy}) \right] \delta\phi d\Omega \\ & + \vartheta \int_{\Gamma} \left[\tau_{xz} n_x + \tau_{yz} n_y + \frac{1}{2} (m_{xy} \cdot_x n_x - m_{xy} \cdot_y n_y + m_y \cdot_x n_x - m_x \cdot_x n_y) \right] \delta\phi ds \\ & - \vartheta \frac{1}{2} \int_{\Gamma} m_{nt} \delta\phi_{,n} ds + \vartheta \frac{1}{2} \int_{\Gamma} m_n \delta\phi_{,t} ds \end{aligned} \quad (13)$$

where

$$m_n = m_x n_x^2 + m_y n_y^2 + 2m_{xy} n_x n_y \quad (14a)$$

$$m_{nt} = m_{xy} (n_x^2 - n_y^2) + (m_y - m_x) n_x n_y \quad (14b)$$

are the stress resultants and $n_x = \cos a$, $n_y = \sin a$ with $a = \angle x, \mathbf{n}$.

The first line integral in eq (13) represents a line force term along the boundary (the respective shearing force term in the plate bending theory [14]). The last integral in the same equation represents also a line force term and must be converted in order to be inserted into the first line integral. Noting that $\phi_{,t} = \phi_{,s}$ the integration by parts along the boundary Γ of the aforementioned integral gives

$$\begin{aligned} \int_{\Gamma} m_n \delta\phi_{,s} ds &= \int_{\Gamma} (m_n \delta\phi)_{,s} ds - \int_{\Gamma} m_{n,s} \delta\phi ds \\ &= \sum_k [m_n]_k \delta\phi - \int_{\Gamma} m_{n,s} \delta\phi ds \end{aligned} \quad (15)$$

where $[m_n]_k$ is the jump of discontinuity of the twisting moment at the k -th corner. Thus, eq (13) becomes

$$\begin{aligned} \delta\Pi = & -\vartheta \int_{\Omega} \left[\tau_{xz,z} + \tau_{yz,y} + \frac{1}{2} (m_{xy,xx} - m_{xy,yy} + m_{y,xy} - m_{x,xy}) \right] \delta\phi d\Omega \\ & + \vartheta \int_{\Gamma} \left[\tau_{xz} n_x + \tau_{yz} n_y + \frac{1}{2} (m_{xy,x} n_x - m_{xy,y} n_y + m_{y,y} n_x - m_{x,x} n_y) - \frac{1}{2} m_{n,s} \right] \delta\phi ds \\ & - \vartheta \frac{1}{2} \int_{\Gamma} m_{nt} \delta\phi_{,n} ds + \vartheta \frac{1}{2} \sum_k [m_n]_k \delta\phi \end{aligned} \quad (16)$$

By applying the principle of total minimum potential energy, i.e., $\delta\Pi = 0$ for the stable equilibrium and the fundamental lemma of the calculus of variation (e.g. [15]) the governing equilibrium differential equation of the micro-bar is obtained as

$$\tau_{xz,x} + \tau_{yz,y} + \frac{1}{2} (m_{xy,xx} - m_{xy,yy} + m_{y,xy} - m_{x,xy}) = 0 \quad \text{in } \Omega \quad (17)$$

together with the boundary conditions

$$\tau_{xz} n_x + \tau_{yz} n_y + \frac{1}{2} (m_{xy,x} n_x - m_{xy,y} n_y + m_{y,y} n_x - m_{x,x} n_y) - \frac{1}{2} m_{n,s} = 0 \quad (18a)$$

$$m_{nt} = 0 \quad (18b)$$

on Γ and

$$\sum_k [m_n]_k = 0 \quad (18c)$$

at the k -th corner.

Eqs (17) and (18a,b) can be also verified by substituting eqs (7)-(10) into the general equilibrium equations

$$\text{div} \boldsymbol{\sigma} + \frac{1}{2} \text{curl}(\text{divm} + \mathbf{c}) + \mathbf{b} = \mathbf{0} \quad \text{in } \Omega \quad (19)$$

produced by Park and Gao [12], together with the boundary conditions

$$\boldsymbol{\sigma} \mathbf{n} + \frac{1}{2} \mathbf{n} \times [\text{divm} - \nabla(\mathbf{m} : \mathbf{n} \otimes \mathbf{n}) + \mathbf{c}] = \tilde{\mathbf{t}} - \frac{1}{2} \mathbf{n} \times \nabla(\tilde{\mathbf{s}} \cdot \mathbf{n}) \quad (20a)$$

$$\mathbf{m} \mathbf{n} - (\mathbf{m} : \mathbf{n} \otimes \mathbf{n}) \mathbf{n} = \tilde{\mathbf{s}} - (\tilde{\mathbf{s}} \cdot \mathbf{n}) \mathbf{n} \quad (20b)$$

on Γ , of a three-dimensional deformable body for the modified couple stress theory of Yang et al. [6], in the absence of body force, body couple, traction and surface couple. In eqs (20) and in whichever follows, the tilde over a symbol represents prescribed quantity.

Substituting eqs (9)-(10) into eq (17)-(18) yields the governing equation of the micro-bar in terms of the warping function

$$\frac{l^2}{4} \nabla^4 \phi - \nabla^2 \phi = 0 \quad \text{in } \Omega \quad (21)$$

and the boundary conditions

$$\phi_{,n} - \frac{l^2}{4} \left[\nabla^2 \phi_{,n} + 2(\phi_{,nt})_{,s} \right] = y n_x - x n_y, \quad \phi_{,tt} - \phi_{,nn} = 0 \quad (22a,b)$$

on Γ .

On the end cross-sections $z = 0$ and $z = L$, it is $n_x = n_y = 0$ and $n_z = 1$. Thus, the nonzero boundary conditions (20) are

$$t_x = \tau_{xz} - \frac{1}{2} (m_{xy,x} + m_{y,xy}) = G \vartheta \left(\phi_{,x} - y + \frac{l^2}{4} \nabla^2 \phi_{,x} \right) \quad (23a)$$

$$t_y = \tau_{yz} + \frac{1}{2} (m_{x,xy} + m_{xy,y}) = G \vartheta \left(\phi_{,y} + x + \frac{l^2}{4} \nabla^2 \phi_{,y} \right) \quad (23b)$$

Along the boundary Γ of the surface is also present a line force with components

$$g_x = \frac{1}{2}n_y(m_y - m_x) + n_x m_{xy} = G\vartheta \left[-l^2(n_y\phi_{,xy} - n_x\phi_{,yy}) - \frac{l^2}{2}n_x\nabla^2\phi \right] \quad (24a)$$

$$g_y = \frac{1}{2}n_x(m_y - m_x) - n_y m_{xy} = G\vartheta \left[-l^2(n_x\phi_{,xy} - n_y\phi_{,xx}) - \frac{l^2}{2}n_y\nabla^2\phi \right] \quad (24b)$$

in the x and y direction, respectively.

We can readily prove that the stress resultants of the tractions (23) and line forces (24) vanish. Namely,

$$\int_{\Omega} t_x d\Omega + \int_{\Gamma} g_x ds = 0, \quad \int_{\Omega} t_y d\Omega + \int_{\Gamma} g_y ds = 0 \quad (25a,b)$$

The moment resultant on the cross-section is going to be

$$M_t = \int_{\Omega} (xt_y - yt_x) d\Omega + \int_{\Gamma} (xg_y - yg_x) ds \quad (26)$$

which, after the substitution of eqs (23), (24) takes the form

$$M_t = G\vartheta \int_{\Omega} (x^2 + y^2 + x\phi_{,y} - y\phi_{,x}) d\Omega + 3l^2 G\vartheta \quad (27)$$

Setting

$$I_t = \int_{\Omega} (x^2 + y^2 + x\phi_{,y} - y\phi_{,x}) d\Omega + 3l^2 \quad (28)$$

we arrive at

$$M_t = G\vartheta I_t \quad (29)$$

The torsional constant I_t does not depend only on the shape of the cross-section, as it happens in the classical Saint-Venant theory, but it depends also on the microstructure of the micro-bar.

The domain integral in eq (28) can be converted into a boundary line integral [13]. Thus, eq (28) finally becomes

$$I_t = \int_{\Gamma} [(xy^2 - y\phi)n_x + (yx^2 + x\phi)n_y] ds + 3l^2 \quad (30)$$

The plate analogue. The equation of a plate with bending stiffness D subjected to a uniform tensile membrane force N in absence of external load, is written as

$$D\nabla^4 w - N\nabla^2 w = 0 \quad \text{in } \Omega \quad (31)$$

Further, we consider the natural boundary conditions

$$Nw_{,n} + V_n w = yn_x - xn_y, \quad M_n w = 0 \quad (32a,b)$$

on Γ , where V_n and M_n are differential operators defined as

$$V_n = -D \left[\frac{\partial}{\partial n} \nabla^2 - (\nu - 1) \frac{\partial}{\partial s} \left(\frac{\partial^2}{\partial n \partial t} \right) \right], \quad M_n = -D \left[\nabla^2 + (\nu - 1) \frac{\partial^2}{\partial t^2} \right] \quad (33a,b)$$

which represent the effective shear force and bending moment, respectively, on the boundary.

It is apparent that eqs (21) and (22) can be obtained from eqs (31) and (32) for $w = \phi$, $N = 1$, $D = l^2 / 4$ and $\nu = -1$. Thus, in this case the warping function represents the deflection of a plate subjected to a uniform tensile membrane force $N = 1$ with bending stiffness $D = l^2 / 4$ and Poisson's ratio $\nu = -1$ in the absence of external load. Note that, for $D = 0$ it is $V_n = M_n = 0$ and eqs (31) and (32) give

the membrane analogue for the classical Saint-Venant problem. It should be mentioned that the deflection surface is not uniquely determined, since the boundary conditions permit a rigid body motion. This, however, does not influence the deformation of the cross-section [13].

The modified couple stress torsion model of Tong et al. In the work of Tong et al. [4], the couple stress model of Lam et al. [5] -with three additional material length scale parameters- is applied to the Saint-Venant torsion problem. Since the dilatational strain gradients vanish identically, the torsion model contains only two material length scale parameters, namely l_1 and l_2 . The governing equation of the micro-bar in terms of the warping function is

$$\left(\frac{8l_1^2}{15} + \frac{l_2^2}{4}\right) \nabla^4 \phi - \nabla^2 \phi = 0 \quad \text{in } \Omega \quad (34)$$

and the boundary conditions are

$$\phi_{,n} - \left(\frac{8l_1^2}{15} + \frac{l_2^2}{4}\right) \nabla^2 \phi_{,n} - \left(\frac{2l_1^2}{3} + \frac{l_2^2}{2}\right) (\phi_{,nt})_{,s} = ym_x - xm_y, \quad \left(\frac{8l_1^2}{15} + \frac{l_2^2}{4}\right) \nabla^2 \phi - \left(\frac{2l_1^2}{3} + \frac{l_2^2}{2}\right) \phi_{,tt} = 0 \quad (35a,b)$$

on Γ . The boundary tractions on the end cross-sections are

$$t_x = \tau_{xz} - \frac{1}{2}(m_{xy,x} + m_{y,y}) = G\vartheta \left[\phi_{,x} - y - \left(\frac{16l_1^2}{15} - \frac{l_2^2}{4}\right) \nabla^2 \phi_{,x} \right] \quad (36a)$$

$$t_y = \tau_{yz} + \frac{1}{2}(m_{x,x} + m_{xy,y}) = G\vartheta \left[\phi_{,y} + x - \left(\frac{16l_1^2}{15} - \frac{l_2^2}{4}\right) \nabla^2 \phi_{,y} \right] \quad (36b)$$

while the moment resultant on the cross-section takes the form

$$M_t = G\vartheta \int_{\Omega} (x^2 + y^2 + x\phi_{,y} - y\phi_{,x}) d\Omega + 3l_2^2 G\vartheta \quad (37)$$

Note that setting $l_1 = 0$ and $l_2 = l$ in the above equations yield eqs (21)-(23) and (27) of the proposed model.

Equations (34) and (35) can be also obtained from eqs (31) and (32) for $w = \phi$, $N = 1$ and

$$D = \frac{8l_1^2}{15} + \frac{l_2^2}{4}, \quad \nu = 1 - \left(\frac{2l_1^2}{3} + \frac{l_2^2}{2}\right) / \left(\frac{8l_1^2}{15} + \frac{l_2^2}{4}\right) \quad (38a,b)$$

The numerical solution

Using the Betti's reciprocal theorem for the plate equation, in the absence of external load, we obtain the integral representation of the solution as [16]

$$w(P) = \int_{\Gamma} \left(v V_n w - w V_n v - \frac{\partial v}{\partial n} M_n w + \frac{\partial w}{\partial n} M_n v \right) ds - \sum_k (v [Tw]_k - w [Tv]_k), \quad P : \{x, y\} \in \Omega \quad (39)$$

where v is the fundamental solution of eq (31), i.e. a singular particular solution of the following equation

$$\nabla^4 v - \mu^2 \nabla^2 v = \delta(P - Q) \quad (40)$$

given as

$$v = \frac{1}{2\pi\mu^2} [K_0(\mu r) - \ln r] \quad (41)$$

with K_0 being the zero-order modified Bessel function of the second kind and $\mu^2 = N/D$. T is a differential operator defined as

$$T = D(1 - \nu) \frac{\partial^2}{\partial n \partial t} \tag{42}$$

which represents the twisting moment M_{nt} along the boundary and $\llbracket Tw \rrbracket_k$ its jump of discontinuity at the k -th corner.

Obviously, the boundary integral equations will result for $P \rightarrow p \in \Gamma$. Thus, the warping function can be established by developing the direct BEM.

However, in order to avoid rather complicated computations of singular integrals, the problem is solved using the AEM with [16] or without [17] domain discretization which employs the simple fundamental solution

$$v = \frac{1}{8\pi D} r^2 \ln r \tag{43}$$

of the biharmonic equation. The results are cross checked using the MFS as it was applied for plates [18].

Numerical Example

On the base of the procedure described in previous section a FORTRAN program has been written for establishing the torsional response of the micro-bars. In the MFS the source points are placed equally on a virtual boundary – outside the domain – at a distance 20% greater than that of the actual one.

Square micro-bar. For reasons of comparisons a square micro-bar ($a/b = 1$, $N = 100$) is investigated employing both couple stress models. In Fig. 1 is depicted the normalized torsional constant I_t / I_t^c (I_t^c is the torsional constant of the classical Saint Venant theory) versus the non-dimensional material length scale parameter l_2/a . The results from the AEM and MFS solution employing the Tong et al. model [4] ($l_1 = l_2$) are found to be in excellent agreement with that obtained from their analytical solution. We can also observe that the torsional constant estimated by the proposed one-parameter model ($l_1 = 0$, $l_2 = l$) is smaller as the non-dimensional material length scale parameter increases to the value of $l_2/a = 0.3$, while, for greater values the difference between the two models becomes negligible. The presented results indicate that the torsional constant of the bar increases nonlinearly with the increase of l_2/a in both models. Moreover, Fig. 2 shows the warping surface for the case $l_1 = l_2 = 0.3$.

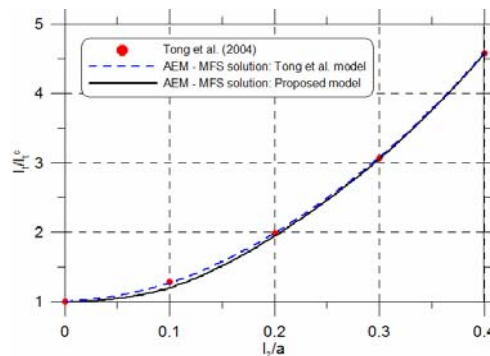


Figure 1: Normalized torsional constant versus the non-dimensional material length scale parameter

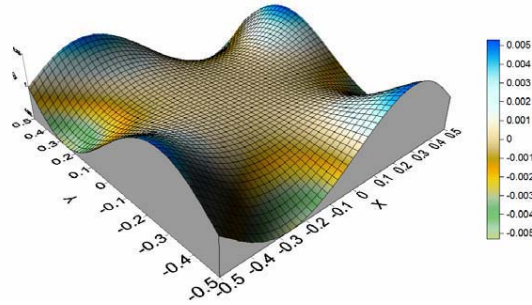


Figure 2: Warping surface

References

- [1] I.Vardoulakis and J.Sulem, *Bifurcation Analysis in Geomechanics*. Blackie/Chapman and Hall, London (1995).
- [2] G.E.Exadaktylos and I.Vardoulakis Microstructure in linear elasticity and scale effects: a reconsideration of basic rock mechanics and rock fracture mechanics. *Tectonophysics* **335**, 81–109 (2001).
- [3] K.Tsepoura, S.Papargyri-Beskou, D.Polyzos and D.E.Beskos Static and dynamic analysis of gradient elastic bars in tension. *Arch. Appl. Mech.* **72**, 483–497 (2002).
- [4] P.Tong, F.Yang, D.C.C.Lam and J.Wang Size effects of hair-sized structures-Torsion. *Key Eng. Mater.* **261-263**, 11-22 (2004).
- [5] D.C.C.Lam, F.Yang, A.C.M.Chong, J.Wang and P.Tong Experiments and theory in strain gradient elasticity. *J. Mech. Phys. Solids* **51**, 1477–1508 (2003).
- [6] F.Yang, A.C.M.Chong, D.C.C.Lam and P.Tong Couple stress based strain gradient theory of elasticity. *Int. J. Solids Struct.* **39**, 2731–2743 (2002).
- [7] R.D.Mindlin Micro-structure in linear elasticity. *Arch. Ration. Mech. Anal.* **16**, 51–78 (1964).
- [8] W.T.Koiter Couple stresses in the theory of elasticity, I and II. *Proc. K. Ned. Akad. Wet. (B)* **67**, 17–44 (1964).
- [9] S.K.Park and X.-L.Gao Bernoulli–Euler beam model based on a modified couple stress theory. *J. Micromech. Microeng.* **16**, 2355–2359 (2006).
- [10] S.Kong, S.Zhou, Z.Nie and K.Wang The size-dependent natural frequency of Bernoulli-Euler microbeams. *Int. J. Eng. Sci.* **46**, 427-437 (2008).
- [11] H.M.Ma, X.-L.Gao and J.N.Reddy A microstructure-dependent Timoshenko beam model based on a modified couple stress theory. *J. Mech. Phys. Solids* **56**, 3379-3391 (2008).
- [12] S.K.Park and X.-L.Gao Variational formulation of a modified couple stress theory and its application to a simple shear problem. *Z. angew. Math. Phys.* **59**, 904–917 (2008).
- [13] J.T.Katsikadelis *Boundary Elements: Theory and Applications*. Elsevier, Amsterdam-London (2002).
- [14] J.T.Katsikadelis and A.E.Armenakas New boundary equation solution to the plate problem. *J. Appl. Mech.-T. ASME* **56**, 364-374 (1989).
- [15] J.N.Reddy *Theory and Analysis of Elastic Plates*. Taylor and Francis, Philadelphia (1999).
- [16] J.T.Katsikadelis and N.G.Babouskos Nonlinear flutter instability of thin damped plates. An AEM Solution. *J. Mech. Mater. Struct.* in press, (2009).
- [17] N.G.Babouskos and J.T.Katsikadelis Flutter instability of damped plates under combined conservative and nonconservative loads. *Arch. Appl. Mech.* doi: 10.1007/s00419-008-0290-x (2009).
- [18] A.Poullikkas, A.Karageorghis and G.Georgiou Methods of fundamental solutions for harmonic and biharmonic boundary value problems. *Comp. Mech.* **21**, 416-423 (1998).

A multidomain approach of the SBEM in the plate bending analysis

Panzeca T., La Mantia A., Salerno M., Terravecchia S.

Disag, Università di Palermo, Viale delle Scienze, 90128 Palermo, Italy

tpanzeca@tiscali.it, lamantia@stru.diseg.unipa.it, mgsalerno@unipa.it,
terravecchia@diseg.unipa.it

Keywords: plates, Symmetric Boundary Element Method, multidomain approach.

Abstract. The aim of this paper is to apply the multidomain approach of the SBEM to the plate bending analysis. The plate is subdivided into macro-elements connected each other along the interface boundary. Every macro-element is defined by an elastic relation which connects the generalized shear force and moments at the interface to the nodal displacements and rotations of the same boundary and to the loads. This approach allows a considerable reduction of the variables through a condensation process which leaves the interface kinematical unknowns, only.

The assembly process may be obtained through the regularity conditions prescribed at the interface.

Introduction

The multidomain approach in the Symmetric Boundary Element Method (SBEM), introduced by Maier et al. [1], allows the analysis of a continuous solid through the subdivision into zones, each having different physical and geometrical properties. This approach has been applied to the in-plane loaded two-dimensional solids by several researchers, as Gray and Paulino [2], Panzeca et al. [3], Vodička et al. [4]. In the collocation BEM De Paiva and Aliabadi [5,6] have used a subregion technique to the analysis of zoned plates in bending.

The aim of this paper is to apply the multidomain approach of the SBEM to the plate bending analysis. The plate is subdivided into macro-elements connected each other along the interface boundary. The proposed strategy consists in the following steps:

- the subdivision of the plate in macro-elements;
- the specification of the different types of the boundary;
- the analytical computation for every macro-element of the characteristic matrix in which the causes are the distribution of the mechanical and kinematical quantities defined by nodal values, whereas the effects are analogous generalized quantities evaluated along all the boundary sides;
- the use of the previous matrix in order to determine an elastic relation which connects the generalized shear force and moments at the interface to the nodal displacements and rotations of the same boundary and to the loads;
- the assembly of the macro-elements by imposing the strong regularity conditions on the kinematical quantities (equal displacements and rotations at the interface nodes), and the weak ones on the mechanical quantities (generalized equilibrium between the traction and moment distributions along the interface boundaries).

We obtain a displacement formulation in which the algebraic operators are characterized by a stiffness matrix and a load vector, analogously to the FEM.

An innovative aspect of the paper is the use of linear shape functions for the modeling of the mechanical and kinematical quantities and for the weighting of the corresponding generalized ones, differently from that performed by other researches who use shape functions having higher degrees.

The evaluation in closed form of the coefficients is carried out using a technique of decomposition of the causes and of superposition of the effects, analogously to that introduced in the plate bending analysis by Panzeca et al. [7] in the case of quadratic shape functions.

1. The multidomain approach

Let us consider the bending problem for a linearly elastic plate of domain Ω and boundary Γ , distinguished in constrained Γ_1 and free Γ_2 . The plate is subjected to the following external actions:

- body forces \bar{p} normally applied to the middle surface in the domain Ω ;
- displacements and rotations $\bar{\mathbf{u}} = [\bar{u}_n \quad \bar{\varphi}_n \quad 0]^T$ imposed on the constrained boundary Γ_1 ;
- forces and couples $\bar{\mathbf{f}} = [\bar{f}_n \quad \bar{c}_n \quad 0]^T$ given on the free boundary Γ_2 .

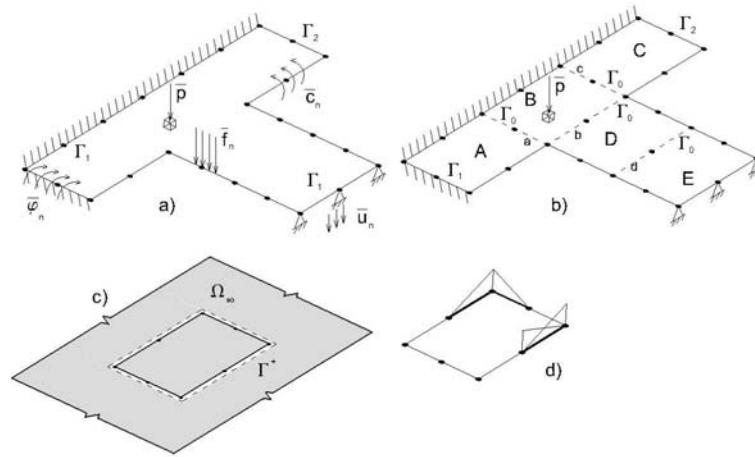


Fig. 1: a) the plate, b) subdivision of the plate in macro-elements A, ..., E, c) macro-element J embedded in the unlimited domain Ω_∞ , d) modeling of the forces and moments and of the displacements and rotations.

In the plate the physical and geometric properties may be different in every zone. We want to obtain by the displacement formulation the elastic response to the known external actions in terms of boundary quantities, defined along the elements, each characterized by the outward normal \mathbf{n} :

- shear forces and couples $\mathbf{f} = [f_n \quad c_n \quad 0]^T$ on Γ_1 ;
- displacement and rotations $\mathbf{u} = [u_n \quad \varphi_n \quad \varphi_{sn}]^T$ on Γ_2 .

In order to analyze the plate we operate an appropriate subdivision of the solid in macro-elements. This subdivision involves the introduction of an interface boundary Γ_0 between contiguous macro-elements.

To study the plate a general strategy is used, based on the introduction of a matrix, called characteristic.

To derive the characteristic matrix no distinction is made between the constraint, free and interface boundaries. It involves that the whole boundary is subjected to a distribution of layered mechanical actions \mathbf{f} and to a distribution of double layered kinematical discontinuities $\Delta \mathbf{u} = -\mathbf{u}$.

Through the use of Somigliana's Identities the kinematical \mathbf{u} and mechanical \mathbf{t} quantities may be computed on the boundary Γ^+ .

By imposing the boundary conditions $\mathbf{u}^+ = \mathbf{0}$ and $\mathbf{t}^+ = \mathbf{0}$ on Γ^+ , we obtain the following equation written in compact form:

$$\mathbf{u}^+ = \mathbf{u}^+ [\mathbf{f}] + \mathbf{u}_{pv}^+ [-\mathbf{u}] - \frac{1}{2} \mathbf{u} + \hat{\mathbf{u}}^+ [\bar{\mathbf{p}}] = \mathbf{0} \quad (1a)$$

$$\mathbf{t}^+ = \mathbf{t}_{pv}^+ [\mathbf{f}] - \frac{1}{2} \mathbf{t} + \mathbf{t}^+ [-\mathbf{u}] + \hat{\mathbf{t}}^+ [\bar{\mathbf{p}}] = \mathbf{0} \quad (1b)$$

where the following positions are valid:

$$\mathbf{u}^+ [\mathbf{f}] = \int_{\Gamma} \mathbf{G}_{uu} \mathbf{f} d\Gamma, \quad \mathbf{u}_{pv}^+ [-\mathbf{u}] = \int_{\Gamma} \mathbf{G}_{ut} (-\mathbf{u}) d\Gamma, \quad \hat{\mathbf{u}}^+ [\bar{\mathbf{p}}] = \int_{\Omega} \mathbf{G}_{uu} \bar{\mathbf{p}} d\Omega \quad (2a-c)$$

$$\mathbf{t}_{pv}^+ [\mathbf{f}] = \int_{\Gamma} \mathbf{G}_{tu} \mathbf{f} d\Gamma, \quad \mathbf{t}^+ [-\mathbf{u}] = \int_{\Gamma} \mathbf{G}_{tt} (-\mathbf{u}) d\Gamma, \quad \hat{\mathbf{t}}^+ [\bar{\mathbf{p}}] = \int_{\Omega} \mathbf{G}_{tu} \bar{\mathbf{p}} d\Omega \quad (2d-f)$$

being \mathbf{G}_{hk} ($h, k = u, t$) the fundamental solutions matrices defined in Panzeca et al. [7].

Let us operate the discretization of the boundary and introduce linear shape functions Ψ_t and Ψ_u to model the layered mechanical and the double layered kinematical quantities:

$$\mathbf{f} = \Psi_t \mathbf{F}, \quad \mathbf{u} = \Psi_u \mathbf{U} \quad (3a,b)$$

where \mathbf{F} and \mathbf{U} are the vectors collecting nodal quantities.

Let us perform the weighting process in accordance with the Galerkin approach in the eqs. (1a,b), so obtaining the following boundary integral equations (for the details see Panzeca et al. [8]):

$$\mathbf{W}^+ = \mathbf{A}_{uu} \mathbf{F} + \mathbf{A}_{ut} (-\mathbf{U}) + \frac{1}{2} \mathbf{C}_{ut} (-\mathbf{U}) + \hat{\mathbf{W}} = \mathbf{0} \quad (4a)$$

$$\mathbf{P}^+ = \mathbf{A}_{tu} \mathbf{F} + \mathbf{A}_{tt} (-\mathbf{U}) - \frac{1}{2} \mathbf{C}_{tu} \mathbf{F} + \hat{\mathbf{P}} = \mathbf{0} \quad (4b)$$

In compact form one has:

$$\mathbf{B} \mathbf{X} + \hat{\mathbf{L}} = \mathbf{0} \quad (5)$$

where the characteristic matrix \mathbf{B} is unsymmetrical and singular.

In the present paper all the coefficients of the matrix \mathbf{B} have been computed in closed form.

Once the matrix \mathbf{B} associated to the j -th macro-element is written, it is possible to derive a reduced form of the algebraic operators, expressed in terms of interface quantities. In order to get this aim, a selection of the rows and columns of the characteristic matrix and its rearrangement is

performed, as consequence of the subdivision into the constrained Γ_1 , free Γ_2 and interface Γ_0 boundaries.

The nodal vectors \mathbf{F} and \mathbf{U} are redefined in the following way:

$$\mathbf{F} = [\bar{\mathbf{F}}_2^T \quad \mathbf{F}_1^T \quad \mathbf{F}_0^T]^T, \quad (-\mathbf{U}) = [-\mathbf{U}_2^T \quad -\bar{\mathbf{U}}_1^T \quad -\mathbf{U}_0^T]^T \quad (6a,b)$$

where a distinction is made among known and unknown nodal quantities and among different boundaries.

In analogous way the vectors of the weighted quantities \mathbf{W}^+ and \mathbf{P}^+ are redefined as follows:

$$\mathbf{W}^+ = [\mathbf{W}_2^{+T} \quad \mathbf{W}_1^{+T} \quad \mathbf{W}_0^{+T}]^T, \quad \mathbf{P}^+ = [\mathbf{P}_2^{+T} \quad \mathbf{P}_1^{+T} \quad \mathbf{P}_0^{+T}]^T \quad (7a,b)$$

In order to obtain the algebraic operators for the solution of the problem, we introduce some conditions, written in weighted form on the boundary elements:

- the generalized Dirichlet and Neumann conditions on the Γ_1^+ and Γ_2^+ boundaries, respectively

$$\mathbf{W}_1^+ = \mathbf{0} \text{ on } \Gamma_1^+, \quad \mathbf{P}_2^+ = \mathbf{0} \text{ on } \Gamma_2^+ \quad (8a,b)$$

- the generalized kinematical condition written at the interface boundary Γ_0^+

$$\mathbf{W}_0^+ = \mathbf{0} \text{ on } \Gamma_0^+. \quad (8c)$$

Besides the vector \mathbf{P}_0 collecting the tractions weighted along the boundary Γ_0 and associated to the interface nodes may be written depending on the vectors of the nodal quantities, known and unknown. This rearrangement allows to derive the following equations, being the boundary and domain quantities inside the load vector:

$$\begin{bmatrix} \mathbf{W}_1^+ = 0 \\ \mathbf{W}_0^+ = 0 \\ \mathbf{P}_2^+ = 0 \\ \mathbf{P}_0 \end{bmatrix} = \begin{bmatrix} \mathbf{A}_{u1,u1} & \mathbf{A}_{u1,u0} & \mathbf{A}_{u1,f2} & \mathbf{A}_{u1,f0} \\ \mathbf{A}_{u0,u1} & \mathbf{A}_{u0,u0} & \mathbf{A}_{u0,f2} & \bar{\mathbf{A}}_{u0,f0} \\ \mathbf{A}_{f2,u1} & \mathbf{A}_{f2,u0} & \mathbf{A}_{f2,f2} & \mathbf{A}_{f2,f0} \\ \mathbf{A}_{f0,u1} & \mathbf{A}_{f0,u0} & \mathbf{A}_{f0,f2} & \mathbf{A}_{f0,f0} \end{bmatrix} \begin{bmatrix} \mathbf{F}_1 \\ \mathbf{F}_0 \\ -\mathbf{U}_2 \\ -\mathbf{U}_0 \end{bmatrix} + \begin{bmatrix} \hat{\mathbf{W}}_1^+ \\ \hat{\mathbf{W}}_0^+ \\ \hat{\mathbf{P}}_2^+ \\ \hat{\mathbf{P}}_0 \end{bmatrix} \quad (9)$$

The eq.(9) may be written in a more compact form:

$$\mathbf{0} = \mathbf{H} \mathbf{X} + \mathbf{H}_0 (-\mathbf{U}_0) + \hat{\mathbf{L}} \quad (10)$$

$$\mathbf{P}_0 = \mathbf{H}_0^T \mathbf{X} + \mathbf{H}_{00} (-\mathbf{U}_0) + \hat{\mathbf{L}}_0 \quad (11)$$

by using the following positions

$$\mathbf{X} = [\mathbf{F}_1^T \quad \mathbf{F}_0^T \quad -\mathbf{U}_2^T]^T \quad (12a)$$

$$\mathbf{H} = \begin{bmatrix} \mathbf{A}_{u1,u1} & \mathbf{A}_{u1,u0} & \mathbf{A}_{u1,f2} \\ \mathbf{A}_{u0,u1} & \mathbf{A}_{u0,u0} & \mathbf{A}_{u0,f2} \\ \mathbf{A}_{f2,u1} & \mathbf{A}_{f2,u0} & \mathbf{A}_{f2,f2} \end{bmatrix}, \quad \mathbf{H}_0 = \begin{bmatrix} \mathbf{A}_{u1,f0} \\ \bar{\mathbf{A}}_{u0,f0} \\ \mathbf{A}_{f2,f0} \end{bmatrix}, \quad \mathbf{H}_{00} = [\mathbf{A}_{f0,f0}], \quad \hat{\mathbf{L}} = \begin{bmatrix} \hat{\mathbf{W}}_1^+ \\ \hat{\mathbf{W}}_0^+ \\ \hat{\mathbf{P}}_2^+ \end{bmatrix}, \quad \hat{\mathbf{L}}_0 = [\hat{\mathbf{P}}_0]. \quad (12b-f)$$

The vector \mathbf{U}_0 collects the kinematical quantities of the Γ_0 boundary nodes.

By performing a variables condensation through the replacement of the \mathbf{X} vector, obtained by eq.(10) into eq.(11), we get the following generalized stresses - nodal displacements equation:

$$\mathbf{P}_0 = \mathbf{D}_{00} \mathbf{U}_0 + \hat{\mathbf{P}}_0 \tag{13}$$

where it has been set:

$$\mathbf{D}_{00} = \mathbf{H}_0^T \mathbf{H}^{(-1)} \mathbf{H}_0 - \mathbf{H}_{00}, \quad \hat{\mathbf{P}}_0 = \hat{\mathbf{L}}_0 - \mathbf{H}_0^T \mathbf{H}^{(-1)} \hat{\mathbf{L}}. \tag{14a,b}$$

Eq.(13) is referred to j-th macro-element and relates the generalized mechanical quantities \mathbf{P}_0 associated to the nodes of Γ_0 to the kinematical quantities \mathbf{U}_0 of the same boundary nodes and to the load vector $\hat{\mathbf{P}}_0$. The algebraic operator \mathbf{D}_{00} is the stiffness matrix of the macro-element and it is symmetric and singular.

Hereafter the subscript 00 is suppressed and the subscript J is introduced to denote the j-th macro-element.

2. The assembly process.

The stiffness matrix \mathbf{D}_j , associated to the interface nodes of the plate, is employed for the analysis of the plates. We consider J macro-elements, with $J = A, B, \dots, N$.

We introduce a global relation connecting the weighted mechanical quantities to the kinematical ones at the interface nodes, i.e:

$$\mathbf{P} = \mathbf{D} \mathbf{U} + \hat{\mathbf{P}} \tag{15}$$

with

$$\mathbf{P} = [\mathbf{P}_A^T \quad \mathbf{P}_B^T \quad \dots \quad \mathbf{P}_N^T]^T, \quad \hat{\mathbf{P}} = [\hat{\mathbf{P}}_A^T \quad \hat{\mathbf{P}}_B^T \quad \dots \quad \hat{\mathbf{P}}_N^T]^T, \tag{16a-d}$$

$$\mathbf{U} = [\mathbf{U}_A^T \quad \mathbf{U}_B^T \quad \dots \quad \mathbf{U}_N^T]^T, \quad \mathbf{D} = \text{diag}[\mathbf{D}_A \quad \mathbf{D}_B \quad \dots \quad \mathbf{D}_N]$$

where the vectors \mathbf{P} and $\hat{\mathbf{P}}$ collect the generalized interface mechanical quantities (tractions and moments) and the load terms of all the macro-elements, whereas the vector \mathbf{U} collects the corresponding nodal kinematical quantities (displacements and rotations) at the same plate interfaces.

Let us introduce the displacements vector of the interface nodes, common to the contiguous macro-elements, the subscript small letter characterizing the interface side:

$$\mathbf{u} = [\mathbf{u}_a^T \quad \mathbf{u}_b^T \quad \dots \quad \mathbf{u}_m^T]^T \tag{17}$$

The regularity condition of the kinematical quantities have to be imposed, and as a consequence

$$\mathbf{U} = \mathbf{Z} \mathbf{u} \tag{18}$$

where \mathbf{Z} is an appropriate compatibility matrix.

The equilibrium condition of the weighted mechanical quantities takes on the form

$$\mathbf{Z}^T \mathbf{P} = \mathbf{0}. \tag{19}$$

The use of the eqs.(15), (18) and (19) leads to the following solving equations:

$$\mathbf{K} \mathbf{u} = \hat{\mathbf{f}}. \quad (20)$$

where one has set

$$\mathbf{K} = \mathbf{Z}^T \mathbf{D} \mathbf{Z}, \quad \hat{\mathbf{f}} = \mathbf{Z}^T \mathbf{P}. \quad (21a,b)$$

The latter matrix \mathbf{K} is symmetric and definite.

Likewise to the finite element method, the solving equations are obtained in terms of the nodal displacements. The remaining boundary quantities of the plates, regarding the reactive forces and moments \mathbf{F}_1 at the nodes of the constrained boundary Γ_1 , the kinematical quantities \mathbf{U}_2 at the free nodes of Γ_2 and the mechanical quantities \mathbf{F}_0 at the nodes of boundary Γ_0 are obtainable by using eq.(10) for every macro-element.

3. Application.

The proposed multidomain approach of SBEM has been checked by analyzing a two-zoned plate studied by De Paiva and Aliabadi in [5,6] in the collocation context. The square plate of Fig.2 is subdivided in two zones of different stiffness having a ratio $D_B/D_A = 3.375$. We have assumed the following properties:

- material elastic constants: Young's modulus $E_A = 72900$ and $E_B = 100000$, Poisson's ratio $\nu = 0.3$;
- thicknesses: $h_A = 0.1$ and $h_B = 0.135$.

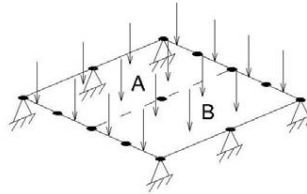


Fig. 2: A two-zoned plate.

The characteristic matrix \mathbf{B} has been computed with the purpose to consider several constraint conditions. In this case we have studied a plate supported at two opposite sides and free in the other two, subjected to a uniformly distributed load acting normally on the middle surface of the plate.

The coefficients of the load vector have been calculated in closed form by means of a double integration, the first regarding the cause through domain integrals, and the other one regarding the effect through boundary integrals.

The boundary of every macro-element is discretized by 8 elements in which the modelling of the quantities and the weighting of the response is supposed linear. In [5,6] the interface is discretized by 10 elements, whereas in the present case only in 2 elements.

At first the macro-elements are separately analyzed and the related stiffness matrices and the load vectors are computed. Then, through the assembly process, the nodal displacements at the interface are obtained and they are shown in Fig.3 by black dots and by related numerical values.

The function of the vertical displacement along the interface, determined by using the Somigliana's Identities, is represented in Fig.3 through a dotted line and it is compared with the

piece-wise function in [5], obtained by collocation BE method, and with a FE analysis performed by the same authors. Although the discretization of the proposed approach is very coarse, we observe a good agreement of the results.

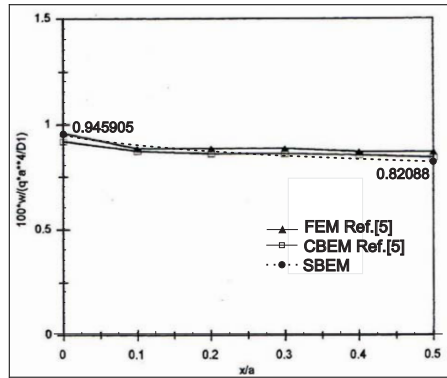


Fig. 3: Functions of the displacements at the interface.

Once the displacements at the interface nodes are computed, the mechanical quantities F_0 are obtainable by using eq.(10) for every macro-element. Particularly the moments m_y are shown in Fig.4, indicating by black dots and related numerical values the results obtained.

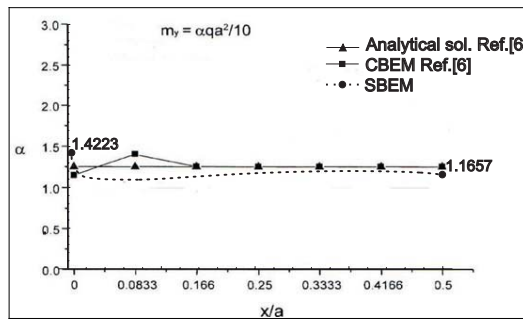


Fig. 4: Functions of moments m_y at the interface.

The function of the moments m_y along the interface, determined by using the Somigliana's Identities, is represented in Fig. 4 through a dotted line and it is compared with the piece-wise function in [6], obtained by collocation BE method, and with the analytical solution shown in the same reference.

Also in this case a good agreement with the collocation BE method may be observed.

References

- [1] Maier, G., Diligenti, M., Carini, A., 1991. A variational approach to boundary element elastodynamics analysis and extension to multidomain problems. *Comp. Meth. Appl. Mech. Engng.* 92,193-213.
- [2] Gray, L.Y., Paulino, G.R., 1997. Symmetric Galerkin boundary integral formulation for interface and multi-zone problems. *Int. J. Num. Meth. Engng.* 40, 3085-3101.
- [3] Panzeca, T., Salerno, M., 2000. Macro-elements in the mixed boundary value problems. *Comp. Mech.* 26, 437-446.
- [4] Vodička, R., Mantič, V., París, F., 2007. Symmetric Variational Formulation of BIE for Domain Decomposition Problems in Elasticity – An SGBEM approach for Nonconforming Discretizations of curved Interfaces. *CMES* 4, 31-50.
- [5] De Paiva, J.B, Aliabadi M.H., 2000. Boundary element analysis of zoned plates in bending. *Comp. Mech.* 25, 560-566.
- [6] De Paiva, J.B, Aliabadi M.H., 2004. Bending moments at interfaces of thin zoned plates with discrete thickness by the boundary element method. *Engng. Anal. Bound. Elem.* 28, 747-751
- [7] Panzeca, T., Milana, V., Salerno, M., 2009. A symmetric Galerkin BEM for plate bending analysis. *Eur. J. Mech. A/Solids*, 28, 1, 62-74.
- [8] Panzeca T., Cucco F., Salerno M., Characteristic matrix in the bending plate analysis by SBEM, BeTeq IX. International Conference on Boundary Element Techniques IX, Seville July 9-11, 2008, Spain, in: *Advances in Boundary Element Techniques IX*, pp.347-354, Abascal R. and Aliabadi M.H. (Eds.), Eastleigh, United Kingdom, 2008.

Elastoplastic analysis by the Multidomain Symmetric Boundary Element Method

Panzeca T.^{1,a}, Cucco F.², Parlavecchio E.^{1,b}, Zito L.^{1,c}

¹Disag, Viale delle Scienze, 90128 Palermo, Italy,

^atpanzeca@tiscali.it, ^bparlavecchio@diseg.unipa.it, ^clzito@diseg.unipa.it

²Università Kore di Enna, Cittadella universitaria, 94100 Enna, Italy, filippo.cucco@unikore.it

Keywords: Elastoplasticity, Symmetric Boundary Element Method, Multidomain Approach, Singular Domain Integral.

Abstract. The paper shows a strategy utilizing step by step algorithms for the study of elastoplastic problem. Such a formulation uses a multi-domain analysis, in the ambit of Symmetric Boundary Element Method (SBEM), for the definition of elastic behaviour and a path-following technique, based on Extremal Path theory, for the definition of nonlinear one. This strategy has been implemented inside the Karnak.sGbem code developed by some of the present authors and a numerical test is presented, showing the computational advantages of the method.

Introduction

The SBEM has been applied to elastoplastic analysis of bodies subdivided in substructures or bem elements (bem-e). This methodology has been developed in according to the following strategies:

1. the use of displacements method, in the ambit of multi-domain SBEM analysis, for the evaluation of the elastic predictor,
2. the extremal paths theory for the evaluation of inelastic quantities that characterize the plastic behaviour of each bem-e,
3. the transformation of the domain inelastic integrals of the bem-e into corresponding boundary ones.

The elastic analysis is performed by using the SBEM displacement approach [1] that shows the advantage to obtain a solving system having unknown nodal kinematical quantities on the interface boundaries only, computationally more advantageous than other formulations which use either interface mixed variables or all kinematical nodal variables.

The elastoplastic solution utilizes a strain driven strategy characterized by the evaluation of the elastic predictor by using the analysis method previously indicated in function of the initial conditions and of the load increment. The predictor phase is followed by the use of a return mapping algorithm [2], which is defined by using the extremal paths theory developed by Ponter and Martin [3].

The plastic strains, evaluated by the strategy previously indicated, are considered as constant imposed inelastic actions introduced into the bem-e in a step by step analysis. Their presence involves domain integrals having singular kernels. These integrals are considered as Cauchy Principal Values to which the Bui free term is associated. Therefore the regularization techniques may be applied at the aim to cut off the strong singularity, then the Radial Integral Method (RIM) [4] is used to transform the domain integrals into boundary ones of each bem-e.

1. Multidomain analysis by displacement approach

For every bem-e we want to determine an elasticity equation connecting the quantities associated to the interface zone by using a SBEM multi-domain approach.

This strategy foresees the study of each bem-e embedded in a unlimited domain having the same physical properties and the same thickness of the examining bem-e. It is necessary to distinguish the boundary as Γ of Ω or as Γ^+ of the complementary domain $\Omega_\infty \setminus \Omega$. As a consequence the

boundary quantities take on a different meaning: the forces acting on the boundary must be interpreted as layered force distribution, whereas the displacements must be thought as a double layered displacement distribution.

Let us impose the classical Dirichlet and Neumann conditions on the boundary of the bem-e, i.e.:

$$\mathbf{u}_1 = \bar{\mathbf{u}}_1 \text{ on } \Gamma_1, \quad \mathbf{t}_2 = \bar{\mathbf{f}}_2 \text{ on } \Gamma_2 \quad (1a,b)$$

When we introduce the Somigliana Identities (S.I.) of the displacements and of the tractions in the previous eqs.(1a,b) and evaluate the displacement \mathbf{u}_0 and traction \mathbf{t}_0 vectors on Γ_0 , i.e. in the interface zone, the following boundary integral equations in compact form may be obtained:

$$\begin{aligned} \mathbf{u}_1 &= \mathbf{u}_1[\mathbf{f}_1, -\mathbf{u}_2, \mathbf{f}_0, -\mathbf{u}_0] + \mathbf{u}_1[\bar{\mathbf{f}}_2, -\bar{\mathbf{u}}_1] + \mathbf{u}_1[\bar{\boldsymbol{\varepsilon}}^P] && \text{on } \Gamma_1 \\ \mathbf{t}_2 &= \mathbf{t}_2[\mathbf{f}_1, -\mathbf{u}_2, \mathbf{f}_0, -\mathbf{u}_0] + \mathbf{t}_2[\bar{\mathbf{f}}_2, -\bar{\mathbf{u}}_1] + \mathbf{t}_2[\bar{\boldsymbol{\varepsilon}}^P] && \text{on } \Gamma_2 \\ \mathbf{u}_0 &= \mathbf{u}_0[\mathbf{f}_1, -\mathbf{u}_2, \mathbf{f}_0, -\mathbf{u}_0] + \mathbf{u}_0[\bar{\mathbf{f}}_2, -\bar{\mathbf{u}}_1] + \mathbf{u}_0[\bar{\boldsymbol{\varepsilon}}^P] && \text{on } \Gamma_0 \\ \mathbf{t}_0 &= \mathbf{t}_0[\mathbf{f}_1, -\mathbf{u}_2, \mathbf{f}_0, -\mathbf{u}_0] + \mathbf{t}_0[\bar{\mathbf{f}}_2, -\bar{\mathbf{u}}_1] + \mathbf{t}_0[\bar{\boldsymbol{\varepsilon}}^P] && \text{on } \Gamma_0 \end{aligned} \quad (2a-d)$$

where $\bar{\boldsymbol{\varepsilon}}^P$ is the plastic strains vector which evaluation strategy is defined in the next section.

In addition when the solution is reached, the traction \mathbf{t}_0 , obtained by eq.(2d) and defined in the equilibrium equation $\mathbf{f}_0 = -\mathbf{t}_0^+ + \mathbf{t}_0$ on the boundary Γ_0 , identifies oneself with the layered force \mathbf{f}_0 because on Γ_0^+ the traction must be $\mathbf{t}_0^+ = 0$.

Let us modify the eqs.(2a-c) by grouping together on the left side all the terms and leaving unchanged the eq.(2d). We obtain an integral equation system where the eqs.(2a-c) may be interpreted as the response of the body on the boundaries Γ_1^+ , Γ_2^+ , Γ_0^+ , respectively, whereas eq.(2d) maintains the same meaning of traction valued on the actual interface boundary Γ_0 :

$$\begin{aligned} \mathbf{u}_1^+[\mathbf{f}_1, -\mathbf{u}_2, \mathbf{f}_0, -\mathbf{u}_0] + \mathbf{u}_1^+[\bar{\mathbf{f}}_2, -\bar{\mathbf{u}}_1] + \mathbf{u}_1^+[\bar{\boldsymbol{\varepsilon}}^P] &= \mathbf{0} && \text{on } \Gamma_1^+ \\ \mathbf{t}_2^+[\mathbf{f}_1, -\mathbf{u}_2, \mathbf{f}_0, -\mathbf{u}_0] + \mathbf{t}_2^+[\bar{\mathbf{f}}_2, -\bar{\mathbf{u}}_1] + \mathbf{t}_2^+[\bar{\boldsymbol{\varepsilon}}^P] &= \mathbf{0} && \text{on } \Gamma_2^+ \\ \mathbf{u}_0^+[\mathbf{f}_1, -\mathbf{u}_2, \mathbf{f}_0, -\mathbf{u}_0] + \mathbf{u}_0^+[\bar{\mathbf{f}}_2, -\bar{\mathbf{u}}_1] + \mathbf{u}_0^+[\bar{\boldsymbol{\varepsilon}}^P] &= \mathbf{0} && \text{on } \Gamma_0^+ \\ \mathbf{t}_0 &= \mathbf{t}_0[\mathbf{f}_1, -\mathbf{u}_2, \mathbf{f}_0, -\mathbf{u}_0] + \mathbf{t}_0[\bar{\mathbf{f}}_2, -\bar{\mathbf{u}}_1] + \mathbf{t}_0[\bar{\boldsymbol{\varepsilon}}^P] && \text{on } \Gamma_0 \end{aligned} \quad (3a-d)$$

Let us introduce the boundary discretization into the boundary elements by making the following modelling for the variables to be computed:

$$\mathbf{f}_1 = \boldsymbol{\Psi}_f \mathbf{F}_1, \quad \mathbf{u}_2 = \boldsymbol{\Psi}_u \mathbf{U}_2, \quad \mathbf{f}_0 = \boldsymbol{\Psi}_f \mathbf{F}_0, \quad \mathbf{u}_0 = \boldsymbol{\Psi}_u \mathbf{U}_0 \quad (4a-d)$$

where the capital letters define the values of the reactions (\mathbf{F}_1 on Γ_1 and \mathbf{F}_0 on Γ_0) and of the displacements (\mathbf{U}_2 on Γ_2 and \mathbf{U}_0 on Γ_0) in the nodes of the boundary elements.

Let us perform now the weighting of all the coefficients of the eqs.(3a-d), so it is possible to obtain the following block system:

$$\begin{array}{c|ccc|ccc|c|c} \mathbf{W}_1^+ = \mathbf{0} & \mathbf{A}_{u1,u1} & \mathbf{A}_{u1,f2} & \mathbf{A}_{u1,u0} & \mathbf{A}_{u1,f0} & \mathbf{F}_1 & \hat{\mathbf{W}}_1^+ \\ \mathbf{P}_2^+ = \mathbf{0} & \mathbf{A}_{f2,u1} & \mathbf{A}_{f2,f2} & \mathbf{A}_{f2,u0} & \mathbf{A}_{f2,f0} & -\mathbf{U}_2 & \hat{\mathbf{P}}_2^+ \\ \mathbf{W}_0^+ = \mathbf{0} & \mathbf{A}_{u0,u1} & \mathbf{A}_{u0,f2} & \mathbf{A}_{u0,u0} & \mathbf{A}_{u0,f0} & \mathbf{F}_0 & \hat{\mathbf{W}}_0^+ \\ \mathbf{P}_0 & \mathbf{A}_{f0,u1} & \mathbf{A}_{f0,f2} & \mathbf{A}_{f0,u0} & \mathbf{A}_{f0,f0} & -\mathbf{U}_0 & \hat{\mathbf{L}}_0 \end{array} = \quad (5)$$

In the latter equation the conditions $\mathbf{W}_1^+ = \mathbf{0}$ and $\mathbf{P}_2^+ = \mathbf{0}$ have to be considered as the classical Dirichlet and Neumann conditions of the continuum, written on the boundary elements Γ^+ of the complementary domain, in terms of generalized (or weighted) quantities. The other two expressions regard quantities of the interface zone: in particular the condition $\mathbf{W}_0^+ = \mathbf{0}$ represents the generalized displacement, null on the boundary Γ_0^+ , whereas the term \mathbf{P}_0 collects the values of the

generalized tractions defined on the boundary elements of Γ_0 . For all the coefficients in eq.(5) see Panzeca et al. [1,4].

The eq.(5) may be expressed, with obvious symbol meaning, in the following compact form:

$$\mathbf{0} = \mathbf{A}\mathbf{X} + \mathbf{A}_0(-\mathbf{U}_0) + \hat{\mathbf{L}} \tag{6a}$$

$$\mathbf{P}_0 = \tilde{\mathbf{A}}_0\mathbf{X} + \mathbf{A}_{00}(-\mathbf{U}_0) + \hat{\mathbf{L}}_0 \tag{6b}$$

where the vector \mathbf{X} collects \mathbf{F}_1 , $(-\mathbf{U}_2)$ and \mathbf{F}_0 , whereas $(-\mathbf{U}_0)$ collects the displacements of the nodes in the interface zone, changed in sign. The vector \mathbf{P}_0 represents the generalized traction defined in the boundary elements of the same interface zone, obtained as a response to all the known and unknown actions, regarding boundary and volume quantities.

By performing a variable condensation through the replacement of the \mathbf{X} vector extracted from eq.(6a) into eq.(6b), we obtain:

$$\mathbf{P}_0 = \mathbf{D}_{00}\mathbf{U}_0 + \hat{\mathbf{P}}_0 \tag{7}$$

where the following positions have been made:

$$\mathbf{D}_{00} = \tilde{\mathbf{A}}_0\mathbf{A}^{-1}\mathbf{A}_0 - \mathbf{A}_{00}, \quad \hat{\mathbf{P}}_0 = \hat{\mathbf{L}}_0 - \tilde{\mathbf{A}}_0\mathbf{A}^{-1}\mathbf{L} \tag{8a,b}$$

Eq.(7) is called characteristic equation of the bem-e. It relates the generalized tractions \mathbf{P}_0 to the displacements \mathbf{U}_0 of the nodes of the interface boundary and to the load term $\hat{\mathbf{P}}_0$, this latter being the generalized traction vector, as the effect evaluated on the same boundary elements and caused by the external actions. Moreover, \mathbf{D}_{00} is the stiffness matrix associated to the bem-e.

The eq.(7), valid for each bem-e, is formally identical to that written in the ambit of the Finite Element Method, but it shows the advantage that the involved variables refer to quantities related at the interface zone.

For every bem-e, equations like eq.(7) may be written:

$$\mathbf{P}_0^i = \mathbf{D}_{00}^i \mathbf{U}_0^i + \hat{\mathbf{P}}_0^i \quad \text{for } i = 1, 2, \dots, n \quad \text{bem} - e \tag{9}$$

Now, imposing the regularity conditions for the nodal displacements and for the generalized tractions on the boundaries belonging to the i -th bem-e simultaneously, we obtain the elastic solution in terms of the displacements \mathbf{U}_0 through the following solving equation:

$$\mathbf{K}_{00} \mathbf{U}_0 + \hat{\mathbf{f}}_0 = \mathbf{0} \tag{10}$$

The remaining nodal quantities, regarding the reactive forces \mathbf{F}_1 on Γ_1 , the displacements \mathbf{U}_2 on Γ_2 and the forces \mathbf{F}_0 on Γ_0 , all variables collected in the vectors \mathbf{X}^i , are obtainable by using equations like eq.(6a), written for each bem-e.

Now is possible to evaluate the elastic predictor $\boldsymbol{\sigma}^*$ on the Gauss point of each bem-e by using the following stress S.I.:

$$\boldsymbol{\sigma}^* = \boldsymbol{\sigma}[\mathbf{F}_1, -\mathbf{U}_2, \mathbf{F}_0, -\mathbf{U}_0] + \boldsymbol{\sigma}[\bar{\mathbf{F}}_1, -\bar{\mathbf{U}}_1] + \boldsymbol{\sigma}[\bar{\boldsymbol{\varepsilon}}^P] \quad \text{on } \Omega_i \tag{11}$$

where $\bar{\boldsymbol{\varepsilon}}^P$ is the plastic strain vector, imposed inside each bem-e, that will be defined in the following section.

2. A return mapping algorithm for elasto-plasticity

The elastoplastic solution utilizes a strain driven strategy characterized by two phases:

- the evaluation of the elastic predictor by using the analysis method previously shown;
- the evaluation of the corrector by using a return mapping algorithm.

Because the elastoplastic response is path-dependent, the solution is not easily obtainable if not through a space and time discretization.

Let's start from the known conditions in terms of stress $\boldsymbol{\sigma}_n$, total $\boldsymbol{\varepsilon}_n$ and plastic $\boldsymbol{\varepsilon}_n^p$ strains related at an instant t_n . The unknown response in terms of $\boldsymbol{\sigma}_{n+1}$, $\boldsymbol{\varepsilon}_{n+1}$, $\boldsymbol{\varepsilon}_{n+1}^p$ related at an instant t_{n+1} has to be evaluated.

The integration of $\dot{\boldsymbol{\varepsilon}}^p$ in the interval $[t_n, t_{n+1}]$, leads to following relation:

$$\boldsymbol{\varepsilon}_{n+1}^p = \boldsymbol{\varepsilon}_n^p + \int_n^{n+1} \dot{\gamma} \frac{\partial \mathbf{F}}{\partial \boldsymbol{\sigma}} dt \quad (12)$$

from which, integrating by parts and assuming the condition $\gamma [t_n] = 0$, it follows:

$$\boldsymbol{\varepsilon}_{n+1}^p = \boldsymbol{\varepsilon}_n^p + \gamma_{n+1} \left. \frac{\partial \mathbf{F}}{\partial \boldsymbol{\sigma}} \right|_{n+1} - \int_n^{n+1} \gamma \frac{d}{dt} \frac{\partial \mathbf{F}}{\partial \boldsymbol{\sigma}} dt \quad (13)$$

Let's assume that the loading history be defined by an extremal path, according to the theory proposed by Ponter and Martin [2,3]. The approach is based on the exact integration of the constitutive law $\boldsymbol{\sigma} = \mathbf{E}(\boldsymbol{\varepsilon} - \boldsymbol{\varepsilon}^p)$ either along a particular stress path which maximizes the complementary work or along a particular strain path which minimizes the deformation work. Therefore the extremal paths are elastic ones connecting, in the stress space, the starting point $\boldsymbol{\sigma}_n$ and the final point $\boldsymbol{\sigma}_{n+1}$, so assuming that the plastic process has to take place in the final point. Thus eq.(13) takes the form:

$$\boldsymbol{\varepsilon}_{n+1}^p = \boldsymbol{\varepsilon}_n^p + \gamma_{n+1} \left. \frac{\partial \mathbf{F}}{\partial \boldsymbol{\sigma}} \right|_{n+1} \quad (14)$$

So, under extremal path hypothesis the plastic response is path-independent.

The elastic predictor $\boldsymbol{\sigma}_{n+1}^*$ is function of the initial conditions $\boldsymbol{\sigma}_n$ and the load increment, i.e.:

$$\boldsymbol{\sigma}_{n+1}^* = \boldsymbol{\sigma}_n + \mathbf{E} \Delta \boldsymbol{\varepsilon} [\Delta \mathbf{u}] \quad (15)$$

Then, if $F[\boldsymbol{\sigma}_{n+1}^*] > 0$, a return mapping algorithm is required. In the present approach such an algorithm utilizes eq.(14) and is obtained by solving the following nonlinear equations system having the three stress components $\boldsymbol{\sigma}_{n+1}$ and the plastic multiplier γ_{n+1} as unknown terms [2]:

$$\begin{cases} \boldsymbol{\sigma}_{n+1} - \boldsymbol{\sigma}_{n+1}^* + \gamma_{n+1} \mathbf{E} \left. \frac{\partial \mathbf{F}}{\partial \boldsymbol{\sigma}} \right|_{n+1} = \mathbf{0} \\ F[\boldsymbol{\sigma}_{n+1}] = 0 \end{cases} \quad (16)$$

In particular, with referring to the case of 2D continuous solid and in the hypothesis of plane strain condition, we utilize the elastic-perfectly plastic von Mises law:

$$F[\boldsymbol{\sigma}_{n+1}] = \frac{1}{2} \boldsymbol{\sigma}_{n+1}^T \mathbf{P} \boldsymbol{\sigma}_{n+1} - \sigma_y^2 \quad \text{with} \quad \mathbf{P} = \begin{bmatrix} 2 & -1 & 0 \\ -1 & 2 & 0 \\ 0 & 0 & 6 \end{bmatrix}. \quad (17)$$

As a consequence the eq.(16) takes the form:

$$\begin{cases} \boldsymbol{\sigma}_{n+1} - \boldsymbol{\sigma}_{n+1}^* + \gamma_{n+1} \mathbf{E} \mathbf{P} \boldsymbol{\sigma}_{n+1} = \mathbf{0} \\ \frac{1}{2} \boldsymbol{\sigma}_{n+1}^T \mathbf{P} \boldsymbol{\sigma}_{n+1} - \sigma_y^2 = 0 \end{cases} \quad (18)$$

Therefore the approximate solution of this nonlinear problem is obtained applying the standard Newton-Raphson procedure.

Let us introduce the set of the unknowns $\mathbf{x} = [\boldsymbol{\sigma}_{n+1}^T \quad \gamma_{n+1}]^T$ and approximate eq.(18) as follows:

$$\begin{cases} \boldsymbol{\sigma}_{n+1}^j - \boldsymbol{\sigma}_{n+1}^* + \gamma_{n+1}^j \mathbf{E} \mathbf{P} \boldsymbol{\sigma}_{n+1}^j + (\mathbf{I} + \gamma_{n+1}^j \mathbf{E} \mathbf{P})(\boldsymbol{\sigma}_{n+1}^{j+1} - \boldsymbol{\sigma}_{n+1}^j) + (\mathbf{E} \mathbf{P} \boldsymbol{\sigma}_{n+1}^j)(\gamma_{n+1}^{j+1} - \gamma_{n+1}^j) = \mathbf{0} \\ (\frac{1}{2} \boldsymbol{\sigma}_{n+1}^j)^T \mathbf{P} \boldsymbol{\sigma}_{n+1}^j - \sigma_y^2 + (\mathbf{P} \boldsymbol{\sigma}_{n+1}^j)(\boldsymbol{\sigma}_{n+1}^{j+1} - \boldsymbol{\sigma}_{n+1}^j) = 0 \end{cases} \quad \text{with } j = 1, 2, \dots, \text{tol} \quad (19)$$

The latter, expressed by matrix form,

$$\left| \begin{array}{c|c} \mathbf{I} + \gamma_{n+1}^j \mathbf{E} \mathbf{P} & \mathbf{E} \mathbf{P} \boldsymbol{\sigma}_{n+1}^j \\ \hline \mathbf{P} \boldsymbol{\sigma}_{n+1}^j & 0 \end{array} \right| \left| \begin{array}{c} \boldsymbol{\sigma}_{n+1}^{j+1} - \boldsymbol{\sigma}_{n+1}^j \\ \gamma_{n+1}^{j+1} - \gamma_{n+1}^j \end{array} \right| = \left| \begin{array}{c} -(\boldsymbol{\sigma}_{n+1}^j - \boldsymbol{\sigma}_{n+1}^* + \gamma_{n+1}^j \mathbf{E} \mathbf{P} \boldsymbol{\sigma}_{n+1}^j) \\ -(\frac{1}{2} \boldsymbol{\sigma}_{n+1}^j)^T \mathbf{P} \boldsymbol{\sigma}_{n+1}^j + \sigma_y^2 \end{array} \right| \quad (20)$$

leads to the following solution:

$$\left| \begin{array}{c} \boldsymbol{\sigma}_{n+1}^{j+1} \\ \gamma_{n+1}^{j+1} \end{array} \right| = \left| \begin{array}{c} \boldsymbol{\sigma}_{n+1}^j \\ \gamma_{n+1}^j \end{array} \right| - \left| \begin{array}{c|c} \mathbf{I} + \gamma_{n+1}^j \mathbf{E} \mathbf{P} & \mathbf{E} \mathbf{P} \boldsymbol{\sigma}_{n+1}^j \\ \hline \mathbf{P} \boldsymbol{\sigma}_{n+1}^j & 0 \end{array} \right|^{-1} \left| \begin{array}{c} \boldsymbol{\sigma}_{n+1}^j - \boldsymbol{\sigma}_{n+1}^* + \gamma_{n+1}^j \mathbf{E} \mathbf{P} \boldsymbol{\sigma}_{n+1}^j \\ (\frac{1}{2} \boldsymbol{\sigma}_{n+1}^j)^T \mathbf{P} \boldsymbol{\sigma}_{n+1}^j + \sigma_y^2 \end{array} \right| \quad (21)$$

that written in compact form becomes:

$$\mathbf{x}^{j+1} = \mathbf{x}^j - \mathbf{J}(\mathbf{x}^j)^{-1} \mathbf{f}(\mathbf{x}^j) \quad (22)$$

In the latter equation, the Jacobian matrix \mathbf{J} contains the derivatives of the functions defined in eq.(18), \mathbf{x}^{j+1} is the vector of the unknowns, \mathbf{x}^j and $\mathbf{f}(\mathbf{x}^j)$ are the known vectors evaluated in the j -th step [2]. Eq.(22) permits to evaluate the plastic strain vector $\bar{\boldsymbol{\epsilon}}^p$ given in eq.(14). Their presence in eqs.(3) involves domain integrals having singular kernels to be studied appropriately.

3. Computational aspects for plastic domain actions

Within the elasto-plasticity field treated by SBEM [4] some difficulties regard the removal of the strong singularities arising in the kernels of the domain integrals. It happens because the differential operator necessary to obtain the stress is applied to a singular displacements field.

The present approach acts in the displacements field, at first substituting the domain integrals by boundary ones and successively applying the differential operator to a regular field in order to obtain the stress field.

The starting point of the elastic problem is the S.I. of the displacements. If we ignore the mass forces, this latter expression takes on the following form:

$$\mathbf{u}[\mathbf{f}, -\mathbf{u}, \bar{\boldsymbol{\epsilon}}^p] = \int_{\Gamma} \mathbf{G}_{uu} \mathbf{f} d\Gamma + \int_{\Gamma} \mathbf{G}_{ut} (-\mathbf{u}) d\Gamma + \int_{\Omega} \mathbf{G}_{u\sigma} \bar{\boldsymbol{\epsilon}}^p d\Omega \quad (23)$$

The displacements are caused by mechanical \mathbf{f} and kinematical $-\mathbf{u}$ layered discontinuities vectors, both collecting known and unknown quantities, but also by the plastic strain $\bar{\boldsymbol{\epsilon}}^p$ defined by using the strategy shown in Section 2, which in the present formulation is assumed constant in Ω .

The compatibility condition gives the following strain field:

$$\boldsymbol{\epsilon} = \boldsymbol{\epsilon}' - \bar{\boldsymbol{\epsilon}}_Q^p = \boldsymbol{\epsilon}'[\mathbf{f}, -\mathbf{u}, \bar{\boldsymbol{\epsilon}}^p] - \bar{\boldsymbol{\epsilon}}_Q^p = \mathbf{D}_x \mathbf{u}[\mathbf{f}, -\mathbf{u}, \bar{\boldsymbol{\epsilon}}^p] - \bar{\boldsymbol{\epsilon}}_Q^p \quad (24)$$

where $\bar{\boldsymbol{\epsilon}}_Q^p$ is the vector containing the plastic strains defined at point Q. The differential operator \mathbf{D}_x gives rise to the following equation:

$$\boldsymbol{\epsilon} = \int_{\Gamma} \mathbf{G}_{eu} \mathbf{f} d\Gamma + \int_{\Gamma} \mathbf{G}_{et} (-\mathbf{u}) d\Gamma + \mathbf{D}_x \int_{\Omega} \mathbf{G}_{u\sigma} \bar{\boldsymbol{\epsilon}}^p d\Omega - \bar{\boldsymbol{\epsilon}}_Q^p \quad (25)$$

where the positions $\mathbf{G}_{eu} = \mathbf{D}_x \mathbf{G}_{uu}$ and $\mathbf{G}_{et} = \mathbf{D}_x \mathbf{G}_{ut}$ are assumed. In the domain integral, which evaluates the effects of the plastic strain field $\bar{\boldsymbol{\epsilon}}^p$, the differential operator involves the presence of a hypersingularity in the displacement gradient.

If we subdivide the domain into two subdomains where Ω_e is a circular domain of exclusion of the point Q, the latter integral of eq.(25) may be written as follows:

$$\mathbf{D}_x \int_{\Omega} \mathbf{G}_{u\sigma} \bar{\boldsymbol{\varepsilon}}^p d\Omega = \lim_{\varepsilon \rightarrow 0} (\mathbf{D}_x \int_{\Omega - \Omega_\varepsilon} \mathbf{G}_{u\sigma} \bar{\boldsymbol{\varepsilon}}^p d\Omega) + \lim_{\varepsilon \rightarrow 0} (\mathbf{D}_x \int_{\Omega_\varepsilon} \mathbf{G}_{u\sigma} d\Omega \cdot \bar{\boldsymbol{\varepsilon}}_Q^p) \quad (26)$$

The previous strain expression is regularized in the following way:

$$\mathbf{D}_x \int_{\Omega} \mathbf{G}_{u\sigma} \bar{\boldsymbol{\varepsilon}}^p d\Omega = \lim_{\varepsilon \rightarrow 0} \mathbf{D}_x \int_{\Omega - \Omega_\varepsilon} \mathbf{G}_{u\sigma} (\bar{\boldsymbol{\varepsilon}}^p - \bar{\boldsymbol{\varepsilon}}_Q^p) d\Omega + \lim_{\varepsilon \rightarrow 0} \mathbf{D}_x \int_{\Omega - \Omega_\varepsilon} \mathbf{G}_{u\sigma} d\Omega \cdot \bar{\boldsymbol{\varepsilon}}_Q^p \quad (27)$$

The first integral of the previous equation is regular and the differential operator may be applied directly to the kernel. The second integral is transferred on the boundary by using the RIM technique before the application of the differential operator, so obtaining:

$$\mathbf{D}_x \int_{\Omega} \mathbf{G}_{u\sigma} \bar{\boldsymbol{\varepsilon}}^p d\Omega = \int_{\Omega} \mathbf{G}_{\varepsilon\sigma} (\bar{\boldsymbol{\varepsilon}}^p - \bar{\boldsymbol{\varepsilon}}_Q^p) d\Omega + \mathbf{D}_x \int_{\Gamma} \mathbf{G}_{u\sigma} \mathbf{n}' r d\Gamma \cdot \bar{\boldsymbol{\varepsilon}}_Q^p \quad (28)$$

If now we apply the differential operator into the second integral and consider the position $\mathbf{D}_x(\cdot) = -\mathbf{D}_x'(\cdot)$, one obtains:

$$\mathbf{D}_x \int_{\Gamma} \mathbf{G}_{u\sigma} \mathbf{n}' r d\Gamma \cdot \bar{\boldsymbol{\varepsilon}}_Q^p = \int_{\Gamma} \mathbf{G}_{\varepsilon\sigma} \mathbf{n}' r d\Gamma \cdot \bar{\boldsymbol{\varepsilon}}_Q^p - \int_{\Gamma} \mathbf{N}' \mathbf{G}_{u\sigma} d\Gamma \cdot \bar{\boldsymbol{\varepsilon}}_Q^p. \quad (29)$$

Because the first term is a circular integral, the following condition is valid

$$\int_{\Gamma} \mathbf{G}_{\varepsilon\sigma} \mathbf{n}' r d\Gamma = \mathbf{0}, \quad (30)$$

therefore the strain and stress fields take on the following regularized form:

$$\boldsymbol{\varepsilon} = \int_{\Gamma} \mathbf{G}_{\varepsilon u} \mathbf{f} d\Gamma + \int_{\Gamma} \mathbf{G}_{\varepsilon t} (-\mathbf{u}) d\Gamma + \int_{\Omega} \mathbf{G}_{\varepsilon\sigma} (\bar{\boldsymbol{\varepsilon}}^p - \bar{\boldsymbol{\varepsilon}}_Q^p) d\Omega - (\int_{\Gamma} \mathbf{N}' \mathbf{G}_{u\sigma} d\Gamma + \mathbf{I}) \cdot \bar{\boldsymbol{\varepsilon}}_Q^p \quad (31a)$$

$$\boldsymbol{\sigma} = \mathbf{E} \boldsymbol{\varepsilon} = \int_{\Gamma} \mathbf{G}_{\sigma u} \mathbf{f} d\Gamma + \int_{\Gamma} \mathbf{G}_{\sigma t} (-\mathbf{u}) d\Gamma + \int_{\Omega} \mathbf{G}_{\sigma\sigma} (\bar{\boldsymbol{\varepsilon}}^p - \bar{\boldsymbol{\varepsilon}}_Q^p) d\Omega - \mathbf{E} (\int_{\Gamma} \mathbf{N}' \mathbf{G}_{u\sigma} d\Gamma + \mathbf{I}) \cdot \bar{\boldsymbol{\varepsilon}}_Q^p \quad (31b)$$

If we apply the Cauchy formula in eq.(31b), the S.I. of the traction on an element having the slope defined by \mathbf{n} is obtained:

$$\mathbf{t} = \int_{\Gamma} \mathbf{G}_{tu} \mathbf{f} d\Gamma + \int_{\Gamma} \mathbf{G}_{tn} (-\mathbf{u}) d\Gamma + \int_{\Omega} \mathbf{G}_{t\sigma} (\bar{\boldsymbol{\varepsilon}}^p - \bar{\boldsymbol{\varepsilon}}_Q^p) d\Omega - \mathbf{N}^T \mathbf{E} (\int_{\Gamma} \mathbf{N}' \mathbf{G}_{u\sigma} d\Gamma + \mathbf{I}) \cdot \bar{\boldsymbol{\varepsilon}}_Q^p \quad (32)$$

In order to evaluate the traction on the discretized boundary element, it is necessary to make a limit operation from the inner of the body. Indeed the first integral is performed as CPV to which the free term $\mathbf{f}/2$ must be added, whereas the fourth integral, where the Bui free term [5] is present in implicit form, gives rise to a term equivalent to the CPV and to a free term.

The fourth integral in eq.(32) is evaluated through a limit operation. In Fig.1, Q represents the point, distant d from the boundary, where the traction has to be computed on a slope characterized by a normal unit vector assumed parallel to the normal vector to the generic boundary element.

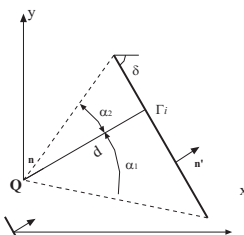


Fig. 1: Traction contribution on the boundary element.

The limit operation gives rise to a coefficient obtainable in closed form. Two jump terms are added to this coefficient: the first corresponds to a half of Bui free term, i.e. $(1/2)\mathbf{N}^T \mathbf{E} \mathbf{J}$, the second one $\mathbf{N}^T \mathbf{E} \mathbf{J}_b$ contains a trigonometric function.

In particular:

First jump term: when the point Q approaches to the boundary ($d \rightarrow 0$) from the inner of the body, the contribution $(1/2)\mathbf{N}^T \mathbf{E} \mathbf{J}$ is obtained putting $\alpha_1 \rightarrow -\pi/2$, $\alpha_2 \rightarrow \pi/2$. Some simple geometrical considerations permit to observe that, whatever the body geometry may be, the same contribution arises for each side, whereas the other half depends on the remaining boundary.

Second jump term: the additional term $\mathbf{N}^T \mathbf{E} \mathbf{J}_b$ depends on the slope of the boundary element Γ_i towards which the infinitesimal element approaches.

In detail:

$$\lim_{d \rightarrow 0^-} \mathbf{N}^T \mathbf{E} \int_{\Gamma_i} \mathbf{N}' \mathbf{G}_{u\sigma} d\Gamma_i = \mathbf{N}^T \mathbf{E} \oint_{\Gamma_i} \mathbf{N}' \mathbf{G}_{u\sigma} d\Gamma_i + \mathbf{N}^T \mathbf{E} \left(\frac{1}{2} \mathbf{J} + \mathbf{J}_b \right) \quad (33)$$

In the hypothesis of $\bar{\epsilon}^p = \text{const.}$, the latter condition permits to rewrite eq.(32), here reported together with eq.(24). This latter has been modify by using only RIM technique.

$$\begin{aligned} \mathbf{u} &= \int_{\Gamma} \mathbf{G}_{uu} \mathbf{f} d\Gamma + \oint_{\Gamma} \mathbf{G}_{ut} (-\mathbf{u}) + \frac{1}{2} \mathbf{u} + \int_{\Gamma} \mathbf{G}_{u\sigma} (\mathbf{n}^T \mathbf{r}) d\Gamma \cdot \bar{\epsilon}_Q^p \\ \mathbf{t} &= \oint_{\Gamma} \mathbf{G}_{tu} \mathbf{f} d\Gamma + \frac{1}{2} \mathbf{f} + \int_{\Gamma} \mathbf{G}_{tt} (-\mathbf{u}) d\Gamma - \mathbf{N}^T \mathbf{E} \oint_{\Gamma} \mathbf{N}' \mathbf{G}_{u\sigma} d\Gamma \cdot \bar{\epsilon}_Q^p - \mathbf{N}^T \mathbf{E} \left(\frac{1}{2} \mathbf{J} + \mathbf{J}_b \right) \cdot \bar{\epsilon}_Q^p \end{aligned} \quad (34a,b)$$

In order to obtain the coefficients of system (5), the terms present in eqs.(34) must be weighted on the boundary in according with symmetric Galerkin BEM.

4. Numerical results

In order to show the efficiency of the proposed method, a traction test, by using the SBEM code Karnak.sGbem [6], has been performed. In the present example a notched specimen, subjected to tensile load $q = 5000 \text{ daN/m}$ amplified by λ , has been analyzed in the hypothesis of plain strain condition. Von Mises yield criterion and a perfect plastic material have been assumed. The material parameters are the Young's modulus $E = 200000 \text{ daN/cm}^2$, Poisson's ratio $\nu = 0.18$ and uniaxial yield value $\sigma_y = 300 \text{ daN/cm}^2$. The geometrical data and the mesh used in this analysis are given in Fig.2.a. The load-displacement curve related at the displacement of the point A is shown in Fig.2.b and the solution has been compared to a finite element solution [2].

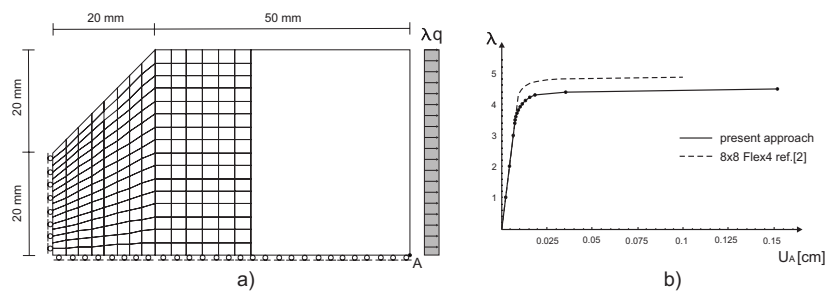


Fig. 2. Notched specimen: a) problem description; b) load-displacement curve.

References

- [1] Panzeca T., Cucco F., Terravecchia S., (2002), "Symmetric boundary element method versus Finite element method". *Comp. Meth. Appl. Mech. Engng.*, 191, 3347-3367.
- [2] Bilotta A., Casciaro R., (2006). A high-performance element for the analysis of 2D elastoplastic continua. *Comput. Meth. Appl. Mech. Engng.*, 196, 818-828.
- [3] Ponter A. R. S., Martin J. B., (1972). "Some extremal properties and energy theorems for inelastic materials and their relationship to the deformation theory of plasticity". *J. Mech. Phys. Solids*, 20, 281-300.
- [4] Panzeca T., Terravecchia S., Zito L., (2008) The thermoelasticity by the Symmetric Boundary Element Method. *IXth International Conference on Boundary Element Techniques* (Beteq 2008).
- [5] Bui H. D., (1978), "Some remarks about the formulation of three-dimensional thermoelastoplastic problems by integral equation". *Int. J. of Solids and Structures.*, 14, 935-939.
- [6] Cucco F., Panzeca T., Terravecchia S., (2002), *The program Karnak.sGbem Release 1.0.*

A boundary element model for nonlinear viscoelasticity

Stavros Syngellakis¹ and Jiangwei Wu²

¹ School of Engineering Sciences, University of Southampton, Southampton SO17 1BJ, UK,
ss@soton.ac.uk

² Department of Mechanical Engineering, Shanghai Maritime University, 1550 Pu Dong Avenue,
Shanghai 200135, P. R. China, jiangwei_wu@hotmail.com

Keywords: Polymers, viscoelasticity, non-linearity, fracture, boundary elements, singular integrals.

Abstract. The boundary element methodology is applied to the analysis of non-linear viscoelastic solids. The adopted non-linear model uses the same relaxation moduli as the respective linear relations but with a time shift depending on the volumetric strain. Nonlinearity introduces an irreducible domain integral into the original integral equation derived for linear viscoelastic solids. This necessitates the evaluation of domain strains, which relies on proper differentiation of an integral with a strong kernel singularity. A time domain formulation is implemented through a numerical integration algorithm. The effectiveness of the developed numerical tool is demonstrated through the analysis of a plate with a central crack. The results are compared with respective predictions by the finite element method.

Introduction

Many polymers exhibit highly nonlinear viscoelastic behaviour in areas of stress or strain concentrations such as those arising from the presence of cracks. Material non-linearity manifests itself as considerable strain softening near the crack tip. The development of numerical techniques for the implementation of relevant constitutive models describing such behaviour has been an important research objective. Non-linear viscoelastic solutions, based on the finite element method (FEM), have been formulated and tested for efficiency and stability [1].

The boundary element method (BEM) has been extensively and very effectively used in modelling linear viscoelastic behaviour [2]. It has, in particular, been found a reliable tool for the analysis of viscoelastic fracture mechanics problems [3]. It seems, however, that there has not been any previous attempt to extend such formulations to modelling the nonlinear behaviour of polymers.

Various constitutive models have been proposed for representing nonlinear viscoelasticity in polymers [4]. Schapery [5] proposed a quite general and frequently applied model, which includes the principle of time-stress superposition. The latter is accounted for through the definition of 'reduced time', a concept originally introduced to account for temperature variation [6]. Based on experimental studies, Knauss and Emri [7, 8] linked the time-stress superposition model to the concept of free volume. This constitutive model has been applied to various problems [9, 10] and found to be a very effective analysis tool for assessing the effect of nonlinearity on the behaviour of polymer materials.

The non-linear visco-elastic model employed in the present BEM formulation is based on the reduced time concept, which is, in turn, considered as a function of mechanical free-volume changes. The relaxation moduli of linear visco-elasticity are thus employed in the Boltzmann constitutive equations with a time shift depending on the volumetric strain. The difference between the actual stress tensor and its linear counterpart generates an irreducible domain integral into the original integral equation derived for linear viscoelastic solids. Domain strains are obtained by differentiation of a domain integral with a strong kernel singularity resulting in a singular integral and a regular free term. A time domain formulation is implemented through a numerical integration algorithm. The effectiveness of the developed numerical tool is demonstrated through the analysis of a plate with a central crack subjected to remote tension. The results are compared with respective predictions by the finite element method.

Background theory

The linear viscoelastic model adopted in earlier BEM formulations [11] is, in accordance with Boltzmann's principle, of hereditary integral type

$$\sigma_{ij} = G_{ijkl}(t)\varepsilon_{kl}(0) + \int_0^t G_{ijkl}(t-\tau) \frac{\partial \varepsilon_{kl}(\tau)}{\partial \tau} d\tau \quad (1)$$

where σ_{ij} , ε_{ij} are the stress and small strain tensors, respectively, and $G_{ijkl}(t)$ the relaxation moduli in the general case of an anisotropic medium. The problem is described relative to a Cartesian frame of reference x_i , $i = 1, 2, 3$, adopting the summation convention for repeated indices. Introducing the notation for the Stieltjes convolution of two functions [12], eq (1) can be more concisely written as

$$\sigma_{ij} = G_{ijkl} * d\varepsilon_{kl} \quad (2)$$

The nonlinear constitutive equations adopted here are [9]

$$\sigma_{ij} = \int_{-\infty}^t G_{ijkl}[\zeta(t) - \zeta(\tau)] \frac{\partial \varepsilon_{kl}(\tau)}{\partial \tau} d\tau = G_{ijkl}[\zeta(t)]\varepsilon_{kl}(0) + \int_0^t G_{ijkl}[\zeta(t) - \zeta(\tau)] \frac{\partial \varepsilon_{kl}(\tau)}{\partial \tau} d\tau \quad (3)$$

where $\zeta(t)$ is the reduced or intrinsic time, which may account for the effect of temperature [6], moisture and pressure variations on the relaxation moduli. A general definition of $\zeta(t)$ is

$$\zeta(t) = \int_0^t \frac{d\tau}{\phi[v(\tau)]} \quad (4)$$

and ϕ is a shift factor, which depends on the fractional free volume v . Here, only the influence of mechanically induced aging is considered, thus v is expressed only in terms of volumetric strain by

$$v = v_0 + C\varepsilon_{kk} \quad (5)$$

where v_0 is the fractional free volume at some reference state and C is a material parameter which, in many cases, may be taken equal to unity. A possible expression for ϕ is [7]

$$\phi = \exp \left[b \left(\frac{1}{v} - \frac{1}{v_0} \right) \right] \quad (6)$$

where b is another material parameter.

Formulation

The derivation of an integral equation for non-linear viscoelastic problems begins with the reciprocal theorem of linear viscoelasticity [12]. Given two linear viscoelastic states $(\varepsilon_{ij}, \sigma_{ij})$ and $(\tilde{\varepsilon}_{ij}, \tilde{\sigma}_{ij})$, satisfying the constitutive eq (2) in the viscoelastic domain Ω , then

$$\int_{\Omega} \tilde{\varepsilon}_{ij} * d\sigma_{ij} d\Omega = \int_{\Omega} \varepsilon_{ij} * d\tilde{\sigma}_{ij} d\Omega \quad (7)$$

In a non-linearly deformed viscoelastic material, it is possible to define the notional stress field σ_{ij}^L related to the actual strain components by

$$\sigma_{ij}^L = G_{ijkl} * d\varepsilon_{kl} \quad (8)$$

Then, the actual stress developing in the non-linear material can be written as

$$\sigma_{ij} = \sigma_{ij}^L + \sigma_{ij}^{NL} \tag{9}$$

where σ_{ij}^{NL} represents the effect of material non-linearity on stress, that is, the stress difference resulting from using constitutive eq (3) rather than eq (2). The reciprocity relation (7) is only valid for σ_{ij}^L ; hence, for the non-linear problem, it should take the form

$$\int_{\Omega} \tilde{\epsilon}_{ij} * d(\sigma_{ij} - \sigma_{ij}^{NL}) d\Omega = \int_{\Omega} \epsilon_{ij} * d\tilde{\sigma}_{ij} d\Omega \tag{10}$$

Substitution of the small strains-displacement relations into eq (10), integration by parts and the application of divergence theorem, gives

$$\int_{\Gamma} \tilde{u}_i * dp_i d\Gamma + \int_{\Omega} \tilde{u}_i * df_i d\Omega = \int_{\Gamma} u_i * d\tilde{p}_i d\Gamma + \int_{\Omega} u_i * d\tilde{f}_i d\Omega + \int_{\Omega} \tilde{\epsilon}_{ij} * d\sigma_{ij}^{NL} d\Omega \tag{11}$$

where Γ is the boundary of Ω while u_i, p_i and f_i are, respectively, the components of the displacement, traction and body force corresponding to the actual, nonlinear problem while \tilde{u}_i, \tilde{p}_i and \tilde{f}_i are the respective quantities for a second hypothetical linear field. The latter is assumed due to the body force

$$\tilde{f}_{ki} = \delta_{ki} \delta(\mathbf{x} - \boldsymbol{\xi}) H(t) \tag{12}$$

acting on an infinite isotropic linearly viscoelastic domain, where δ_{ki} is the Kronecker delta, $\delta(\mathbf{x} - \boldsymbol{\xi})$ the delta function and $H(t)$ the Heaviside step function. Then, eq (11) is transformed to

$$\kappa_{ij} u_j(t) = \int_{\Gamma} (\tilde{u}_{ij} * dp_j - \tilde{p}_{ij} * du_j) d\Gamma + \int_{\Omega} \tilde{u}_{ij} * df_j d\Omega - \int_{\Omega} \tilde{\epsilon}_{ijk} * d\sigma_{jk}^{NL} d\Omega \tag{13}$$

where $\tilde{u}_{ij}(\mathbf{x} - \boldsymbol{\xi}, t)$ is the time-dependent fundamental solution while $\tilde{\epsilon}_{ijk}$ and \tilde{p}_{ij} are the corresponding strain and edge traction components. In eq (13), $\kappa_{ij} = \delta_{ij}$ for interior source points and $\kappa_{ij} = (1/2)\delta_{ij}$ for points on a smooth boundary.

The Laplace transform of \tilde{u}_{ij} can be derived from the fundamental solution of the respective elastic problem via the correspondence principle. Inversion from the transform to the real time domain leads to the general form [11]

$$\tilde{u}_{ij}(\mathbf{x}, \boldsymbol{\xi}, t) = A(t) g_{ij}(\mathbf{x} - \boldsymbol{\xi}) + B(t) h_{ij}(\mathbf{x} - \boldsymbol{\xi}) \tag{14}$$

where the time functions $A(t)$ and $B(t)$ also depend implicitly on the relaxation moduli of the material while the spatial functions $g_{ij}(\mathbf{x} - \boldsymbol{\xi})$ and $h_{ij}(\mathbf{x} - \boldsymbol{\xi})$ also depend on the dimensionality of the problem.

Eq (13) is not a true boundary integral equation because of the presence of an irreducible domain integral dependent on material non-linearity. An iterative scheme accounting for that integral complements an existing time-stepping boundary element formulation [11] for solving the linear part of eq (13). The scheme relies on the evaluation of σ_{ij}^{NL} at internal points using eq (9) and the constitutive relations (1) and (3). The strains are given in terms of the displacement gradients, which are obtained from eq (13) with $\kappa_{ij} = \delta_{ij}$:

$$\frac{\partial u_i(\boldsymbol{\xi}, t)}{\partial \xi_l} = \int_{\Gamma} \left[\frac{\partial \tilde{u}_{ij}}{\partial \xi_l} * dp_j - \frac{\partial \tilde{p}_{ij}}{\partial \xi_l} * du_j \right] d\Gamma + \int_{\Omega} \frac{\partial \tilde{u}_{ij}}{\partial \xi_l} * df_j d\Omega - \frac{\partial}{\partial \xi_l} \int_{\Omega} \tilde{\epsilon}_{ijk} * d\sigma_{jk}^{NL} d\Omega \tag{15}$$

Differentiation of the singular domain integral. The strong singularity of the kernel $\partial \tilde{e}_{ijk} / \partial \xi_l$, whose behaviour is of order $O(r^{-2})$, does not allow differentiation under the domain integral sign in the third term on the right-hand side of eq (15). The correct expression for that gradient is derived using a method proposed by Bui [13]. Thus, the irreducible domain integral is separated into two parts,

$$\frac{\partial}{\partial \xi_l} \int_{\Omega} \tilde{e}_{ijk} * d\sigma_{jk}^{NL} d\Omega = \lim_{R \rightarrow 0} \left[\frac{\partial}{\partial \xi_l} \int_{\Omega - \Omega_R} \tilde{e}_{ijk} * d\sigma_{jk}^{NL} d\Omega + \frac{\partial}{\partial \xi_l} \int_{\Omega_R} \tilde{e}_{ijk} * d\sigma_{jk}^{NL} d\Omega \right] \quad (16)$$

where Ω_R is a small circle of radius R , centred at the source point ξ .

It can be shown that the second volume integral on the right-hand side of eq (16) is of the order $O(R^2)$. The proof requires that σ_{ij}^{NL} as well its first and second derivatives to be continuous functions of \mathbf{x} in the neighbourhood of ξ . Then, a Taylor's series expansion of σ_{ij}^{NL} around ξ leads to

$$\int_{\Omega_R} \tilde{e}_{ijk}(\mathbf{x}, \xi, t) * d\sigma_{jk}^{NL}(\mathbf{x}, t) d\Omega = R^2 D_{ijkm}(t) * d\sigma_{jk}^{NL}(\xi, t) \quad (17)$$

where $D_{ijkm}(t)$ are linear combinations of $A(t)$ and $B(t)$, independent of ξ . Hence the gradient of the right-hand side of eq (17) involves second derivatives of σ_{ij}^{NL} and therefore vanishes as $R \rightarrow 0$.

Since Ω_R depends on ξ , differentiation of the first domain integral on the right-hand side of eq (16) produces an additional convective term. Thus

$$\frac{\partial}{\partial \xi_l} \int_{\Omega - \Omega_R} \tilde{e}_{ijk} * d\sigma_{jk}^{NL} d\Omega = \int_{\Omega - \Omega_R} \frac{\partial \tilde{e}_{ijk}}{\partial \xi_l} * d\sigma_{jk}^{NL} d\Omega - \int_{\Gamma_R} n_l \tilde{e}_{ijk} * d\sigma_{jk}^{NL} d\Gamma \quad (18)$$

where Γ_R is the periphery of the circle with radius R and \mathbf{n} is the outward unit normal to that circle. Using the formulas [14]

$$\int_{\Gamma_R} r_i r_j d\Gamma = \pi R \delta_{ij}, \quad \int_{\Gamma_R} r_i r_j r_k r_l d\Gamma = \frac{\pi R}{4} (\delta_{ij} \delta_{kl} + \delta_{ik} \delta_{jl} + \delta_{il} \delta_{jk}) \quad (19)$$

where $r = |\mathbf{x} - \xi|$, the last term on the right-hand side of eq (18) is reduced to a sum of simple convolution integrals.

As $R \rightarrow 0$, the first integral on the right-hand side of eq (18) becomes the Cauchy principal value of the singular integral, whose existence has been proved and the methods to evaluate is presented below. The strain components corresponding to \tilde{u}_{ij} and their gradients are obtained by successive differentiation of Eq. (14).

Evaluation of the Cauchy principal value. The domain integral on the right-hand side of eq (18) is evaluated by dividing the domain into cells, that is, two-dimensional subdomains Ω_c bounded by contours Γ_c . The integration is performed over each cell using an approximate model for the unknown σ_{ij}^{NL} . The radial integration method [14] was used to evaluate the Cauchy principal value of that integral over the cell containing the source point. The integration over all other cells was performed using numerical quadrature.

The domain integral on the right-hand side of eq (18) can be expressed as

$$\int_{\Omega_c} \frac{\partial \tilde{e}_{ijk}(\mathbf{x}, \xi, t)}{\partial \xi_l} * d\sigma_{jk}^{NL}(\mathbf{x}, t) d\Omega = \left[\int_{\Omega_c} \frac{\partial \tilde{e}_{ijk}(\mathbf{x}, \xi, t)}{\partial \xi_l} d\Omega \right] * d\sigma_{jk}^{NL}(\xi, t)$$

$$+ \int_{\Omega_c} \frac{\partial \tilde{\epsilon}_{ijk}(\mathbf{x}, \xi, t)}{\partial \xi_l^c} * [d\sigma_{jk}^{NL}(\mathbf{x}, t) - d\sigma_{jk}^{NL}(\xi, t)] d\Omega \tag{20}$$

The second integral on the right-hand side of eq (20) can be shown to be regular and therefore evaluated by standard numerical schemes; the strong singularity remains in the first integral. A polar coordinate system (r, θ) is defined with the origin at the source point ξ . It can be shown that, relative to this system, the singular integral on the right-hand side of eq (20) can be transformed to

$$\int_{\Omega_c} \frac{\partial \tilde{\epsilon}_{ijk}(\mathbf{x}, \xi, t)}{\partial \xi_l^c} d\Omega = \int_{\Gamma_c} \left[\frac{1}{r} \frac{\partial r}{\partial n} \right] \psi_{ijkl}(\theta, t) \int_0^{r(\Gamma)} \frac{dr}{r} d\Gamma \tag{21}$$

where

$$\frac{\partial \tilde{\epsilon}_{ijk}}{\partial \xi_l^c} = \frac{1}{r^2} \psi_{ijk}(\theta, t)$$

Since the integration is carried out in the Cauchy principal value sense, a small circle of radius R around the singular point ξ can be cut off. Thus, eq (21) becomes,

$$\int_{\Omega_c - \Omega_R} \frac{\partial \tilde{\epsilon}_{ijk}(\mathbf{x}, \xi, t)}{\partial \xi_l^c} d\Omega = \int_{\Gamma_c} \left[\frac{\ln r}{r} \frac{\partial r}{\partial n} \right] \psi_{ijkl}(\theta, t) d\Gamma + \ln R \int_0^{2\pi} \psi_{ijkl}(\theta, t) d\theta \tag{22}$$

where $\partial r / \partial n = -1$ has been used in the second integral along the circle Γ_R . Using relations (19), it can be shown that the last integral on the right-hand side of eq (22) is identical to zero; this is an intrinsic property of ψ_{ijkl} . Hence, as $R \rightarrow 0$, eq (22) becomes

$$\int_{\Omega_c} \frac{\partial \tilde{\epsilon}_{ijk}(\mathbf{x}, \xi, t)}{\partial \xi_l^c} d\Omega = \int_{\Gamma_c} \left[\frac{\ln r}{r} \frac{\partial r}{\partial n} \right] \psi_{ijkl}(\theta, t) d\Gamma \tag{23}$$

Now the strongly singular domain integral has been transformed into a boundary integral. Since the source point is located inside the domain, no singularity occurs and standard Gaussian quadrature formulas can be used to calculate this integral.

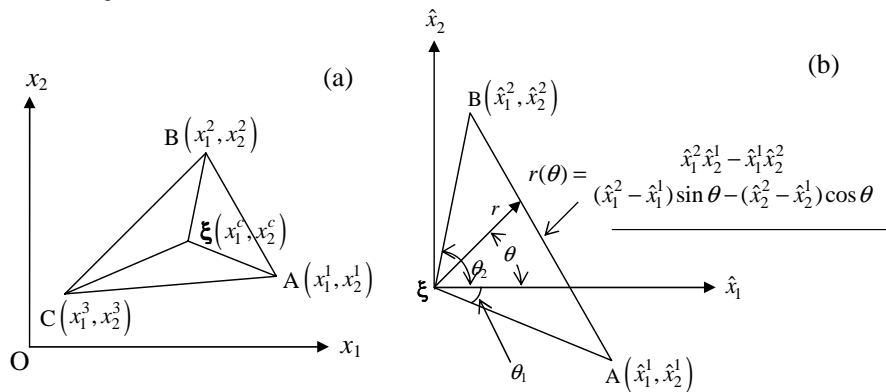


Figure 1 Triangular cell (a) and polar coordinate system with origin at the singular point ξ (b)

The domain was divided into small triangular cells, such as the one shown in Figure 1(a), with the source point ξ at the centre of the triangle. Relative to a polar frame of reference with origin at the centre of the triangle, the equation of side A(\hat{x}_i^1)-B(\hat{x}_i^2) of the triangle, shown in Fig. 1(b), can be expressed in terms of the local corner co-ordinates $\hat{x}_i^j = x_i^j - \xi_j$, where x_i^j are the co-ordinates of corner j .

Thus, in this case, the contour integral on the right-hand side of eq (23) is evaluated along each side of the triangle. Adopting a 'constant' cell model for σ_{jk}^{NL} , the stress difference in eq (20) vanishes and therefore

$$\int_{\Omega_c} \frac{\partial \tilde{\varepsilon}_{ijk}(\mathbf{x}, \xi, t)}{\partial \xi_l} * d\sigma_{jk}^{NL}(\mathbf{x}, t) d\Omega = \left[\sum_{\theta_m}^{\theta} \int_{\theta_m}^{\theta} \ln[r(\theta)] \psi_{ijkl}(\theta, t) d\theta \right] * d\sigma_{jk}^{NL}(\xi, t) \quad (24)$$

The integrals on the right-hand side of eq (24) can be calculated by the standard Gaussian quadrature formulas.

Numerical algorithm

Constant boundary elements were used in the present numerical implementation of BEM formulation based on integral eq (13), which also requires modelling in the time dimension. If the boundary surface Γ is discretised in E elements Γ_e , the following representation can be adopted,

$$u_j(\mathbf{x}, t) = u_j^e(t), \quad p_j(\mathbf{x}, t) = p_j^e(t) \quad (25)$$

where $u_j^e(t)$ and $p_j^e(t)$ are the time dependent nodal values of displacement and traction, respectively. Over a cell, strain was modelled as uniform and, as a consequence of eqs (1), (3), (5) and (6), the shift factor as well as both linear and non-linear contributions to the stress are also constant within each cell.

It was assumed that the boundary variables $u_i(x, t)$ and $p_i(x, t)$ as well as the nonlinear part of total stress $\sigma_{jk}^{NL}(\mathbf{x}, t)$ in the domain are linear with respect to time t within a small time step $\Delta t_\kappa = t_\kappa - t_{\kappa-1}$. With the viscoelastic fundamental solutions in the general form:

$$\tilde{u}_{ij} = b_{ij}^0 + \sum_{n=1}^N b_{ij}^n e^{-\beta_n t}, \quad \tilde{p}_{ij} = a_{ij}^0 + \sum_{m=1}^M a_{ij}^m e^{-\alpha_m t}, \quad \tilde{\varepsilon}_{ijk} = c_{ijk}^0 + \sum_{q=1}^Q c_{ijk}^q e^{-\gamma_q t} \quad (26)$$

the discretised form of eq (13) was obtained as

$$\begin{aligned} \kappa_{ij}(\xi) u_i^{(K)}(\xi) &= \sum_{n=0}^N B_j^{n(K)}(\xi) + \sum_{\kappa=1}^K \sum_{n=1}^N [B_j^{n(\kappa-1)}(\xi) e^{-\beta_n(t_\kappa - t_{\kappa-1})} (e^{-\beta_n \Delta t_\kappa} - 1)] \\ &\quad - \sum_{m=0}^M A_j^{m(K)}(\xi) - \sum_{\kappa=1}^K \sum_{m=1}^M [A_j^{m(\kappa-1)}(\xi) e^{-\alpha_m(t_\kappa - t_{\kappa-1})} (e^{-\alpha_m \Delta t_\kappa} - 1)] \\ &\quad - \sum_{q=0}^Q C_j^{q(K)}(\xi) - \sum_{\kappa=1}^K \sum_{q=1}^Q [C_j^{q(\kappa-1)}(\xi) e^{-\gamma_q(t_\kappa - t_{\kappa-1})} (e^{-\gamma_q \Delta t_\kappa} - 1)] \end{aligned} \quad (27)$$

where, for simplicity, the body force was assumed to be zero and

$$A_i^{m(K)}(\xi) = \int_{\Gamma} a_{ij}^m u_j^{(K)} d\Gamma, \quad B_i^{n(K)}(\xi) = \int_{\Gamma} b_{ij}^n p_j^{(K)} d\Gamma, \quad C_i^{q(K)}(\xi) = \int_{\Omega} c_{ijk}^q \sigma_{jk}^{NL(K)} d\Omega$$

$$u_i^{(K)}(\mathbf{x}) = u_i(\mathbf{x}, t_\kappa), \quad p_i^{(K)}(\mathbf{x}) = p_i(\mathbf{x}, t_\kappa), \quad \sigma_{jk}^{NL(K)}(\mathbf{x}) = \sigma_{jk}^{NL}(\mathbf{x}, t_\kappa)$$

An iterative scheme is proposed for solving eq (27) since the current values of the stresses σ_{jk}^{NL} are not known at the beginning of a time step. At the first iteration, the boundary displacements and tractions are determined at time $t = t_k$ assuming $\sigma_{jk}^{NL}(t_k) = \sigma_{jk}^{NL}(t_{k-1})$. Then displacement gradients are determined from eq (15) leading to initial estimates of domain strains and subsequently of stresses through constitutive eqs (1) and (3). The value of the domain integral can thus be revised and the procedure repeated until results from two successive iterations agree within an acceptable tolerance. Convergence of boundary displacements was the adopted criterion for terminating the iteration. It should be noted that, at $t = 0$ all unknown boundary values can be calculated when the integral eq (13) governs only the initial elastic response due to any non-zero initial values of the boundary or loading conditions. At the following time $t = t_1$ (step $\kappa = 1$), the respective unknown boundary values can be obtained from eq (27) with the current boundary conditions and the additional terms depending on the solution at the initial step as well as the non-linear contribution of the current step. The solution progresses to the next time step $\kappa = 2$ in a similar manner and a step-wise procedure is thus established which advances the solution until the final time step is reached. A suite of FORTRAN programs was developed for implementing this formulation.

Numerical results

Specimen geometry and material model. As a numerical test, the developed non-linear analysis was applied to a plate with a central crack under constant tension. The input data are approximately the same as those used by Moran and Knauss [9] who solved this problem using FEM. Due to symmetry relative to two orthogonal axes, only a quarter of the plate was modelled. The plate half-width was 13.44 mm, half-height 12 mm, and the crack half-length $a = 1$ mm. The material behaviour was represented by a standard linear solid model in shear

$$\mu(t) = \mu_0[\lambda + (1 - \lambda)e^{-\eta t}]$$

with $\mu_0 = 4800$ MPa, $\lambda = 0.1$, $\eta = 0.4$ and a constant Poisson's ratio $\nu = 1/3$. In order to simplify the evaluation of the volumetric strain, plane strain conditions were applied.

In order to calculate ϕ using eq (6), v_0 was assumed to be 0.01, and b was chosen equal to 0.05 [9]. A remote tension $\sigma_0 = 0.001E(0)$ was applied, where $E(0)$ is the initial value of the tensile relaxation modulus.

Boundary and domain meshing. 'Constant' boundary elements with variable element length were adopted. The two smallest elements, located on either side of the crack tip, were 0.005 mm long, the largest element at the loading edge of the plate was 3 mm long. In conformity with the boundary mesh, the domain mesh was arranged to be much denser near the crack tip, where the stress concentration and high nonlinearity occur.

Nonlinear stress field. Fig. 2 shows the normalized nonlinear stress field near the crack tip. For a linear viscoelastic plate with a constant Poisson's ratio under constant tensile loading, the stress field is constant over the time history. For nonlinear viscoelastic problems, the material undergoes considerable strain softening around the crack tip, where the high stress and strain occur. From Fig. 2 it is very clear that the stress field drops with time due to the strain softening, and this drop slows down with time becoming less significant as the strain itself changes more slowly. The stresses far from the crack tip were increased in order that overall equilibrium is satisfied. This response is similar to that predicted by FEM [9].

The program was also run with the parameter λ changed to 0.001 implying a more pronounced material time-dependence than originally assumed. From the respective results, it was clear that the effect of nonlinearity was higher than previously under the same loading conditions, though not as significant as predicted by FEM [9]. One possible reason for this is that an initial region of K -dominance is assumed in their paper, inside this region the strains are assumed to be infinite and the time-shift factor reduces to a constant value.

Concluding remarks

An initial attempt was made to validate the developed formulation and the resulting software through their application to a fracture problem. Although the cell size distribution around the crack tip was not ideal for capturing the local stress concentration, this mesh was considered acceptable for an initial assessment of the performance of the proposed method. The numerical results obtained confirmed the expected effect of non-linearity on the stress time history, which is highest in the neighbourhood of the crack tip. Compared however with those reported in a previous FEM study [9], significant discrepancy was noted. There was also a degree of

inconsistency between the calculated boundary tractions and domain stresses. Further numerical test are required to assess the sensitivity of the solution to mesh refinements as well as other input and control parameters.

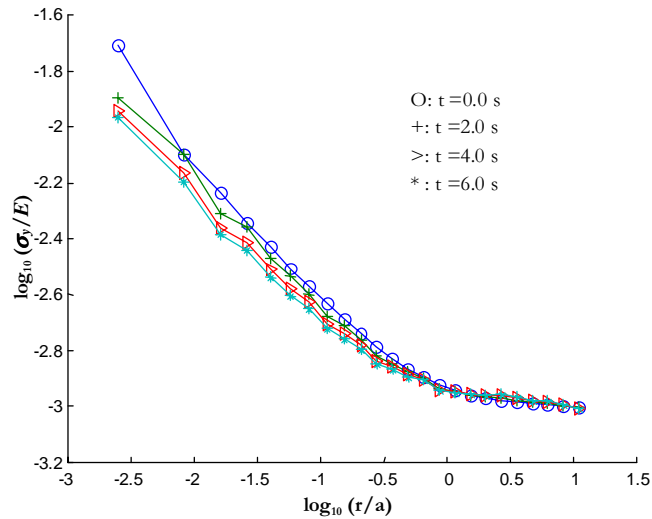


Figure 2. Normalized nonlinear stress field near the crack tip ($\lambda = 0.1$)

References

- [1] J. G. J. Beijer and J. L. Spoomaker *Computers & Structures*, **80**, 1213-1229 (2002).
- [2] S. Syngellakis *Engineering Analysis with Boundary Elements*, **27**, 125-135 (2002).
- [3] S. Syngellakis and H. W. Wu *Engineering Fracture Mechanics*, **75**, 1251-1265 (2008).
- [4] P. J. Dooling, C. P. Buckley and S. Hinduja *Polymer Engineering and Science*, **38**, 892-904 (1998).
- [5] R. A. Schapery *Polymer Engineering and Science*, **9**, 295-310 (1969).
- [6] L. W. Morland and E. H. Lee *Transactions of the Society of Rheology*, **4**, 233-263 (1960).
- [7] W. G. Knauss and I. J. Emri *Computers & Structures*, **13**, 123-128 (1981).
- [8] W. G. Knauss and I. Emri *Polymer Engineering and Science*, **27**, 86-100 (1987).
- [9] B. Moran and W. G. Knauss *Journal of Applied Mechanics-Transactions of the ASME*, **59**, 95-101 (1992).
- [10] A. Wineman and R. Kolberg *International Journal of Non-Linear Mechanics*, **32**, 863-883 (1997).
- [11] S. Syngellakis and J. W. Wu *Engineering Analysis with Boundary Elements*, **28**, 733-745 (2004).
- [12] M. E. Gurtin and E. Sternberg *Archive for Rational Mechanics and Analysis*, **11**, 291-356 (1962).
- [13] H. D. Bui *International Journal of Solids and Structures*, **14**, 935-939 (1978).
- [14] X. W. Gao and T. G. Davis *International Journal of Solids and Structures*, **37**, 4987-5008 (2000).

A Non-linear BEM for surface-piercing hydrofoils

Vimal Vinayan¹, Spyros A. Kinnas²

¹vvinayan@mail.utexas.edu, ²kinnas@mail.utexas.edu

Ocean Engineering Group, Dept. of Civil, Architectural and Environmental Engineering
The University of Texas at Austin
Austin, Texas, USA

Abstract Surface piercing propellers can exhibit high efficiency of propulsion when installed on high-speed ships. The OE group at UT Austin has been involved for over a long time with the development of computational methods for the prediction of performance of high-speed propulsors. These methods entail the modeling of vapor cavities or free-surfaces, which all involve the application of a constant pressure condition. In particular, a method had been developed in the past for the modeling of a surface piercing blade as it entered and exited the water surface. This method was applying linearized free-surface conditions, enforced via the "negative" image method, and was found to predict the entry or exit stage of the blade poorly, even though the mean performance was found to be predicted reasonably well. The authors have started the modeling of a surface piercing hydrofoil by using a BEM in the context of non-linear wave theory. The BEM is used at each time step to solve for the unknown velocities of the particles on the free-surface, and a fourth-order Runge-Kutta scheme is utilized in order to determine the free-surface location in time. Results from the application of the method on surface-piercing hydrofoils are compared with those from linear theory and from fully viscous methods which involve the volume of fluid approach to determine the location of the free-surface. It is shown that the pressures and forces are significantly under-predicted in the case of linear theory. The results from the present method (pressures and the shapes of the free-surface or the ventilated surface) are shown to be in very good agreement to those from the viscous solver, as well as to those measured.

Introduction

Surface piercing propellers are known to provide better efficiency at high speeds in comparison to conventional subcavitating or supercavitating propellers [1]. Some of the factors that contribute to the efficient performance are the reduction in the appendage drag, a reduction in the blade surface friction due to ventilation and the absence of diameter limitations imposed by draft and hull clearance requirements [2]. The numerical modeling of the real phenomena associated with a surface-piercing propeller is too difficult a task to undertake and can only be made feasible through a series of simplifying assumptions [2, 3]. [3] developed a 3-D numerical model for the design and analysis of surface piercing propellers based on the assumptions, (i) the Froude number is large, (ii) the free-surface jets, formed as the blade enters and exits the free-surface, are negligible (i.e. the free-surface is treated as a flat surface and its effect is taken into account using the negative image method) (iii) the cavities are fully ventilated, i.e. the pressure on the cavity is constant and equal to the atmospheric pressure. In spite of the simplifying assumptions, in general the predicted ventilation patterns and blade forces agreed well with the experimental measurements of [4]. Discrepancies between the predicted and measured individual blade forces were observed especially at high rotational speeds. [2] attributed these to - (i) inadequate simulation of the blade entry phenomena (ii) inability of the method to capture the increase in free-surface elevation, and (iii) inability of the method to model the effect of blade vibrations.

As noted earlier, including the effects of jet sprays and nonlinear free-surface conditions would add to the computational difficulties in the 3-D model. It is prudent to first focus on a systematic 2-D study to quantify the added hydrodynamic forces associated with jet sprays generated at the entry and exit phases of a blade section (or a surface piercing hydrofoil). The focus of the current research work is to find a simplified approach to quantify the added hydrodynamic forces due to slamming and the change in free-surface elevation. This is done through the development of a numerical tool to model the entry and exit phases of a ventilating surface-piercing hydrofoil within the framework of potential theory using a Boundary Element Method (BEM). The study of a 2-D surface piercing hydrofoil falls under the category of water entry of two-dimensional bodies and slamming, a subject that has been studied extensively over the years. The pioneering study of the slamming loads on bodies can be attributed to [5] which was later extended by [6]. A detailed review of the subject can be found in [7]. Both analytical (self-similar solutions) and various numerical solutions have been developed over the years. A critical difference between the study of slamming and the entry of surface-piercing hydrofoils

is the possibility of ventilation (complete or partial) at sufficiently large angles of attack. The phenomenon of ventilation is different from cavitation that could occur as a result of the slamming of bodies with small angles of dead-rise. A key similarity is the generation of free-surface jets along the wetted part of the body and the current research work borrows heavily from the analytical and numerical treatment of these jets which has been studied extensively in the case of slamming. In the context of ventilating surface piercing hydrofoils, [8] applied a linearized theory to study the water entry and exit of a thin foil, and a symmetric wedge with ventilation. Similar linearized theories were put forward by [9] and [10, 11]. More recent works include the analytical solutions presented in [12]. In terms of experimental work, [13] conducted a series of experiments on a surface piercing wedge (symmetric wedge) at different angles of attacks and velocity of entry.

2D Surface-Piercing Hydrofoils

This section presents the potential Boundary Element Method (BEM) based scheme used to model the water entry of a surface-piercing hydrofoil. The BEM scheme used here was developed initially in the context of the roll-motion of FPSO hull-sections. Only a brief summary of the mathematical and numerical formulation is presented here and the complete details of the scheme can be found in [14], [15] and [16]. In essence the problem is formulated as an initial boundary value problem (IBVP) for a velocity potential that satisfies the Laplace equation. The IBVP is solved by combining the mixed Eulerian-Lagrangian method of [17], for tracking the free-surface, with the solution of a Boundary Integral Equation (BIE) at each time-step.

Previous numerical work

[18, 19] solved the flow field around a fully ventilated two-dimensional surface-piercing hydrofoil using a time-marching low-order boundary element method. The method solved for the shape of the ventilated cavity and the pressure on the surface of the hydrofoil in the entry-phase. The important characteristics of the method is the use of linearized free-surface boundary conditions enforced using a “negative” image method.

Current Work

The scheme considers a rigid, 2-D hydrofoil entering an initially calm domain with a constant velocity \vec{V} and an angle of attack α , as shown in Fig. (1). An ideal fluid is considered and the flow is assumed to be irrotational. A *fixed* (non-rotating) Cartesian coordinate system is chosen to represent the flow with its origin at the undisturbed water level. The flow is represented in terms of a harmonic function $\phi(\mathbf{x}, t)$ commonly referred to as the *velocity potential*. Also, the local fluid velocity is given as $\vec{q}(\mathbf{x}, t) = \nabla\phi = (\phi_x, \phi_y) = (u, v)$. Here, $\mathbf{x} = (x, y)$ represents the spatial location with respect to the fixed coordinate system, with x being the horizontal measure and y the vertical measure positive upward. The fluid domain and the corresponding boundary surfaces are shown in Figure 1. $S_{WB}(t)$ represents the “wetted” part of the hydrofoil surface, $S_F(t)$ is the free-surface that also includes a part of the ventilated surface on the suction side of the hydrofoil and S_∞ is the far-field boundary placed *far* enough to minimize reflection.

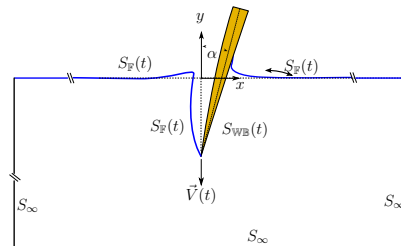


Figure 1: Entry of a surface-piercing wedge : Fluid domain and corresponding boundaries

A boundary integral equation is solved at each time-step of a fourth-order Runge-Kutta time-stepping scheme in order to obtain the velocity potential. Once the solution is obtained at a particular time, the time dependent kinematic and dynamic free-surface boundary conditions are used to update the free-surface and the solution scheme progresses onto the next one using a Mixed-Eulerian-Lagrangian approach. The initial conditions for this problem depend on the angle of attack α and the existence of a ventilated cavity on the suction

side of the hydrofoil. For a fully wetted flow, a tiny fraction of the wedge is assumed to be initially immersed. The solution is started impulsively and allowed to progress until the hydrofoil is completely immersed. The treatment of the fully ventilated case requires special attention. For a sharp hydrofoil, ventilation is triggered right at the leading edge and during the process of the development of the method, it was found extremely difficult to numerically trigger ventilation at the leading edge. In the current scheme, this difficulty is circumvented by locally modifying the shape of the hydrofoil at the leading edge to add a wetted appendage. The length of the appendage is a tiny fraction of the overall length of the hydrofoil and its root serves as a fixed separation point.

Linear iso-parametric elements form the basis for the numerical solution of the boundary integral equation. A *double node* approach is used at the corners of the domain. However, the boundary integral equation is not solved at a *double node* if it happens to be a separation point. The treatment of the jet that forms along the wetted side of the hydrofoil is similar to that presented in [20] and [21]. The jet is allowed to grow until a threshold angle is reached between the jet and the adjoining body surface. Once this limiting angle is reached a new panel is created at an angle larger than the threshold value. The intersection of the new panel with body surface becomes the new body- free-surface intersection point. The angle is continuously monitored during the solution and the *cut-off* process is implemented every time it is smaller than the threshold value. The value of the threshold angle is chosen to be $\frac{\pi}{15}$, a value chosen to be in par with the analytical solutions presented in [22]. A re-paneling scheme is implemented to maintain sufficient and uniform resolution in the area of the jet. Even though linear elements are used to model the free-surface, re-paneling is performed using a cubic spline scheme with the arc-length of the surface as a parameter instead of the Euclidean distance.

A multiphase (volume-of-fluid) model based on a commercial RANSE solver is also developed to look into the effects of viscosity. A detailed explanation of the viscous model is provided in [16] and results for only a few configurations are presented here.

Results

The convergence characteristics of the current numerical scheme are shown in Figures (2a) and (2b) with the results corresponding to a non-ventilating entry of a symmetric wedge with an included angle of 18° (deadrise angle of 81°) in the absence of gravity. The grid on the free-surface is constructed in two parts consisting of a region that has panels of equal length (h) followed by a region on which an expansion ratio is applied. The characteristic panel length on the wetted hydrofoil surface is also specified as (h) for numerical stability. Fig. (2a) shows the spatial convergence of the free-surface elevations for three different panel lengths $h (= 0.003m)$, $h/2$ and $h/3$ respectively. It can be observed that the convergence of the scheme is satisfactory. The results shown in Fig. (2a) correspond to a $\Delta t = 1 \times 10^{-4} s$ and no discernible differences were observed in the case of $\Delta t = 1 \times 10^{-5} s$. Fig. (2b) presents the corresponding convergence characteristics of the pressure coefficient (C_p) on the hydrofoil surface with panel length $h, h/2$ and $h/3$ (equivalent to 50, 100 and 150 panels on the wetted side of the hydrofoil). The pressure coefficient is defined with atmospheric pressure and entry velocity of the wedge as reference values. In Fig. (2b), s is the arc-length measured along the wetted part of the hydrofoil with $s = 0$ corresponding to the apex (leading edge) and $s = 0.15m$ corresponding to the intersection point with the free-surface. It can be observed that the value of C_p converges quickly with panel size except at the apex which is a singular point.

According to [23] and [24], for the water entry problem (self-similar flow in the absence of gravity), the arc-length between two particles at the free-surface, as measured along the free-surface, remains a constant in the motion. For an impulsive start of the wedge this condition is not satisfied initially in the numerical scheme. However as the solution progresses, a state of self-similarity is attained relatively quickly and maintained thereon. This aspect of the flow is illustrated in Figures (3) and (4). In Fig. (3), the free-surface elevations at $t = 0.016s$ and $t = 0.0443s$ are presented in terms of the spatial variables x and y . Fig. (4) makes the corresponding comparison in terms of the similarity variables $X/(Vt)$ and $Y/(Vt)$. $t = 0.016s$ corresponds to the earliest time at which the flows starts to exhibit self-similarity. It can be observed in Fig. (4) that the free-surface elevations at different times are identical, which is equivalent to the arc-length being a constant. Minor differences are observed in the region very close to the intersection point of the free-surface and the hydrofoil and these can be attributed to the cutting of the free-surface jet. Also note that all free-surface elevations between $t = 0.016s$ and $t = 0.0443s$ overlap when expressed in terms of the similarity variables. Figure (3) also shows

the effects of gravity on the flow characteristics. In the initial stages of entry, the Froude number based on the local wedge immersion as a length scale is large and hence the effect of gravity is negligible. This aspect is seen at time $t = 0.016s$ when the flow is almost self-similar. The deviation from self-similarity tends to increase with increase in immersion as seen at time $t = 0.0443s$. Figure (5) illustrates the self-similar characteristics of the ventilated cavity surface predicted (in the absence of gravity) in the case of a hydrofoil entering the water surface at an angle of attack of 10° . On the whole, the current nonlinear scheme retains the self-similar characteristics. Differences are observed where the ventilated surface meets the horizontal free-surface as the current nonlinear scheme smooths out the spray tip formed in the vicinity. Analytical models [12] predict the formation of a spray tip in this region.

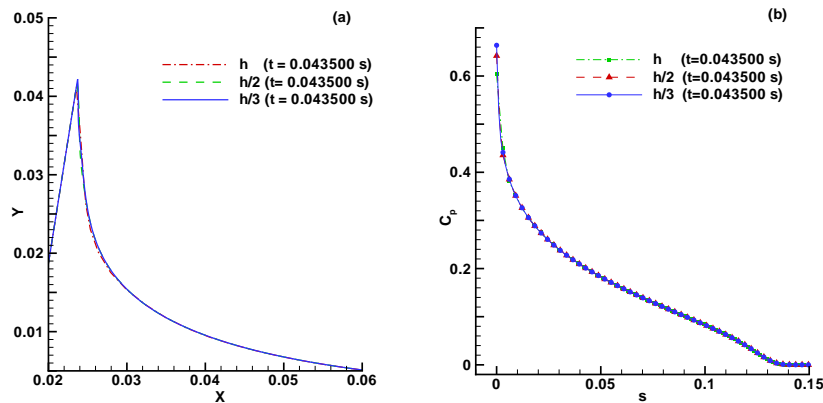


Figure 2: (a) Convergence of the free-surface elevation with change in characteristic panel length (h), (b) Convergence of the pressure coefficient (C_p) on the wetted part of the hydrofoil with change in characteristic panel length

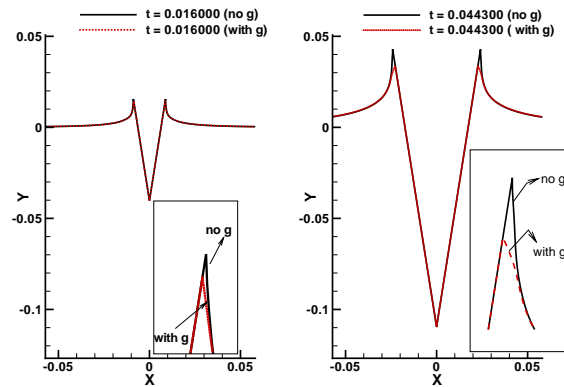


Figure 3: Free-surface elevations at $t = 0.016s$ and $t = 0.0443s$ indicating the effects of gravity. Note that the insets represent a magnified view of the corresponding free-surface elevations.

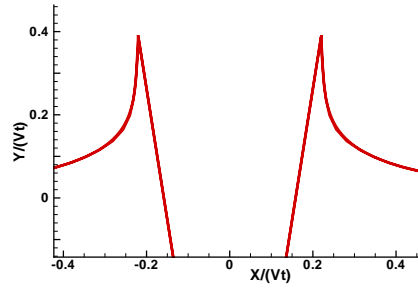


Figure 4: Self-similar characteristics of the free-surface predicted by the current nonlinear scheme in the absence of gravity. Free-surface profiles are shown overlaid from $t = 0.016s$ to $t = 0.0443s$. (Note that all profiles predicted overlap due to self-similarity)

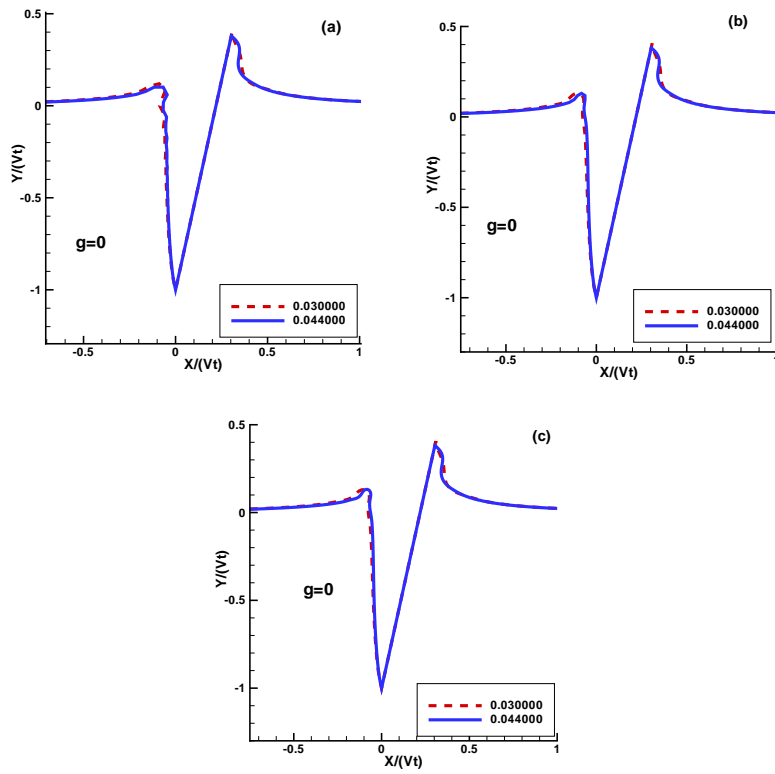


Figure 5: Self-similar characteristics of the ventilated cavity surface predicted by the current nonlinear scheme in the absence of gravity. Comparison shown with respect to change in number of panels (N) on the ventilated cavity surface (a) $N=125$, (b) $N=250$, (c) $N=500$

Fig. (6) (from [16]) shows the ventilated cavity shapes predicted by the current nonlinear scheme for the vertical entry of a wedge with and without the effects of gravity. The figure on the left corresponds to the case with gravity and the one on the right corresponds to the case without gravity. The hydrofoil has a geometry of length 6'' and base thickness 0.5'' and this geometry corresponds to the wedge used in [13] to perform a set of experiments. The vertical entry velocity is about 2.45 m/s which corresponds to a free fall from a height of 12'' from the undisturbed free-surface and the angle of attack is 10° . Also shown in Fig. (6) is the comparison with the RANS VOF model. In both the cases (with and without gravity), the ventilated cavity shapes predicted by the VOF and current BEM model compare well. Differences are observed in the predicted free-surface on the wetted side of the hydrofoil and this is primarily due the truncation of the jet. A very important aspect that needs to be emphasized here is the relative computational efficiency of the VOF and BEM schemes. Up to the point of comparison, shown in Fig. (6), the BEM scheme takes approximately an hour while the VOF scheme takes about 40 hours run parallel on 8 cores (2.4 GHz Intel Xeon quad-core processor).

The next set of results show in Figures (7) and (8) compare the the pressure coefficients (on the wetted side of the hydrofoil) predicted by the linear free-surface BEM model (SPPAN [18, 19]), the current nonlinear scheme and the VOF model. Fig. 7 shows the comparison between the linear and nonlinear schemes at time $t = 0.01109s$ and corresponds to the initial stages of entry of the surface-piercing hydrofoil at an angle of attack of 10° . Fig. (8) makes a comparison at $t = 0.04435s$ and corresponds to the time when the wetted part of the hydrofoil is completely immersed. Figures (7) and (8) illustrate the deficiencies of the linear scheme (based on the *negative image method*) in predicting the pressures and hence forces on the wetted part of the ventilating hydrofoil. In the initial stages of entry, differences are only observed in the region corresponding to the extent of the free-surface jet. However, with increase in immersion, the differences in pressures becomes more pronounced.

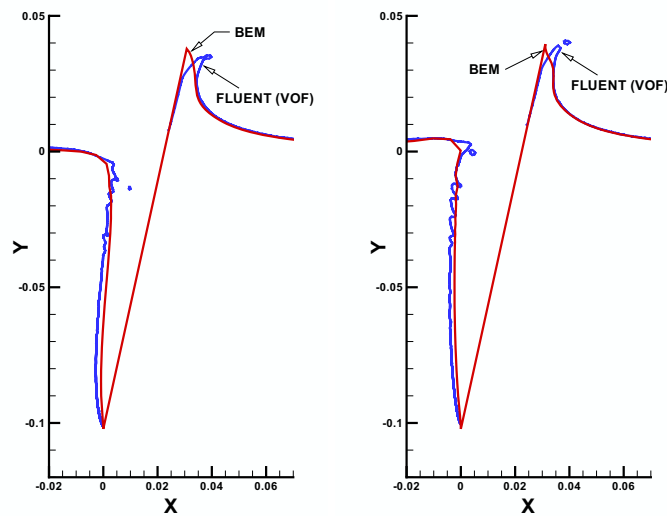


Figure 6: Comparison of BEM and FLUENT results corresponding to $\alpha = 10^\circ$ and $V_w = 2.45$ m/s. (left) ventilated cavity and free-surface predicted with effects of gravity included, (right) ventilated cavity and free-surface predicted without the effects of gravity

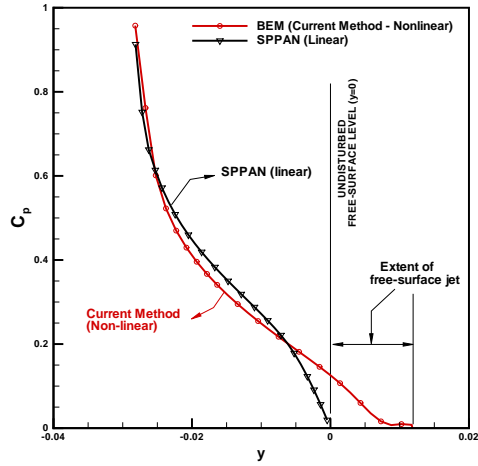


Figure 7: Comparison of pressure coefficients predicted by the linear (SPPAN) and nonlinear BEM schemes at time $t = 0.01109s$

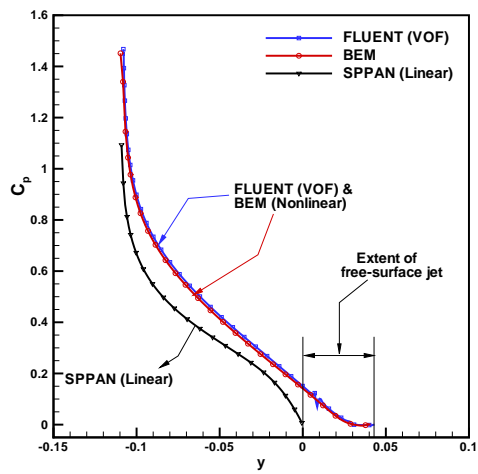


Figure 8: Comparison of pressure coefficients predicted by the linear (SPPAN) and nonlinear BEM schemes at time $t = 0.04435s$

Conclusions

A 2D boundary element method with fully nonlinear boundary conditions was developed to numerically model the fully ventilated flow around a surface piercing hydrofoil. The treatment of the jets is done in a robust way and the scheme is able to sustain the self-similar nature of the flow in a stable manner. A commercial RANSE multiphase code was used to understand the effects of viscosity in the development of the ventilated cavities. The overall comparison between the RANSE and BEM codes, in terms of the pressure distribution and the ventilated cavity shapes, was found to be satisfactory. It is clearly evident from the comparisons made with the current nonlinear scheme that the linear (negative image) method under-predicts the pressures on the wetted side of the hydrofoil, especially in the region of the free-surface jet. The BEM scheme presented here provides a fast and reliable way to predict the ventilated cavity shapes and to quantify the errors resulting from the linear assumptions made in the modeling of surface-piercing propellers. The authors plan to extend the current scheme in the case of a 3-D surface piercing hydrofoil and believe that the insight gained through this extension could be used to improve and develop better numerical models for surface-piercing propellers.

Acknowledgement

Support for this research was provided by the Office of Naval Research (Contract N00014-07-1-0932, Monitor: Ms. Kelly Cooper) and is gratefully acknowledged. The authors also wish to thank Dr. Bruce Cox for sharing with them information on his experimental observations.

References

- [1] John L. Allison. Propellers for High Performance Craft. *Marine Technology*, 15(4):335–380, October 1978.
- [2] Y.L. Young. *Numerical Modeling of Supercavitating and Surface-piercing Propellers*. PhD thesis, University of Texas at Austin, 2002.
- [3] Y.L. Young and S.A. Kinnas. Numerical modeling of supercavitating propeller flows. *Journal of Ship Research*, 47(1):pp. 48–62, 2003.
- [4] N. Olofsson. *Force and flow characteristics of a partially submerged propeller*. PhD thesis, Department of Naval Architecture and Ocean Engineering, Division of Hydromechanics, Chalmers University of Technology, Göteborg, Sweden, 1996.
- [5] Th. Von Karman. The impact of seaplane floats during landing. Technical report, NACA TN321, 1929.
- [6] H. Wagner. Über stoss- und gleitvorgänge an der oberfläche von flüssigkeiten. *Z. Angew. Math. Mech.*, 12(4):pp. 192–215, 1932.
- [7] A. A. Korobkin and V. V. Pukhnachov. Initial Stage of Water Impact. *Annual Reviews in Fluid Mechanics*, 20(1):159–185, 1988.
- [8] B. Yim. Linear theory on water entry and exit problems of a ventilating thin wedge. *Journal of Ship Research*, 18(1):pp. 1–11, 1974.
- [9] A G Terent'ev. Oblique entry of a thin body into incompressible liquid. *Izv. Akad. Nauk SSSR Mekh. Zhidk. Gaza*, 5:16–24, 1977.
- [10] D.P. Wang. Water entry and exit of a fully ventilated foil. *Journal of Ship Research*, 21:pp. 44–68, 1977.
- [11] D.P. Wang. Oblique water entry and exit of a fully ventilated foil. *Journal of Ship Research*, 23:pp. 43–54, 1979.
- [12] O. M. Faltinsen and Y. A.. Semenov. Nonlinear problem of flat-plate entry into an incompressible liquid. *Journal of Fluid Mechanics*, 611:151–173, 2008.

- [13] B. Cox. *Hydrofoil Theory for Vertical Water Entry*. PhD thesis, Department of Naval Architecture, MIT, May 1971.
- [14] V. Vinayan, S. A. Kinnas, and Y.-H. Yu. Modeling of the flow around FPSO hull sections subject to roll motion: Effect of nonlinear boundary conditions. *Proceedings 24th Int. Conference of Offshore Mech. and Arct. Eng.(OMAE2005), Halkidiki, Greece*, 3:805–815, 2005.
- [15] V. Vinayan and S. A. Kinnas. A BEM for the propagation of nonlinear planar free-surface waves. *Electronic Journal of Boundary Elements*, 5(1):pp 17–40, 2007.
- [16] V. Vinayan and S. A. Kinnas. Numerical modeling of surface piercing hydrofoils and propellers. In *Proceedings of the 27th Symposium on Naval Hydrodynamics*, Seoul, Korea, October 2008.
- [17] M. S. Longuet-Higgins and E. D. Cokelet. The deformation of steep surface waves on water. I. A numerical method of computation. *Proceedings of the Royal Society of London. Series A, Mathematical and Physical Sciences*, 350(1660):1–26, July 30 1976.
- [18] C. M. Savineau. A time marching boundary element method for the prediction of the flow around surface piercing hydrofoils. Master's thesis, Department of Ocean Engineering, MIT, February 1996.
- [19] C. Savineau and S. Kinnas. A numerical formulation applicable to surface piercing hydrofoils and propellers. In *24th American Towing Tank Conference*, Texas A&M University, College Station, TX, 1995.
- [20] H. Kihara. Numerical modeling of flow in water entry of a wedge. In *Nineteenth IWWWFB*, Cortona, Italy, 2004.
- [21] H. Sun and O. M. Faltinsen. The influence of gravity on the performance of planing vessels in calm water. *Engineering Mathematics*, 2007.
- [22] Z. N. Dobrovolskaya. On some problems of similarity flow of fluid with a free surface. *Journal of Fluid Mechanics*, 36:pp. 805–829, 1969.
- [23] P. R. Garabedian. Oblique Water Entry of a Wedge. *Communications on Pure and Applied Mathematics*, 6:157–165, 1953.
- [24] A. G. Mackie. The Water Entry Problem. *Q J Mechanics Appl Math*, 22(1):1–17, 1969.

On the Effective Elastic Properties of Composite Medium by BEM

Sonia Parvanova and Gospodin Gospodinov

Department of Civil Engineering, University of Architecture Civil Engineering and Geodesy
1 Hristo Smirnenski blv, 1046 Sofia, Bulgaria, slp_fce@uacg.bg, gospgosp_fr@uacg.bg

Keywords: Boundary elements, Effective elastic properties, Composite medium

Abstract An efficient 2D boundary element method is applied in this paper as a micromechanical tool for predicting the effective elastic properties of composite medium. In this way the analysis of macroscopic heterogeneous composite structure can be performed on the equivalent homogeneous system with the calculated effective orthotropic properties. The present micromechanical numerical simulations have been carried out on a smallest volume of the heterogeneous material. That is a unit cell square plate with known material properties of matrix and fiber constituents and it is shown that the BEM is very well suited for the case considered. Few types of boundary conditions are explored, namely: homogeneous displacement, homogeneous traction and periodic (mixed). It is demonstrated that by increasing the number of inclusions in the unit volume, the apparent engineering moduli in the first two cases of boundary conditions converge to the effective moduli, obtained for the case of periodic type boundary conditions having a single inclusion only.

1. Introduction

The composites consist of the matrix and inclusions like fibers, particles, voids or cracks [1]. In particular the fiber-reinforced composites are widely used in engineering applications due to their superior mechanical performance [2]. In this class of materials, interphases are often presented between the fibers and the surrounding matrix due to some well-known reasons such as protective coating of the fibers and chemical reactions during the manufacturing process. Although small in thickness, the interphases have significant effects on the micromechanical behavior as well as on the overall macroscopic properties of the fiber-reinforced composites [3].

Generally, the inclusions are distributed in matrix randomly. For the sake of simplification, it is regarded that the inclusions have uniform and periodic distribution in the matrix. In this way, the composite is considered as an assembled body with periodic unit cells. A unit cell is a repeatable cell of the composite material and its statistical characters, for example, the volume fraction, are taken to be the same as those measured in the whole composite - see Fig. 1.

The micromechanical static analyses for prediction of macroscopic moduli of heterogeneous materials are usually performed by means of a powerful numerical approach, namely the finite element method [2,4], or boundary element method [3,5]. Two concepts, concerning the geometric representations of the composite structures and the required boundary conditions, are usually applied. The first one is the concept of representative volume element (RVE), and it is based on the equivalence of homogeneous traction and displacement boundary conditions. The repeating unit cell (RUC) concept, which characterizes periodic heterogeneous materials, is based on combined periodic displacement and traction boundary conditions. The question of the number of inclusions contained in the analyzed heterogeneous subvolume, so it responds like an RVE under the chosen boundary conditions, is very important and needs a special attention [4]. In many cases the DOF for the problem in hand is very big, so an effective variant of numerical method employed is needed. In this paper an effective BE approach is developed for predicting the overall elastic properties of a unidirectional composite having a uniform cell of coated fibers.

2. The application and development of the boundary element method

It is well known that the BEM has been very successfully established and applied in engineering as numerical tool [6], but the development of new advanced techniques nowadays, based on it, is attractive issue in computational mechanics. In paper [7] the present authors presented a nonlinear variant of the dual boundary element method, using a discontinuous double-node linear boundary element. Due to space limitation the details will be omitted, so we shall briefly explain the theoretical idea on which the program extension is made and numerical results are obtained.

Consider a heterogeneous plane structure occupying a finite region Ω_m with an external boundary Γ_m , for which the heterogeneous microstructure constitutes a number of spatially repeated, doubly periodic circular fibers each one having an interphase layer - Fig. 1(a). The material properties of the matrix, fibers and interphases are known and given on the right side of Fig.1 (b).

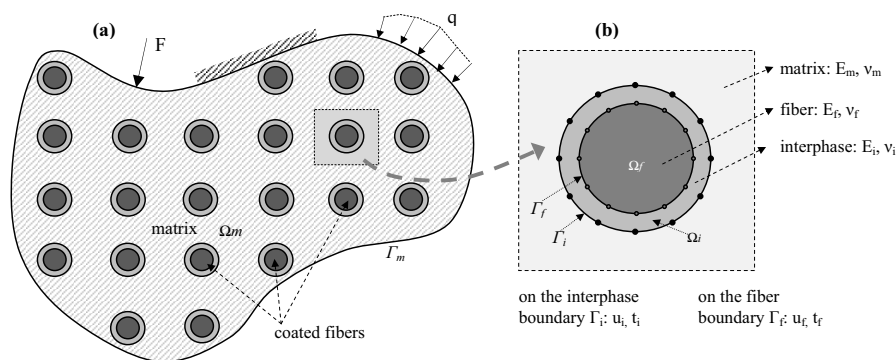


Fig. 1 (a) Unidirectional fiber composite in a plane strain state containing a matrix with number of doubly periodic circular fibers with interphase layer; (b) The BE model of a single inclusion, material data and the boundary traction and displacement vectors

The boundary elements modelling requires a discretization on the external contour Γ_m , fiber and interphase contours ($\Gamma_f + \Gamma_i$) of every single inclusion in the matrix domain Ω_m . On the other hand, additional compatibility and equilibrium conditions must be satisfied on the fiber-interphase and interphase-matrix interfaces. Bearing in mind that the number of inclusions necessary to form a RVE is very large, we need a new computational strategy in order to reduce the DOF and CPU time.

In this study it is presumed that the geometry and elastic properties of the fibers and interphases are identical. Consider a single inclusion composed by two subregions Ω_f and Ω_i and the respective contours Γ_f and Γ_i discretized with boundary elements (Fig. 1 (b)). In the following matrix and vector notations the superscript indicates the subregion (f for Ω_f and i for Ω_i) and the first and the second (if there is a second one) subscripts indicate the boundary where the source point node and the field point node are located.

First, we generate the boundary integral equations and the subsequent system of algebraic equations for the fiber domain itself

$$\mathbf{G}^f \cdot \mathbf{t}_f - \mathbf{H}^f \cdot \mathbf{u}_f = \mathbf{0}, \quad (1) \quad \text{which lead to} \quad \mathbf{t}_f = (\mathbf{G}^f)^{-1} \cdot \mathbf{H}^f \cdot \mathbf{u}_f = \mathbf{C}^f \cdot \mathbf{u}_f, \quad (2)$$

where \mathbf{u}_f and \mathbf{t}_f are the displacement and traction vectors of the contour Γ_f , \mathbf{G}^f and \mathbf{H}^f are the well known BEM influence matrices for the fiber domain Ω_f with boundary Γ_f , and \mathbf{C}^f is a product of influence matrices, which expresses the relation between the tractions and displacements on the fiber boundary Γ_f .

Next, let us consider the interphase subdomain Ω_i having two closed boundaries Γ_f and Γ_i . After the BEM collocation procedure we generate the system of algebraic equations, written in an extended quasi-matrix form, as follows

$$\begin{bmatrix} \mathbf{G}_{ii}^i & \mathbf{G}_{if}^i \\ \mathbf{G}_{fi}^i & \mathbf{G}_{ff}^i \end{bmatrix} \begin{Bmatrix} \mathbf{t}_i \\ \mathbf{t}_f \end{Bmatrix} = \begin{bmatrix} \mathbf{H}_{ii}^i & \mathbf{H}_{if}^i \\ \mathbf{H}_{fi}^i & \mathbf{H}_{ff}^i \end{bmatrix} \begin{Bmatrix} \mathbf{u}_i \\ \mathbf{u}_f \end{Bmatrix}, \quad (3)$$

from which, similarly to eq. (2) we get

$$\begin{Bmatrix} \mathbf{t}_i \\ \mathbf{t}_f \end{Bmatrix} = \begin{bmatrix} \mathbf{G}_{ii}^i & \mathbf{G}_{if}^i \\ \mathbf{G}_{fi}^i & \mathbf{G}_{ff}^i \end{bmatrix}^{-1} \begin{bmatrix} \mathbf{H}_{ii}^i & \mathbf{H}_{if}^i \\ \mathbf{H}_{fi}^i & \mathbf{H}_{ff}^i \end{bmatrix} \begin{Bmatrix} \mathbf{u}_i \\ \mathbf{u}_f \end{Bmatrix} = \begin{bmatrix} \mathbf{C}_{ii}^i & \mathbf{C}_{if}^i \\ \mathbf{C}_{fi}^i & \mathbf{C}_{ff}^i \end{bmatrix} \begin{Bmatrix} \mathbf{u}_i \\ \mathbf{u}_f \end{Bmatrix}. \quad (4)$$

After some simple manipulations of eq. (4) and bearing in mind (2), we arrive at the following final equation

$$\mathbf{t}_i = \left(\mathbf{C}_{ii}^i + \mathbf{C}_{if}^i \cdot (\mathbf{C}^f - \mathbf{C}_{ff}^i)^{-1} \cdot \mathbf{C}_{fi}^i \right) \cdot \mathbf{u}_i. \quad (5)$$

The matrix eq. (5) gives the relationship between the traction \mathbf{t}_i and displacement \mathbf{u}_i vectors on the interphase outer boundary Γ_i . Note that the contribution of the fiber is included in it by involvement of eq. (2). Once the relationship (5) is established in advance for one fiber + interphase inclusion in advance, it is valid for all inclusions, providing their geometry and elastic material properties are identical.

The final analysis step is to perform a boundary element solution for the boundary value problem formulated in Fig. 1 (a). The boundary element discretization is made on the external contour Γ_m and outer interphase contours Γ_i of all inclusions. That is a well established BE procedure, since the inclusions are already treated like openings, but their boundaries are not stress free. The relationship (5) must be included in the boundary element code in order take into account the fiber+interphase contribution. The final boundary elements model is shown in Fig. 2.

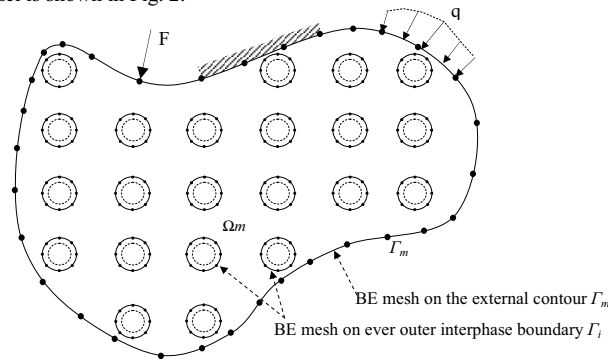


Fig. 2 The final boundary element mesh

3. The effective elastic properties and computational model

Following paper [4], we consider a periodic array of cylindrical inclusions in a square pattern extended to infinity in a plane transverse to the inclusion axis. The smallest repeating unit cell for this array is a square with single inclusion in the center with two orthogonal planes of symmetry - see Fig. 3. We presume a plane strain state, which upon homogenization will yield 3 independent effective moduli - these are the effective transverse Young's modulus $E_1^{eff} = E_2^{eff} = E^{eff}$, the effective shear modulus G_{12}^{eff} , and the effective Poisson's ratio $\nu_{12}^{eff} = \nu_{21}^{eff} = \nu^{eff}$. In this paper we do not deal with the calculation of the effective shear modulus. Therefore, we have to solve the problem given in Fig. 3 for two loading cases: (1) by application of uniform strain or stress in x_1 direction; (2) by application of uniform strain or stress in x_2 direction. In this way we shall generate the necessary two independent equations to calculate E^{eff} and ν^{eff} .

It is shown in [4] that the apparent engineering moduli, obtained by a homogenization procedure performed on a heterogeneous subvolumes under homogeneous displacement and traction boundary conditions (BC) approach the effective moduli of the same subvolumes under periodic BC from above and below by increasing the number of inclusions. Without any details we describe the three types of the boundary conditions with respect to the unit cell square, shown in Fig. 3.

Homogeneous displacement boundary conditions

If we choose the first loading case by the application of $\epsilon_{11}^0 = const.$ and $\epsilon_{22}^0 = 0$, that will lead to the following displacement boundary conditions on the boundaries S_1, S_2, S_3 and S_4 (Fig. 3 (a)):

$$\begin{aligned} u_1(S_1) &= \varepsilon_{11}^0 a / 2, & u_1(S_3) &= -\varepsilon_{11}^0 a / 2, & u_1(S_2) &= \varepsilon_{11}^0 x_1, & u_1(S_4) &= \varepsilon_{11}^0 x_1, \\ u_2(S_1) &= 0, & u_2(S_3) &= 0, & u_2(S_2) &= 0, & u_2(S_4) &= 0. \end{aligned} \quad (6)$$

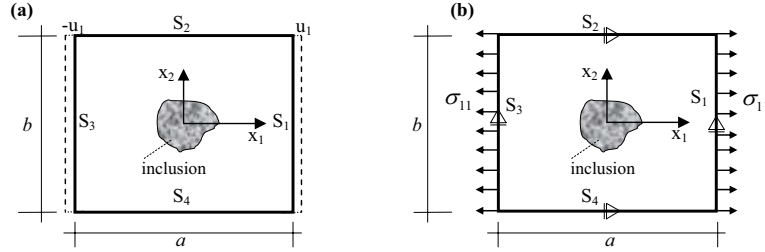


Fig. 3 Unit cell with inclusion: (a) Displacement boundary conditions; (b) Traction boundary conditions

By using the definition of the volume average stresses in RVE and applying the divergence theorem [4,5], the volume average stresses $\bar{\sigma}_{11}$ and $\bar{\sigma}_{22}$ can be expressed in terms of the boundary tractions only (the symmetry conditions are taken into account):

$$\bar{\sigma}_{11} = \frac{1}{V} \int_S T_1 x_1 dS = \frac{1}{ab} \left(a \int_{S_1} t_1 dx_2 + 2 \int_{S_2} t_1 x_1 dx_1 \right), \quad \bar{\sigma}_{22} = \frac{1}{V} \int_S T_2 x_2 dS = \frac{1}{ab} \left(2 \int_{S_3} t_2 x_2 dx_2 + b \int_{S_4} t_2 dx_1 \right). \quad (7)$$

Accordingly, the second loading case follows the same pattern by applying the procedure in x_2 direction.

Homogeneous traction boundary conditions

The first loading case is treated again by the application of the boundary stresses $\sigma_{11}^0 = \text{const.}$ and $\sigma_{22}^0 = 0$, which will lead to the following traction boundary conditions (Fig. 3 (b)):

$$\sigma_{11}(S_1) = \sigma_{11}^0, \quad \sigma_{12}(S_1) = 0; \quad \sigma_{22}(S_2) = \sigma_{12}(S_2) = 0; \quad \sigma_{11}(S_3) = \sigma_{11}^0; \quad \sigma_{12}(S_3) = 0; \quad \sigma_{22}(S_4) = \sigma_{12}(S_4) = 0. \quad (8)$$

The required volume average strains $\bar{\varepsilon}_{11}$ and $\bar{\varepsilon}_{22}$ for this case can be calculated as follows (n_1 and n_2 are the directional cosines of the normal to the boundary):

$$\bar{\varepsilon}_{11} = \frac{1}{2V} \int_S (u_1 n_1 + u_1 n_1) dS = \frac{2}{ab} \int_{S_1} u_1 dx_2, \quad \bar{\varepsilon}_{22} = \frac{1}{2V} \int_S (u_2 n_2 + u_2 n_2) dS = \frac{2}{ab} \int_{S_3} u_2 dx_1. \quad (9)$$

Homogeneous periodic boundary conditions [4]

$$\begin{aligned} u_1(S_1) &= \varepsilon_{11}^0 a / 2, & u_1(S_3) &= -\varepsilon_{11}^0 a / 2, & u_2(S_2) &= 0, & u_2(S_4) &= 0, \\ \sigma_{12}(S_1) &= 0, & \sigma_{12}(S_3) &= 0, & \sigma_{12}(S_2) &= 0, & \sigma_{12}(S_4) &= 0, \end{aligned} \quad (10)$$

and after the solution the required volume average stresses $\bar{\sigma}_{11}$ and $\bar{\sigma}_{22}$ are:

$$\bar{\sigma}_{11} = \frac{1}{V} \int_S T_1 x_1 dS = \frac{1}{ab} \left[a \int_{S_1} t_1 dx_2 \right], \quad \bar{\sigma}_{22} = \frac{1}{V} \int_S T_2 x_2 dS = \frac{1}{ab} \left[b \int_{S_3} t_2 dx_1 \right]. \quad (11)$$

Calculation of the effective elastic properties

The calculated volume average stresses and strains for the "effective RVE" can be expressed through the compliance-based generalized Hooke's law $\bar{\varepsilon}_{ij} = \bar{S}_{ijkl} \bar{\sigma}_{kl}$, where \bar{S}_{ijkl} are the elements of effective compliance tensor. For the case of plane stress state we have:

$$\begin{aligned} \bar{\varepsilon}_{11} &= \bar{\sigma}_{11} \bar{S}_{1111} + \bar{\sigma}_{22} \bar{S}_{1122} = \bar{\sigma}_{11} \frac{1}{E_1^{\text{eff}}} - \bar{\sigma}_{22} \frac{\nu_{21}^{\text{eff}}}{E_2^{\text{eff}}}, \\ \bar{\varepsilon}_{22} &= \bar{\sigma}_{11} \bar{S}_{2121} + \bar{\sigma}_{22} \bar{S}_{2222} = -\bar{\sigma}_{11} \frac{\nu_{12}^{\text{eff}}}{E_1^{\text{eff}}} + \bar{\sigma}_{22} \frac{1}{E_2^{\text{eff}}}, \end{aligned} \quad (12)$$

and for the case considered we simplify by:

$$\bar{S}_{12} = \bar{S}_{21}, E_1^{eff} = E_2^{eff} = E^{eff}, \nu_{12}^{eff} = \nu_{21}^{eff} = \nu^{eff}. \tag{13}$$

In addition, if the effective constants are obtained under plane strain condition [3], the effective Young's modulus and Poisson's ratio in the transverse direction for the composite should be adjusted by using the following well known relations:

$$E = \frac{1 + 2\nu'}{(1 + \nu')^2} E', \nu = \frac{\nu'}{1 + \nu'}. \tag{14}$$

4. Numerical results and comparisons

In the following example we perform a boundary element analysis to study the effective properties of a glass/epoxy composite with fibers having a coating interphase. The same problem was considered by Wacker et al. [2] and Wang et al. [3], so their results are given in the tables for comparison. The fiber to matrix volume ratio is 0.5 and the elastic properties of the constituent materials are as follows (see Fig. 4): epoxy matrix - $E_m=4$ GPa, $\nu_m=0.34$; E-glass fiber - $E_f=84$ GPa, $\nu_f=0.34$. We assume a plain strain condition and consider five different Young's moduli for the interphases: $E_i=4, 6, 8, 12, 84$ GPa, $\nu_i=0.34$. All inclusions have identical radius $r_0=8.5 \mu m$, whereas the radius of the interphase is $r_1=9.5 \mu m$. The dimensions of the unit cell square are: $a=b= 21.30634 \mu m$.

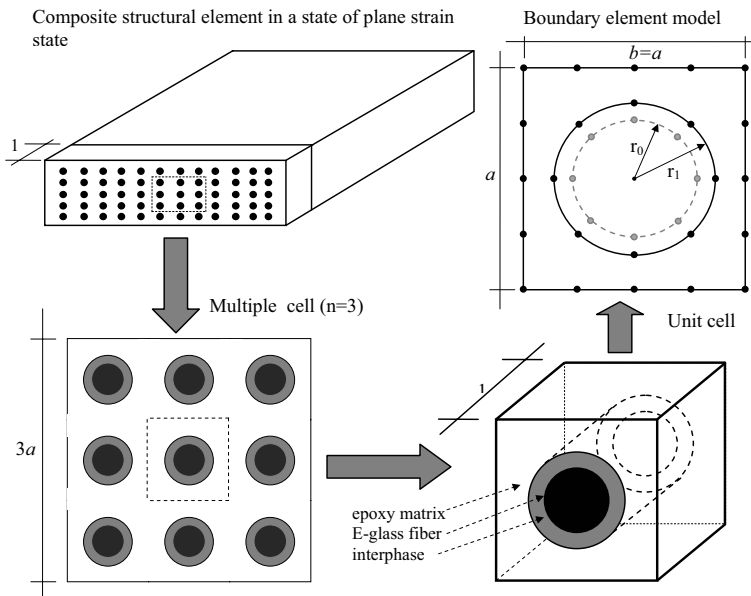


Fig.4 Unidirectional fiber composite structural element and the boundary element model

By using periodic boundary conditions a boundary element analysis was performed on the unit cell model for all different values of E_i and the results for the effective elastic properties (E^{eff} and ν^{eff}) are given in tables 1 and 2. It is worth noting that the present results are in good agreement with the results, given in references [2] and [3]. A FEM simulation using ANSYS was also carried out and the results for the effective Poisson's ratio are given in Table 2.

Table 1: Results for E^{eff} for different E_i values

E_i (GPa)	Ref. [2]	Ref. [3]	Present
4	12.25	12.137	12.096
6	13.71	13.686	13.635
8	14.68	14.645	14.586
12	15.91	15.773	15.704
84	-	-	18.222

Table 2: Results for ν^{eff} for different E_i values

E_i (GPa)	FEM (ANSYS)	Present
4	0.253	0.253
6	0.244	0.244
8	0.238	0.238
12	0.231	0.231
84	-	0.219

Fig. 5 demonstrates the asymptotic behaviour of the two effective moduli E^{eff} and ν^{eff} , to the corresponding periodic values (received for a unit cell RVE) with increasing number of inclusions n^2 (n in this case is the number of inclusions for one row/column of a multiple cell) within RUC subjected to homogeneous displacement and homogeneous traction boundary conditions. The boundary element simulations and the homogenization procedure are performed with the value of interphase modulus $E_i=6$ and for 4 cases regarding the number of inclusions n^2 , namely: $n^2=1, 4, 16$ and 36 . As expected [4], the calculated transverse effective Young's moduli using the homogeneous displacement and traction boundary conditions tend to the value of periodic boundary conditions above and below. For the effective Poisson's ratio however this behaviour is reversed. It should be also noted that the results received by applying homogeneous displacement boundary conditions are more accurate if compare to the traction boundary conditions results for the same value of n .

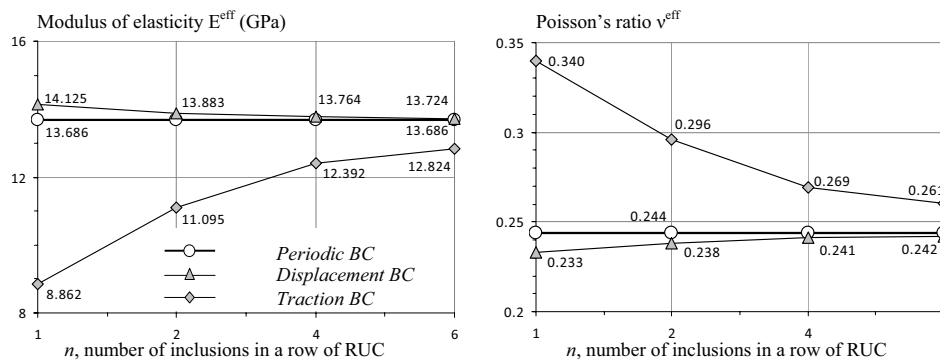


Fig. 5 Comparison of effective engineering moduli of the composite as a function of number of n^2 inclusions in a RUC under homogeneous displacement, traction and periodic boundary conditions

Acknowledgement

This research is financially supported by the Research and Design Centre of the University of Architecture, Civil Engineering and Geodesy, Sofia, Bulgaria.

References

- [1] D. Gross and T. Seelig. *Fracture Mechanics with an Introduction to Micromechanics*. Springer-Verlag, Berlin, Heidelberg, 2006.
- [2] G. Wacker, A. Bledzki, A. Chate. Effect of interphase on the trasverse Young_s modulus of glass/epoxy composites. *Composites Part A*, 29A, 619–26, 1998.
- [3] J. Wang, S. Crouch, S. Mogilevskaia, Numerical modeling of the elastic behavior of fiber-reinforced composites with inhomogeneous interphases. *Composites Science and Technology*, 66, 1-18, 2006.
- [4] A. Drago and M. Pindera. Micro-macromechanical analysis of heterogeneous materials: Macroscopically homogeneous vs periodic microstructures. *Composites Science and Technology*, 67, 1243–1263, 2007.
- [5] C. Y. Dong. Effective elastic properties of doubly periodic array of inclusions of various shapes by the boundary element method. *International Journal of Solids and Structures*, 43, 7919-7938, 2002.
- [6] M. H. Aliabadi. *Boundary Element Method, Volume 2: Applications in Solids and Structures*. John Wiley and Sons Ltd., London, 2002.
- [7] S. Parvanova and G. Gospodinov, *Dual Boundary Elements for Crack Propagation by Means of Linear Fracture Mechanics*, Proceedings of Beteq 2007, Naples, Italy, (2007).

Fast Time Dependent Boundary Element Method based on ACA and the Convolution Quadrature Method

Martin Schanz^{1,a}, Matthias Messner^{1,b}

¹Institute for Applied Mechanics, Technikerstraße 4/II, 8010 Graz, Austria

^am.schanz@tugraz.at, ^bm.messner@tugraz.at,

Keywords: Time domain BEM, CQM, ACA, 3-d elastodynamics

Abstract. Focusing on wave propagation problems a formulation in time domain is preferable. But, it is also well known that the BEM with its dense matrices becomes prohibitive with respect to storage and computing time. Several approaches have been developed to overcome these drawbacks. Approaches, such as Fast Multipole and Panel Clustering gain their efficiency basically from an analytic kernel approximation. The main difficulty of these methods is that the so called degenerate kernel has to be known explicitly.

Hence, the present work focuses on a purely algebraic approach, the adaptive cross approximation (ACA). This technique has been applied successfully to elliptic problems. That is why the time discretisation is done with the Convolution Quadrature Method resulting in uncoupled problems in Laplace domain with a straight forward representation of the time dependent solution. This methodology is introduced and one example is presented.

Introduction

Boundary Element formulations for wave propagation in elastic continua have been published in time domain based essentially on the work of Mansur. Beside this formulation direct in time domain the calculation can also be performed in Laplace or Fourier domain with an inverse transformation. Alternatively, there exists the possibility to utilize the Convolution Quadrature Method (CQM) proposed by Lubich [6]. BE formulation based on this technique (see [8]) result in the same time stepping procedure which requires the storage of the system matrices for all time steps. Fast methodologies for time domain result often in very complicated expansion formulas for the integral kernels [7] and may also destroy the linear complexity of the technique with respect to the time steps [4].

With a different view on the CQM the time stepping algorithm can be transformed in a calculation of decoupled problems in Laplace domain preserving all advantages of the CQM. This idea to reformulate the CQM has been published by Banjai and Sauter [1] for the Helmholtz-equation in acoustics. Hence, all fast techniques known for elliptic problems can be applied within a time stepping formulation.

Here, this reformulation of the CQM will be applied to the elastodynamic boundary integral equations. After briefly stating the necessary boundary integral equations and the introduction of the discretisation, the reformulated CQM will be used to establish a set of decoupled problems in Laplace domain. Next, the adaptive cross approximation (ACA) is applied to each of the elliptic problems. A short numerical example shows that the methodology works.

Throughout this paper, tensorial values are denoted by bold faced letters and matrices/vectors by upright sans serif fonts, e.g., \mathbf{U} . The Laplace transformed function is marked by $\hat{(\)}$.

Boundary integral equation

In a domain $\Omega \subset \mathbb{R}^3$ with the boundary $\Gamma = \partial\Omega$ and $\Gamma = \Gamma_D \cup \Gamma_N$ a mixed elastodynamic boundary value problem in the time domain is formulated

$$\begin{aligned} -(\lambda + \mu)\nabla\nabla \cdot \mathbf{u}(\tilde{\mathbf{x}}, t) - \mu\Delta\mathbf{u}(\tilde{\mathbf{x}}, t) &= -\rho\ddot{\mathbf{u}}(\tilde{\mathbf{x}}, t) & \tilde{\mathbf{x}} \in \Omega \\ \mathbf{u}(\mathbf{y}, t) &= \mathbf{g}_D(\mathbf{y}, t) & \mathbf{y} \in \Gamma_D \\ \mathbf{t}(\mathbf{y}, t) = (\mathcal{T}_y\mathbf{u})(\mathbf{y}, t) &= \mathbf{g}_N(\mathbf{y}, t) & \mathbf{y} \in \Gamma_N \\ \mathbf{u}(\tilde{\mathbf{x}}, t = 0) = \dot{\mathbf{u}}(\tilde{\mathbf{x}}, t = 0) &= 0 & \tilde{\mathbf{x}} \in \Omega, \end{aligned} \quad (1)$$

with ∇ and Δ denoting the Nabla and Laplace operator, respectively, and overdots denote the derivative with respect to time. In (1), the surface displacements $\mathbf{u}(\mathbf{y}, t)$ and tractions $\mathbf{t}(\mathbf{y}, t)$ are prescribed by some given data $\mathbf{g}_D(\mathbf{y}, t)$ on Γ_D and $\mathbf{g}_N(\mathbf{y}, t)$ on Γ_N , respectively. The stress operator \mathcal{T}_y describes the stress-strain relation based on Hooke's law. λ and μ are the Lamé constants. For a given time t the displacement field $\mathbf{u}(\tilde{\mathbf{x}}, t)$ at an interior point $\tilde{\mathbf{x}} \in \Omega$ is given by the representation formula

$$\mathbf{u}(\tilde{\mathbf{x}}, t) = \int_{\Gamma} \mathbf{U}(\mathbf{y} - \tilde{\mathbf{x}}, t) * (\mathcal{T}_y\mathbf{u})(\mathbf{y}, t) \, d\Gamma - \int_{\Gamma} (\mathcal{T}_y\mathbf{U})^T(\mathbf{y} - \tilde{\mathbf{x}}, t)\mathbf{u}(\mathbf{y}, t) \, d\Gamma \quad (2)$$

with the fundamental solution $\mathbf{U}(\mathbf{y} - \tilde{\mathbf{x}}, t)$ and the $*$ denotes the convolution in time. In order to obtain the symmetric boundary integral formulation both boundary integral equations (BIEs) are needed. The first one is derived by performing a limiting process $\mathbf{u}(\mathbf{x}, t) := \lim_{\Omega \ni \tilde{\mathbf{x}} \rightarrow \mathbf{x} \in \Gamma} \mathbf{u}(\tilde{\mathbf{x}}, t)$ on (2). The second one is derived by applying the traction operator to (2) and performing a limiting process $\mathbf{t}(\mathbf{x}, t) := \lim_{\Omega \ni \tilde{\mathbf{x}} \rightarrow \mathbf{x} \in \Gamma} (\mathcal{T}_x\mathbf{u})(\tilde{\mathbf{x}}, t)$ on it. By using the first BIE on Γ_D and the second BIE on Γ_N the variational form of the symmetric Galerkin formulation for the unknown Cauchy data $\tilde{\mathbf{u}}(\mathbf{x}, t)$ and $\tilde{\mathbf{t}}(\mathbf{x}, t)$ is introduced

$$\begin{aligned} \langle \mathcal{V} * \tilde{\mathbf{t}}, \mathbf{w} \rangle_{\Gamma_D} - \langle \mathcal{K} * \tilde{\mathbf{u}}, \mathbf{w} \rangle_{\Gamma_D} &= \langle \mathbf{f}_D, \mathbf{w} \rangle_{\Gamma_D} & \text{with} & \quad \mathbf{f}_D = \left(\frac{1}{2}\mathcal{I} + \mathcal{K}\right) * \mathbf{g}_D - \mathcal{V} * \mathbf{g}_N \\ \langle \mathcal{K}' * \tilde{\mathbf{t}}, \mathbf{v} \rangle_{\Gamma_N} + \langle \mathcal{D} * \tilde{\mathbf{u}}, \mathbf{v} \rangle_{\Gamma_N} &= \langle \mathbf{f}_N, \mathbf{v} \rangle_{\Gamma_N} & & \quad \mathbf{f}_N = \left(\frac{1}{2}\mathcal{I} - \mathcal{K}'\right) * \mathbf{g}_N - \mathcal{D} * \mathbf{g}_D \end{aligned} \quad (3)$$

using some appropriate test functions $\mathbf{w}(\mathbf{x})$ and $\mathbf{v}(\mathbf{x})$. The operators \mathcal{V} , \mathcal{K} , \mathcal{K}' , and \mathcal{D} denote the single layer, double layer, adjoint double layer operator, and the hyper-singular integral operator, respectively. Special care has to be taken when treating the different singularities within these operators [5].

Boundary Element formulation

A boundary element formulation is achieved following the usual procedure. First, the boundary surface Γ is discretised by elements where polynomial shape functions are defined. These are chosen to be linear for the displacements defined on F nodes and constant for the tractions defined on E elements. The semi-discretised form of (3) can then be written in a linear block equation system

$$\begin{bmatrix} \mathbf{V} & -\mathbf{K} \\ \mathbf{K}^T & \mathbf{D} \end{bmatrix} * \begin{bmatrix} \mathbf{t} \\ \mathbf{u} \end{bmatrix} = \begin{bmatrix} \mathbf{f}_D \\ \mathbf{f}_N \end{bmatrix} \quad (4)$$

where $\mathbf{V} \in \mathbb{R}^{F \times F}$, $\mathbf{K} \in \mathbb{R}^{F \times E}$, and $\mathbf{D} \in \mathbb{R}^{E \times E}$ are dense matrices.

Beside the spatial discretisation also a time discretisation is necessary. Here, the CQM is used. As usual in CQM based boundary element formulations N intervals of equal duration Δt are used. Further, an A-stable multistep method has to be chosen where the quotient of the characteristic polynomials is denoted by $\gamma(z)$. These steps result in the following boundary element time stepping formulation for $n = 0, 1, \dots, N-1$

$$\sum_{k=0}^n \frac{\mathcal{R}^{-(n-k)}}{L} \sum_{\ell=0}^{L-1} \begin{bmatrix} \hat{V}(s_\ell) & -\hat{K}(s_\ell) \\ \hat{K}^T(s_\ell) & \hat{D}(s_\ell) \end{bmatrix} \begin{bmatrix} \mathbf{t}(k\Delta t) \\ \mathbf{u}(k\Delta t) \end{bmatrix} \zeta^{-(n-k)\ell} = \begin{bmatrix} \mathbf{f}_D(n\Delta t) \\ \mathbf{f}_N(n\Delta t) \end{bmatrix} \quad s_\ell = \frac{\gamma(\zeta^\ell \mathcal{R})}{\Delta t} \quad \zeta = e^{\frac{2\pi i}{L}}. \quad (5)$$

Different to older publications on this topic, the integration weights of the CQM are not abbreviated with ω_{n-k} , instead they are explicitly inserted in (5). In the right hand side of (5) the same operations as on the left hand side are performed, however, for the sake of brevity it is not written explicitly.

Now, it should be remembered that the integration weights are set to zero for negative indices, i.e., the causality is ensured. This can be used such that the sum over k can be extended to $L-1$. This requires that n is always smaller than $L-1$, which is ensured because L is usually chosen as N to use the techniques known from FFT (for details see [8]). The two sums in (5) are exchanged. Further, \mathcal{R} as well as ζ have the exponent $n-k$ and are splitted in two expressions with the exponents k and n separately. These operations yield

$$\frac{\mathcal{R}^{-n}}{L} \sum_{\ell=0}^{L-1} \begin{bmatrix} \hat{V}(s_\ell) & -\hat{K}(s_\ell) \\ \hat{K}^T(s_\ell) & \hat{D}(s_\ell) \end{bmatrix} \sum_{k=0}^{L-1} \mathcal{R}^k \begin{bmatrix} \mathbf{t}(k\Delta t) \\ \mathbf{u}(k\Delta t) \end{bmatrix} \zeta^{k\ell} = \begin{bmatrix} \mathbf{f}_D(n\Delta t) \\ \mathbf{f}_N(n\Delta t) \end{bmatrix}. \quad (6)$$

Both inner sums can be seen as a weighted FFT of the time dependent nodal values. These expression will be abbreviated with

$$\mathbf{u}_\ell^* = \sum_{k=0}^{L-1} \mathcal{R}^k \mathbf{u}(k\Delta t) \zeta^{k\ell} \quad \mathbf{t}_\ell^* = \sum_{k=0}^{L-1} \mathcal{R}^k \mathbf{t}(k\Delta t) \zeta^{k\ell}, \quad (7)$$

where the respective inverse operation is

$$\mathbf{u}(n\Delta t) = \frac{\mathcal{R}^{-n}}{L} \sum_{\ell=0}^{L-1} \mathbf{u}_\ell^* \zeta^{-n\ell} \quad \mathbf{t}(n\Delta t) = \frac{\mathcal{R}^{-n}}{L} \sum_{\ell=0}^{L-1} \mathbf{t}_\ell^* \zeta^{-n\ell}. \quad (8)$$

With this in mind the hyperbolic integral equation (3) is reduced to the solution of L elliptic problems for the complex 'frequency' $s_\ell, \ell = 0, 1, \dots, L-1$

$$\begin{bmatrix} \hat{V}(s_\ell) & -\hat{K}(s_\ell) \\ \hat{K}^T(s_\ell) & \hat{D}(s_\ell) \end{bmatrix} \begin{bmatrix} \mathbf{t}^*(s_\ell) \\ \mathbf{u}^*(s_\ell) \end{bmatrix} = \begin{bmatrix} \hat{\mathbf{f}}_D(s_\ell) \\ \hat{\mathbf{f}}_N(s_\ell) \end{bmatrix}, \quad (9)$$

with now $\mathbf{V} \in \mathbb{C}^{F \times F}$, $\mathbf{K} \in \mathbb{C}^{F \times E}$, and $\mathbf{D} \in \mathbb{C}^{E \times E}$. Looking closely on the expression ζ in (5) makes it obvious that the equations (7) and (8) can be computed fast with the technique known from the FFT for $L = N$. Further, due to the structure of s_ℓ in (5) only $L/2$ problems have to be solved because the other half is determined as the complex conjugate solution. Finally, the time dependent response is achieved with (8).

Adaptive cross approximation

As mentioned above the matrices in (9) are dense but, fortunately, the system (9) is elliptic. For such systems several fast techniques are available.

The aim is to find an algorithm which allows to describe them in a data sparse way within a prescribed accuracy ε . Due to the fact that the kernel functions κ of the operators in (3) are asymptotically smooth, the \mathcal{H} -matrix format [3] can be applied to the matrices of (9). For a standard matrix the kernel function κ is evaluated on the whole block $X_{\mathcal{J}} \times Y_{\mathcal{J}}$ with the matrix index sets \mathcal{I} and \mathcal{J} . However, when using \mathcal{H} -matrices κ can be evaluated on subblocks $X_t \times Y_s$ with $t \subset \mathcal{I}, s \subset \mathcal{J}$, which are found by a hierarchical subdivision of the initial matrix block based on geometrical considerations. Each subblock A is imposed to the admissibility condition

$$\min\{\text{diam}Y_t, \text{diam}X_s\} < \eta \text{dist}\{X_s, Y_t\}, \quad (10)$$

where $0 < \eta < 1$ is a given admissibility parameter. If this condition holds, A can be approximated by a low rank matrix $\tilde{A}_k = UV$ with $U \in \mathbb{C}^{t \times k}$ and $V \in \mathbb{C}^{s \times k}$ of rank k . Otherwise A will have its full rank.

Since possible low rank blocks of the the matrices in (9) are identified now, several approximation algorithms can be applied. Methods such as Fast Multipole, Panel Clustering etc. are based on a direct decomposition of the generating kernel into a finite sum of separable functions. Since the adaptation of an existing code to these methods is rather invasive, in this work an algebraic method, namely the Adaptive Cross Approximation (ACA) [2] is used. Hereby, the large advantage is that only some matrix entries based on the algorithms choice must be computed. Basically, an admissible subblock is decomposed into $A = \tilde{A}_k + R_k$, with the low rank approximant \tilde{A}_k and the residual R_k . In every iteration step v an additional dyadic product $u^{(v)}v^{(v)T}$ is determined by the largest residual value, the so called pivot value. Adding it to the so far computed approximant $\tilde{A}_k = \sum_{i=0}^{v-1} u^{(i)}v^{(i)T} + u^{(v)}v^{(v)T}$ increases its rank $k = v$ and reduces R_k until the stopping criterion

$$\|u^{(v)}\|_F \|v^{(v)}\|_F \leq \varepsilon \|\tilde{A}_k\|_F \quad (11)$$

holds. However, when dealing with elastodynamics the entries are not scalar but matrix valued. Since a matrix valued ACA did not converge, due to the difficulties of finding the pivot entries and of normalizing them, in this work the matrices in (9) are repartitioned for all degrees of freedom. Thus, for the symmetric $(V)_{ij}$ and $(D)_{ij}$ six, and for $(K)_{ij}$ nine equally structured \mathcal{H} -matrices must be stored. Then, these \mathcal{H} -matrices can be approximated sequentially by using a standard ACA.

Numerical examples

A one dimensional (1-d) column of length 3 m as sketched in figure 1(a) is considered. At the top, the stress vector $t_y = -1 \text{ N/m}^2 H(t)$ is prescribed and the bottom is fixed. This 1-d column has been solved analytically and its result is compared to the boundary element solution for a 3-d rod ($3 \text{ m} \times 1 \text{ m} \times 1 \text{ m}$, for the mesh see 1(b)). Material data used are those of steel modified with Poisson's ratio set to zero ($E = 2.11 \cdot 10^{11} \text{ N/m}^2, \nu = 0, \rho = 7850 \text{ kg/m}^3$). For the underlying multistep method $\gamma(z)$ a BDF 2 and $L = N$ is chosen as suggested in [8].

In Fig. 2, the traction in the mid point of the fixed bottom is plotted versus time for different ε of the ACA-algorithm. The largest $\varepsilon = 10^{-2}$ shows deviations from the final solution, whereas for higher precision the final solution is not influenced. It should be mentioned that the same precision ε is used for the iterative solver. The compression rates of the hyper-singular operator, which is the largest matrix in this example, are presented in Fig. 3 versus the frequency steps. To give an idea about the values of the used frequencies a few special steps are given in the figure. It can be clearly observed that there is a frequency range where the compression is bad. On the other hand, the example is not large enough such that the methodology can show its power.

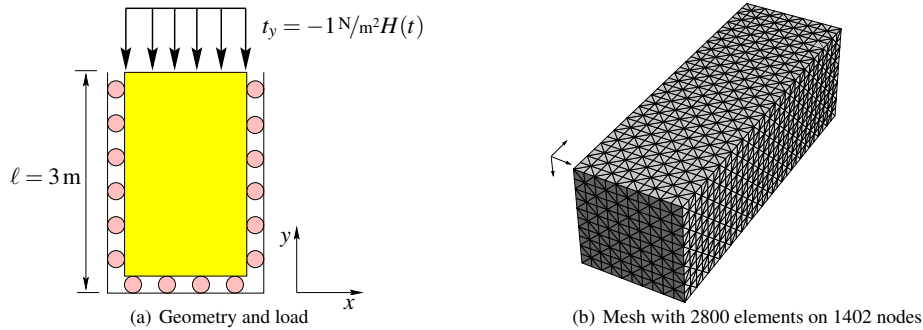


Figure 1: Geometry, loading and the mesh of the column

Conclusions

A reformulated version of the Convolution Quadrature Method has been applied to the elastodynamic boundary integral equation in time domain. Overall the presented methodology reduces the storage requirement to the size of one complex valued system matrix and shows the same sensitivity on the time step size as the older formulation presented in [8]. The price to be paid for this reduction in storage is that in each step the system of equations has to be solved. For each elliptic problem ACA is applied to reduce computation and storage further.

References

- [1] L. Banjai and S. Sauter. Rapid solution of the wave equation in unbounded domains. *SIAM J. Numer. Anal.*, 47(1):227–249, 2009.
- [2] M. Bebendorf. Approximation of Boundary Element matrixes. *Numer. Math.*, 86(4):565–589, 2000.
- [3] W. Hackbusch. A sparse matrix arithmetic based on \mathcal{H} -matrices. part I: Introduction to \mathcal{H} -matrices. *Computing*, 62:89–108, 1999.
- [4] W. Hackbusch, W. Kress, and S. A. Sauter. Sparse convolution quadrature for time domain boundary integral formulations of the wave equation by cutoff and panel-clustering. In M. Schanz and O. Steinbach, editors, *Boundary Element Analysis: Mathematical Aspects and Applications*, volume 29 of *Lecture Notes in Applied and Computational Mechanics*, pages 113–134. Springer-Verlag, Berlin Heidelberg, 2007.
- [5] L. Kielhorn and M. Schanz. Convolution quadrature method based symmetric Galerkin boundary element method for 3-d elastodynamics. *Int. J. Numer. Methods. Engrg.*, 76(11):1724–1746, 2008.
- [6] C. Lubich. Convolution quadrature and discretized operational calculus. I/II. *Numer. Math.*, 52:129–145/413–425, 1988.
- [7] Y. Otani, T. Takahashi, and N. Nishimura. A fast boundary integral equation method for elastodynamics in time domain and its parallelisation. In M. Schanz and O. Steinbach, editors, *Boundary Element Analysis: Mathematical Aspects and Applications*, volume 29 of *Lecture Notes in Applied and Computational Mechanics*, pages 161–185. Springer-Verlag, Berlin Heidelberg, 2007.
- [8] M. Schanz. *Wave Propagation in Viscoelastic and Poroelastic Continua: A Boundary Element Approach*, volume 2 of *Lecture Notes in Applied Mechanics*. Springer-Verlag, Berlin, Heidelberg, New York, 2001.

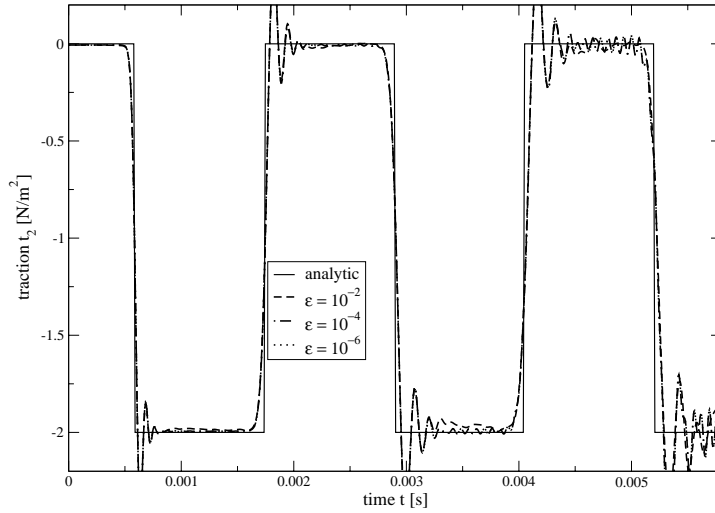


Figure 2: Tractions at the bottom of the column versus time for different precisions of ACA

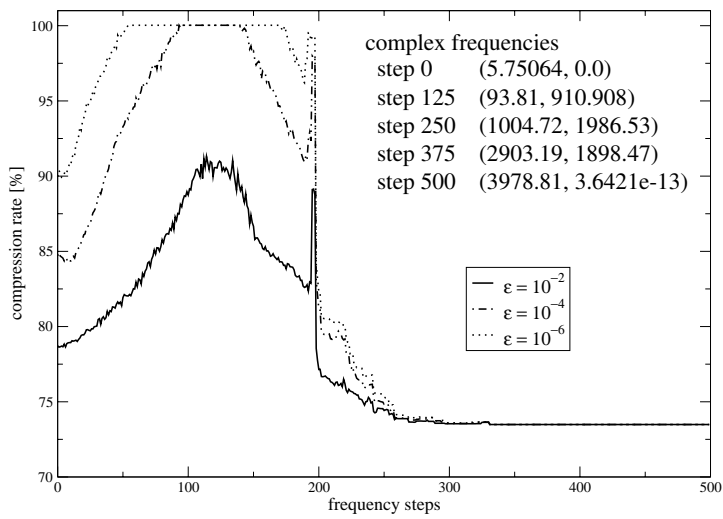


Figure 3: Compression rates of the hyper-singular operator versus the frequency steps

Boundary Integral Equations in Frequency Domain for the Dynamic Behaviour Analysis of Unsaturated Soils

Pooneh Maghoul^a, Behrouz Gatmiri^{b,a}, Denis Duhamel^a

^a Université Paris-Est, Institut Navier, Ecole des Ponts, ParisTech, Marne-la-Vallée, France
Email: Maghoulp@lami.enpc.fr

^b Department of Civil Engineering, University of Tehran, Tehran, Iran
Email: Gatmiri@enpc.fr

Keywords: Boundary element method; Boundary integral equations; fundamental solution; frequency domain; unsaturated soil; porous media; dynamic behaviour

Abstract. In this paper, the boundary integral equations are presented for the set of fully coupled governing differential equations of hydro-mechanical behaviour of unsaturated porous media subjected to dynamic loadings in frequency domain. These boundary integral equations are derived via the use of weighted residuals method for the first time in a way that permits an easy discretization and implementation in a Boundary Element code. The formulation is accomplished using the solid skeleton displacement, water pressure and gas pressure as independent variables.

Introduction

It has long been recognized that surface topographies can have crucial influences on damage severity and its spatial distribution during severe earthquakes. The site effects generated by topographical features are among the sources of amplifications and de-amplifications of the seismic signals, which can be important over large frequency domains. Site response analysis of topographical structures could only be solved accurately, economically and under realistic conditions, with the aid of numerical methods such as the Finite Element Method (FEM), Boundary Element Method (BEM) etc. The FEM is very useful for problems with complex geometries and material properties. However, it has a disadvantage when the problem involves a semi-infinite or infinite domain because of its difficulty in modeling such domains. For example, for domains of infinite extensions, the domain type discretization such as a FE mesh, leads to wave reflections at the edges of the mesh, which could be only partly eliminated for some cases by using the so-called transmitting, silent and non-reflecting viscous boundaries. The BEM, on the other hand, is a very effective numerical tool for dynamic analysis of linear elastic bounded and unbounded media. The method is very attractive for wave propagation problems, because the discretization is done only on the boundary, yielding smaller meshes and systems of equations. Another advantage is that this method represents efficiently the outgoing waves through infinite domains, which is very useful when dealing with scattered waves by topographical structures. When this method is applied to problems with semi-infinite domains, there is no need to model the far field. The two-dimensional wave scattering due to the presence of topographical irregularities has been studied recently with the aid of a hybrid numerical technique, combining finite elements in the near field and boundary elements in the far field by [1, 2 and 3].

The basic idea of BEM consists of the transformation of a partial differential equation into a boundary integral equation and obtaining the fundamental solutions of the corresponding adjoint partial differential equations. Then a system of algebraic equations can be formed by bringing the field point to the surface, discretizing of surface and integrating numerically over it.

The comprehensive state-of-the-art review by [4, 5, and 6] provides clearly presented information on the fundamental solution applied in the saturated soil. For *unsaturated soils*, the first Green functions for the nonlinear governing differential equations for static and quasi-static poroelastic media for both two and three-dimensional problems have been derived by [7, 8 and 9]. The thermo-poro-elastic Green functions for the nonlinear governing differential equations for static and quasi-static poroelastic media for both two and three-dimensional problems have been derived by [10, 11 and 12].

In this paper firstly, the set of fully coupled governing differential equations of hydro-mechanical behaviour of unsaturated porous media including the equilibrium, air and water transfer equations subjected to dynamic loadings is presented based on the suction-based mathematical model presented by [13]. Secondly, the boundary integral equation for multiphase poroelasticity is derived in frequency domain via the use of weighted residuals method for the first time in a way that permits an easy discretization and implementation in a numerical code. The formulation is accomplished using the solid skeleton displacement, water pressure and gas pressure as independent variables.

Governing Equations

An unsaturated soil is represented as the superposition, in time and space, of three continua; the skeleton continuum, the water continuum and the gas continuum.

The displacement field is defined by the displacements of the solid skeleton \mathbf{u} (or u_i) and the displacement of the fluids relative to the solid \mathbf{w}^α (or w_i^α).

Relative Flow Vector of a Fluid Volume. In order to describe the material motion of an unsaturated porous medium, the movement of the α fluid particles relative to the initial configuration of the skeleton now needs to be specified ($\alpha = w, g$). With that purpose in mind let $d\Gamma$ be an infinitesimal skeleton material surface oriented by unit normal \mathbf{n} ($d\Gamma = \mathbf{n} d\Gamma$). At time t and per unit of time, a fluid volume written as

$$q_\alpha d\Gamma = \dot{\mathbf{w}}^\alpha \cdot \mathbf{n} d\Gamma; \quad \alpha = w, g \quad (1)$$

flows through this surface $d\Gamma$ which is followed in the movement of the constituting skeleton particles. The term q_α represents the relative fluid volume flux per unit of surface area. Since \mathbf{w}^α is the displacement vector of the α fluid relative to the solid skeleton, the vector $\dot{\mathbf{w}}^\alpha(\mathbf{x}, t)$ is the Eulerian relative flow vector of fluid volume (with respect to the skeleton) or Darcy flow velocity for α fluid. Next, let $\mathbf{v}^{\alpha,s}(\mathbf{x}, t)$ be the α fluid particle velocity relative to the skeleton particle. From a kinematic point of view, the velocity $\mathbf{v}^{\alpha,s}(\mathbf{x}, t)$ can be written as

$$\mathbf{v}^{\alpha,s} = \mathbf{v}^\alpha - \mathbf{v}^s; \quad \alpha = w, g \quad (2)$$

Where $\mathbf{v}^\alpha(\mathbf{x}, t)$ is the Eulerian absolute fluid velocity and it is equal to $\dot{\mathbf{U}}^\alpha$ in which \mathbf{U}^α is the absolute displacement of the fluids and it is defined in such a way that the volume of fluid displaced through unit area normal to the x_i direction is $nS_\alpha U_i^\alpha$.

Here, the relative velocity $\mathbf{v}^{\alpha,s}(\mathbf{x}, t)$ can be defined from the relative flow vector of fluid volume $\dot{\mathbf{w}}^\alpha$ through the relation

$$\dot{\mathbf{w}}^\alpha = n_\alpha \mathbf{v}^{\alpha,s} = n_\alpha S_\alpha \mathbf{v}^{\alpha,s} = n_\alpha S_\alpha (\dot{\mathbf{U}}^\alpha - \dot{\mathbf{u}}); \quad \alpha = w, g \quad (3)$$

Mass Conservation of Solid Skeleton. The mass of the solid skeleton in a representative elementary volume can be written as

$$(1-n) \frac{d\rho_s}{dt} - \rho_s \frac{dn}{dt} + (1-n) \rho_s \operatorname{div} \mathbf{v}^s = 0 \quad (4)$$

By the hypotheses of the incompressibility of the soil grains, we obtain

$$\frac{dn}{dt} = (1-n) \operatorname{div} \mathbf{v}^s = (1-n) \dot{u}_{i,i} \quad (5)$$

This equation states that the deformation of the solid skeleton consists in the rearrangement of the grains only.

Mass Conservation of Water. The mass of the water in a representative elementary volume can be written as

$$n S_w \frac{d\rho_w}{dt} + n \rho_w \frac{dS_w}{dt} + S_w \rho_w \frac{dn}{dt} + n S_w \rho_w \dot{u}_{i,i}^s + \rho_w \dot{w}_{i,i}^w = \gamma_w^m \quad (6)$$

By the hypotheses of the incompressibility of the soil grains, eq. (5), we obtain

$$\frac{n S_w}{K_w} \frac{dP_w}{dt} + n \frac{dS_w}{dt} + S_w \dot{u}_{i,i} + \dot{w}_{i,i}^w = \gamma_w^v \quad (7)$$

Where $1/K_w = d\rho_w/(\rho_w dP_w)$ and γ_w^V is the source density (the rate of injected fluid volume per unit volume of the porous milieu).

Numerous relations have been introduced to define the degree of saturation of unsaturated soils, but the logarithmic form based on suction variations is one of the most common and reliable ones. Logarithmic form of the degree of saturation is chosen here in the form of:

$$S_w = a_s + b_s \log(P_g - P_w) \quad (8)$$

In which a_s and b_s are constants. By choosing $a_s = 1$ and assuming a negative b_s , one can see that any increase in suction results a decrease in S_w and any decrease in suction results the approach of S_w to one (saturated) [8]. Then, the final mass equation can be written as

$$\dot{W}_{i,i}^w = -S_w \dot{\varepsilon}_{ii} + C_{ww} \dot{P}_w + C_{wg} \dot{P}_g + \gamma_w^V \quad (9)$$

Where $C_{ww} = n(g_1 - S_w/K_w)$ and $C_{wg} = C_{gw} = -n.g_1$ in which $g_1 = dS_w/d(P_g - P_w)$.

Transfer Equation of Water. This equation is written based on the generalized Darcy's law. This equation describes the balance of the forces acting on the liquid phase of representative elementary volume, namely the gradient of suction, the inertia and the resistance force of water due to its viscosity.

$$-P_{w,i} = \rho_w \ddot{u}^s + \frac{\dot{W}^w}{k_w} - \rho_w g \quad (10)$$

Mass Conservation of Gas. With the same approach presented before, the mass conservation of gas can be written as

$$\dot{W}_{i,i}^g = -S_g \dot{\varepsilon}_{ii} + C_{wg} \dot{P}_w + C_{gg} \dot{P}_g + \gamma_g^V \quad (11)$$

Where $C_{gg} = (n.g_1 - n.S_g/K_g)$, $C_{wg} = C_{gw} = -n.g_1$ and $S_g = 1 - S_w$

Transfer Equation of Gas. This equation is written based on the generalized Darcy's law with the same approach presented for the transfer equation of water

$$-P_{g,i} = \rho_g \ddot{u}^s + \frac{\dot{W}^g}{k_g} - \rho_g g \quad (12)$$

Solid Skeleton. The equilibrium equation and the constitutive law for the soil's solid skeleton including the effects of suction [14]:

$$(\sigma_{ij} - \delta_{ij} P_g)_{,j} + P_{g,i} + F_i = \rho \ddot{u}_i \quad (13)$$

$$d(\sigma - \delta P_g) = \mathbf{D} : d\varepsilon - \mathbf{F}_s : \delta d(P_g - P_w) \quad (14)$$

Where $\delta = \delta_{ij}$, $\mathbf{F}_s = \mathbf{D} : (\mathbf{D}^s)^{-1}$, $\mathbf{D} : d\varepsilon = D_{ijkl} d\varepsilon_{kl}$ and $\mathbf{F}_s : \delta d(P_g - P_w) = (F_s)_{,ijkl} \delta_{kl} d(P_g - P_w)$

The constitutive tensor \mathbf{D} for linear elastic behaviour is written as:

$$D_{ijkl} = \lambda \delta_{ij} \delta_{kl} + \mu (\delta_{ik} \delta_{jl} + \delta_{il} \delta_{jk}) \quad (15)$$

Summary of the Governing Differential Equations in Laplace Domain

By introducing Eqs.(14&15) into (13), (10) into (9) and (12) into (11), we obtain the final set of governing equations

$$(\lambda + \mu) u_{\beta,\alpha\beta} + \mu u_{\alpha,\beta\beta} + F_s P_{w,\alpha} + (1 - F_s) P_{g,\alpha} - \rho \ddot{u}_\alpha + f_\alpha = 0 \quad (16)$$

$$-S_w \dot{u}_{\alpha,\alpha} + \rho_w k_w \ddot{u}_{\alpha,\alpha} + k_w P_{w,\alpha\alpha} + C_{ww} \dot{P}_w + C_{wg} \dot{P}_g + \gamma_w^V = 0 \quad (17)$$

$$-S_g \dot{u}_{\alpha,\alpha} + \rho_g k_g \ddot{u}_{\alpha,\alpha} + k_g P_{g,\alpha\alpha} + C_{wg} \dot{P}_w + C_{gg} \dot{P}_g + \gamma_g^V = 0 \quad (18)$$

One of the most common and straightforward methods for eliminating the time variable of a partial differential equation is to apply the Laplace transform. In this manner, after solving the differential equation in Laplace transform domain, one can obtain the time domain solution by applying an inverse Laplace transform on the Laplace transform domain solution. We remember that [15]

$$L \{ f(x,t) \} = \tilde{f}(x,s) = \int_0^\infty e^{-st} f(x,t) dt \quad (19)$$

And assuming $u_{i(t=0)} = w_{i(t=0)}^w = w_{i(t=0)}^g = 0$ and $P_{w(t=0)} = P_{g(t=0)} = 0$, Eqs (16), (17) and (18) will be reduced to

$$(\lambda + \mu)\tilde{u}_{\beta,\alpha\beta} + \tilde{\mu}u_{\alpha,\beta\beta} + F_s\tilde{P}_{w,\alpha} + F_s^g\tilde{P}_{g,\alpha} - \rho \cdot s^2 \cdot \tilde{u}_\alpha + \tilde{f}_\alpha = 0 \tag{20}$$

$$-s \cdot \theta_1 \tilde{u}_{\alpha,\alpha} + k_w \tilde{P}_{w,\alpha\alpha} + C_{ww} \cdot s \cdot \tilde{P}_w + C_{wg} \cdot s \cdot \tilde{P}_g + \tilde{\gamma}_w^V = 0 \tag{21}$$

$$-s \cdot \theta_2 \tilde{u}_{\alpha,\alpha} + C_{wg} \cdot s \cdot \tilde{P}_w + k_g \tilde{P}_{g,\alpha\alpha} + C_{gg} \cdot s \cdot \tilde{P}_g + \tilde{\gamma}_g^V = 0 \tag{22}$$

Where $F_s^g = (1 - F_s)$, $\theta_1 = (S_w - \rho_w \cdot k_w \cdot s)$ and $\theta_2 = (S_g - \rho_g \cdot k_g \cdot s)$.

We would like to rewrite compactly the transformed coupled differential equation system Eqs (20), (21) and (22) into the following matrix form:

$$B_{ij} \tilde{U}_j = \tilde{F}_i \tag{23}$$

Where i, j varies from one to four in two dimensional problems, $\tilde{U}_j = \{\tilde{u}_1, \tilde{u}_2, \tilde{P}_w, \tilde{P}_g\}$ and

$\tilde{F}_i = \{-\tilde{f}_1, -\tilde{f}_2, -\tilde{\gamma}_w^V, -\tilde{\gamma}_g^V\}$. The components of B_{ij} for two dimensional problems are: $B_{i3} = F_s \delta_i$,

$B_{i4} = (1 - F_s) \delta_i$, $B_{ij} = \delta_{ij} (\mu \Delta - \rho s^2) + (\lambda + \mu) \delta_i \delta_j$, $B_{3i} = -s \theta_1 \delta_i$, $B_{33} = k_w \Delta + C_{ww} \cdot s$, $B_{4i} = -s \theta_2 \delta_i$, $B_{44} = k_g \Delta + C_{gg} \cdot s$,

$B_{34} = B_{43} = C_{wg} \cdot s$.

Where $i, j = 1, 2$ and Δ is Laplace operator.

Boundary Integral Equation

There are several methods of deriving the boundary integral equations: the *reciprocal theorem*, the *variational approach* and the *weighted residual concept*. Here, the boundary integral equations for dynamic poro-elastic problem will be derived by taking the fundamental solution as the weighted function and using the method of weighted residuals, which is essentially an integration by parts technique. The advantage of using weighted residuals is its generality in most principles and theories (like Betti's theorem, Green's third identity, virtual work and so on.). It permits the extension of the method to solve more complex partial differential equations. It can also be used to relate boundary elements to other numerical techniques and can be easily understood by engineers [16].

Furthermore, let \mathcal{C}^0 and \mathcal{C}^0^* represent the corresponding fundamental solution and adjoint fundamental solution, respectively, implying that

$$\tilde{B}_{ij} \tilde{G}_{jk} + \delta_{ik} \delta(x - \xi) = 0 \tag{24}$$

$$\tilde{B}_{ij}^* \tilde{G}_{jk}^* + \delta_{ik} \delta(x - \xi) = 0 \tag{25}$$

With Kronecker delta function δ_{ik} , Dirac delta function $\delta(x - \xi)$, and \tilde{B}_{ij}^* as the adjoint differential operator.

To obtain the boundary integral problem, the differential equation (23) is transformed into an integral equation using the method of weighted residuals. On the other hand, a set of integral equations can be derived in a direct manner by equating the inner product of equation (23) and \mathcal{C}_{ik}^0 to a null vector, i.e.

$$\int_V (\tilde{B}_{ij} \tilde{U}_j - \tilde{F}_i) \tilde{G}_{il}^* dV = 0 \quad (i, j, l = 1, 2, 3, 4) \tag{26}$$

Where the integration is performed over the volume V . Substituting \tilde{B}_{ij} , \tilde{U}_j and \tilde{F}_i into Eq.(26) yields

$$\int_V \left[\begin{aligned} &(\lambda + \mu) \tilde{G}_{\alpha j}^* \tilde{u}_{\beta,\beta\alpha} + \mu \tilde{G}_{\alpha j}^* \Delta \tilde{u}_\alpha - \rho \cdot s^2 \cdot \tilde{u}_\alpha \tilde{G}_{\alpha j}^* + F_s \tilde{G}_{\alpha j}^* \tilde{P}_{w,\alpha} + (1 - F_s) \tilde{G}_{\alpha j}^* \tilde{P}_{g,\alpha} \\ &+ k_w \tilde{G}_{3j}^* \Delta \tilde{P}_w - s \cdot \theta_1 \cdot \tilde{G}_{3j}^* \tilde{u}_{\alpha,\alpha} + C_{ww} \cdot s \cdot \tilde{G}_{3j}^* \tilde{P}_w + C_{wg} \cdot s \cdot \tilde{G}_{3j}^* \tilde{P}_g \\ &+ k_g \tilde{G}_{4j}^* \Delta \tilde{P}_g - s \cdot \theta_2 \cdot \tilde{G}_{4j}^* \tilde{u}_{\alpha,\alpha} + C_{wg} \cdot s \cdot \tilde{G}_{4j}^* \tilde{P}_w + C_{gg} \cdot s \cdot \tilde{G}_{4j}^* \tilde{P}_g \\ &-\tilde{F}_i \tilde{G}_{ij}^* \end{aligned} \right] dV \tag{27}$$

For each term in Eq (27), integrating by parts twice over the domain within the inner product to transfer all derivatives from \tilde{U}_j to \mathcal{C}_{ik}^0 and applying divergence theorem respectively, we arrive at:

$$\int_V \mu \tilde{G}_{\alpha j}^* \tilde{u}_{\beta,\beta\alpha} dV = \mu \int_S \tilde{G}_{\alpha j}^* \tilde{u}_{\beta,\alpha} n_\beta dS - \mu \int_S \tilde{G}_{\beta j,\alpha}^* \tilde{u}_\alpha n_\beta dS + \mu \int_V \tilde{G}_{\beta j,\alpha\beta}^* \tilde{u}_\alpha dV \tag{28a}$$

$$\int_V \lambda \tilde{G}_{\alpha j}^* \tilde{u}_{\beta,\beta\alpha} dV = \lambda \int_S \tilde{G}_{\alpha j}^* \tilde{u}_{k,k} n_\beta \delta_{\alpha\beta} dS - \lambda \int_S \tilde{u}_\alpha \tilde{G}_{\beta j,k}^* n_\beta \delta_{\alpha\beta} dS + \lambda \int_V \tilde{u}_\alpha \tilde{G}_{\beta j,\alpha\beta}^* dV \tag{28b}$$

$$\mu \int_V \tilde{G}_{\alpha j}^* \Delta \tilde{u}_\alpha dV = \mu \int_V \tilde{G}_{\alpha j}^* \tilde{u}_{\alpha,\beta\beta} dV = \mu \int_S (\tilde{G}_{\alpha j}^* \tilde{u}_{\alpha,\beta} - \tilde{u}_\alpha \tilde{G}_{\alpha j,\beta}^*) n_\beta dS + \mu \int_S \Delta \tilde{G}_{\beta j}^* \tilde{u}_\alpha dS \tag{28c}$$

$$F_s \int_V \tilde{G}_{\alpha j}^* \tilde{P}_{w,\alpha} dV = F_s \int_S \tilde{G}_{\alpha j}^* \tilde{P}_w n_\beta \delta_{\alpha\beta} dS - F_s \int_V \tilde{G}_{\alpha j,\alpha}^* \tilde{P}_w dV \tag{28d}$$

$$(1 - F_s) \int_V \tilde{G}_{\alpha j}^* \tilde{P}_{g,\alpha} dV = (1 - F_s) \int_S \tilde{G}_{\alpha j}^* \tilde{P}_g n_\beta \delta_{\alpha\beta} dS - (1 - F_s) \int_V \tilde{G}_{\alpha j,\alpha}^* \tilde{P}_g dV \quad (28e)$$

$$k_w \int_V \tilde{G}_{3j}^* \Delta \tilde{P}_w dV = k_w \int_V \tilde{G}_{3j}^* \tilde{P}_{w,\alpha\alpha} dV = k_w \int_S \tilde{G}_{3j}^* \tilde{P}_{w,n} dS - k_w \int_S \tilde{G}_{3j,n}^* \tilde{P}_w + k_w \int_V \Delta \tilde{G}_{3j}^* \tilde{P}_w dV \quad (28f)$$

$$-s.\theta_1 \int_V \tilde{G}_{3j}^* \tilde{u}_{\alpha,\alpha} dV = -s.\theta_1 \int_S \tilde{G}_{3j}^* \tilde{u}_\alpha n_\beta \delta_{\alpha\beta} dS + s.\theta_1 \int_V \tilde{u}_\alpha \tilde{G}_{3j,\alpha}^* dV \quad (28g)$$

$$k_g \int_V \tilde{G}_{4j}^* \Delta \tilde{P}_g dV = k_g \int_V \tilde{G}_{4j}^* \tilde{P}_{g,\alpha\alpha} dV = k_g \int_S \tilde{G}_{4j}^* \tilde{P}_{g,n} dS - k_g \int_S \tilde{G}_{4j,n}^* \tilde{P}_g dS + k_g \int_V \Delta \tilde{G}_{4j}^* \tilde{P}_g dV \quad (28h)$$

$$-s.\theta_2 \int_V \tilde{G}_{4j}^* \tilde{u}_{\alpha,\alpha} dV = -s.\theta_2 \int_S \tilde{G}_{4j}^* \tilde{u}_\alpha n_\beta \delta_{\alpha\beta} dS + s.\theta_2 \int_V \tilde{u}_\alpha \tilde{G}_{4j,\alpha}^* dV \quad (28i)$$

Where $i, j = 1, 2, 3, 4$; $\alpha, \beta, k = 1, 2$.

Substituting Eqs (28a) to (28i) into (27) yields

$$\int_S \left[(\lambda \tilde{u}_{k,k} - F_s (\tilde{P}_g - \tilde{P}_w) + \tilde{P}_g) n_\beta \delta_{\alpha\beta} + \mu (\tilde{u}_{\beta,\alpha} + \tilde{u}_{\alpha,\beta}) n_\beta \right] \tilde{G}_{\alpha j}^* dS - \int_S \tilde{u}_\alpha \left[(\lambda \tilde{G}_{kj,k}^* + s.\theta_1 \tilde{G}_{3j}^* + s.\theta_2 \tilde{G}_{4j}^*) n_\beta \delta_{\alpha\beta} + \mu (\tilde{G}_{\alpha j,\beta}^* + \tilde{G}_{\beta j,\alpha}^*) \right] dS + k_w \int_S (\tilde{P}_{w,n} \tilde{G}_{3j}^* - \tilde{P}_w \tilde{G}_{3j,n}^*) dS + k_g \int_S (\tilde{P}_{g,n} \tilde{G}_{4j}^* - \tilde{P}_g \tilde{G}_{4j,n}^*) dS + \int_V (-\tilde{F}_m + \tilde{U}_i \tilde{B}_{im}^*) \tilde{G}_{mj}^* dV = 0 \quad (29)$$

As mentioned above, \tilde{B}_{im}^* is the adjoint operator of \tilde{B}_{ij} : $B_{13} = s\theta_1 \partial_i$, $B_{14} = s\theta_2 \partial_i$,

$$B_{ij} = \delta_{ij} (\mu \Delta - \rho_w s^2) + (\lambda + \mu) \partial_i \partial_j, \quad B_{3i} = -F_s \partial_i, \quad B_{33} = k_w \Delta + C_{ww} s, \quad B_{4i} = -(1 - F_s) \partial_i, \quad B_{44} = k_g \Delta + C_{gg} s,$$

$$B_{34} = B_{43} = C_{wg} s$$

By substituting Equation (25) into (29) and using the property of Dirac's delta function, and neglecting external forces \tilde{F}_i we arrive at the transformed unsaturated poro-elasto-dynamic boundary integral representation for the transformed internal displacements and pressures i.e.,

$$c_{ij} \tilde{U}_j(\xi, s) = \int_{\Gamma_i} \left[\tilde{t}_\alpha(x, s) \tilde{G}_{\alpha j}^*(x, \xi; s) - \tilde{q}_w(x, s) \tilde{G}_{3j}^*(x, \xi; s) - \tilde{q}_g(x, s) \tilde{G}_{4j}^*(x, \xi; s) \right] d\Gamma_i - \int_{\Gamma_i} \left[\tilde{u}_\alpha(x, s) \tilde{F}_{\alpha j}^*(x, \xi; s) + \tilde{P}_w(x, s) \tilde{F}_{3j}^*(x, \xi; s) + \tilde{P}_g(x, s) \tilde{F}_{4j}^*(x, \xi; s) \right] d\Gamma_i \quad (30)$$

Where

$$\begin{aligned} \tilde{t}_\alpha &= \left[(\lambda \tilde{u}_{k,k} - F_s (\tilde{P}_g - \tilde{P}_w) + \tilde{P}_g) n_\beta \delta_{\alpha\beta} + \mu (\tilde{u}_{\beta,\alpha} + \tilde{u}_{\alpha,\beta}) n_\beta \right] \\ \tilde{q}_w &= -k_w (\tilde{P}_{w,n} + \rho_w s^2 \tilde{u}_\alpha n_\alpha), \quad \tilde{q}_g = -k_g (\tilde{P}_{g,n} + \rho_g s^2 \tilde{u}_\alpha n_\alpha) \\ \tilde{F}_{\alpha j}^* &= \left[(\lambda \tilde{G}_{kj,k}^* + s.S_w \tilde{G}_{3j}^* + s.S_g \tilde{G}_{4j}^*) \delta_{\alpha\beta} + \mu (\tilde{G}_{\alpha j,\beta}^* + \tilde{G}_{\beta j,\alpha}^*) \right] n_\beta \\ \tilde{F}_{3j}^* &= k_w \tilde{G}_{3j,n}^*, \quad \tilde{F}_{4j}^* = k_g \tilde{G}_{4j,n}^* \end{aligned} \quad (31)$$

The matrix c_{ij} depends only upon the local geometry at ξ , and reduces to a generalized delta function $\delta_{\alpha\beta}$

for ξ inside S and to $\frac{1}{2} \delta_{\alpha\beta}$ for ξ on a smooth portion of the boundary surface.

This can be further compacted by generalizing the displacement and traction vector to include pressures and fluids fluxes. Thus, in Eq. (30) for the 2-D case let $\tilde{u}_i = (\tilde{u}_1, \tilde{u}_2, \tilde{P}_w, \tilde{P}_g)^T$, $\tilde{t}_i = (\tilde{t}_1, \tilde{t}_2, \tilde{q}_w, \tilde{q}_g)^T$ and also $\tilde{G}_{\alpha j}^*(x, \xi; s) = \tilde{G}_{\alpha j}^*(x, \xi; s)$, $\tilde{G}_{3j}^*(x, \xi; s) = -\tilde{G}_{3j}^*(x, \xi; s)$, $\tilde{G}_{4j}^*(x, \xi; s) = -\tilde{G}_{4j}^*(x, \xi; s)$, $\tilde{F}_{ij}^*(x, \xi; s) = \tilde{F}_{ij}^*(x, \xi; s)$, $\tilde{F}_{3j}^*(x, \xi; s) = \tilde{F}_{3j}^*(x, \xi; s)$ and $\tilde{F}_{4j}^*(x, \xi; s) = \tilde{F}_{4j}^*(x, \xi; s)$, Eq (30) becomes simply

$$c_{ij} \tilde{U}_j(\xi, s) = \int_S \left[\tilde{t}_i(x, s) \tilde{G}_{ij}^*(x, \xi; s) - \tilde{u}_i(x, s) \tilde{F}_{ij}^*(x, \xi; s) \right] dS \quad (32)$$

By considering the adjoint differential operator \tilde{B}_{im}^* , one finds the kernel functions (fundamental solutions) in Eq. (32) as follows

$$\tilde{G}_{\alpha\beta}^*(x, \xi; p) = \tilde{G}_{\alpha\beta}(x, \xi; p) \quad (33a)$$

$$\tilde{G}_{\alpha 3}^*(x, \xi; p) = -\tilde{G}_{3\alpha}(x, \xi; p) \quad (33b)$$

$$\tilde{G}_{\alpha 4}^*(x, \xi; p) = -\tilde{G}_{4\alpha}(x, \xi; p) \quad (33c)$$

$$\tilde{G}_{3\alpha}^*(x, \xi; p) = -\tilde{G}_{\alpha 3}(x, \xi; p) \quad (33d)$$

$$\tilde{G}_{33}^*(x, \xi; p) = \tilde{G}_{33}(x, \xi; p) \quad (33e)$$

$$\tilde{G}_{34}^*(x, \xi; p) = \tilde{G}_{43}(x, \xi; p) \quad (33f)$$

$$\tilde{G}_{4\alpha}^*(x, \xi; p) = -\tilde{G}_{\alpha 4}(x, \xi; p) \quad (33g)$$

$$\tilde{G}_{43}^*(x, \xi; p) = \tilde{G}_{34}(x, \xi; p) \quad (33h)$$

$$\tilde{G}_{44}^*(x, \xi; p) = \tilde{G}_{44}(x, \xi; p) \quad (33i)$$

Conclusion. In this paper, the boundary integral equations for multiphase poroelastodynamic milieu are derived in frequency domain which can be used for an easy development of BEM codes to solve more practical problems related to the site response analysis of topographical structures.

References

- [1] B.Gatmiri, C. Arson, K.V. Nguyen *Soil Dynamics and Earthquake Engineering* **28(8)**, 632-645 (2008).
- [2] B.Gatmiri, C. Arson *Soil Dynamics and Earthquake Engineering* **28(8)**, 646-661 (2008).
- [3] B.Gatmiri, P.Maghoul, C.Arson *Soil Dynamics and Earthquake Engineering* **29(1)**, 51-70 (2009).
- [4] B.Gatmiri, M.Kamalian *International Journal of Geomechanics* **2(4)**, 381-398 (2002).
- [5] M.Kamalian, B.Gatmiri, M.J.Sharahi *Communications in Numerical Methods in Engineering* **24(9)**, 749-759 (2008).
- [6] B.Gatmiri, K.V.Nguyen *Communications in Numerical Methods in Engineering* **21(3)**, 119-132 (2005).
- [7] B.Gatmiri, E.Jabbari *5th International Conference on Boundary Element Techniques* (M.H.Aliabadi, V.M.A.Leitão), EC:, Lisbon, 217-221 (2004).
- [8] B.Gatmiri, E.Jabbari *International Journal of Solids and Structures* **42(23)**, 5971-5990 (2005).
- [9] B.Gatmiri, E.Jabbari *International Journal of Solids and Structures* **42(23)**, 5991-6002 (2005).
- [10] E.Jabbari, B.Gatmiri *International Journal of Computer Modelling in Engineering and Sciences* **18(1)**, 31-43 (2007).
- [11] B.Gatmiri, P.Maghoul, D.Duhamel *International Journal of Solids and Structures II*. (submitted).
- [12] P.Maghoul, B.Gatmiri, D.Duhamel *International Journal of Numerical and Analytical Methods in Geomechanics* (submitted)
- [13] B.Gatmiri, P.Maghoul, D.Duhamel *International Journal of Solids and Structures I*. (submitted).
- [14] B.Gatmiri, P.Delage, M.Cerrolaza *Advances in Engineering Software* **29(1)**, 29-43 (1998).
- [15] M.Abramowitz, I.A.Stegun *Handbook of Mathematical Functions*, National Bureau of Standards, Washington, D.C. (1965).
- [16] C.A.Brebbia, J.Dominguez *Boundary elements an introductory course*, Second edition, Computational Mechanics Publications, McGraw-Hill (1992).

The Response of an Elastic Half-Space with Circular Trenches Around a Rigid Surface Foundation Subjected to Dynamic Horizontal Loads

Pérsio Leister de Almeida Barros¹ and Euclides Mesquita²

¹University of Campinas, C. P. 6021, CEP 13083-852, Campinas SP, Brazil
persio@fec.unicamp.br

²University of Campinas, C. P. 6122, CEP 13083-970, Campinas, SP, Brazil
euclides@fem.unicamp.br

Keywords: wave propagation, soil-structure interaction, elastodynamics, boundary elements.

Abstract: The dynamic response of a rigid massless disk foundation resting over a (visco-)elastic, transversely isotropic half-space with two concentric cylindrical empty trenches excavated to a certain depth around it, subjected to a time-harmonic dynamic horizontal external load is analyzed. An indirect formulation of the Boundary Element Method, along with a substructuring technique is used. The half-space is divided in an outer and two inner subdomains delimited by the trenches. Those subdomains are modeled separately and then equilibrium and displacements continuity conditions are imposed along the base contact between them. Influence functions, which are elastic solutions distributed loads applied inside a transversely isotropic half-space are used in the formulation. The influence of trenches position and depth on the isolation efficiency is investigated through numerical examples. Also, the influence of medium degree of anisotropy on the response is addressed.

Introduction

In wave propagation control problems, trenching is one of the most widely used methods of foundation isolation. Trenches can be used either for blocking the elastic waves originating at a foundation which carries a dynamic load or for blocking externally originated waves from reaching a foundation carrying a vibration sensitive equipment. Trenches excavated around the protected foundation can be left empty or can be filled either with massive rigid materials, such as concrete, or with energy absorbing materials, such as foam or rubber.

Numerical methods, such as the Boundary Element Method, have been used to simulate the wave propagation throughout the soil by a number of authors, in order to access trench screening efficiency. But most of those simulations are restricted to the medium response to vertical dynamic loads applied on the foundation.

This article analyzes the dynamic behavior of the elastic half-space with a rigid massless disk foundation resting over it and with one or two cylindrical empty trenches excavated to a certain depth around the foundation. Time-harmonic, dynamic, horizontal, external loads are applied to the foundation.

An indirect formulation of the Boundary Element Method, along with a substructuring technique is used in the analysis. The half-space is divided in subdomains delimited by the trenches. Those subdomains are modeled separately and then equilibrium and displacements continuity conditions are imposed along the base contact between them. In this way, the presence of trenches with negligible thickness can be modeled. The field experiments [1] and numerical models [2] have showed that the trench width has almost no effect on the screening capability of the trench.

Influence functions, which are elastic solutions for distributed loads, developed for horizontally and vertically distributed loads applied inside a transversely isotropic half-space are used in the formulation. This approach provides two main benefits. First, the top free surface needs no discretization; only the soil-foundation interface, the trenches and the base contact between the subdomains are discretized by constant traction boundary elements. Second, the fictitious loads used in the indirect formulation of the BEM can be applied along the true boundary of the subdomains and the soil-foundation interface, because the influence functions used in the formulation are free of singularities. The influence functions were obtained by analytical integration of the Green's functions for ring loads applied inside a transversely isotropic half space, developed by Rajapakse and Wang [3].

A formulation which uses those influence functions have also been successfully used to model embedded foundations [4] and disk foundations surrounded by trenches, but subjected to vertical loads [5].

Problem Formulation

The soil-structure system considered in the present study is shown on Fig. 1, where a rigid, massless disk foundation is bonded to the top of a visco-elastic, transversely isotropic half space, and circled by two cylindrical open trenches with negligible width. Both trenches present the same depth. The foundation is subjected to a time-harmonic horizontal load, which generates elastic waves in the half space. These waves propagate away from the foundation and causes vibration in neighboring areas. The trenches are meant to block the elastic waves, thus reducing the vibration at points along the soil surface, outside of the trenches.

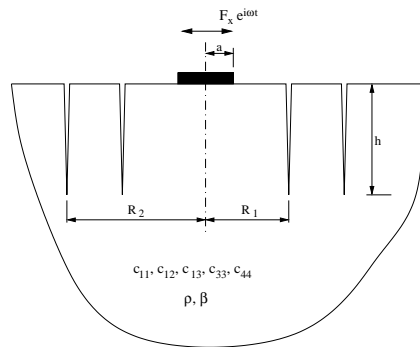


Figure 1: Disk foundation and cylindrical trenches

The problem geometry is characterized by the foundation radius a , the trenches radii R_1 and R_2 , and the trench depth h . The visco-elastic medium is characterized by its elastic constants $c_{11}, c_{12}, c_{13}, c_{33}$ and c_{44} ; the mass density ρ and the damping factor β . The material axis of isotropy coincides with the axis of symmetry of the geometric problem.

For the solution, the half space is divided in three regions or subdomains. Region 1 is formed the cylinder of soil delimited by the inner trench and the horizontal disk at its base. Region 2 is formed by the soil in between the two trenches and region 3 is formed by the remaining soil (see Fig. 2).

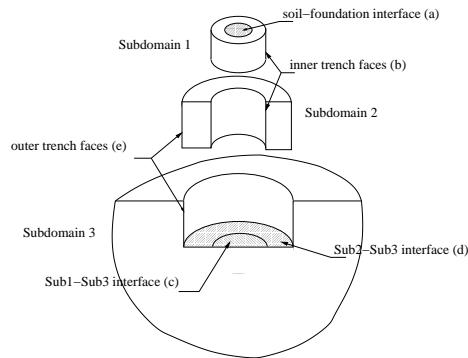


Figure 2: Half space divided in three regions

The displacement and traction relations along the faces of each region are formulated through an indirect version of the Boundary Element Method which uses influence functions. These functions are the solutions for the displacements and stresses caused by a distributed load applied inside the half space. Solutions for

horizontal, distorting, and moment loads (see Fig. 3) distributed along annular and cylindrical surfaces are used [4].



Figure 3: Horizontal, distorting, and moment loads

The soil-foundation and the interfaces of subdomains 1-3 and 2-3 are discretized in annular elements while the faces of the two trenches are discretized in cylindrical elements. Along each element, uniformly distributed fictitious loads, horizontal q_h , distorting q_d , and moment q_m , are applied and the effect of these loads at the center point of each element is determined by the influence functions:

$$\mathbf{u}_i = \mathbf{U}_i \mathbf{q}_i \quad (1)$$

$$\mathbf{t}_i = \mathbf{T}_i \mathbf{q}_i, \quad i = 1, 2, 3 \quad (2)$$

where the vectors \mathbf{u}_i and \mathbf{t}_i are the horizontal u_h, t_h , distorting u_d, t_d , and rotating u_m, t_m displacements and tractions at the elements on the boundary of region i , vector \mathbf{q}_i is the fictitious q_h, q_d, q_m loads applied at the elements on the boundary of region i , and matrices \mathbf{U}_i and \mathbf{T}_i are the displacement and stresses influence functions which gives the effect of a distributed load applied in a viscoelastic, transversely isotropic half space.

The kinematic compatibility and equilibrium conditions imposed on the soil-foundation interface (a) are expressed by:

$$\mathbf{u}_{1a} = \mathbf{C} \mathbf{u}_0 \quad (3)$$

$$\mathbf{f} = \mathbf{D} \mathbf{t}_{1a} \quad (4)$$

where \mathbf{u}_0 is the foundation displacement vector (horizontal displacement and rotation) and \mathbf{f} is the external load vector (horizontal force and rocking moment).

The trench faces (b) and (e) are traction free. So the boundary conditions at (b) and (e) are:

$$\mathbf{t}_{1b} = \mathbf{0}, \quad \mathbf{t}_{2b} = \mathbf{0} \quad (5)$$

$$\mathbf{t}_{2e} = \mathbf{0}, \quad \mathbf{t}_{3e} = \mathbf{0} \quad (6)$$

At the regions 1-3 and 2-3 interfaces (c) and (d), respectively, displacement compatibility and traction equilibrium are imposed. In this way, the boundary conditions at (c) and (d) are:

$$\mathbf{u}_{1c} - \mathbf{u}_{3c} = \mathbf{0}, \quad \mathbf{u}_{2d} - \mathbf{u}_{3d} = \mathbf{0} \quad (7)$$

$$\mathbf{t}_{1c} + \mathbf{t}_{3c} = \mathbf{0}, \quad \mathbf{t}_{2d} + \mathbf{t}_{3d} = \mathbf{0} \quad (8)$$

The conditions for regions 1,2, and 3 can be combined in the following systems of equations:

$$\begin{bmatrix} \mathbf{U}_{1a} & -\mathbf{C} \\ \mathbf{T}_{1b} & \mathbf{0} \\ \mathbf{T}_{1c} & \mathbf{0} \\ \mathbf{D}\mathbf{T}_{1a} & \mathbf{0} \end{bmatrix} \begin{bmatrix} \mathbf{q}_{1a} \\ \mathbf{q}_{1b} \\ \mathbf{q}_{1c} \\ \mathbf{u}_0 \end{bmatrix} = \begin{bmatrix} \mathbf{0} \\ \mathbf{0} \\ \mathbf{t}_{1c} \\ \mathbf{f} \end{bmatrix}, \quad (9)$$

$$\begin{bmatrix} \mathbf{T}_{2b} \\ \mathbf{T}_{2d} \\ \mathbf{T}_{2e} \end{bmatrix} \begin{bmatrix} \mathbf{q}_{2b} \\ \mathbf{q}_{2d} \\ \mathbf{q}_{2e} \end{bmatrix} = \begin{bmatrix} \mathbf{0} \\ \mathbf{t}_{2d} \\ \mathbf{0} \end{bmatrix}, \quad \begin{bmatrix} \mathbf{T}_{3c} \\ \mathbf{T}_{3d} \\ \mathbf{T}_{3e} \end{bmatrix} \begin{bmatrix} \mathbf{q}_{3c} \\ \mathbf{q}_{3d} \\ \mathbf{q}_{3e} \end{bmatrix} = \begin{bmatrix} \mathbf{t}_{3c} \\ \mathbf{t}_{3d} \\ \mathbf{0} \end{bmatrix} \quad (10)$$

The solution of these systems of equations, together with equation (1) can be put in the following form:

$$\mathbf{u}_{1c} = \mathbf{M}_1 \mathbf{t}_{1c} + \mathbf{m}_1 \mathbf{f} \quad (11)$$

$$\mathbf{u}_{2d} = \mathbf{M}_2 \mathbf{t}_{2d} \quad (12)$$

$$\mathbf{u}_{3c} = \mathbf{M}_{3cc} \mathbf{t}_{3c} + \mathbf{M}_{3cd} \mathbf{t}_{3d} \quad (13)$$

$$\mathbf{u}_{3d} = \mathbf{M}_{3dc} \mathbf{t}_{3c} + \mathbf{M}_{3dd} \mathbf{t}_{3d} \quad (14)$$

Using the conditions expressed by equations (7) and (8), the final system of equations is obtained:

$$\begin{bmatrix} \mathbf{M}_1 + \mathbf{M}_{3cc} & \mathbf{M}_{3cd} \\ \mathbf{M}_{3dc} & \mathbf{M}_2 + \mathbf{M}_{3dd} \end{bmatrix} \begin{bmatrix} \mathbf{t}_{1c} \\ \mathbf{t}_{2d} \end{bmatrix} = \begin{bmatrix} -\mathbf{m}_1 \mathbf{f} \\ \mathbf{0} \end{bmatrix} \quad (15)$$

The solution of this system of equations furnishes the tractions $\mathbf{t}_{1c} = -\mathbf{t}_{3c}$ at the regions 1-3 interface and $\mathbf{t}_{2d} = -\mathbf{t}_{3d}$ at the regions 2-3 interface, which can be used to calculate the fictitious loads \mathbf{q}_i and the foundation displacement \mathbf{u}_0 , through the equations (9) and (10). Then, the fictitious loads \mathbf{q}_i can be used to evaluate the displacements and stresses at any point in regions 1, 2, and 3.

Numerical Results

In order to test the ability of the proposed method to model the effect of a trench on the wave propagation phenomenon, numerical tests with two different materials were performed. The visco-elastic characteristics of those materials are shown in Table 1.

Material	c_{11}/c_{44}	c_{12}/c_{44}	c_{13}/c_{44}	c_{33}/c_{44}	β
Isotropic ($\nu = 0.25$)	3	1	1	3	0.01
Anisotropic	3	1	2.28	6	0.01

Table 1: Visco-elastic characteristics of the materials

The anisotropic material was chosen as to have approximately the same horizontal stiffness and the same Rayleigh wave-speed of the isotropic material. The damping factor was incorporated into the influence functions evaluation by considering complex valued elastic constants $c_{ij}^* = c_{ij}(1 + i\beta)$, where $i = \sqrt{-1}$.

The influence of the trench radii R_1, R_2 and depth h on the screening efficiency was investigated. The screening efficiency can be expressed by the amplitude ratio A_h defined as the ratio between the horizontal displacement amplitudes with the trenches and without them. The nondimensional frequency $a_0 = a\omega\sqrt{\rho}/c_{44} = 1$ was used in the efficiency investigation and the Rayleigh wave length for this frequency is $\lambda_R \approx 6a$.

The plots in Fig 4 show the amplitude ratio A_h along the half space surface, for the isotropic material, for three different trench configurations. The screening efficiency is clearly better with two trenches, when compared with the single trench configuration, for all cases. Also, it is noted that the screening efficiency increases as the trench depth increases. The usual requirement of 75% reduction in the amplitude vibration for a project to be considered successful is attained by the double trench configuration with $R_1 = 4a, R_2 = 8a, h = 4a$. It should be noted that the minimum depth normally required to get that efficiency with only one trench is of the same order as the Rayleigh wave length.

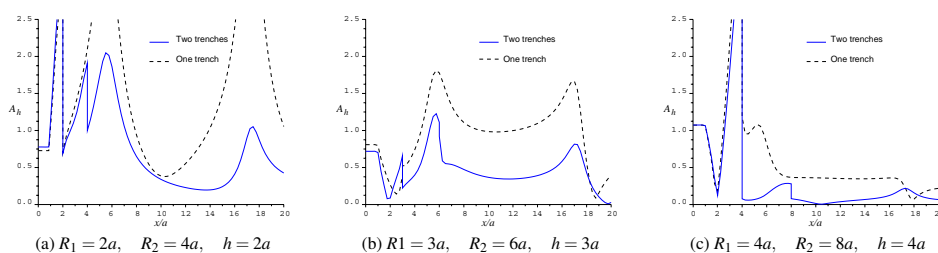


Figure 4: Amplitude ratio A_h along the surface of the isotropic medium

It is interesting to note that, for the two configurations using shallower depths, the amplitude ratio can be greater than the unity. This means that the presence of the trenches actually increases the vibration along the surface. This phenomenon may be due to the decreasing of the system global stiffness.

The plots in Fig. 5 show the amplitude ratio A_h along the surface for the same three trench configurations, but for the anisotropic medium. The differences between these plots and those in Fig. 4 are substantial. For the anisotropic case, the trenches provides much less reduction in the vibration amplitudes. In fact, the double trench configuration seems to be less effective then the single trench configuration for the two smaller trench dimensions, where A_h is greater than one. Even for the third trench configuration, the advantage of using two trenches instead of one is not clear.

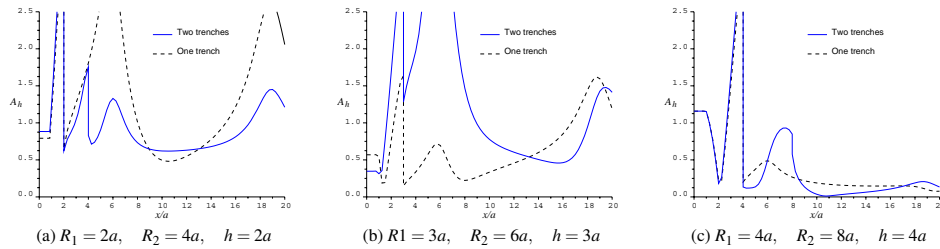


Figure 5: Amplitude ratio A_h along the surface of the anisotropic medium

It should be pointed out that only the horizontal displacement along the half space surface was used to generate the plots in Figs. 4 and 5. The points along the surface present vertical displacement also, which can be of the same order as the horizontal displacement. Those vertical displacement should be taken in account too in a complete analysis. Additionally, the same formulation and numerical implementation can be applied to the case of a rocking moment applied to the foundation, since the two cases, horizontal force and rocking moment, are coupled.

Concluding Remarks

A numerical method for the dynamic analysis of a rigid disk foundation bonded to a transversely isotropic half space with two concentric cylindrical trenches, using an indirect formulation of the Boundary Element Method with half space influence functions was presented. The proposed method was applied to a set of different cases of trench radii and depth and the obtained results show the advantage of using two trenches over a single one in most cases. The soil anisotropy has a marked effect on the amplitude ratio along the ground surface. Additional analyses are necessary to better understand the role of the material's elastic characteristics on the screening capability of the trenches. The numeric implementation can also be used to analyze the case of dynamic rocking moment applied to the foundation. The proposed method can be extended to deal with in-filled trenches. Both rigid and flexible filling materials can be considered in this case.

Acknowledgment

This work was partially supported by the Fundação de Amparo à Pesquisa do Estado de São Paulo, FAPESP.

References

- [1] R.D Woods, "Screening of Surface Waves by Trenches," *J. Soil Mech. and Found. Engrg.*, ASCE, **94**(4), 951–979 (1968).
- [2] S. Ahmad, T.M. Al-Hussaini and K.L. Fishman, "Investigation on Active Isolation of Machine Foundations by Open Trenches," *J. Geotech. Engrg.*, ASCE, **122**(6), 454–461 (1996).
- [3] R.K.N.D Rajapakse and Y. Wang, "Green's functions for transversely isotropic elastic half space," *J. Engrg. Mech.* ASCE. **119**(9), 1724–1746 (1993).

- [4] P.L.A. Barros, "Impedances of Rigid Cylindrical Foundations Embedded in Transversely Isotropic Soils," *Int. J. Anal. and Num. Meth. in Geomech.*, **30**(7), 683–702 (2006).
- [5] P.L.A. Barros and E. Mesquita, "Screening Efficiency of Double Circular Trenches as Active Isolation for Surface Foundations Subjected to Dynamic Loads," *18th Engineering Mechanics Division Conference*, ASCE, Blacksburg, VA, USA (2007).

The Method of Fundamental Solutions applied to Linear Elasticity with the use of a Genetic Algorithm.

Li Chong Lee B. de Castro¹, Glauceny Cirne de Medeiros² and Paul William Partridge³

^{1,2,3} Departamento de Engenharia Civil e Ambiental, Universidade de Brasília – UnB, Campus Universitário Darcy Ribeiro – 70910-900 - Brasília, DF, Brazil

¹ lichonglee@unb.br, ² glauceny@unb.br, ³ paulp@unb.br

Keywords. Fundamental Solutions, Dual Reciprocity, Genetic Algorithm, Optimization.

Abstract. The method of fundamental solutions (MFS) is an indirect boundary technique that avoids singularities by defining a fictitious surface which involves all of the problem domain. The method does not require any mesh or integration. In spite of these advantages the MFS was not immediately successful and one of the factors which contributed to this was the definition of the fictitious surface, given that in some cases the precision of the results depends on the distance which separates the fictitious surface from the geometry. Recently, the MFS has been applied successfully to problems of potential and elasticity considering the fictitious surface proposed by Bogomolny [2], which consists of a circle or a sphere for 2D or 3D problems, respectively.

Here the MFS is applied to linear elasticity problems with body forces employing the circle as proposed by Bogomolny and using a Genetic Algorithm in order to determine the radius of the same. In order to model the non homogeneous terms the MFS is combined with the Dual Reciprocity Method (DRM) in a similar way as is done in BEM, using a polyharmonic spline approximation function.

Introduction

The Method of Fundamental Solutions is attributed to Kupradze, [2]. It is an indirect boundary method which does not require a mesh or integration. The method avoids singular points by defining a fictitious surface which involves all of the problem domain. Optimization techniques have been used to calculate the position of each point on the fictitious surface, but such methods can be expensive, [1, 12, 13]. It has been shown by Bogomolny [2], that the fictitious surface is a circle for 2D problems and a sphere for 3D ones. The MFS using the circle as defined by Bogomolny, has been successfully employed in several recent papers such as [6, 8, 10, 15, 19]. A review paper about the different applications of the method was published by Fairweather and Karageorgis [7].

The MFS, in a similar way to BEM, can only be used in its pure form for cases in which a fundamental solution to the complete equation exists. If the problem involves a non homogeneous term some other method should be employed, such as for instance the Dual Reciprocity Method (DRM), [16, 20]. Here problems in linear elasticity with body forces are considered. The homogeneous part of the Navier equation is modeled with the MFS, using the circle of fictitious points proposed by Bogomolny, and the non homogeneous terms are modeled using DRM employing the Polyharmonic Spline approximation function. Here the MFS is applied to linear elasticity problems with body forces employing the circle as proposed by Bogomolny and using a Genetic Algorithm in order to determine the radius of the same. In order to model the non homogeneous terms the MFS is combined with the Dual Reciprocity Method (DRM) in a similar way as is done in BEM, using a polyharmonic spline approximation function with augmentation functions up to third order, [9, 19]. The radius of Bogomolny's circle is calculated using a Genetic Algorithm, [5, 11].

The Method of Fundamental Solutions.

Consider a linear elastic problem with body forces governed by the Navier equation eq (1):

$$Gu_{j,kk} + \frac{G}{(1-2\nu)}u_{k,kj} + b_j = 0 \quad (1)$$

Where G is given by $G = E/2(1+\nu)$.

The fundamental solutions employed are those used in BEM, [3].

We consider a domain Ω with boundary Γ enclosed within a fictitious circular surface

S, as shown in Fig. 1.

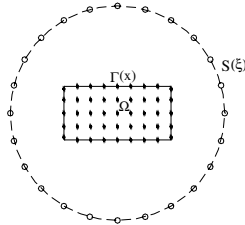


Fig 1 –Circle of fictitious points

Consider a point with coordinate (x) , belonging to boundary Γ_1 , having a boundary condition $u_i = u_i$. One can write,

$$\bar{u}_i - \hat{u}_i = \sum_{a=1}^N \left[u_{1i}^*(\xi_a, x) \cdot \alpha_a + u_{2i}^*(\xi_a, x) \cdot \alpha_{a+N} \right] \tag{2}$$

where u_{1i}^* and u_{2i}^* are fundamental solutions, and α_a are initially unknown coefficients. \hat{u}_i is a particular solution for the body force b_i , in eq. (1), to be considered later, N is the number of points on Γ . In the same way, for another point x belonging to Γ_2 , having a boundary condition $p_i = p_i$, one can write:

$$\bar{p}_i - \hat{p}_i = \sum_{a=1}^N \left[p_{1i}^*(\xi_a, x) \cdot \alpha_a + p_{2i}^*(\xi_a, x) \cdot \alpha_{a+N} \right] \tag{3}$$

where p_{1i}^* are p_{2i}^* fundamental solutions for surface tractions, \hat{p}_i is a particular solution and α_a the same coefficients seen in eq. (2).

The particular solutions \hat{u}_i and \hat{p}_i can be approximated using DRM as follows. For a given approximation function f , the particular solutions \hat{U}_{mk} are obtained in such a way that:

$$G \hat{U}_{mk, ll}^j + \frac{G}{(1-2\nu)} \hat{U}_{lk, lm}^j = f^j \delta_{mk} \tag{4}$$

The body forces b_i are approximated by:

$$b_i^j = \sum_{j=1}^M f^{ij} \beta_i^j \tag{5}$$

where β_i is a set of initially unknown coefficients, where $\beta_i \neq \alpha_i$ and j are collocation points which may belong to the boundary Γ or to the interior Ω , total M . Knowing the values b_i , the coefficients β_i are obtained using:

$$\beta_i = F^{-1} b_i \tag{6}$$

It is observed that each direction is independent. Writing the Navier equation using operator L :

$$L(\hat{u}_l) = G \hat{u}_{l, kk} + \frac{G}{(1-2\nu)} \hat{u}_{k, kl} \tag{7}$$

One obtains:

$$L(\hat{u}_l) = b_l \tag{8}$$

In such a way that

$$L(\hat{u}_l^i) = b_l^i \approx \sum_{j=1}^M f^{ij} \beta_l^j = L \sum_{j=1}^M \hat{U}_{lk}^{ij} \beta_k^j \tag{9}$$

Considering the first and last terms in eq (9):

$$\hat{u}_l^i = \sum_{j=1}^M \hat{U}_{lk}^{ij} \beta_k^j \tag{10}$$

In the same way, \hat{p}_i in eq. (3) can be obtained using:

$$\hat{p}_l^i = \sum_{j=1}^M \hat{P}_{lk}^{ij} \beta_k^j \tag{11}$$

In this way the particular solutions for the unknowns \hat{u} and \hat{p} can be obtained from the particular solutions for the approximation functions, \hat{U} and \hat{P} , and then we can obtain the following matrix equation using eqs. (2-3),

$$A\alpha = y \tag{12}$$

where A is a matrix of size $2N \times 2N$. Once a solution for α is obtained, one can calculate the unknown values of u_i , both on the boundary Γ_2 and on the interior, using eq. (2) transferring the particular solution to the right hand side. Values of p_i on Γ_1 can be found in a similar way using eq.(3). A similar procedure can be used to obtain values for stresses both for boundary points Γ and interior points Ω , [15].

To model the body forces with DRM the Polyharmonic Splines approximation functions $f=r^{2n} \log r$, are employed. In the case $n = 2$, one obtains the TPS (*Thin Plate Spline*), for which the particular solutions \hat{U}_{lk} and \hat{P}_{lk} were obtained, [4]. In the general 2D case for $f=r^{2n} \log r$, for $n = 2,4,6,\dots$, the particular solutions are given in [15].

Some results for particular solutions for augmentation functions can be found in [4,15].

Genetic Algorithm

Genetic Algorithms can be considered as a family of computational models inspired on evolution [11]. These algorithms use as a starting point a set or population of chromosomes in which each one contains a possible solution to the problem. Genetic operators are applied (selection, crossover and mutation) which recombine the information contained in the chromosomes, preserving and improving the critical information. Optimization is done by minimizing an objective function, which for the examples considered is in terms of the radius of the circle of fictitious points. Here a GA with binary coding is used as detailed in [5]. For a search space with continuous variables one has

$$\ell \geq \log_2(x^U - x^L) / \varepsilon \tag{13}$$

where ℓ is the representation of the values distributed continuously in the search space $[x^L, x^U]$, and ε is the decimal precision.

The convergence criteria was established as being that 80% of individuals should be the same. The population was fixed at 50 individuals, following a suggestion in [14]. A maximum of 200 generations was stipulated for the evolutionary process. If convergence was not obtained up to generation 160, the fitness function was changed from linear to exponential. If the last generation was reached the algorithm would return the best solution obtained. An elitist process was used in order that the two best individuals of a generation would pass automatically to the next, assuring that the best solution from the previous generation is not lost.

Genetic operators are applied after the selection of individuals by means of the roulette wheel method [11]. Three to six point crossover between pares of selected chromosomes, being 1 to 2 per alleles. All of the bits of all of the chromosomes , with the exception of the first and second were submitted to mutation with a probability of 2%.

Numerical Examples

The examples considered here and others were analyzed in [15] without considering the genetic algorithm. All the examples use Neumann-Dirichlet boundary conditions and are in plane stress.

For the problems considered a fitness function including a penalty function was employed transforming the problem with restrictions into a problem without restrictions (eq. (14)). This is an effective form of dealing with restrictions. The part *penal* (x) is defined for the problems considered in eq. (15).

$$F(x) = f(x) + penal(x) = Stress + penal(Stress, Displacement) \tag{14}$$

$$F(R_i) = \sigma_i + \alpha \sum_i \left[\begin{array}{c} \sigma_i \\ \sigma_{Exact} \end{array} \right] + \left[\begin{array}{c} u_i \\ u_{Exact} \end{array} \right] \text{ where } \alpha = 10000 \tag{15}$$

Gravitational Load problem. The geometry shown in fig. 2 was used. Elastic constants $E = 10000 \text{ MPa}$ and $\nu = 0.3$ were employed with $b_x = \rho g = 1$ and $b_y = 0$. 28 boundary points and 7 internal points equally spaced on the line $y = 0$ were considered.

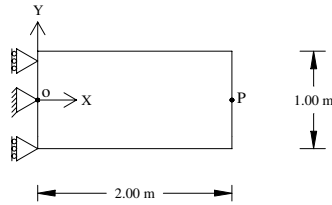


Fig. 2 – Geometry for the Gravitational Load problem.

The exact solution along OP is given in [17].

This problem is done according to eq. (15). The chromosome was coded using eq. (13). A search space in the interval [0;500] was chosen with a precision of 4 decimal places; in this way

$$\ell \geq \log_2 \frac{x^U - x^L}{\epsilon} \text{ and } \ell > 22,22$$

Given the above $\ell = 23$.

The best solution was obtained when an accuracy of 5 decimal places was considered for which case the displacements given in Table 2 were obtained.

Note that the accuracy influences directly the displacements obtained.

The MRM results (i) and (ii) differ because of different constants used in the solution and were obtained from [17], as were the exact solutions.

Table 1: Convergence for the radius of the circle of fictitious points for different values of accuracy.

Attempt	Accuracy	Generation	Radius
1	0.0001	27	346.3077
2	0.00001	17	460.84802

Table 2: Displacements at point P for the gravitational problem

Model	Displacement P
This paper	0.2000×10^{-3}
Medeiros et al [15]	0.2015×10^{-3}
MRM [17]	Solution (i) 0.2017×10^{-3} Solution(ii) 0.1988×10^{-3}
DRBEM with ATPS[18]	0.2012×10^{-3}
Exact Solution	0.2000×10^{-3}

In [15] circles of fictitious points with radiuses of 10, 100 and 1000 were used. In order to model the non homogeneous term the approximating function $f=r^2 \log r$ augmented with a 1 was employed. The same results were obtained considering approximating functions $f=r^4 \log r$ and $f=r^6 \log r$ augmented with a 1. In this case the augmentation term is sufficient to correctly model the constant body force, [18].

The SVD algorithm, [21], was used to solve the system eq. (12) This procedure showed itself to be better than the alternatives.

Centrifugal Load Problem. For this example the geometry shown in Fig. 3 was used.

The parameters employed were $a = 10$, $b = 20$, $\rho = 1$ and $\omega = 10$. r is the distance from the origin to the point considered and w is the angular velocity.

The problem was solved using 4 uniform sub-regions with 18 points each.

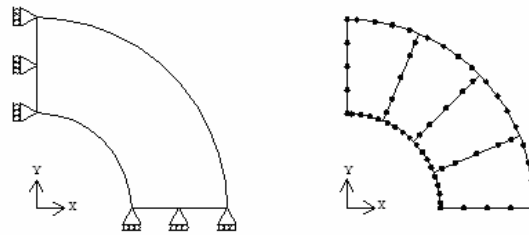


Fig . 3 Discretization of disc with subregions

The elastic constants considered were $E = 210000 \text{ MPa}$ and $\nu = 0.3$.

Eq. (15) is used for this problem. The chromosome is codified using eq. (13). For the search space in the interval $[0;500]$ was chosen and an accuracy of 5 decimal places was used.

Table 3: Convergence of the radius of the circle of fictitious points as a function of the accuracy.

Case	Accuracy	Generation	Radius
1	0.00001	127	135.94302

Results are given in table 4 for points on the boundary $x=0$. In [15] the radius of the circle of fictitious points is considered to be 100.

One circle of fictitious points was employed for each sub-region, using the same number of points as tem nodes on the sub-region, 18. The approximating function $f=r^2 \log r$, augmented with linear terms was used to model the non-homogeneous term. Tests with the approximating functions $f=r^4 \log r$ and $f=r^6 \log r$ produced the same results as in the previous example. The use of SVD was not necessary in this case.

Table 4: Results for the problem with centrifugal load.

Y	$\sigma_{\theta\theta}$			σ_{rr}			u_r		
	Present paper	MFS[15]	Exact	Present Paper	MFS[15]	Exact	Present paper	MFS[15]	Exact
10.0	34750	34763	34750	0.0	0.0	0.0	1.654	1.653	1.654
12.5	27468	27463	27468	3603	3636	3603	1.570	1.569	1.570
15.0	22614	22608	22614	4010	4000	4010	1.529	1.528	1.529
17.5	18739	18711	18739	2604	2621	2604	1.496	1.495	1.496
20.0	15250	15258	15250	0.0	0.0	0.0	1.452	1.451	1.452

Conclusions

Here a Genetic Algorithm of the generational type with binary coding and an elitist strategy was employed for optimization in association with the Method of Fundamental solutions applied to problems of linear elasticity with body forces. The circle of fictitious points due to Bogomolny was employed. The restrictions were considered using an objective function modified by the addition of a penalty term. In this way problems with restrictions can be treated as problems without restrictions. The penalty functions were defined using parameters constant during the whole process.

The methodology did not present any deficiency, for all the examples considered the expected result, the exact solution was obtained. Many other cases were examined which cannot be presented here for reasons of space.

Acknowledgements

The authors gratefully acknowledge the support of the Brazilian agency CNPq in financing this work.

References

- [1] J.R. Berger and A. Karageorghis *Journal for Numerical Methods in Engineering*, **45**, 1681-1694 (1999).
- [2] A. Bogomolny *Society for Industrial and Applied Mathematics Journal*, **22**, 644-669 (1984).
- [3] C.A. Brebbia and J. Dominguez *Boundary Elements an Introductory Course*, Computacional Mechanics Publications and McGraw-Hill Book Company (1989).
- [4] T.R. Bridges and L.C. Wrobel *Communications in Numerical Methods in Eng.* **12**, 209-220 (1996)
- [5] L.L.B. Castro and P.W. Partridge *Latin Am. J. Solids Struct.* **3**, 107-23 (2006).
- [6] C.S. Chen *Communications in Numerical Methods in Engineering*, **11**, 675-681 (1995).
- [7] G. Fairweather and A. Karageorghis *Advances in Computational Mathematics*, **9**, 69-95 (1998).
- [8] M.A. Golberg *Engineering Analysis with Boundary Elements*, **16**, 205-213 (1995).
- [9] M.A. Golberg and C.S. Chen *Boundary Element Communications*, **5** 57-61 (1994)
- [10] M.A. Golberg, C.S. Chen and S.R. Karur *Eng. Analysis with Boundary Elements*, **18**, 9-17 (1996).
- [11] D.E. Goldberg *Genetic algorithms in search, optimization and learning*, Addison Wesley (1989)
- [12] A. Karageorghis and G. Fairweather *Journal for Numerical Methods in Eng.* **44**, 1653-1669 (1999).
- [13] A. Karageorghis *Journal of Computational Physics*, **98**, 119-127 (1992).
- [14] N. Khan *Population Sizing in Genetic and Evolutionary Algorithms – Lecture Notes*, University of Illinois at Urbana-Champaign (2002).
- [15] G.C. Medeiros, P.W. Partridge and J.O. Brandão *Eng. Anal. with Boundary Elements* **28** 453-461 (2004)
- [16] D. Nardini, and C.A. Brebbia, C. A. *Boundary Element Methods in Eng.* 312-326, Springer (1982).
- [17] A.C. Neves, and C.A. Brebbia, *Int. Journal for Numerical Methods in Eng.* **31** 709-727 (1991)
- [18] P.W. Partridge and B. Sensale *Communications in Numerical Methods in Eng.* **13** 83-94 (1997).
- [19] P.W. Partridge and B. Sensale *Engineering Analysis with Boundary Elements* **24** 633-641 (2000).
- [20] P.W. Partridge, C.A. Brebbia and L.C. Wrobel *The Dual Reciprocity Boundary Element Method*, Computacional Mechanics Publications and Elsevier, (1992).
- [21] W.H. Press, B. P. Flannery, S.A. Teukolsky and V.T. Vetterling *Numerical Recipes, The art of scientific computing*, Cambridge University Press, Cambridge, (1986).